

Wave heating of the solar chromosphere

by

Momchil E. Molnar

B.Sc., Massachusetts Institute of Technology, 2016

M.Sc., University of Colorado, Boulder, 2018

A thesis submitted to the

Faculty of the Graduate School of the

University of Colorado in partial fulfillment

of the requirements for the degree of

Doctor of Philosophy

Department of Astrophysics and Planetary Science

2022

Committee Members:

Professor Steven Cranmer, Chair

Dr. Kevin Reardon

Professor Adam Kowalski

Professor Meredith MacGregor

Professor Cora Randall

Molnar, Momchil E. (Ph.D., Astrophysics)

Wave heating of the solar chromosphere

Thesis directed by Dr. Kevin Reardon and Professor Steven Cranmer

The solar chromosphere is well known to be in a radiative balance that requires an unaccounted source of heating. In this thesis I present observational constraints on the wave energy flux in the solar chromosphere, which is one of the favored chromospheric heating mechanisms. We employ chromospheric diagnostics ranging from the ultraviolet through the optical to the millimeter parts of the spectrum. We explore the formation mechanism of the millimeter solar continuum radiation first. We find that out-of-statistical equilibrium electron density determines its interpretation. We constrain the observed wave fluctuations in the solar atmosphere with cotemporal observations with the Atacama Large Millimeter Array (ALMA) and optical data from the Dunn Solar Telescope (DST). We combine these data with radiative hydrodynamic modeling with the RADYN code and find that the derived estimate for the acoustic wave energy flux is insufficient to maintain the radiative output of the solar chromosphere. Next we extend our work to higher layers in the solar atmosphere, by using the Interface Region Imaging Spectrograph (IRIS). We examine the acoustic flux in the upper chromosphere and find that acoustic waves are most probably not maintaining the chromosphere and the corona in their thermal state based on the estimates from advanced 3D Bifrost simulations. We also examine the center-to-limb variation of the velocity fluctuations observed with IRIS in order to constrain the transverse amplitudes in the solar chromosphere, which is an important input into coronal and chromospheric heating models. The signatures of transverse wave fluctuations in our analysis can serve as a spectroscopic constraint on the amplitudes of Alfvén waves in the solar chromosphere. In the last chapter we describe future avenues to extend our understanding of wave propagation in the solar atmosphere.

Dedication

To everyone who supported me along my path.

Acknowledgements

My deepest gratitude goes to my advisors and friends, Kevin and Steve, without whom this work would have been impossible. They have been exceptional mentors whose guidance through graduate school harnessed my scattered curiosity into a coherent drive to answer bigger questions.

I would also like to thank all my teachers and colleagues in CU and NSO, who were always available for a chat about radiative transfer, probability, inversions, and mostly my misunderstanding of the Sun – especially Dr. Ivan Milić, Dr. Gianna Cauzzi, Dr. Han Uitenbroek, Dr. Benoit Tremblay, Ryan Hoffman, and Neeraj Kulkarni. A major part of this thesis would not have been possible without the wonderful DST operators – in particular Doug Gilliam.

My interest for the cosmos was sparked by my family; it all started with my grandfather showing me the stars one clear night. My parents, further kindled my interest with encyclopedias about space. My family selflessly encouraged me to relocate across the globe to pursue my dream of becoming an astronomer, for which I am eternally grateful.

My Boulderite friends, who taught me so much about the mountains and the people living on their slopes, made the last six years an unforgettable adventure. You provided me with the needed respite from my solar qualms, while having a bit too much fun than advisable.

And thank you Amanda, for always being there for me. The greatest thing coming out of this pandemic is that we are still together (the main body of this work is the second). Also, I have to acknowledge our dogs – Vesta and Spas, who always distracted me when I needed a break.

Contents

Chapter

1	The solar chromosphere – the contemporary solar ignorosphere	1
1.1	History of chromospheric studies	4
1.2	The missing heating source of the chromosphere: a modern view	7
1.3	Chromospheric spectral line diagnostics formation	11
1.3.1	Formation of spectral lines under non-LTE conditions	12
1.3.2	Optical and UV spectral lines	17
1.3.3	The millimeter continuum – a chromospheric thermometer let loose	19
 2	 Methods for studying the chromosphere	 22
2.1	Observing facilities discussed throughout this work	22
2.1.1	The Interface Region Spectrograph (IRIS) in the UV	23
2.1.2	Optical and Near-IR observations with the Interferometric Bidimensional Spectrograph (IBIS) at the Dunn Solar Telescope	24
2.1.3	Millimeter observations with the Atacama Large Millimeter Array (ALMA)	26
2.2	Modern numerical tools for chromospheric studies	28
2.2.1	Models of the solar chromosphere	28
2.2.2	Synthesizing chromospheric spectral lines with the RH code	31

3	Solar Chromospheric Temperature Diagnostics: a joint ALMA-$H\alpha$ analysis	33
3.1	Introduction	33
3.2	Observations	35
3.2.1	DST/IBIS Observations	36
3.2.2	ALMA Observations and Processing	37
3.3	Diagnostics Comparison	39
3.3.1	IBIS Line Widths	39
3.3.2	ALMA Band 3 Intensity	40
3.3.3	Comparison between the ALMA Band 3 intensity and $H\alpha$ line width	40
3.4	Synthetic Spectral Diagnostics with RH	42
3.5	Conclusions	49
4	Acoustic fluxes inferred from IBIS and ALMA	52
4.1	Introduction	52
4.2	Observations and Data Processing	56
4.2.1	DST observations	57
4.2.2	ALMA observations	63
4.2.3	Solar feature classification	64
4.3	Observed high-frequency power in the spectral diagnostics	65
4.3.1	Observed high-frequency power in chromospheric spectral diagnostics	68
4.3.2	Properties of the observed power spectra	72
4.3.3	Velocity oscillations at different viewing angles	80
4.4	Modeling the observational signatures of acoustic waves in the chromosphere	85
4.4.1	Propagation of acoustic waves in the solar atmosphere	86

4.4.2	Synthesizing wave observables with RADYN	87
4.4.3	Estimating the acoustic flux in the Ca II854.2 nm data based on RADYN	91
4.4.4	Estimating the acoustic flux in the ALMA data based on RADYN	93
4.5	Inferred high frequency wave flux in the solar atmosphere	95
4.5.1	Wave flux inferred from the Ca II854.2 nm data	95
4.5.2	Inferred wave flux from the ALMA observations	101
4.6	Conclusions and future work	105
5	Wave fluxes derived from UV observations and 3D rMHD simulations	110
5.1	Introduction	110
5.2	Observations	112
5.2.1	Processing of the IRIS data	113
5.2.2	Processing of the IBIS data	116
5.3	Properties of the observed power spectra	117
5.3.1	Observed power law properties	117
5.3.2	Correlation between intensity and velocity oscillations	121
5.4	Acoustic wave propagation in solar simulations: 1D vs 3D models	124
5.4.1	RADYN models used	126
5.4.2	Bifrost models	126
5.4.3	Properties of the synthetic observables from Bifrost	128
5.5	Systematics of acoustic wave flux estimation from 3D vs 1D models	132
5.5.1	Measuring velocity fluctuations, but where?	134
5.5.2	Density of formation is model dependent	136
5.5.3	Transmission coefficient \mathcal{T} uncertainty	139

5.6	Inferring the acoustic wave flux	142
5.7	Discussion and conclusions	145
6	Center-to-limb variation of the observed wave properties	147
6.1	Introduction	147
6.2	Observations	151
6.3	Center-to-limb variation of high frequency velocity fluctuations	153
6.3.1	Doppler Velocity fluctuations	153
6.3.2	Intensity fluctuations	155
6.3.3	Correlation between intensity and velocity fluctuations	156
6.4	CLV of Doppler velocities and intensity from MHD models	158
6.4.1	Interpreting the observed CLV of the velocity fluctuations through geometric arguments	160
6.4.2	Spectral synthesis from inclined MHD cubes	165
6.5	Conclusions and discussion	166
7	Conclusions and outlooks for future work	167
7.1	Major results from this thesis	167
7.2	Future investigations motivated by the results in this thesis	170
7.2.1	Phase delays between chromospheric diagnostics observed with ALMA, IRIS and IBIS	170
7.2.2	The quiet solar chromosphere as a resonant cavity	173
7.2.3	Hi-C 2.1 coordination: Observing the chromosphere and corona in high-resolution	175

Bibliography	177
---------------------	------------

Appendix

A Monte-Carlo estimation of the white noise floor in the power spectra of spectrally derived quantities from first principles	194
B Appendix of the used acronyms and specific jargon	196

Tables

Table

4.1	Observations used in this work.	58
4.2	Summary of the power law properties.	72
4.3	Velocity oscillations decomposition properties.	84
5.1	IRIS observations used in this work.	113
5.2	Average power spectra properties.	117
5.3	Density of line formation and attenuation coefficients used for the wave energy flux calculations.	142
6.1	IRIS observations used for the CLV study.	152

Figures

Figure

2.1	Example observations from IRIS, IBIS and ALMA.	23
3.1	Context observations from SDO and IRIS.	35
3.2	IBIS H α observations.	37
3.3	Comparison of ALMA and IBIS observations.	43
3.4	Scatter plot of H α -ALMA comparison vs FAL models.	44
3.5	Results from the mm-wavelength RH synthesis.	45
4.1	Context observations from SDO and IRIS.	56
4.2	Average spectral profile of the observed spectral lines.	59
4.3	Context observations from IBIS.	60
4.4	Average ALMA brightness temperature maps.	62
4.5	Segmentation of FOV 2 of the solar surface.	66
4.6	Segmentation of FOV 1 of the solar surface.	67
4.7	Average power spectra of the derived spectral diagnostics.	69
4.8	Properties of the white noise of the observations.	71
4.9	Average observed velocity power spectra.	73
4.10	Total oscillatory power in observed spectral diagnostics.	74

4.11	Histogram of the observed power slopes.	76
4.12	Correlation between ALMA brightness temperature fluctuations and PSD properties.	77
4.13	Segmentation of FOV 2 observed with ALMA.	78
4.14	ALMA Band 3 PSD for different regions.	79
4.15	ALMA brightness temperature vs temperature fluctuations.	81
4.16	Close-to-limb velocity oscillation power.	82
4.17	Center-to-limb variation of velocity fluctuations.	83
4.18	Bottom boundary wave driver power spectra.	89
4.19	Acoustic flux in the RADYN models.	90
4.20	Synthesis results from the RADYN models.	96
4.21	Acoustic flux map from the IBIS observations.	97
4.22	Histogram of IBIS acoustic flux estimates.	100
4.23	Frequency-dependent contribution to the acoustic flux in the IBIS observations.	102
4.24	ALMA derived acoustic wave fluxes.	103
4.25	ALMA acoustic flux frequency contribution.	104
4.26	Comparison of ALMA and IBIS derived fluxes.	105
5.1	Preview of the data used in this study.	114
5.2	Properties of the observed power spectra.	118
5.3	Oscillation power between 5 and 20 mHz in the observations and the used Bifrost simulation.	122
5.4	Observed correlation between velocity and intensity oscillations.	123
5.5	Results from the Bifrost synthesis.	127
5.6	Amount of acoustic wave flux in the Bifrost model.	131

5.7	Comparison of synthetic Doppler velocities with atmospheric properties.	133
5.8	Plasma density of the line formation regions.	137
5.9	Comparison of Doppler velocity amplitudes and atmospheric velocity amplitudes. . .	140
5.10	Acoustic flux estimates from Bifrost simulations for IBIS and IRIS data.	143
6.1	Center-to-limb variation of the observed Doppler velocity fluctuations.	154
6.2	Center-to-limb variation of the observed intensity fluctuations.	157
6.3	Correlations of the integrated amplitudes of the observed intensity and velocity fluctuations.	159
6.4	Magnetic field inclination θ_B of the used Bifrost models.	161
6.5	Geometric models of the CLV of the observed Doppler velocity.	162
7.1	Phase delays of observed spectral diagnostics.	171
7.2	A resonant peak in the $H\alpha$ line COG velocity.	174
7.3	Hi-C 2.1 data overview.	175

Chapter 1

The solar chromosphere – the contemporary solar ignorosphere

The Sun is one of the most fascinating and important astrophysical objects – it provides our small, mostly blue, planet with the warmth and light required to sustain life. Without the blazing Sun, Earth would be a frozen piece of differentiated metal, rock and ice floating through space – without any of the beauty of our amazing biosphere. Throughout the history of our species the Sun has fueled the imagination of our ancestors and there have been numerous religious followings that place it as the central deity.

Nowadays, we understand that the Sun does not dwell in a central place in the universe. However, our favorite star still keeps a very special, but sometimes adverse, role for our civilization – beyond the electromagnetic energy input to our planet, it also creates the so-called space weather around Earth. Space weather is a term encompassing the plasma and electromagnetic conditions in space throughout the Solar system and is mainly determined by the output of the Sun. Space weather events can negatively affect our (semi-)conductor technology and vulnerable bodies. Hence, understanding space weather is crucial for being successful spacefarers.

My PhD thesis is about modeling a very particular part of the Sun, that might be the least understood currently – the chromosphere.¹ The chromosphere is a thin boundary layer, that is observed only with great effort and holds the keys to the connection between the observed solar

¹The title of this chapter was inspired by a quote from the SHINE 2022 meeting.

surface and the rest of the heliosphere. Why is the chromosphere important? To describe the rest of the solar atmosphere as a holistic system, that is interconnected by the magnetic fields and the mass flux across it, we need to understand how energy and mass flows through the chromosphere. The chromosphere is also important for the chemistry in planetary atmospheres, through its UV output. Understanding stellar chromospheres tells us about the habitability and possible false biomarkers of the exoplanets orbiting that star.

When we look at the Sun with our unaided eye, we see the bright visible surface of the Sun or the photosphere. This layer has a temperature of about 5,700 K and has one ten thousandth of the ambient atmospheric density at sea level on Earth. We perceive this as a *surface* because this is the first layer from which the solar photons can escape freely into the cold and dark Universe. In this photosphere, the plasma is in a regime wherein fluid effects dominate above the magnetic fields (plasma $\beta \gg 1$)².

Through the photosphere, the density continues to decrease quickly, with a density scale height (1/e decrease) of about 150 km and the temperature follows suit up to a certain height of about 500 km. One would expect that the temperature would continue to decrease the higher we go in the atmosphere, but if that was the case, this thesis would not exist. The layer where we see an initial increase in temperature with height above the solar surface is called the chromosphere. The chromosphere is a thin interface layer with a thickness of few a few thousand kilometers in which plasma and magnetic effects are roughly equally important (plasma $\beta \sim 1$) and non-ideal magnetohydrodynamic (MHD) effects are non-negligible. The low density of the chromospheric plasma decouples the radiation field from the local plasma conditions due to the low collisional rates. Hence, the light emitted from the chromosphere is often not-readily interpretable in terms of the local physical conditions. This, and a few other physical effects (time-dependent ionization,

²Plasma β is the ratio of the plasma to magnetic pressure.

long relaxation timescales) make the chromosphere very hard to model numerically, but with recent advances in massively parallel computing techniques have enabled large scale 3D simulations of this layer.

Above the chromosphere is the corona. The corona is the tenuous extension of the Sun that we observe during total solar eclipses. Magnetic field effects dominate the coronal dynamics (plasma $\beta \ll 1$), opposite to the situation in the photosphere. Since we cannot currently measure the global magnetic field vector in the corona, we rely on modeling the global solar magnetic field, based on the underlying photospheric field, to infer the magnetic properties of the coronal structure and its dynamic evolution. The continuous outward stream of plasma, the solar wind, originates from the solar corona. Our whole solar system is immersed in the solar wind, ourselves included, and if we want to be able to predict space weather events more accurately, we need to understand better the physical mechanisms that transport energy and mass through the solar atmosphere. In particular, the chromosphere is the interface between the reservoir of energy that the surface of the Sun is (photosphere) and the extended solar corona, where the solar wind and coronal mass ejections originate.

This introductory chapter stands as an abridged solar physics background to acquaint the reader with the topics discussed in this thesis. In section 1.1, I briefly provide a historical overview of chromospheric research, which provides a perspective of our rapid progress of chromospheric understanding. It also highlights the persisting overarching questions that are driving the field today which are still somewhat similar with those of a hundred years ago. Since this thesis is about addressing the biggest of those outstanding scientific questions – why is there a chromosphere in the first place? – an abridged summary of our current understanding of the heating mechanisms of the solar atmosphere is presented in section 1.2. Advancing our knowledge about the aforementioned question is only possible using the newest available methods in observations and modeling and

those are described in chapter 2.

1.1 History of chromospheric studies

A proper introduction to the history of chromospheric physics should start from the pioneers of this field, whose initial awe and challenges still haunt us 150 years later. The chromosphere extends 0.5% of the solar radius above the visible solar surface, which means it can be seen for a few seconds at the start and end of total solar eclipses as the reddish arc surrounding the solar limb, or sometimes as the suspended crimson clouds above the lunar limb due to large prominences. Catching this detail requires sharp vision, but in principle is observable with the naked eye. Even though in the following paragraphs we will discuss the discoverers of the chromosphere, most probably some of our ancient ancestors witnessed these phenomena during a total solar eclipse and could be considered co-discoverers of the chromosphere.

Generally, systematic solar chromospheric exploration is considered to have started during the total solar eclipse of 1860. At that eclipse the chromosphere was photographed for the first time. This effort was led independently by Father Angelo Secchi and Warren de la Rue, whose combined efforts showed that prominences were connected to the Sun, not the Moon. The name chromosphere was later suggested by the British scientists Norman Lockyer and E. Frankland, who were mesmerized by the multiple brightly colored emission lines originating from the chromospheric spectrum. Hence, the root of the word is *chromos*, which means color in Greek.

During the same time, spectroscopy was becoming a dominant tool in the astronomical domain. In 1868, Pierre Janssen and Lockyer independently showed that the chromosphere (and in particular prominences) could be routinely observed above the solar limb in bright spectral lines outside of eclipses. They performed their mostly observations in the hydrogen Balmer series lines. The extent of the solar chromosphere was measured to be between 5 and 11 Mm with a

radial orientation of their spectrograph slits. Using these spectrograph techniques, Father Secchi described with striking clarity the limb structures of the solar chromosphere. His account resembles very much what we call type-1 spicules – elongated thin “hairs” that pointed in various directions outward and had widths of a few hundred kilometers (which is an underestimation from what we know from modern instruments).

The next major milestone in observing the chromosphere was obtaining the first “flash” spectrum. Before 1869, observers had not yet observed a spectrum in which the chromospheric emission is not contaminated by the photospheric continuum. Charles Young was the first to observe this phenomenon during the eclipse of 1870 – he pointed his spectrograph slit radially toward the location of second contact. In the moment when the Moon covered the solar disc, he saw a multitude of emission lines for a few seconds. It wasn’t until the eclipse of 1883 when the flash spectrum was photographed for the first time. Flash spectra are valuable observations for studying the chromospheric plasma conditions, as they can provide relative and absolute photometric measurements of many lines which is a fundamental basis for modeling the chromospheric conditions (see the book by [van de Hulst, 1953](#), for a detailed account of eclipse results from that era).

With the advent of spectroheliographs – instruments which use a translating slit to take still images of the Sun in a narrow wavelength range – in the late 1890s and early 1900s, George Hale at Mount Wilson Observatory and Henri-Alexandre Deslandres at the Meudon Observatory discovered the multitude of structures of the solar chromosphere. They observed the Sun in the hydrogen Balmer lines and the Ca II H and K lines, which showed exquisite details of the solar chromosphere – mottles, fibrils and active regions revealed ubiquitous unseen before small scale structures.

The interpretation of the abundant chromospheric observations lagged behind until advances of atomic physics allowed for the correct interpretation of the spectral observations. Based on the

work by M. N. Saha for estimating the ionization state of stellar atmospheres (Saha, 1921) the chromospheric temperature and ionization states were found. In particular, work by Menzel (1931) and Cillié and Menzel (1935) provided some of the first estimates of the temperatures and electron densities in the chromosphere, based on hydrogen Balmer line observations.

These efforts spurred a discussion how the chromosphere can extend higher than expected from a pure radiative and hydrostatic balance. Some of the early theories included preferential heating of the Ca II ions (Milne, 1924) and turbulent pressure support, inferred from the widths of the observed chromospheric line profiles (McCrea, 1929). The theory proposed by McCrea is the first that had a mechanistic origin of the heating, which led to some of the modern ideas of chromospheric heating. A theory of wave heating was first introduced by Biermann (1946) and Schatzman (1949) wherein acoustic waves generated in the photosphere steepen into shocks into the chromosphere where they viscously dissipate. This theory was further advanced by the seminal paper by Lighthill (1952), presenting how sound waves could be generated by the turbulent motions in the photosphere.

Solar magnetic field measurements in the beginning of the 20th century were limited to sunspots, due to the low sensitivity of the available instruments. Hence, most theories of magnetic heating of the solar atmosphere were related to flares, closely confined to the regions of magnetic field concentrations. Giovanelli (1946) proposed for the first time that in the case of flares that the strong magnetic field plays a role in the energy release as the result of an electrical discharge. It was Sweet (1958) who suggested magnetic reconnection as the driving mechanism of solar flares. Hannes Alfvén predicted magnetically conducted waves in 1942 (now called Alfvén waves) and shortly after he proposed them as a viable heating mechanism for the solar atmosphere. Alfvén (1947) proposed that Joule (resistive) heating could dissipate the ubiquitous Alfvén wave energy in the upper solar atmosphere, driven by the turbulent horizontal photospheric plasma motions at

the footpoints.

1.2 The missing heating source of the chromosphere: a modern view

Before delving into the details of the currently favored heating theories of the solar chromosphere, I will introduce the evidence for the radiative balance requiring an additional heating mechanism. The missing heating in the chromosphere rests on the fact that the observed radiative balance requires additional source of energy, with an average additional energy flux on the order of a few kW m^{-2} (Withbroe and Noyes, 1977). To estimate the amount of radiative losses in the chromosphere, earlier work relied on 1D semi-empirical models of the solar atmosphere (Athay, 1976; Vernazza et al., 1981), which derived the atomic populations and radiative transition rates of the contributing atomic species. The most important spectral lines through which the solar chromosphere loses energy are the Ca II H&K lines, the Mg II h&k lines, the Ca II infrared triplet, the Hydrogen Balmer and Lyman line series, and the Fe II lines (Vernazza et al., 1981).

With the recent advent of reliable spectral inversion codes for chromospheric diagnostics (Socas-Navarro et al., 2015; Milić and van Noort, 2018; de la Cruz Rodríguez et al., 2019), more detailed estimates of the radiative losses based on chromospheric line inversions have been produced. Some of these results include time dependent high resolution estimates of the radiative losses in active region and flaring chromosphere (de la Cruz Rodríguez et al., 2019; da Silva Santos et al., 2022) and plage chromosphere (Morosin et al., 2022). These publications agree with the earlier results with the caveat that in very localized heating locations, much larger radiative losses are observed. This is not a surprising finding, as the earlier works were based on time-averaged and lower spatial resolution observations, which resulted in averaged down values of the radiative losses.

There are two major theories for chromospheric heating, one based on magneto-hydrodynamic waves and the other on magnetic reconnection/Joule heating from current dissipation. Observa-

tional evidence suggests that both processes might contribute at the same time to differing degrees in the different regions of the chromosphere, but the definitive evidence for the relative importance of their role is still missing. We describe in the following paragraphs the aforementioned heating mechanisms, their observable signatures and their relative importance for the different solar surface features.

As discussed in the previous section, wave heating of the chromosphere has been studied since the mid 20th century (Biermann, 1946; Schatzman, 1949). The main idea of the theory of acoustic wave heating is that the turbulent plasma in the upper convection zone drives sound waves (Lighthill, 1952), which propagate upward in the solar atmosphere. Due to the rapid decrease of the chromospheric density the waves steepen into hydrodynamic shocks, which are dissipated radiatively.

Since the early 1960s, ubiquitous periodic Doppler motions have been observed in the solar atmosphere (Leighton, 1960; Noyes and Leighton, 1963). Earlier work in the 20th century by Athay and White (1978) looked for line broadening in spectral lines, which would be a signature of unresolved motions due to “microturbulence”. They found that there is not enough wave energy flux in the unresolved wave motions to maintain the chromosphere. Further, Mein and Mein (1976) and Mein and Schmieder (1981) showed that waves with periods above 60 seconds do not carry enough energy to maintain the solar chromosphere. However, their observations suffered from low temporal and spatial resolution, which made their results a lower limit. Reviews of the earlier works on wave heating in the solar atmosphere are presented in Kuperus et al. (1981) and Narain and Ulmschneider (1990) with the references therein.

Fossum and Carlsson (2005, 2006) used TRACE observations (Handy et al., 1999) of the solar UV continuum at 160 nm and 170 nm interpreted with the radiative hydrodynamic code RADYN (Carlsson and Stein, 1992; Allred et al., 2005) to infer acoustic wave flux on the order of

400 $\text{W}\cdot\text{m}^{-2}$. This wave energy flux is too low by an order of magnitude, to maintain the quiet solar chromosphere. However, these studies drew criticism for their relatively low spatial and temporal resolution (Cuntz et al., 2007). Furthermore, using 1D models for interpreting UV continuum radiation were shown to potentially underestimate the solar wave flux (Wedemeyer-Böhm et al., 2007).

More recent work with ground-based telescopes employing adaptive optics, having significantly higher spatial resolution, reveal an order of magnitude higher acoustic wave fluxes. For example, Wunnenberg et al. (2002) using the Göttingen Fabry-Perot spectrometer at the VTT (Koschinsky et al., 2001) measured an acoustic flux in the Fe I upper photospheric spectral line on the order of 3 $\text{kW}\ \text{m}^{-2}$. This work showed the presence of acoustic flux in the base of the chromosphere, sufficient to balance a significant part of its radiative losses. Further work with very similar observational setups with the VTT (Bello González et al., 2009) and from the IMAX balloon-borne mission (Bello González et al., 2010) showed similarly high acoustic flux estimates, on the order of a few $\text{kW}\ \text{m}^{-2}$ at the base of the solar chromosphere. The progression of these studies, with increasingly higher spatial and temporal resolution revealed increasing wave fluxes, providing evidence for the need of even higher quality data.

The observations in the previous paragraph are of spectral lines which are formed in the photosphere. Some of the first acoustic wave flux estimates with Doppler velocities of true chromospheric lines were performed by Sobotka et al. (2016), Abbasvand et al. (2020a), Abbasvand et al. (2020b). They showed that the change in the acoustic wave flux between the photosphere and the chromosphere is on the order of magnitude as the flux required to maintain the solar chromosphere in its radiative state. These authors utilize velocity diagnostics from the Hydrogen Balmer lines and the Ca II IR lines. To calculate the fluxes, they use 1D static atmospheric models, which may not be suitable for describing the dynamic processes of wave propagation in the solar atmosphere,

as described in chapter 5 of this thesis.

The solar atmosphere is permeated with an ever-present magnetic field. Hence, Alfvén wave driven turbulence has been proposed as the heating mechanism of the solar atmosphere (Alfvén, 1947). These waves have been found ubiquitously throughout the solar atmosphere, from the chromosphere (De Pontieu et al. (2007), McIntosh et al. (2011)) to the corona (Tomczyk et al., 2007) and out in the solar wind (Unti and Neugebauer, 1968). The drivers of the Alfvén wave modes are believed to be the motions of the magnetic field footpoints rooted in the solar photosphere. Alfvén wave turbulence has been modeled extensively as a heating mechanism, that could provide the required energy for maintaining the solar chromosphere and corona (van Ballegoijen et al., 2011) and the solar wind (Cranmer et al., 2007). This physical model has been effectively applied for other stars where the mass losses are effectively predicted (Cranmer and Saar, 2011). I will present an observational constraint of the Alfvén wave amplitudes in the chromosphere through observations of the center-to-limb variation of the observed Doppler velocity and line core intensity fluctuations in chapter 6 of this thesis.

Internal gravity waves contain a large amount of energy contained in the solar photosphere. Internal gravity waves are low-frequency oscillations driven by buoyancy that are found ubiquitous across the solar system – in planetary atmospheres, in Earth’s oceans, and in the radiative cores of stars. Internal gravity waves propagate with frequencies lower than the Brunt-Väisälä frequency of the system. Internal gravity waves are evanescent in the chromosphere, but can propagate in the photosphere (Mihalas and Mihalas, 1984). Their energy flux is on the order of 5 kW m^{-2} , similar to the energy requirement for maintaining the solar chromosphere (Straus et al., 2008; Kneer and Bello González, 2011). Since gravity waves can couple to Alfvén waves (Lighthill, 1967), further studies of their properties are needed to constrain their contribution to the energy balance of the upper solar atmosphere.

Electric currents and Joule heating from small scale magnetic energy or current dissipating events are the other broad category for chromospheric heating mechanisms (Rabin and Moore, 1984; Parker, 1988). In this thesis we do not present any constraints to these models, but the author firmly believes that wave and magnetic dissipation processes are intricately connected in the solar atmosphere, leading to both being significant for the observed plethora of phenomena in the solar atmosphere (Gomez et al., 2000; Peter, 2015).

1.3 Chromospheric spectral line diagnostics formation

The relatively low density in the chromosphere leads to lower collisional rates between the plasma particles. This lack of thermalization in the chromosphere leads to a thermodynamic state that is significantly out of local thermodynamic equilibrium (Carlsson et al., 2019). The radiation field does not follow a Planckian distribution corresponding to the the local plasma temperature. Furthermore, atomic populations and ionization states in the chromosphere also depend on the radiation field, which can be non-locally determined. The past state of the plasma could also determine the ionization state due to the long relaxation timescales, compared to the timescales of ionizing events (Carlsson and Stein, 2002). We will refer to these plasma conditions as non-LTE. These physical conditions make the interpretation of spectral lines originating from the chromosphere to be highly model dependent. Recently, spectral inversions have become more accessible for studying chromospheric plasma conditions due to the availability of sufficient computational resources. Spectral inversions are methods that alter solar atmospheric models to reproduce synthetic observables as close as possible to the actual real data (e.g. in Socas-Navarro et al., 2015; Ruiz Cobo et al., 2022). Results from inversions are very impressive in their ability to reproduce solar observations, but we need to keep their limitations in mind – they operate under the approximation of hydrostatic equilibrium and do not account for the temporal history of the ionization state of the

chromospheric plasma (Hofmann et al., 2022). Furthermore, their inability to return an absolute height scale makes the interpretation and comparison of separate columns of the inversion results challenging.

We will describe in this section the physics behind the radiative transfer problem and the peculiarities of the formation of different parts of the solar spectrum under conditions of non local thermodynamic equilibrium. This chapter is only intended as a short review and the interested reader should seek the in-depth review by Hubeny and Mihalas (2014) for further discussion of astrophysical non-equilibrium radiative transfer.

1.3.1 Formation of spectral lines under non-LTE conditions

To understand the formation of spectral lines in the solar atmosphere we need to define a few physical quantities that are essential for the discussion and conclusions in the following chapters. Let us start with the equation of radiative transfer:

$$\frac{dI_\nu}{dz} = j_\nu - \alpha_\nu I_\nu \quad (1.1)$$

where I_ν is the specific intensity of light at frequency ν ; j_ν is the emissivity of the medium, with units of specific intensity per unit length; and α is the absorption coefficient, with units of inverse length. We note that the specific intensity I is a quantity that depends beside on wavelength and location in the atmosphere, but also on direction. A simple illustration of the intensity directionality is the case of scattering from an electric dipole. In this case the intensity along the dipole moment is zero and perpendicular to it is maximal.

Working in geometrical distance is not convenient for describing the radiation propagation, because the opacity changes are closely related to the scales of the density stratification and temperature changes, not the height scale as much. Hence, to simplify the mathematical description

of the problem we define a new variable, called optical depth τ_ν , defined as:

$$d\tau_\nu = -\alpha_\nu dz \quad (1.2)$$

Optical depth τ_ν is a dimensionless quantity with a unity change signifying a free mean path of a photon with frequency ν . Transforming between geometric distance and optical depth depends on knowing the absorption coefficient. However, an absolute shift of the emitting plasma – if the emitting star is 1 AU away or 100 AU away – is not readily retrievable from the radiative transfer equation alone.

We can rewrite equation 1.1 using the definition of equation 1.2 in optical depth scale:

$$\frac{dI(\tau, \phi, \theta, \lambda)}{d\tau} = S(\tau, \phi, \theta) - I(\tau, \phi, \theta, \lambda) \quad (1.3)$$

where we have noted as S , the quantity called *source function*, defined as the ratio of the specific emissivity to the absorption coefficient $S_\nu = j_\nu/\alpha_\nu$ (Mihalas (1978)). In particular, the intensity is a quantity that depends on the location (τ or \mathbf{x}), direction (ϕ, θ), and wavelength (λ), as well as polarization state. The implicit dependence of the source function on the intensity on the RHS of Equation 1.3 makes it one of the most numerically demanding to solve in large MHD simulations, due to its high dimensionality and high computational cost to obtain. In particular, in the lower solar atmosphere (photosphere and chromosphere) the radiative term in the energy equation is very significant and needs to be accurately estimated. Hence, multiple approximations to the radiative transfer equation solution are made in large scale plasma simulations keep the problem numerically tractable (Leenaarts, 2020).

Equation 1.3 is an ordinary 1st order differential equation, that can be solved readily, if we know the dependence of the source function on optical depth $S(\tau_\nu)$ and the boundary condition

of incident radiation $I^*|_{\tau_\nu=\infty}$. For the simplified case of constant source function S_ν , its solution simplifies to:

$$I_\nu(\tau) = I_\nu^* e^{-\tau_\nu} + S_\nu(1 - e^{-\tau_\nu}) \quad (1.4)$$

This solution of the radiative transfer equation has pedagogical value as it provides us with two asymptotic behaviors of environments with very large and very small optical depths. These two cases are readily observed in the solar atmosphere. In the case when τ_ν is significantly less than one ($\tau_\nu \ll 1$), Equation 1.4 simplifies to the condition that the outgoing intensity is on the order of the incoming intensity I^* plus a small contribution from the source function $S_\nu\tau_\nu$. This is the optically thin regime, because the optical thickness of the emitting plasma is significantly smaller than unity. Coronal spectral lines are formed under such conditions. In off limb coronal observations usually there isn't a significant background illumination ($I^*(\tau_\nu) = 0$), hence the outgoing intensity equals to $S_\nu\tau_\nu$. The coronal source function is determined through both the number density of the emitting species and temperature, which controls the ionization and population states, of the emitting plasma. Hence, coronal spectral observations provide a joint diagnostic for both the temperature and the squared number particle density. To disentangle the two physical quantities a combination (of two or more) of spectral lines are used, or more advanced inversion techniques based on the differential emission measure are employed, which can also tell us about the coronal electron density.

When the optical depth of the medium is significantly larger than unity, the term dominating the solution of equation 1.4 is the source function S_ν . This is the *optically thick* regime, where the original incident intensity does not bear an imprint on the outgoing intensity. For strong chromospheric spectral lines, their cores are formed with optical thickness of $\tau \gg 1$. In this case

knowing the source function is essential for finding the solution of the radiative transfer problem.

Determining the source function in the chromosphere where plasma quantities are not always locally determined is a significant challenge. This is particularly important in situations where radiation illuminating plasma from a far distance creates a non-LTE atomic population, resulting in altered radiative transition. In order to solve this problem, we usually employ numerical tools based on iterative operator methods. An example of one such approach is the Accelerated Lambda Iteration (ALI). ALI is based on the Lambda operator Λ that acts on the source function to return the emerging intensity $I_{\nu\mu} = \Lambda_{\nu\mu}[S_{\nu\mu}]$, where ν indices are frequency and μ are angles (Hubeny, 2003). By iteratively finding the source function and then updating the atomic (and molecular) level populations, we can reach a converging solution of the source function under non-LTE conditions by the subsequent application of the Lambda operator.

To illustrate how ALI works, I will briefly describe the two-level atom system, following the review by Hubeny (2003). Even though this illustration has mostly pedagogical value, it illuminates the internal workings of modern non-LTE chromospheric radiative codes. First, we can integrate over all angles for the frequency of interest; we get an averaged version of the Lambda operator \bar{J} : $\bar{J} = \Lambda[S]$, where \bar{J} is the mean intensity and S is the source function. In the case of a two level atom we can represent the source function as (Mihalas, 1978):

$$S = (1 - \epsilon)\bar{J} + \epsilon B \tag{1.5}$$

where ϵ is the collisional destruction probability of a photon, and B is the Planck function. One way to proceed is to calculate the source function, for a given B and ϵ for an atmosphere, where we can iteratively apply the Lambda operator to update the source function from iteration n to

iteration $n+1$:

$$S^{n+1} = (1 - \epsilon)\Lambda[S^n] + \epsilon B \quad (1.6)$$

This is numerically robust method, that at each iteration the solution for the source function linearly approaches its true value. However, it has very slow convergence properties (Auer, 1991).

The idea behind the accelerated lambda iteration (ALI) method is to split the exact Lambda operator in the sum of approximate Λ^* and exact one Λ :

$$\Lambda = \Lambda^* + (\Lambda - \Lambda^*) \quad (1.7)$$

where the choice of the approximate Lambda operator Λ^* is a non-trivial task. Usually it is chosen be a tri-diagonal matrix, which is easy to invert. The elements of the approximate operator could constitute for example the diagonal elements of the exact Lambda operator, estimating which is an involved process in itself too (Hubeny, 2003).

We can rewrite the source function change δS^{n+1} after an iterative step as:

$$\delta S^{(n+1)} \equiv S^{(n+1)} - S^{(n)} = [1 - (1 - \epsilon)\Lambda^*]^{-1} [S^{FS} - S^{(n)}] \quad (1.8)$$

where S^{FS} is the formal solution of the radiative transfer equation. Fast formal solvers of the radiative transfer equation are readily available and will not be discussed here, but the reader should consult Hubeny (2003) for further references about them. Comparing equation 1.8 with the equation for the regular Lambda iteration: $\delta S^{(n+1)} = S^{FS} - S^{(n)}$, we see that the convergence of the source function is accelerated by the term containing the approximate Lambda operator. This “boosting” is very significant compared to the regular Lambda iterations, on the order of $\epsilon^{-1/2}$, which is very significant for scattering lines with high photon destruction probabilities ($\epsilon \ll 1$).

Many results in this thesis are based on the non-LTE radiative transfer code RH described in Section 2.2.2, which uses an operator method very similar to the one described above (Uitenbroek, 2001).

1.3.2 Optical and UV spectral lines

Observing the chromosphere on disk against the background of the denser and brighter at most wavelengths photosphere is challenging, due to the superposition of the photospheric continuum over the fainter chromospheric emission. However, there are multiple spectral lines that are formed in the chromosphere, such as the hydrogen Lyman and Balmer series lines, singly ionized magnesium and calcium resonant doublet states (including the infamous Ca II H&K and the Mg II h&k lines). The physical complication of interpreting these lines are the fact that their source functions are not well correlated with the local plasma conditions, because they are strongly scattering lines, making their formation non-LTE. In particular, the source function could have significant scattering contributions (similar to the first term on the right hand side of equation 1.5) or the atomic populations are not in equilibrium with the local temperatures, which could result in departing from equilibrium emissivity. Current solar models do not reproduce these lines with great accuracy, which makes them an important benchmark in future modeling efforts (Carlsson et al., 2016). Furthermore, the chromospheric radiative losses in those lines are important drivers of the thermodynamic state of the chromosphere itself.

Observing the optical and near infrared (near-IR, less than 1 micron), chromosphere has been performed for the last hundred years due to the available detectors and accessible observing windows from Earth's surface. The solar spectral lines in the optical part of the spectrum have the benefit that they have higher intensities than the ones in the UV, allowing for more precise photometric and spectropolarimetric studies. Furthermore, the observing from the ground allows for bigger aperture

telescopes and more complex instruments with greater flexibility, compared to space-borne missions. However, ground based observing has its own challenges due to Earth’s atmosphere blurring of the images and the time varying atmospheric extinction, complicating radiometric measurements.

Currently, most spectropolarimetric observations are performed in the optical and in the near-IR. In the optical, the most prominent lines for estimating the magnetic field in the solar photosphere are the Fe I 630.1 nm and 630.2 nm lines, observed by Hinode; Fe I 617.3 nm line observed by HMI; Ni I 676.8 nm line observed by GONG. In the chromosphere, lines such as the Ca II 854.2 nm and He I 1083.0 nm are used regularly for high resolution spectropolarimetric studies. Lines like the Hydrogen Balmer series are formed throughout the lower solar atmosphere, providing us with morphological data about the structures there. All of these lines carry information about the thermodynamic state of the plasma in the solar atmosphere, that can be retrieved with spectropolarimetric inversions.

Observing the ultraviolet (UV) part of the spectrum is also challenging, since Earth’s atmosphere absorbs strongly most of the radiation under 300 nm. However, a lot of the chromospheric (and coronal) diagnostics fall in that part of the spectrum, creating the need for UV spacecraft observatories. Skylab, SOHO, Yohkoh, TRACE, SDO, Hinode, IRIS and other space observatories revolutionized our understanding of the hotter upper solar atmosphere. Furthermore, space-borne missions provide moderate resolution and continuous solar observations unaffected by weather. Space-based UV observations do not suffer from atmospheric-induced seeing and can be stably radiometrically calibrated. On average, UV chromospheric and transition region lines are formed higher than the ones observed in the optical, making them a valuable addition to any multi-height study. Recent results from polarimetry in the Mg II h&k lines with the CLASP rocket mission (Kano et al., 2012) successfully estimated the magnetic fields in plage and internetwork regions (Ishikawa et al., 2021). This recent study paved the way for measuring the magnetic field at the

transition region (TR) which will allow for magnetic field extrapolation from the top of the chromosphere, allowing for better coronal magnetic field extrapolations. Another interesting result from the CLASP rocket mission was the hydrogen Lyman- α polarimetric observations, that showed a center-to-limb variation inconsistent with current models (Kano et al., 2017). These transition region observations are hinting at a significantly more corrugated nature of the transition region than our current models predict, pointing toward the need for higher resolution simulations and beyond MHD models (Martínez-Sykora et al., 2020b).

1.3.3 The millimeter continuum – a chromospheric thermometer let loose

Millimeter and submillimeter radiation forms in the typical solar atmosphere from free-free emission processes (Wedemeyer et al., 2016). The millimeter absorption coefficient from ion-electron free-free absorption α_{mm} is given by the following expression (Kundu, 1965):

$$\alpha_{mm} = \xi(T, e) \frac{n_e^2}{n\nu^2 T^{3/2}} \quad (1.9)$$

where $\xi(T, e)$ is a slowly varying function of the plasma temperature and electron density, and is generally equal to about 0.2 for the chromosphere; n is the index of refraction of the medium. The electron density n_e is the quantity through which the ionization state of the plasma enters the millimeter continuum formation. Hence, even though the source function *per se* is in LTE, the opacity of the mm-radiation is significantly out of equilibrium in the chromosphere, due to the out of equilibrium electron density (Carlsson and Stein, 2002).

The millimeter observations do provide however a direct measurement of the temperature of the emitting plasma. Black bodies follow the Rayleigh-Jeans relation in the millimeter and radio regions of the electromagnetic spectrum – in this case, the millimeter intensity scales linearly with the electron temperature of the emitting plasma. For all of our following discussion, we will assume

that in the chromosphere the electron and proton kinetic temperatures are the same.

The actual height of formation of the millimeter continuum is sensitive to the non-LTE ionization state of the chromosphere. Another complication of the millimeter radiation interpretation is that the range of heights contributing to the intensity might be as much as a few scale heights, making the inference of plasma properties to a singular layer in the chromosphere far from straightforward (Wedemeyer et al., 2016). Recent results by da Silva Santos et al. (2018) have shown that Atacama Large Millimeter Array (ALMA) data interpreted with inversion codes can retrieve atmospheric models that are better constrained in the upper chromosphere. However, the inferred quantities do not seem to agree well with other independent chromospheric diagnostics (Hofmann et al., 2022). Some of the shorter wavelengths accessible with ALMA probe the temperature minimum of the solar atmosphere, where many other spectral diagnostics are insensitive to the plasma conditions (Alissandrakis et al., 2022).

Previous work, before the commissioning of ALMA for solar observations, has been based on significantly lower-resolution observations with the James Clerk Maxwell Telescope (Lindsey et al., 1995) and the Berkeley-Illinois-Maryland Array (BIMA) (Loukitcheva et al., 2009). These observations have been used to constrain the electron densities above the solar limb and provided estimates for the chromospheric temperature profiles. However, these observations were not of sufficiently high angular and temporal resolution to explore the small scale structures in the solar chromosphere such as shocks, spicules and fibrils. For example, previous work with BIMA by Loukitcheva et al. (2009) showed the close correlation between photospheric magnetic flux and the solar intensity at 3.5 mm with a spatial resolution of about $3''$ and cadence of 30 seconds.

With the commissioning of ALMA for solar observations, we can start observing the solar chromosphere on the temporal and spatial scales that has been previously studied in the optical and UV. Including the millimeter continuum in inversions will allow for an additional constraint

of the solar thermal structure where only UV observations before were sensitive (da Silva Santos et al., 2018). Ongoing studies include sunspot oscillations, spicules, waves and shock propagation, cold CO clouds and many other solar phenomena (see for more examples Wedemeyer et al., 2016). The capabilities of ALMA are described in detail in Section 2.1.3. We present some of the first results of ALMA science, where we compare in detail optical and mm-derived diagnostics and the derived thermal chromospheric properties in Section 3.

Chapter 2

Methods for studying the chromosphere

Our understanding of solar and stellar chromospheres has been advanced by substantial recent progress in both observational and modeling methods, which I describe in this chapter. The described methods are the foundation for understanding the work presented in the following chapters. I present first the observational tools used throughout this thesis, including UV, optical/near-IR and millimeter telescopes with an emphasis on their suitability for studying waves in the solar chromosphere. To enable the interpretation of the non-LTE chromospheric spectral lines, we rely on (magneto-)hydrodynamic (MHD) models, that include much of the relevant physical processes determining the chromospheric conditions and wave propagation. I briefly describe in the second section of this chapter the numerical tools and models of the solar atmosphere used in this thesis, ranging from 1D semiempirical to 3D *ab-initio* radiative magnetohydrodynamic (rMHD) models. I also describe the methods for synthesizing observables out of these models with the RH code.

2.1 Observing facilities discussed throughout this work

The Sun radiates light in all wavelengths of the electromagnetic spectrum, from gamma-rays to radio waves. Because the emitting mechanisms and location of optical depth unity vary across the spectrum, we can probe various atmospheric layers by observing different wavelengths. The solar chromosphere, our main interest in this work, can be observed in the UV continuum and UV

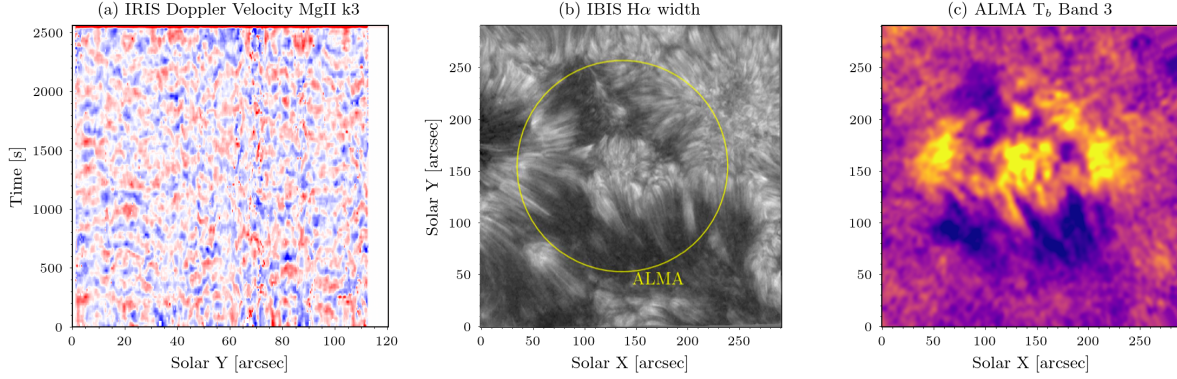


Figure 2.1: Example data products from the three main observatories utilized in this study: Panel (a) shows a map of Doppler velocity from the IRIS spacecraft scaled between ± 2 km/s in the Mn I 280.1 nm line; Panel (b) is a map of the line width of the Hydrogen Balmer- α spectral line taken with IBIS instrument; Panel (c) shows a brightness temperature map observed with ALMA at 3.0 mm wavelength which was cotemporaneously observed as the one in Panel (b).

lines, as well as in optical and in IR lines, and in the millimeter continuum. Each of these spectral regions has different properties, resulting in unique advantages and disadvantages for each one. All are utilized in this work to derive complementary plasma properties at different regions. This multi-height approach is very suitable for studying vertical wave propagation through the solar atmosphere. In the following paragraphs I describe the three instruments used in this thesis to study the chromosphere in the UV, optical, near-IR, and millimeter wavelengths.

2.1.1 The Interface Region Spectrograph (IRIS) in the UV

The Interface Region Spectrograph (IRIS) is a small explorer class (SMEX) NASA space mission designed to observe the connection between the solar chromosphere and transition region through high temporal, spatial, and spectral resolution spectroscopy (De Pontieu et al., 2014). IRIS observes in the UV regions between 133.2-135.8 nm, 138.9-140.7 nm and 278.3-283.4 nm and also provides corresponding slit jaw images in four filter passbands – C II 133 nm, Si IV 140 nm, Mg II k 279.6 nm and Mg II h wing 280.3 nm (slit jaw images are images of the surrounding solar area around the slit giving context about the surrounding solar area). These spectral regions provide

information about the solar atmosphere extending from the photosphere through the chromosphere and transition region (TR). This comprehensive set of observables has allowed many successful studies on topics ranging from the quiet Sun, active regions, flares, and coronal heating.

Throughout my work, I utilize the IRIS capabilities for high-cadence spectroscopy of the the Mg II wavelength window (278.3-283.4 nm), that provides us with multiple spectral lines that sample the photosphere (Mn I 280.1 nm) and the the chromosphere (Mg II h&k lines) (Pereira et al., 2013; Leenaarts et al., 2013). To extract line parameters reliably in the quieter (and often fainter) regions of the solar atmosphere, I relied on using sit-and-stare observations from early in the mission, when the efficiency of the detector and optics was highest (Wülser et al., 2018). The cadence (and exposure times) of the data used for the quiet Sun was 16 seconds (~ 31 mHz Nyquist frequency) and 9 seconds for plage regions (~ 52 mHz Nyquist frequency) and spatial resolution of $0.32''/\text{pixel}$ (sampling of $0.16''/\text{pixel}$). The IRIS observations database is a treasure trove of solar data, allowing for archival studies, as the one in Chapter 6. For extracting the line properties of the IRIS observations, I relied on the excellent SSWIDL IRIS library provided by the IRIS team. A sample Doppler velocity map derived from the IRIS instrument is presented in Figure 2.1, Panel (a).

2.1.2 Optical and Near-IR observations with the Interferometric Bidimensional Spectrograph (IBIS) at the Dunn Solar Telescope

The Dunn Solar Telescope (DST) is an optical telescope in Sunspot, New Mexico, United States of America. The DST has a 76 cm aperture on a turret that redirects the light down to a 64 inch mirror $f/72$ mirror (Dunn, 1964). The high magnification needed for good thermal control results in a long optical path and the main mirror is located about 200 feet below the ground level. The whole optical path of the telescope is in an evacuated chamber, which minimizes the internal

turbulence. The optical beam is directed to a rotating platform centered around the optical axis of the telescope, which is suspended on an 11 metric ton mercury bearing. The liquid mercury bearing allows for the smooth rotation of the telescope while dampening vibrations. The unique, rotating design of this telescope negates the need for an optical image derotator, which reduces the number of reflecting surfaces in the optical path and improves the image quality. The DST employs a high order adaptive optics (AO) system in its optical feed, upstream from the scientific instruments (Rimmele et al., 2004). Using the adaptive optics allows for routine observations with a resolution close to the diffraction limit of the telescope ($\sim 0.2''$).

Throughout my work I utilize the Interferometric Bidimensional Spectrograph (IBIS) extensively and will spend the rest of this section to introduce the instrument (Cavallini, 2006; Reardon and Cavallini, 2008). IBIS is a dual Fabry-Perot based imaging spectrograph that allows 2D imaging of the solar surface at quasi-monochromatic wavelengths. IBIS has high spectral resolution ($R \geq 200,000$) throughout its operational range. The high overall transmission of Fabry-Perot instruments allows for exposure times on the order of tens of milliseconds that allows for (almost) for the freezing of the atmospheric seeing. IBIS also operates a white light camera that is synchronized with the narrowband imager, which provides for measurement and correction of the residual atmospheric seeing. Operating in this regime, we can reconstruct nearly diffraction-limited scientific data over the whole $96''$ field of view, even if the AO system corrects the seeing effects partially and only at at the lock point.

The spacing of the Fabry-Perot cavities can be changed on timescales of tens of milliseconds which allows for scanning through an entire spectral line with 10-30 spectral points on the timescale of seconds. This is ideal for probing the high frequency waves described in section 1.2, as it provides for suitably high Nyquist frequencies. The usable wavelength range of IBIS is between 540 - 860 nm, which makes it suitable to observe multiple photospheric and chromospheric spectral lines in

that interval of the spectrum – for example, He I D₃ (587.6 nm), Na I D₁ (589.6 nm), the Fe I lines (543.4 nm, 630.2 nm, 709.0 nm), H α (656.3 nm), Fe II 722.4 nm, K I 769.9 nm, and the Ca II IR triplet 854.2 nm). The author had the pleasure of spending about a month observing at the DST with IBIS and the data from those observations has been used for parts of this thesis and will be exploited further in future publications.

2.1.3 Millimeter observations with the Atacama Large Millimeter Array (ALMA)

The Atacama Large Millimeter Array (ALMA) is the largest millimeter interferometric observatory ever built. It is comprised of sixty-six 12-meter antennas that can be relocated to different configurations with separations of up to 16 kilometers. The array is located in the Atacama Desert in Chile due to the low atmospheric moisture, which allows for more favorable millimeter observing conditions. The array is complemented with the Atacama Compact Array (ACA) that consists of four 12-meter and twelve 7-meter antennas. The smaller antennas allow ALMA to image objects with larger angular extent on the sky, due to the closer packing that is possible with the smaller antennas.

ALMA started its general scientific operations in 2011 with the observatory being intended to observe faint astrophysical objects. After further testing and verification process, ALMA became available for solar observations in 2016 during Observing Cycle 4 (Phillips et al., 2015; White et al., 2017). Some of the first results from the commissioning to be highlighted are about sunspots (Loukitcheva et al., 2017), comparison with UV diagnostics (Bastian et al., 2017), and spicule observations (Yokoyama et al., 2018).

In the solar case, ALMA observes the millimeter continuum, described in detail in section 1.3.3. The previously available observing configurations offered Band 3 and 6 (3 and 1.25 mm wavelength) with effective resolution of about 2'' and 1'' FWHM, depending on the array con-

figuration and observing conditions. The temporal resolution of the data is 2 seconds and the array could observe continuously for 10 minutes, interrupted by quick off-target recalibration, which requires repointing of the array for approximately two-minutes at a time. These data gaps between the solar observations present us with difficulty in analyzing low frequencies with similar temporal data extents.

ALMA is able to achieve angular resolution orders of magnitude higher than the diffraction limit of its individual dishes by combining the data sampling the different baselines. Every pair of antennas in the ALMA array measures the amplitude of the Fourier power at a particular separation and orientation and hence at one point in the Fourier space (u - v plane) of the image, where increasing separation of the antennas results in increased spatial frequency sampled by the antenna pair. Since the u - v plane of the image needs to be sampled, especially in the solar case of a multiscale extended object, this limits how widely distributed the antennas can be spread and limits the maximum angular resolution achieved by the array. For the same reason, the more compact (ACA) array is essential for reconstructing solar images which extend past the whole field of view of the individual antennas. The datasets obtained during the solar observing campaigns need further reduction steps applied outside of the standard CASA pipeline (Petry and CASA Development Team, 2012) due to significant phase errors in the solar data from the variable atmospheric vapor content and the impossibility of using water vapor monitor when observing the bright Sun. To alleviate the atmospheric seeing effects, self-calibration of the data was performed. The self-calibration procedure is presented in Chai et al. (2022) and takes the following steps: *i*) synthesize an average image for each 10-minute observing interval – the random atmospheric effects should average out on this timescale; *ii*) calculate the phase corrections for each 2 second exposure image in CASA given the model from step *i*; *iii*) apply the corrections from step *ii* to the individual images and generate an intermediate dataset; *iv*) reiterate steps *i-iii* until satisfactory convergence

of the phase errors for the singular images is achieved. This part of the reduction was performed by Dr. Yi Chai at NJIT and is very similar to the method described originally in [Shimojo et al. \(2017a\)](#).

2.2 Modern numerical tools for chromospheric studies

Numerical modeling of the chromosphere has went through a renaissance in the last decades with improved access to increasingly larger supercomputers. The rather difficult physical regime in the solar chromosphere requires significant numerical calculations. We first present the recent advances in modeling of the solar chromosphere from 1D static hydrodynamic models to full time dependent 3D radiative magnetohydrodynamic (rMHD) ones. These simulated atmospheres are extensively utilized in this thesis. We also present a brief description of the RH code that is used to produce the synthetic spectral diagnostics throughout this thesis ([Uitenbroek, 2001](#)).

2.2.1 Models of the solar chromosphere

Due to the high complexity and interconnectedness of the physical conditions in the solar chromosphere, relying on models to interpret solar chromospheric diagnostics is essential. We present in this section the models used throughout this thesis in order of increasing complexity.

The first models of the chromosphere were one-dimensional atmospheres, whose height dependent temperature, electron density and hydrogen populations plasma parameters were empirically adjusted to reproduce a variety of observed spectral diagnostics. The most notable model of these is the VAL C, whose name comes from the initials of the three authors of the seminal study – Vernazza, Avrett and Loeser ([Vernazza et al., 1981](#)). These authors solved the statistical equilibrium equation and then the non-LTE radiative transfer equations for several atomic species (H, He, Si, Mg, Fe) in an iterative way until the observed spectral diagnostics were reproduced. They used the

PANDORA code to solve the radiative transfer problem, where some of the stronger transitions of hydrogen (Lyman- α and Lyman- β) were treated with partial redistribution. The authors used Skylab observations of the EUV solar spectrum between 40 and 140 nm to empirically constrain the plasma properties throughout the solar atmosphere. They created a grid of models, ranging from a quiet Sun (model A) to active plage (model P). The most commonly cited model *C* was constructed for the average quiet Sun. In these models, the temperature decreases upward from the photosphere up until the temperature minimum which reaches a low temperature of 4170 K (Heinzl, 2000). Above the temperature minimum, the chromosphere exhibits a slight temperature rise. The rather flat temperature profile of the chromosphere is actually a phase transition – the hydrogen ionization is slightly increasing with height in the chromosphere, while most hydrogen is neutral around the temperature minimum. When all the hydrogen is finally ionized there is a steep increase in temperature due to the inability of the plasma to radiate away energy through the strong hydrogen emissions. This region of steep temperature increase is called the transition region, which is the interface between the corona and the chromosphere.

VAL models predict a temperature plateau in the transition region at around 20,000 K to match the hydrogen Ly- α line shape. However, a flat temperature profile introduce a problem with eliminating the conductive flux heating, required for maintaining the observed Ly- α radiative losses (Vernazza et al., 1981). This problem was alleviated with the inclusion of ambipolar diffusion in the upper chromosphere by Fontenla et al. (1990), which smooths the aforementioned plateau. In this work I use the more refined FAL models presented in Fontenla et al. (2011), which are more refined descendants of the earlier models. The newer models use optical and millimeter diagnostics to constrain the solar atmospheric properties, in addition to the extreme ultraviolet part of the solar spectrum and seem to reproduce the observed solar spectrum better.

The next significant progress was the development of the RADYN code that solves the full

hydrodynamic set of equations (including the energy one), coupled with the detailed non-LTE radiative transfer equation (Carlsson and Stein, 1995, 1997) in one dimension. The RADYN models showed that the chromosphere is very dynamic and changes on short timescales. In particular, acoustic shocks were shown to dominate the quiet chromosphere (Carlsson and Stein, 1997). These models showed the limitations of the previous static modeling approach – RADYN clearly showed that the average chromospheric spectra can be reproduced by dynamic atmospheres which have very different average properties compared to the averaged semiempirical atmospheres reproducing time-averaged observations. Interestingly, the RADYN chromosphere seemed to exist most of the time in a very cold state, raising concerns if there is even a full-time temperature increase above the temperature minimum (Kalkofen et al., 1999). Furthermore, RADYN results showed that time dependent ionization balance is crucial for the proper treatment of chromospheric plasma, due to the long recombination timescale in chromosphere compared to the dynamical timescales (Carlsson and Stein, 2002). The RADYN code has been further expanded to accommodate flare physics and has been extensively used for such studies (Allred et al., 2005, 2015; Kowalski et al., 2015).

With the advent of modern large scale supercomputers, full three-dimensional rMHD simulations of the solar chromosphere, including time-dependent ionization and non-LTE radiative transfer became possible (Felipe et al., 2010; Gudiksen et al., 2011; Rempel, 2017). In this thesis I utilize the publicly available simulation results from the Bifrost code (Gudiksen et al., 2011) of an enhanced network patch (Carlsson et al., 2016), a coronal hole, and a quiet Sun region (Hansteen et al., 2017). The Bifrost code solves the MHD equations on a staggered Cartesian grid in three dimensions. The optically thick radiative transfer in the chromosphere follows a set of approximations based on RADYN models and 3D radiative transfer calculations (Carlsson and Leenaarts, 2012), whereas the optically thin radiative transitions are treated explicitly for temperatures $\gtrsim 20,000$ K. The detailed radiative transfer approach of Bifrost makes it suitable for chromospheric

wave studies, such as the ones employed in this thesis. The modularity of the code allows for studies of different physical effects, including time-dependent ionization (Carlsson et al., 2016) and non-ideal MHD effects (Martínez-Sykora et al., 2017).

2.2.2 Synthesizing chromospheric spectral lines with the RH code

To synthesize the non-LTE spectral lines emerging from the atmospheric models described in the previous section, we utilize the RH code (Uitenbroek, 2001). The RH code uses the Ψ operator instead of the previously described Λ operator approach to find the escaping intensity from the atmosphere. The difference between the Λ and the Ψ operators are that the Ψ operates on the emissivity to produce the resulting intensity. This is more convenient for the inclusion of the partial redistribution (PRD) effects, as it avoids non-linearities in the estimation of the stimulated emission, following the formalism of Rybicki and Hummer (1991). Partial frequency redistribution is the physical correlation between absorbed and emitted photons from the same atom. The PRD effects are important for modeling of strong overlapping transitions, such as the Mg II h & k lines and triplet or the Ca II H & K lines, which are studied in this thesis.

The RH code works in an iterative manner that takes the following steps: First, the code creates a grid of wavelengths, taking into account the radiative transitions to be treated in non-LTE as well as those to be treated in LTE in the background. Then the code computes an initial atomic-level population estimate under a specific condition (zero radiation or LTE). After this initialization step, the iterative part of the process commences – the code computes the opacity and emissivity from the given atomic population numbers as well as the (PRD) emissivity profiles. With the updated emissivity and opacities the code performs a formal solution and obtains a new estimate of the radiation field in the atmosphere. Then the code reverts back to the first iterative step of computing the emissivity and opacity. This loop is executed until convergence, quantified

by a relative change in the mean intensity field below a certain threshold.

The code outputs all of the aforementioned properties of the radiation field in the atmosphere. These quantities are essential for the analysis of the synthetic observations presented in the forthcoming chapters. I used the originally provided data processing IDL package and I supplemented it with my own routines that read the binary files.

We use the RH15D implementation of the RH code ([Pereira and Uitenbroek, 2015](#)), that is a MPI-enabled version of the RH code. Since 1D (column-wise) radiative synthesis from 3D rMHD simulations is an almost embarrassingly parallel problem, this implementation of the RH one-dimensional solver scales very well on many computational cores. We used it on the NSO Blanca cluster, supported by Research Computing at the University of Boulder. Furthermore, this version of RH15D produces a curated subset of outputs from the original RH code, due to memory limitations from the great number of columns synthesized. RH15D utilizes the HDF5 format for its output, which is easily manageable for large datasets within the scientific Python environment.

Chapter 3

Solar Chromospheric Temperature Diagnostics: a joint ALMA-H α analysis

This article was published in *The Astrophysical Journal*, Volume 881, Issue 2, article id. 99, 9 pp. in August 2019 by Momchil E. Molnar, Kevin P. Reardon, Yi Chai, Dale Gary, Han Uitenbroek, Gianna Cauzzi, and Steven R. Cranmer.

3.1 Introduction

Analysis of visible, UV, and infrared spectral lines has long provided a key method for extracting information about the solar chromosphere. The lines provide valuable information on velocity, magnetic fields, density stratification, and abundances, among other physical observables. However, due to the low-density conditions under which the chromospheric lines are formed, local thermodynamic equilibrium (LTE) typically does not hold. With an atmosphere whose structuring can be dominated by the local dynamics or the magnetic field topology, there is a possibility of steep gradients in density, temperature, or other parameters along the line-of-sight. Therefore, the interpretation of the information encoded in chromospheric line profiles is not straightforward. Efforts at inversions of chromospheric spectral lines appear promising ([Socas-Navarro et al., 2015](#)), even though the robust extraction of atmospheric parameters from these profiles is still a subject of much research ([de la Cruz Rodríguez et al., 2019](#); [Milić and van Noort, 2018](#)).

Previous work has suggested that the bisector width near the core of the Balmer-alpha

transition line of hydrogen ($H\alpha$ from now on) may reveal information about the temperature of the region of the chromosphere where it forms (Cauzzi et al., 2009; Leenaarts et al., 2012a). The high temperature sensitivity of $H\alpha$ width was thought to primarily arise from the low atomic mass of hydrogen, resulting in a significant thermal Doppler broadening. Furthermore, Cauzzi et al. (2009) found strong correlations between the $H\alpha$ line width and the width and core intensity of the Ca II 8542 Å line, which they explained with a temperature dependent microturbulence, and a close coupling with local conditions (temperature), respectively. However, the interpretation of the extreme widths of $H\alpha$ (reaching 1.2 Å and beyond) in terms of Doppler broadening implied temperatures of up to 50,000 K, which would cause the chromosphere to be fully ionized according to 1D models, and which are rarely found in 3D chromospheric models.

The Atacama Large Millimeter Array (ALMA) (Wootten and Thompson, 2009), recently made available for solar observations, can provide an observable directly related to the electron temperature of the chromospheric plasma, supposedly freeing us from the non-LTE complications of other diagnostics (Phillips et al., 2015). The continuum radiation at millimeter wavelengths ($\approx 0.3\text{-}10$ mm) originates from free-free emission in the chromosphere, and the two main opacity sources are the electron-ion free-free absorption and the neutral-electron free-free absorption (away from strong magnetic fields) (for further discussion see Wedemeyer et al. (2016)). These processes are coupled solely to the local properties of the plasma (electron temperature) and, therefore, result in a LTE source function. By using the Rayleigh-Jeans law, we can then interpret the emergent intensity in the millimeter wavelength domain as a local electron temperature. This was verified theoretically by Loukitcheva et al. (2015), who showed that, in 3D MHD models, the ALMA brightness temperature indeed represents the electron temperature at the formation height of the millimeter radiation.

Early results of solar science with ALMA have been discussed by several authors. Among

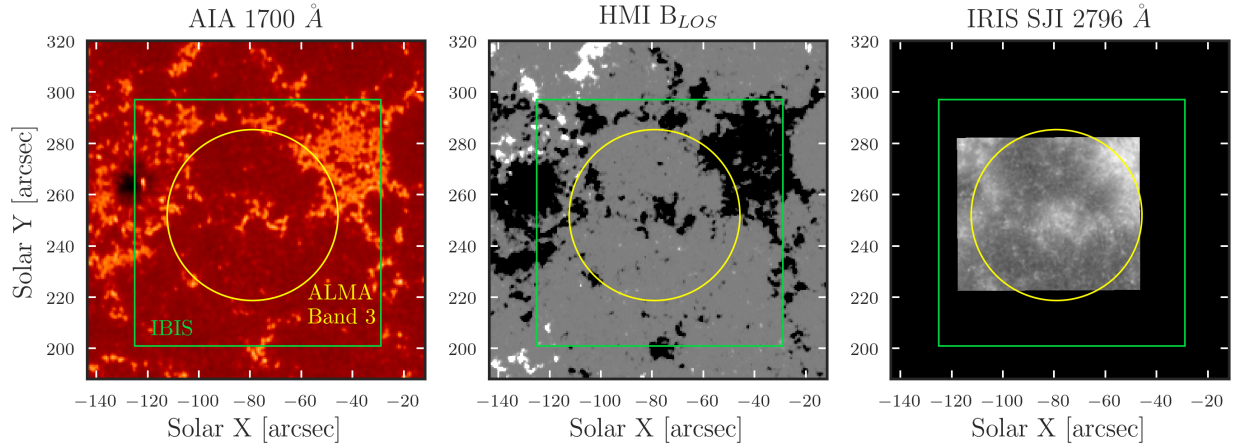


Figure 3.1: Context images of the observed field of view from the following instruments at 17:25 UT: *Left panel*: AIA 1700 Å image; *Central panel*: HMI LOS magnetogram, scaled (non-linearly) between -200 to 200 G.; *Right panel*: IRIS SJI image at 2796 Å, averaged over one minute. The field of view of IBIS is shown as the green square and the ALMA Band 3 field of view is shown as the yellow circle.

others, the visibility of chromospheric structures in full disk ALMA 1.21 mm data has been discussed by [Brajša et al. \(2018\)](#), while the presence and dynamics of chromospheric jets/spicules at the limb is reported by [Yokoyama et al. \(2018\)](#) and [Nindos et al. \(2018\)](#). Using high resolution IRIS observations of the Mg II h line obtained simultaneously, [Bastian et al. \(2017\)](#) showed clearly the difference of temperatures derived from radiative diagnostics (Mg II line intensity) and the plasma temperature derived from ALMA.

In this paper we concentrate on a joint analysis of the intensity measured in ALMA Band 3 and the H α line, to further our understanding of the chromospheric temperature structure. To this end, we employ some of the first simultaneous, high-resolution, high-cadence observations of the Sun in the millimetric range and in the optical and near-IR wavelengths.

3.2 Observations

We obtained a coordinated set of observations between ALMA and the Dunn Solar Telescope ([Dunn and Smartt, 1991](#)) on April 23, 2017. At the DST, the Interferometric Bidimensional Spec-

trometer (IBIS) (Cavallini, 2006; Reardon and Cavallini, 2008), the Facility Infrared Spectrograph (FIRS) (Jess et al., 2010a), and the Rapid Oscillations in the Solar Atmosphere instrument (ROSA) (Jess et al., 2010b) all observed the target region (in the following we concentrate only on the IBIS data). In addition, IRIS De Pontieu et al. (2014) and Hinode (Kosugi et al., 2007) satellites were co-pointing for these observations. Context images were available from SDO/AIA (Lemen et al., 2012) and magnetic field maps from SDO/HMI (Pesnell et al., 2012).

The observed target, shown in Figure 3.1, was an area of magnetic plage in the leading portion of NOAA active region 12651, a stable region with low flaring activity present during the declining phase of the solar cycle. Some quieter areas were present in the southern portion of the field of view (FOV). The center of the target region was at E04, N11 at the time of the observations ($\mu = 0.96$ or heliocentric angle of 16°). The primary leading spot of the active region was located about $60''$ east of the target center, outside the field of view of all of the targeted observations.

3.2.1 DST/IBIS Observations

We observed the target region at the DST from 15:13 to 19:06 UT in conditions of good to excellent seeing. Although several different lines and spectral sampling combinations were obtained within the full observing interval, we focus here on a continuous series of IBIS observations that ran from 17:25 to 18:11 UT, and that included 180 interleaved scans of $H\alpha$ 6563, Ca II 8542, and Na I D1 5896 Å. The lines were scanned with 29, 27, and 24 spectral sampling points, respectively, requiring between 3.4 and 4.0 seconds per line. With an additional overhead of 1.5 seconds to change prefilters, the total cadence for a scan of all three lines was 15.7 seconds. The spatial scale of the images from IBIS was $\sim 0.096''/\text{pixel}$.

We applied linearity, dark correction, flat field, and fringe removal corrections to the IBIS data. In order to correct for optical and atmospheric image distortions, we employed a technique

using the nearest-in-time HMI continuum intensity images in order to precisely map the IBIS spectral data onto a regular, fixed spatial grid with the bulk of the seeing distortions removed¹.

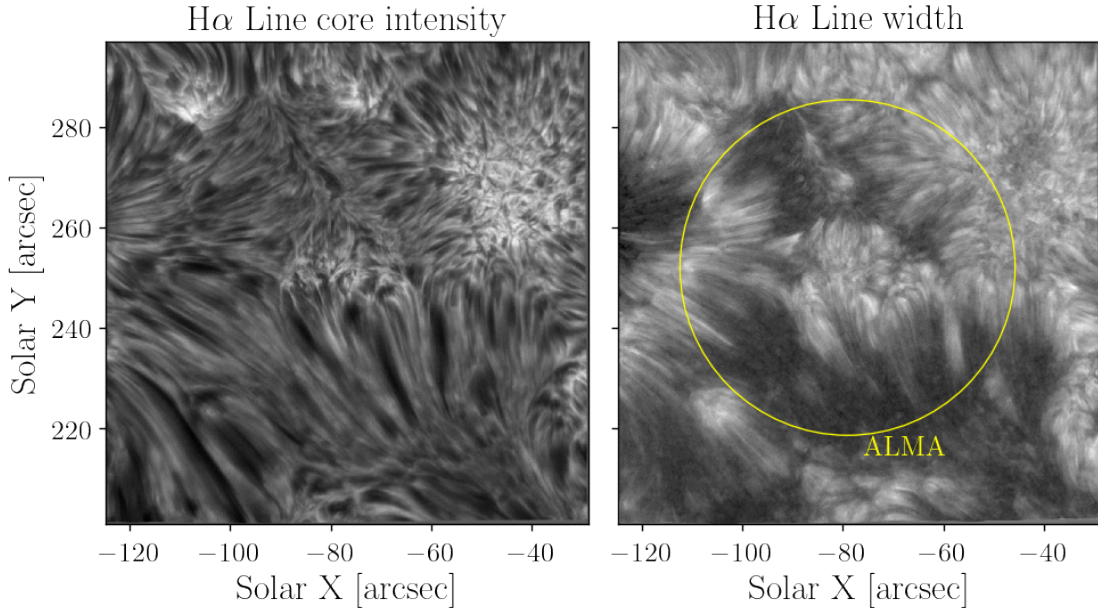


Figure 3.2: *Left panel:* H α core intensity of the region observed by IBIS at 17:25 UT; *Right panel:* H α line core width, scaled from 0.95 to 1.3 \AA , with brighter pixels corresponding to relatively broader profiles. The yellow circle shows the approximate ALMA field of view (see text for more details).

3.2.2 ALMA Observations and Processing

The ALMA data were obtained with the array in configuration C40-3 with a maximum baseline of 460 m. However, due to antenna issues, during these observations the maximum baseline was 396 m. The data analyzed here were obtained in Band 3 (2.8-3.3 mm, 92-108 GHz) in the interval 17:19 to 18:53 UT. The millimetric observations followed a sequence that dwelled for approximately 593 seconds on the target followed by a 145 second gap for observations of a phase calibrator. There were eight observing intervals all together, with the final interval being truncated

¹using Rob Rutten’s very capable software package available at [his website](#).

to 440 seconds due to the end of the allocated observing block. After applying the standard radio interferometer data calibration procedures using CASA (Petry and CASA Development Team, 2012), we found that the ALMA images are heavily influenced by the phase disturbances due to water vapor variations in Earth’s atmosphere, causing small-scale distortions on the images. To counteract this effect, we apply a self-calibration technique. For each 10 minutes observation interval, an average (clean) image is generated and then used to remove the random phase variations in the individual images within that observing interval. This allows us to minimize the image distortions in a self-consistent manner that does not introduce significant artifacts.

The field of view of ALMA band 3 images is only $\sim 60''$ diameter, which can be smaller than some of the large-scale structuring of solar features. To provide information on the background emission from the Sun, single-dish observations that scan the full disk were taken nearly simultaneously with the interferometer array (White et al., 2017), albeit with a significantly lower spatial resolution. Through the feathering process provided in CASA, we combine the two datasets covering the full range of spatial scales. In order to provide an absolute calibration for the measurements, the full-disk image was normalized such that the brightness temperature in the central region of the disk (diameter 190 arcsec) was equal to 7300 K, as determined by (White et al., 2017). This sets the background brightness temperature in our target region. This calibration compensates for any absorption variations in the terrestrial atmosphere and provides an absolute temperature accurate to 2-5% (White et al., 2017).

Figure 3.3 (top row) shows examples from the final results after the calibration and feathering procedures. The effective field of view of these Band 3 observations was approximately $60''$ in diameter; the restoring beam size of the ALMA image, as calculated in CLEAN, is $1.75'' \times 1.91''$ in the x-y directions. The shape of synthesized beam depends on the antenna configuration and the angle between the array and the target, which means it is not circularly symmetric. While the

beam size will change size and shape slightly over time, our observing interval was short enough that there were no significant changes to the beam shape.

3.3 Diagnostics Comparison

3.3.1 IBIS Line Widths

We concentrated on the diagnostics afforded by the $H\alpha$ line, calculating several parameters from the spectral profiles recorded at each pixel and for each time step. The intensity and wavelength of the line-minimum position were determined through fitting of a second-order polynomial to the line core. We calculated the width of the line core following the technique described in [Cauzzi et al. \(2009\)](#) – in short, we measure the separation of the line profile wings at half of the line depth, defined as the difference between the line minimum and the intensity at $\pm 1.0 \text{ \AA}$ from the core position. This determines the line width in the central core of the line profile, which is essentially the portion formed at chromospheric heights. The instrumental profile has a negligible effect on the measured width, and the errors in the line width were determined to be about 0.005 \AA .

Intensity and line width maps for the data acquired at 17:25 UT are shown in [Figure 3.2](#). While the $H\alpha$ core intensity shows the familiar “forest” of chromospheric fibrils originating from magnetic features and covering much of the internetwork regions (compare [Figure 3.1](#)), the line width map shows a significantly different scene. The plage and magnetic network are clearly highlighted as region of large line widths, together with the base and partial length of a selected set of fibrils, as discussed in [Cauzzi et al. \(2009\)](#). There is fine spatial structuring in the line width, down to the resolution limit of the data.

3.3.2 ALMA Band 3 Intensity

The ALMA Band 3 intensity maps are shown in the top row of Figure 3.3. As stated above, the resolution of the ALMA images is $\approx 2.0''$. The top left panel in Figure 3.3 displays a single 2 second ALMA integration, whereas the top right panel is a time average over the 10-minute time block observed between 17:31 UT and 17:41 UT.

From the similarity of the instantaneous and time-averaged maps, it appears that at this spatial resolution the structures remain fairly stable over several minutes, although ALMA movies show subtle evolution; a complete temporal analysis is left for a future work.

The 3 mm intensity maps are clearly brighter (hotter) in network and plage regions, with brightness T_B reaching up to $\sim 12,000$ K in the latter, whereas in the internetwork temperatures are as low as $\sim 6,500$ K. The overall average T_B for our field is ~ 8600 K, reflecting the presence of plage in the FOV; the average in the quieter portions of the FOV is ~ 7500 K. This is consistent with the quiet Sun calibration described in Sec. 3.2.2.

The most interesting property of the ALMA T_B maps, however, might be the presence of several bright ALMA features that appear fibrillar in nature, reminiscent of those observed in the $H\alpha$ line width map of Figure 3.2. They are particularly prominent in the bottom part of the FOV, where some of the strongest $H\alpha$ -width features are seen. To the best of our knowledge, this is the first time that fibrillar structures are clearly identified in on-disk ALMA images. Contrary to the prediction of Rutten (2017), however, we identify them as bright (hence hot) features, rather than dark, strong fibrils coincident with $H\alpha$ line-core intensity features.

3.3.3 Comparison between the ALMA Band 3 intensity and $H\alpha$ line width

The bottom panels of Figure 3.3 show the maps of $H\alpha$ width acquired coterporally to the ALMA maps: a single snapshot in the left column; and the average over the period 17:31 – 17:41

UT in the right column. Contours of the HMI longitudinal magnetic field magnitude at values of greater than 500 Gauss have been drawn in yellow on the right panel to facilitate comparison with Figure 3.1. In order to provide a more relevant comparison, we have degraded the spatial resolution of the IBIS data to best match the appearance of the ALMA data. We find that the minimum difference between the blurred $H\alpha$ width and ALMA images occurs for a circular Gaussian with a FWHM $2.0''$. This is about 8% greater than the mean FWHM of the theoretical ALMA beam, likely due to residual atmospheric smearing at the millimeter wavelengths. Since the ALMA PSF is known to be non-circular due to the orientation of the interferometer array with respect to the object, we apply the ratio between the x and y axes of the ALMA beam (as calculated for our observations by CLEAN) and convolve the IBIS images with an elliptical Gaussian kernel having FWHM in the x-y directions of $1.95'' \times 2.03''$, respectively. In fact, the match is so satisfactory that we were able to align the $H\alpha$ width maps and ALMA images to easily achieve sub-arcsecond accuracy. The alignment between the two diagnostics was done on the time averaged images and, given the spatial resolution, did not appear to produce any artificial superposition of localized features. Because the temporal sampling was higher for ALMA compared to the multi-line IBIS scans (2 vs. 15 seconds), we temporally binned the ALMA data to match the IBIS temporal sampling by combining the eight closest-in-time ALMA brightness maps.

The similarity between ALMA intensity and $H\alpha$ width is striking, with regions of similar size, shape and contrast. High/low brightness temperature in ALMA Band 3 correspond, almost one-to-one, to broad/narrow $H\alpha$ profiles. The HMI contours make clear how the ALMA fibrillar structures represent the lower portion of heated features originating from regions with high magnetic flux, like those seen in $H\alpha$.

To quantify the comparison, a 2D histogram between the temporally coincident maps of ALMA Band 3 brightness temperature and $H\alpha$ width is shown in Figure 3.4. The histogram derived

from the overall time-average of these two diagnostics shows an essentially identical distribution. The correlation is very strong across the full range in temperature present in our FOV, with a Pearson correlation coefficient of 0.84. Because of the scatter present in both measurements, we perform an orthogonal distance regression (Isobe et al., 1990) to find the best linear fit between the two parameters. The best fit equation is $0.533 + 6.12 \times 10^{-5} T$, which is plotted in Figure 3.4.

However, the range of T_B measured with ALMA is not large enough to explain the change of the observed $H\alpha$ line width from 0.95 to 1.2 Å as solely due to thermal Doppler broadening, as hypothesized by Cauzzi et al. (2009). This is because the $H\alpha$ line width already has a significant intrinsic width of around 0.95 Å and this dominates the quadratic sum of broadening components for the observed range of ALMA temperatures. In fact, an increase from 6,000 to 12,000 K (Figure 3.3 top row) would only be expected to increase the line width by 0.025 Å, an order of magnitude smaller than the observed broadening.

Finally, we note the presence of a cluster of points between 6,500-7,500 K for which the $H\alpha$ widths fall 0.03 to 0.05 Å lower than the fitted correlation. These points correspond to quieter regions in the bottom half of the ALMA FOV, and located farther away from the magnetic concentrations.

3.4 Synthetic Spectral Diagnostics with RH

To investigate the mechanisms behind the correlation of Figure 3.4, we utilized the RH code (Uitenbroek, 2001) to synthesize observables for different solar atmospheric models. We chose the 1D Solar Radiation Physical Modeling (SRPM from now on) models (Fontenla et al., 2011) as input for our work. We used models ranging from the Quiet Sun internetwork (model B) to bright facular region (model P), representative of the different solar structures in our field of view. We also included the heritage quiet Sun VAL C model for comparison (Vernazza et al., 1981).

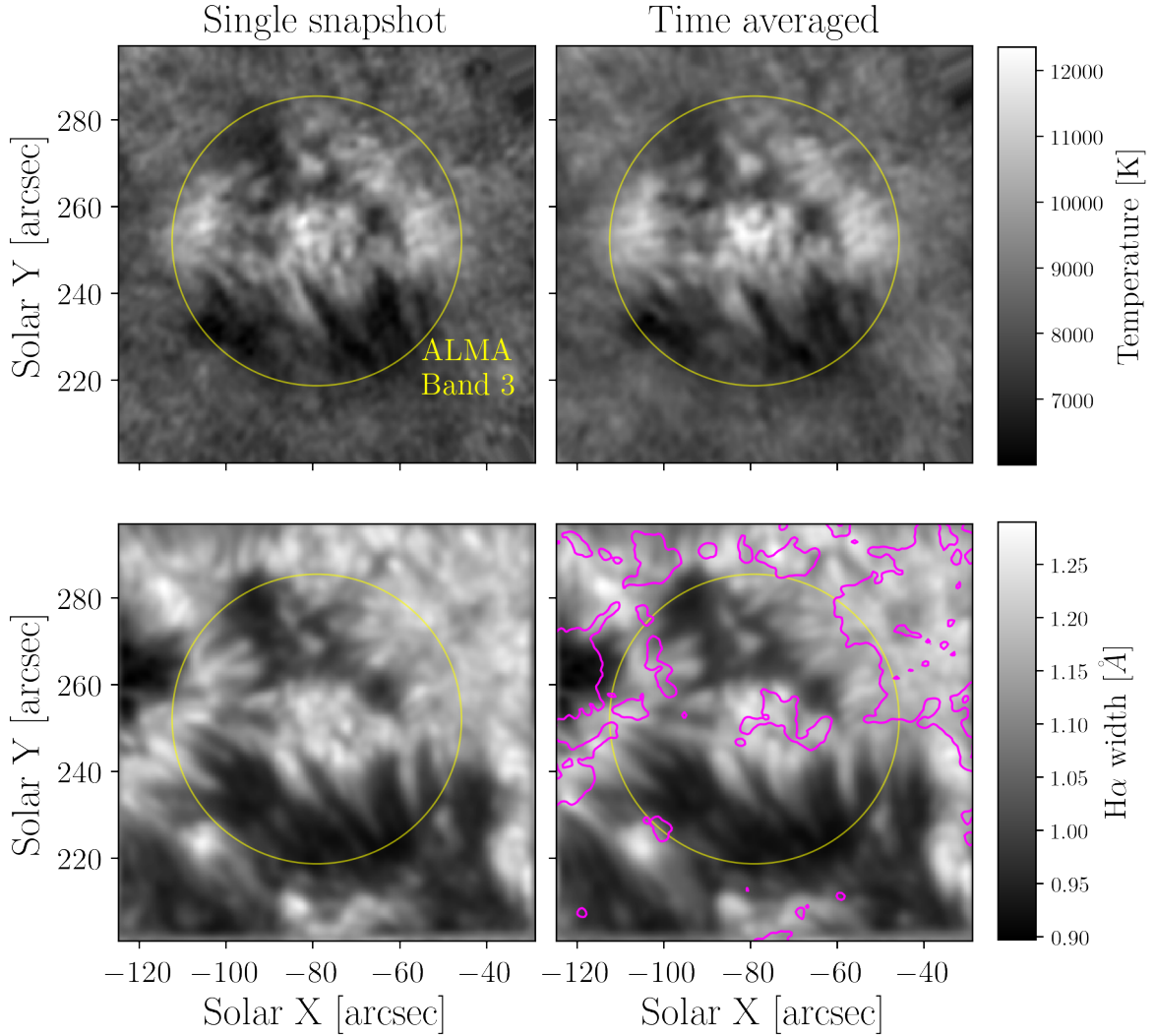


Figure 3.3: Maps of ALMA intensity (top row) and IBIS $H\alpha$ line width (bottom row). The left column shows the two parameters at single time step of the observations, while the right column shows the same two parameters averaged over the ten minutes of a continuous ALMA observation block. The IBIS data have been smoothed to match the resolution of the ALMA data, by using a elliptical Gaussian kernel with FWHM in the x-y directions of $1.95'' \times 2.03''$. The yellow circle with a diameter of $66''$, is slightly larger than the usable field-of-view of ALMA. The purple contours overlaid on the bottom right panel show areas with magnetic field strength above 500 Gauss measured by HMI, showing a prominent correlation between the magnetic flux and millimeter continuum brightness (shown previously in Loukitcheva et al., 2009).

The RH calculations were done using a 4-level (including continuum) hydrogen atom with the Ly-alpha, Ly-beta and Balmer-alpha transitions treated under partial redistribution (PRD), while the rest of the atomic species were treated in LTE. The widths of the chromospheric core of the

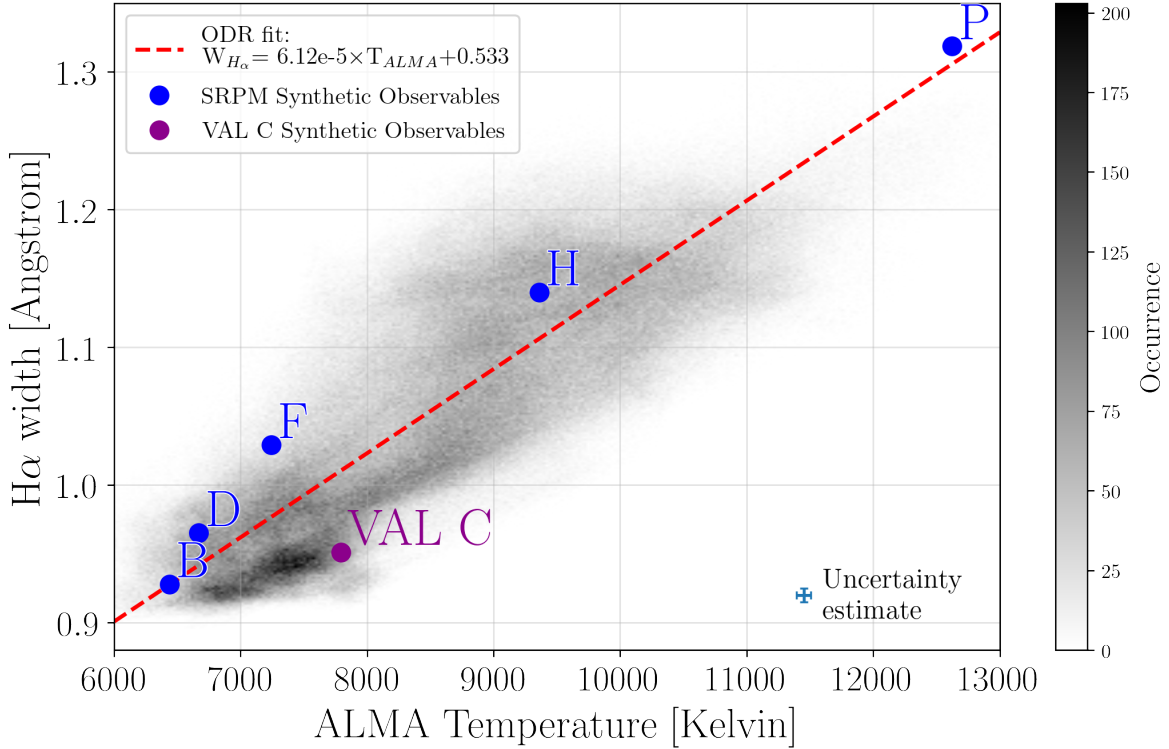


Figure 3.4: 2D histogram of H α core width versus ALMA brightness temperature, clearly showing the correlation between the two quantities. Overlaid as blue dots are the result from the RH spectral synthesis in the SRPM atmospheres and in violet in the VAL C model. The uncertainty estimates in both directions are presented with the marker in the bottom right of the plot. The spread in the figure is physical, as it is significantly larger than the uncertainties in our measurements. Orthogonal distance regression (ODR) was used to fit the observation with a straight line, resulting in the red dashed line.

synthetic H α profiles were measured using the same method used for the observational data. The emergent millimetric radiation was calculated from the synthetic intensity under the Rayleigh-Jeans approximation for a wavelength range of 2.6-3.4 mm (100 GHz), which covers the observed wavelength interval.

The SRPM models have shortcomings as they are 1D, hydro-static, semi-empirical models optimized to reproduce the temporally averaged solar spectrum as observed at a few arcsecond resolution. Yet, given that the data of Figure 3.4 has been smoothed to a similar resolution, we use them as a first attempt to provide some physical insight. It is also worth noticing that modern,

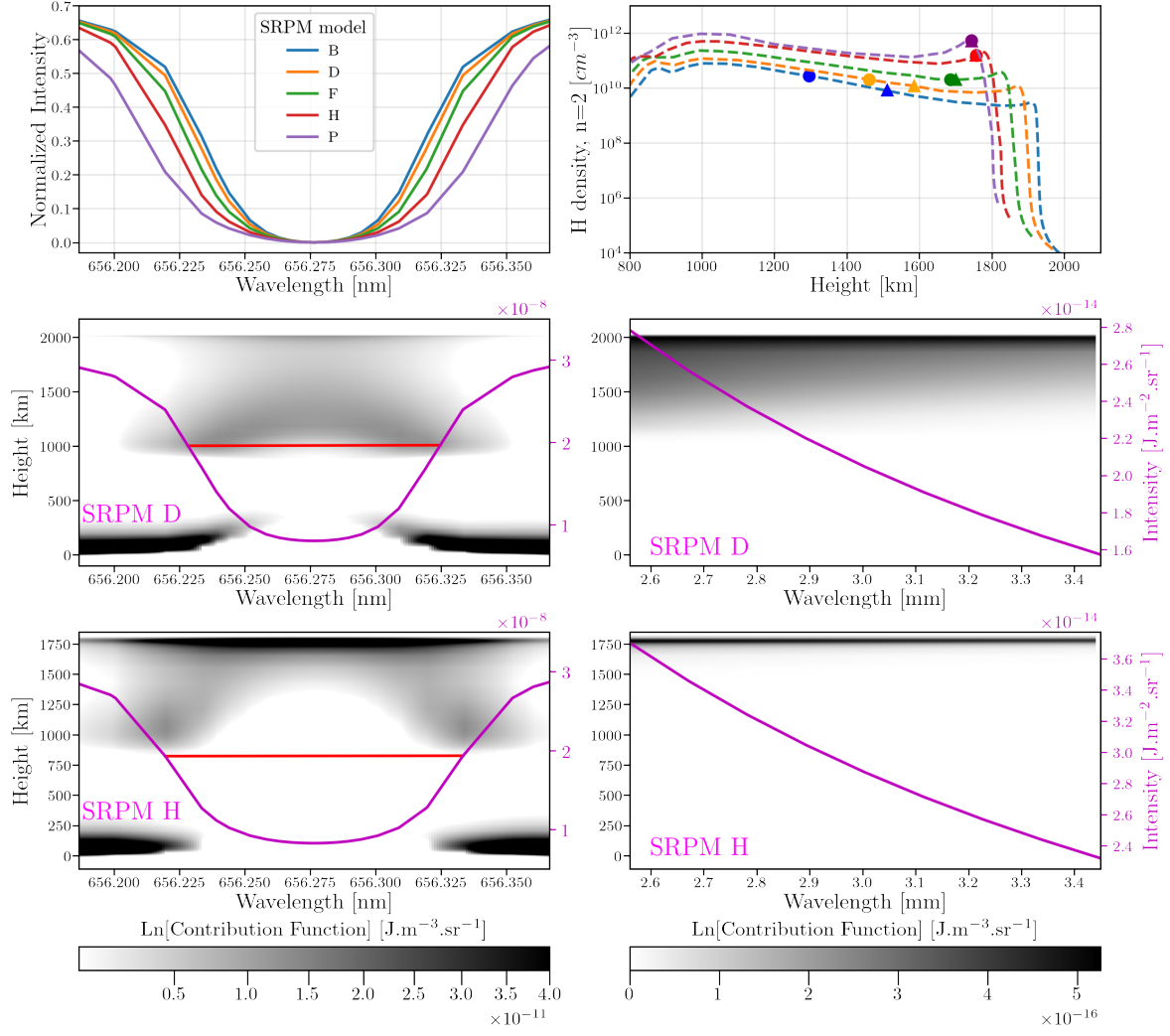


Figure 3.5: Results from the RH spectral synthesis. *Upper left*: $H\alpha$ profiles for the different SRPM atmospheres. *Upper right*: Number density of hydrogen atoms in the $n = 2$ quantum state. The symbols show the height at which $\tau = 1$ for the 3 mm radiation (triangles) and the $H\alpha$ line core intensity (circles), in the corresponding atmosphere. Note that the triangles and circles indicating the $\tau = 1$ surfaces coincide for the hotter models. *Middle left*: intensity contribution function for the $H\alpha$ line for the SRPM D model overlaid with the emergent line profile (in violet). Note the different intensity scaling with respect to the upper panel. The position of the line width measurement described in Section 3.3.1 is illustrated with the red line. *Middle right*: contribution function for the emergent intensity for ALMA Band 3 wavelengths for the SRPM D model, overlaid with the emergent intensity profile (in violet). *Bottom left, right*: as the middle panels, for the SRPM H model.

ab-initio 3D-MHD atmospheric models such as BIFROST (Gudiksen et al., 2011; Carlsson et al., 2016) still lack some significant physical processes in the range of heights of relevance for our work; in particular, they do not reproduce the correct width of chromospheric lines (Leenaarts et al.,

2009), which is obviously crucial for our analysis. In addition, it would be more correct to perform the radiative transfer calculations for $H\alpha$ using full, 3D radiative transfer computations (Leenaarts and Carlsson, 2009), but we leave that to a future work due to complexity and computational requirements.

The results from the RH line synthesis are presented in Figure 3.4 as blue circles, and coincide well with the observational data for models B to P, which are the dominant features in our observations (note that hotter models, e.g. model Q, do not follow the trend shown in Figure 3.4, hinting at a perhaps different behavior for other solar features like active regions). The VAL C result falls below the observed correlation, with too small of a line width, likely due to some of the simplified physical assumptions in that older model (e.g lack of ambipolar diffusion and a different treatment of $Ly\alpha$). The range of ALMA temperatures reproduced by the models is not surprising, since the semi-empirical models were tailored to reproduce observed millimeter continuum brightness, among other diagnostics. The observed range of temperatures and correspondence to the appropriate chromospheric structures in the field confirms the proper calibration of the ALMA brightness temperature and consistency with previous work. However, the SRPM models were not constructed using $H\alpha$ line widths as a parameter, which makes the close correspondence especially pleasing.

Using the RH results, we can investigate the formation of $H\alpha$ and the millimetric radiation in more detail. Figure 3.4 shows the run of relevant parameters for different atmospheric models. In the top left panel, we see how the $H\alpha$ line saturates even in the colder models, and grows broader as the chromospheric temperature rises. Interestingly, this appears directly correlated with sensibly higher populations of the hydrogen $n = 2$ level in the hotter models, as plotted in the top right panel. Indeed, the number density of H atoms in the $n = 2$ level increases two orders of magnitude from model B to model P, suggesting that the broadening of $H\alpha$ could be primarily due to an

opacity effect (akin to a curve-of-growth plot).

The middle and bottom panels of Figure 3.4 show the intensity contribution functions (CFs) for both diagnostics, for the representative models D and H. The emergent intensities over both the H α profile and the ALMA band 3 wavelengths are plotted in violet (in the left panels we also show the width of the resulting H α line, as computed with our method marked with the red line). These panels show that while both diagnostics form over the same general expanse of the chromosphere, their range of formation becomes narrower and more coincident as we move to hotter models. This is represented in the top right panel, where the symbols indicate the heights at which the optical depth $\tau = 1$ for the 3 mm radiation (triangles) and for H α line core (circles).

For model H, a large fraction of the H α core intensity, and essentially all of the millimetric intensity originate from a narrow region at the interface of the chromosphere and the transition zone. For the colder model atmospheres the height separation between the two diagnostics becomes significant. However, some correlation between the diagnostics is still to be expected because both temperature and the hydrogen $n = 2$ level populations (see below) vary very slowly in the relevant range of heights.

We hypothesize that the underlying physical mechanism for the correlation shown in Figure 3.4 could arise from the common sensitivities of both diagnostics to the population numbers in the first excited state of hydrogen, n_2 , in particular as related to excitation in Ly α . Most excitation in Ly α occur via radiative transitions, as not many electrons have sufficient energy to collisionally excite the line at chromospheric temperatures. Opacity in the line core is very high and the radiation field is completely thermalized. However, there is significant excitation in the line wings by radiation coming from the hot transition region above (Uitenbroek, 2003; Leenaarts et al., 2012a). Being this far in the UV, the additional radiative excitation through downward flux of Ly α wing photons is very sensitive to the column mass at which the transition region occurs. In Figure 3.4

(upper right) the effect of the downward radiation in the Ly α wings is visible as the bump on the right side of the n_2 level population plot, on top of the general rise from one model to the next that is caused by the increase in density scale height associated with hotter models.

On the one hand, an enhanced value of n_2 leads to enhanced ionization of hydrogen, as the predominant mechanism for hydrogen ionization in the chromosphere is via the Balmer continuum, which decouples from local conditions already much deeper in the atmosphere (Carlsson and Stein, 2002). Since the radiation field in the Balmer continuum is optically thin, any fractional increase in the $n = 2$ populations will raise ionization levels proportionally. The increase in electrons coming from this increase in $n = 2$ population raises the opacity at 3 mm, moving the formation height of radiation at these wavelengths up in the atmosphere to higher temperatures; this results in raising the millimetric brightness temperature, once hydrogen ionization reaches a few percent.

On the other hand, an increase in n_2 raises the opacity in H α , also increasing the formation height of the core in particular. The line source function of H α is almost flat with height through the chromosphere, resulting in the characteristic flat bottom of the line profile in the core. Changing wavelength from the core outward in the line profile the intensity follows the flat source function inward (Leenaarts et al., 2012a; Rutten and Uitenbroek, 2012), until it suddenly becomes sensitive to the photospheric temperature rise with depth, resulting in the steep wings of the line profile. The further the line core formation moves up in the atmosphere, the further in wavelength we have to move out of the core to see the wings, explaining the dependency of the H α width as an opacity effect, rather than a direct effect from thermal broadening.

Thus, we suggest that both the 3 mm brightness temperature and the H α line width depend coherently on the n_2 level populations of hydrogen in the chromosphere. With higher values of n_2 the formation height of the 3 mm radiation increases through increased hydrogen ionization in the Balmer continuum as explained above. At the same time, an increase in n_2 leads to opacity

broadening of $H\alpha$ through an upward shift of the core formation height (as noted above, for the hotter SPRM Q the trend breaks down as $H\alpha$ forms at the base of the TR where the higher source function leads to an increased line core intensity), and the effect of an almost flat source function of the line through the chromosphere. The n_2 population of hydrogen in the chromosphere is determined by the downward $Ly\alpha$ wing flux (Carlsson and Stein, 2002), and, in turn, the $Ly\alpha$ flux is determined by the column mass at which the TR occurs (Mariska, 1992). Indeed, in our synthesis we found increasing $Ly\alpha$ flux for the hotter models (B to P), whose TR location occurs at increasing column mass. This is in agreement with our conjecture about the correlation between $H\alpha$ width and ALMA brightness temperature.

3.5 Conclusions

We have presented the first observations combining high-spatial-resolution spectral imaging in the traditional chromospheric indicator of $H\alpha$ combined with simultaneous brightness temperature maps at millimeter wavelengths obtained with ALMA. The common, $\sim 60''$ diameter FOV of the two instruments contained plage, network, and some (magnetically) quieter areas.

The ALMA 3-mm images display a structured pattern of bright (hotter) and dark (cooler) features, with spatial sizes down to the spatial resolution of $\sim 2.0''$. The corresponding brightness temperature spans a range between 6,500 and 12,000 K. An interesting property of the ALMA T_B maps is the presence of bright ALMA features that appear fibrillar in nature, particularly prominent in the bottom part of the FOV. The ALMA images bear a striking similarity with the maps of the $H\alpha$ line core width, with features of similar size, shape and contrast (Figure 3.3). This is contrary to the predictions presented in a recent paper by Rutten (2017), that hypothesized the ubiquitous presence of long, opaque ALMA fibrils, with a good dark-dark correspondence with the $H\alpha$ core intensity; as shown also in Cauzzi et al. (2009), the $H\alpha$ core intensity and width are poorly

correlated quantities. We however defer a more detailed comparison of such features to a further work.

Our most important result is the strong quantitative correlation between the intensity of ALMA and the width of the H α line core in the range of observed temperatures, as plotted in Figure 3.4. Using forward synthesis with RH, we showed that the correlation is well reproduced with 1D semi-empirical models of typical solar structures, which further indicates that the H α intensity and the millimeter radiation are formed in a similar span of the middle-upper chromosphere. We note that the synthesis from the VAL C model falls below the observed correlation and away from the other modeling results, most likely due to the inclusion in the SRPM models of ambipolar diffusion and a different, more detailed treatment of the Lyman- α line profile.

The main factor driving the correlation appears to be that the opacity sources for both spectral diagnostics is determined through the $n = 2$ hydrogen population. The mm-wavelength opacity depends on the electron number density, which is related to the $n = 2$ population of hydrogen as the statistically dominant source of free electrons in the upper chromosphere. At the same time, the line-broadening of H α is determined by the column mass of $n = 2$ hydrogen atoms in a manner similar to a curve-of-growth effect. This effect is stronger in hotter atmospheric models, for which the height of formation of both diagnostics coincides almost exactly as it is pushed to the chromosphere-TR boundary. The direct contribution to the H α line width from solely thermal Doppler broadening for the range of temperatures detected with ALMA (between 6,500 K to 12,000 K) is only about 0.025 Å, an order of magnitude smaller than the observed variation of 0.3 Å.

Indeed, the earlier interpretation of H α width as due essentially to thermal broadening (Cauzzi et al., 2009) required a much larger range of electronic temperatures, all the way to $T_e \sim 60,000$ K. With the reliable determination of T_e now provided by ALMA, it appears necessary to revisit the original assumption of negligible changes due to radiative transfer effects (essentially

contained in the “basal” width of the lines in) (Cauzzi et al., 2009), at least for $H\alpha$. A strong correlation between $H\alpha$ width and Ca II 8542 width and core intensity has also been observed in the dataset discussed in this paper, and will be the subject of a future investigation. We note that the smaller temperature range found here to explain the $H\alpha$ line width does not alter the need for a temperature-dependent microturbulent broadening to produce the observed distribution of widths of the Ca II 8542 line.

Of more general utility, we have demonstrated that the $H\alpha$ line width can be as useful and meaningful of an indicator of the temperature of the chromosphere and the initial rise into the transition region as those temperatures derived from ALMA millimeter intensities, at least in the range 6,500 – 12,000 K. While it too suffers from the same changes in the heights of formation as the millimeter radiation, given the above caveats it can represent an easily accessible and straightforward diagnostic of chromospheric temperatures in many regions of the chromosphere. The combination of $H\alpha$ line width and ALMA 3 mm observations has in effect allowed us to calibrate the line-widths in terms of brightness temperature (for observations of network regions and near disk center). Future work should examine the nature of the relationship at different heliocentric angles or for different structures. The values of the linear fit can be used to derive an approximate conversion of the line width to chromospheric 3 mm brightness temperature with an accuracy of better than 1000 K. Given the good matching between the 1-D models and the $H\alpha$ line width, the measured value could provide an efficient method to make better initial guesses of the input atmosphere for spectral inversions of chromospheric lines.

Chapter 4

Acoustic fluxes inferred from IBIS and ALMA

This article was published in *The Astrophysical Journal*, Volume 920, Issue 2, id.125, 21 pp. in October 2021 by Momchil E. Molnar, Kevin P. Reardon, Steven R. Cranmer, Adam F. Kowalski, Yi Chai, and Dale Gary.

4.1 Introduction

Balancing the radiative losses of the non-magnetic chromosphere requires an energy input of about 4 kW m^{-2} (Withbroe and Noyes, 1977). The two most widely accepted theoretical frameworks for chromospheric heating are the same as for the corona: wave dissipation or ubiquitous small scale magnetic reconnection (Carlsson et al., 2019). There is evidence for both mechanisms being at work in the chromosphere, but definitive observations constraining their relative importance are still elusive. In this paper we concentrate on quantifying the contribution from compressive waves in the chromosphere which produce measurable Doppler shifts in chromospheric diagnostics.

The first to suggest that the chromosphere can be kept in its thermal state by dissipation of acoustic waves were Biermann (1946) and Schwarzschild (1948). They suggested that the convective overshoot at the boundary of the the upper convective zone and the photosphere drives acoustic waves with a fairly broad range of periods. Those waves with frequencies above the acoustic cutoff frequency (roughly 5 mHz or 200 seconds) can propagate upward into the chromosphere (Bray and

Loughhead, 1974). As the acoustic waves move into higher layers in the solar atmosphere, they find a strongly decreasing plasma density while the temperature, and hence sound speed, remains (almost) constant, which results in amplitude growth and wave steepening. Waves that steepen into shocks can dissipate their energy and supply the heat needed to maintain the chromospheric plasma in its basal state (Carlsson and Stein, 1992). Intermittent shocks would ionize the hydrogen and helium in the chromosphere out of equilibrium and maintain the chromospheric ionization state away from statistical equilibrium due to the long recombination timescales (Carlsson and Stein, 2002).

The magnetic field in the chromosphere allows for the existence of magnetosonic wave modes and the similarity between the sound and Alfvén speeds allows the easy conversion between them (Cally and Goossens, 2008). The multitude of magneto-acoustic wave modes and their numerous damping mechanisms expands the possible wave propagation scenarios, but does not alter the basic premise of the theory of how energy is being transported from the convection zone to the chromosphere. For a recent review on the subject of magnetosonic waves observations, the reader should see Jess et al. (2015).

The observational evidence constraining the energy contribution of wave heating in the chromosphere has been inconclusive. Wunnenberg et al. (2002), using Fabry-Perot imaging spectroscopy of the Fe I 543.4 nm line, inferred around 0.9 kW m^{-2} acoustic flux from waves with periods between 50 s and 100 s (10-20 mHz) at height of 600 km above the photosphere. They estimated that the large extent in height of the velocity response functions reduced their observed wave amplitudes by a factor of three, and arrived at an actual acoustic flux of 3 kW m^{-2} . On the other hand, Fossum and Carlsson (2005) used TRACE intensity-only observations of the 160 nm UV continuum (sampling the upper photosphere at height of 450 km), coupled with self-consistent simulations of the solar atmospheric oscillations, to derive an acoustic wave flux in the frequency interval 5-28

mHz of 0.4 kW m^{-2} . This would not be sufficient to sustain the non-magnetic chromosphere, but other authors (e.g., [Cuntz et al., 2007](#); [Wedemeyer-Böhm et al., 2007](#)) have argued that the limited angular resolution of the TRACE observations and other model assumptions lead to significant underestimation of the wave flux in that analysis.

Measurements of velocities in two photospheric spectral lines with higher temporal and spatial resolution by [Bello González et al. \(2009, 2010\)](#) showed the presence, after taking into account the width of the velocity response functions, of significant acoustic flux (up to 3.8 kW m^{-2}) in the middle photosphere between 5 and 15 mHz. More recent work by [Abbasvand et al. \(2020a,b\)](#) utilizing observations of the chromospheric Ca II 854.2 nm and H I Balmer- α and Balmer- β lines with a scanning spectrograph reached similar conclusions of about 5 kW m^{-2} flux in the chromosphere. However, the latter authors did not account for the width of the velocity response function ([Mein and Mein, 1980](#)), which makes their flux estimation a lower bound for the actual wave energy flux.

Another still poorly understood aspect of the wave heating theory is the contribution from high-frequency waves, above 30 mHz. The sparsity of observations in this regime has been due to the difficulty of obtaining high-temporal-cadence spectral information of the chromosphere at the high spatial resolution required to resolve the small-scale chromospheric structures. In one of the few studies in this regime, [Hansteen et al. \(2000\)](#) has shown intermittent wavelet power up to 50 mHz in upper-chromospheric and transition-region lines taken with SUMER on the SOHO spacecraft.

Some of the aforementioned studies take into account the attenuation of the observed wave amplitudes when the contribution to the observed spectral signal becomes similar to or greater than the wavelength of the propagating waves ([Mein and Mein, 1980](#)). Consideration of this effect is essential for inferring the flux, as it has been estimated to be a factor of between 2 to 10 for frequencies between 5 and 50 mHz ([Wunnenberg et al., 2002](#); [Bello González et al., 2009](#)). The

latter authors used a static semi-empirical 1D model to calculate the wave response in photospheric lines using a perturbative approach with sinusoidal waves. This approach is not similarly applicable in the chromosphere, where the waves are generally not sinusoidal and could be strongly affected by radiative losses. A more realistic approach is undertaken by [Fossum and Carlsson \(2005\)](#) and [Wedemeyer-Böhm et al. \(2007\)](#) who use time-dependent hydrodynamic simulations to infer the actual wave attenuation including the effect of radiative wave damping. We show in [Section 4.5](#) that this approach is better as it naturally explains the high frequency signal in our observations. Furthermore, we argue that modeling based on semi-empirical 1D atmospheres might be overestimating the contributions from the high-frequency waves. [Reardon et al. \(2008\)](#) showed that Doppler diagnostics in the chromosphere have a power-law behavior from the acoustic cutoff frequency out to 20 mHz. It is not understood whether this trend is due to the true distribution of acoustic oscillations at these frequencies, or the result of a frequency-dependent attenuation of the chromospheric signal.

This paper presents observations of high frequency wave Doppler velocity signal in the solar chromosphere. We obtained a data set of cotemporal observations with the Interferometric Bidimensional Imaging Spectrograph (IBIS) instrument at the Dunn Solar Telescope (DST) and with the Atacama Large Millimeter Array (ALMA) in a sparsely explored temporal regime up to 50 mHz. In [Section 4.3](#) we present evidence for the presence of high-frequency power in the velocity measurements of the $H\alpha$ and Ca II 854.2 nm lines as well in the ALMA brightness temperatures. To infer the wave energy fluxes from our observations we model the propagation of acoustic waves throughout the solar atmosphere with the RADYN code in [Section 4.4](#). The results from the modeling are presented in [Section 4.5](#) and the discussion of our results and the conclusions are summarized in [Section 4.6](#).

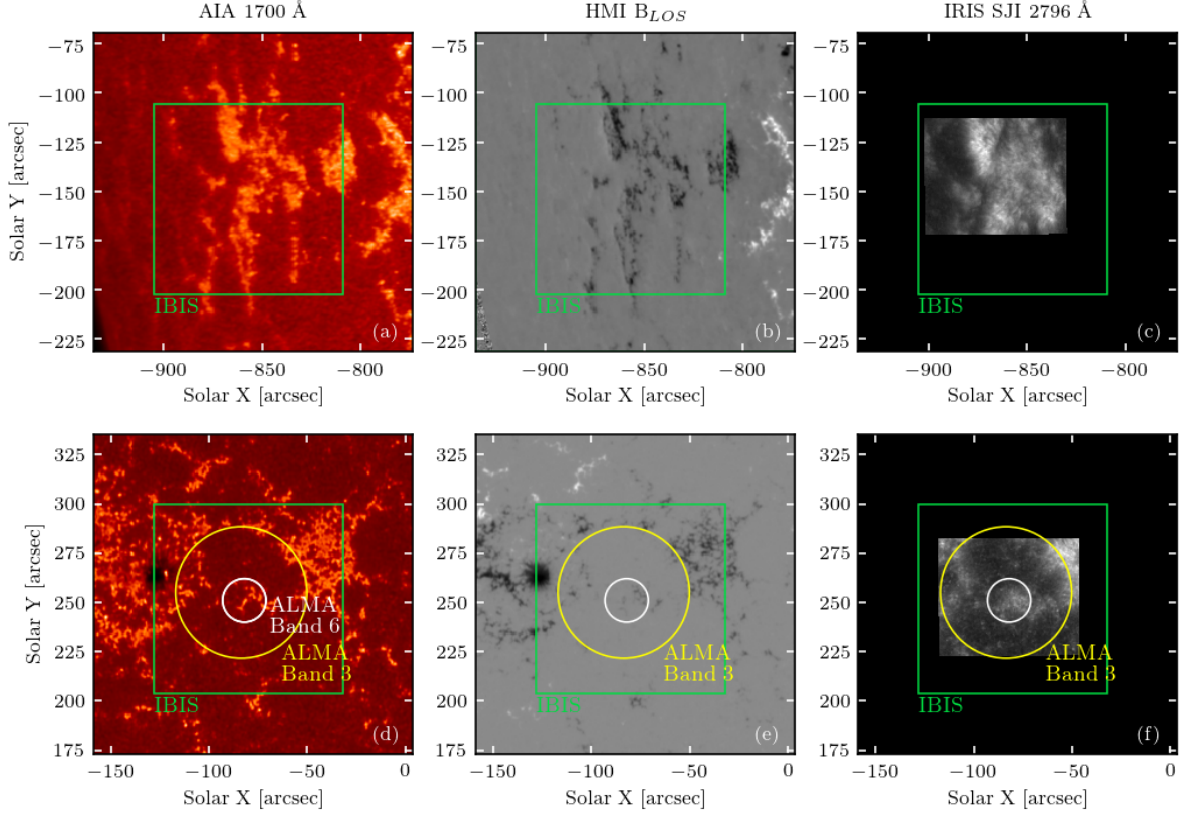


Figure 4.1: Context images of the observed fields of view. The top row (panels *a*, *b* and *c*) are FOV 1 (as seen at 14:25 UT) and the bottom row (panels *d*, *e* and *f*) are FOV 2 (as seen at 15:06 UT). **Left panels:** AIA 1700 Å image showing photospheric emission; **Central panels:** HMI Line-of-sight (LOS) magnetogram, where black and white denote high magnetic flux, gray areas depict close to zero magnetic flux; **Right panels:** IRIS slitjaw image at 2796 Å. The field of view of IBIS is shown as the green rectangle; the FOV of ALMA Band 3 is drawn as the yellow circle and the FOV of ALMA Band 6 as the white circle.

4.2 Observations and Data Processing

We obtained coordinated solar observations with ALMA (Wooten and Thompson, 2009) and the DST (Dunn, 1964; Dunn and Smartt, 1991) on 2017 April 23. These observations were part of ALMA Project ID 2016.1.01129S/Cycle 4. See Molnar et al. (2019) for some of the initial results from this observational campaign.

Two separate fields of view (FOV) were observed on 2017 April 23 and they are referred chronologically as FOV 1, near the limb, and FOV 2, close to disk center. The targets in both cases

were regions of magnetic network or plage, but they were observed at different inclination angles to the solar surface, which is essential for the discussion in Section 4.3.3. Context images of FOV 1 and 2 are provided from SDO/AIA (Lemen et al., 2012), SDO/HMI (Schou et al., 2012), and IRIS (De Pontieu et al., 2014) in Figure 4.1. Further analysis of the IRIS dataset is described in Chapter 5 of this thesis.

FOV 1 was observed with the DST at 13:50–15:14 UT at solar coordinates E 66.2°, S 09.8°, at an inclination of $\mu = 0.41$ (the cosine of the angle between the line of sight and the solar surface normal). FOV 1 was centered on the trailing edge of NOAA Active Region (AR) 12653. Based on the context imaging (top panel of Figure 4.1) FOV 1 contains some active region plage as well as internetwork regions with little magnetic field. The inclined viewing angle results in more confusion among features in the field of view because of projection effects of predominantly vertical features and longer integration along the line of sight.

FOV 2 was observed with the DST at 15:15–18:19 UT at solar coordinates E 4.9°, N 10.9° at an inclination of $\mu = 0.98$. FOV 2 was centered on the leading edge of the active region NOAA AR 12651. There is a magnetic concentration in the center of the field, surrounded by a largely field-free internetwork area, especially in the southern portion of the field. There is a region of plage in the northwestern corner of the field and the leading edge of the penumbra/superpenumbra on the northeastern corner.

4.2.1 DST observations

The DST took observations on 2017 April 23 between 14:00 UT and 18:40 UT, under conditions of excellent to good seeing. The instrument setup included IBIS (Cavallini, 2006; Reardon and Cavallini, 2008), the Facility InfraRed Spectrograph (FIRS, Jaeggli et al., 2010) and the Rapid Oscillations in the Solar Atmosphere instrument (ROSA, Jess et al., 2010a), which provided thor-

<u>Time [UT]</u>	<u>Spectral Interval</u>	<u>Cadence [s] /</u> <u>Number of scans</u>	<u>Target</u>
14:13–14:18	Ca II 854.2 nm	3.13 / 77	FOV 1
15:13–15:18	Ca II 854.2 nm	3.11 / 100	FOV 2
15:18–15:28	H α 656.3 nm	3.68 / 150	FOV 2
15:39–15:46	Ca II 854.2 nm	3.28 / 120	FOV 2
15:53–16:01	ALMA 1.25 mm	2.0 / 238	FOV 2
16:03–16:11	ALMA 1.25 mm	2.0 / 238	FOV 2
17:04–17:11	Ca II 854.2 nm	3.27 / 120	FOV 2
17:11–17:19	H α 656.3 nm	3.67 / 120	FOV 2
17:19–17:29	ALMA 3 mm	2.0 / 300	FOV 2
17:31–17:41	ALMA 3 mm	2.0 / 300	FOV 2

Table 4.1: Observations used in this work.

ough coverage of key spectral lines in the optical and the near-IR parts of the spectrum. All of the instruments were fed by the high-order adaptive optics system (Rimmele, 2004). None of the instruments were run in polarimetric mode, as high temporal cadence was the priority for this study.

IBIS observed the spectral lines of H I Balmer- α 656.3 nm (H α), Ca II 854.2 nm and Na I D₁ 589.6 nm with an average plate scale of 0.096'' pixel⁻¹. Each scan of a single spectral line scan took between 3 and 4 seconds with an overhead of about 1.5 seconds for changing the prefilters. We utilized two different scanning strategies during the observations. At the beginning of each ALMA observing block at a given pointing and frequency band, we ran “fast” scans of H α and Ca II 854.2 nm. Each scan consisted of 25 and 21 wavelength points, respectively and the average profiles from those scans are shown in Figure 4.2. Scanning a single line avoids the overhead for changing IBIS prefilters, resulting in a cadence of about 3.5 seconds for a single spectral scan (the precise cadences are listed in Table 4.1). This observing strategy was adopted to closely match the ALMA two-second sampling rate and allow us to study the high frequency wave regime (with Nyquist sampling of 130 mHz). These scans were intended to capture the fast dynamics of the chromosphere, at high temporal frequencies rarely explored with wide-field, bi-dimensional

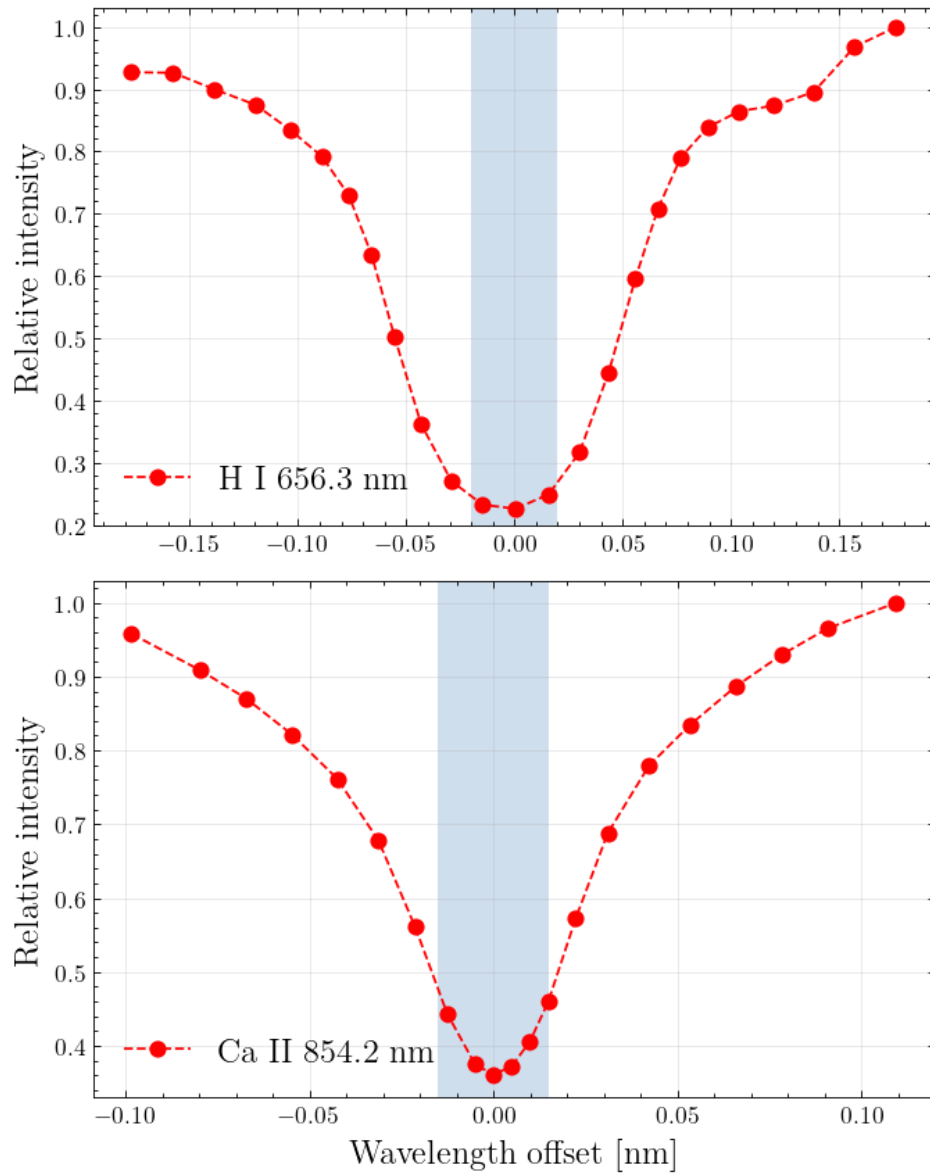


Figure 4.2: Average spectral profiles from the fast scans with IBIS in the H α (656.3 nm) and Ca II 854.2 nm lines. The line cores were sampled more densely to allow for more accurate determination of the line properties derived from the line cores (velocity, intensity and width). The blue shaded regions are used for the line core fitting with a parabola after a resampling on a finer (0.005 nm) grid.

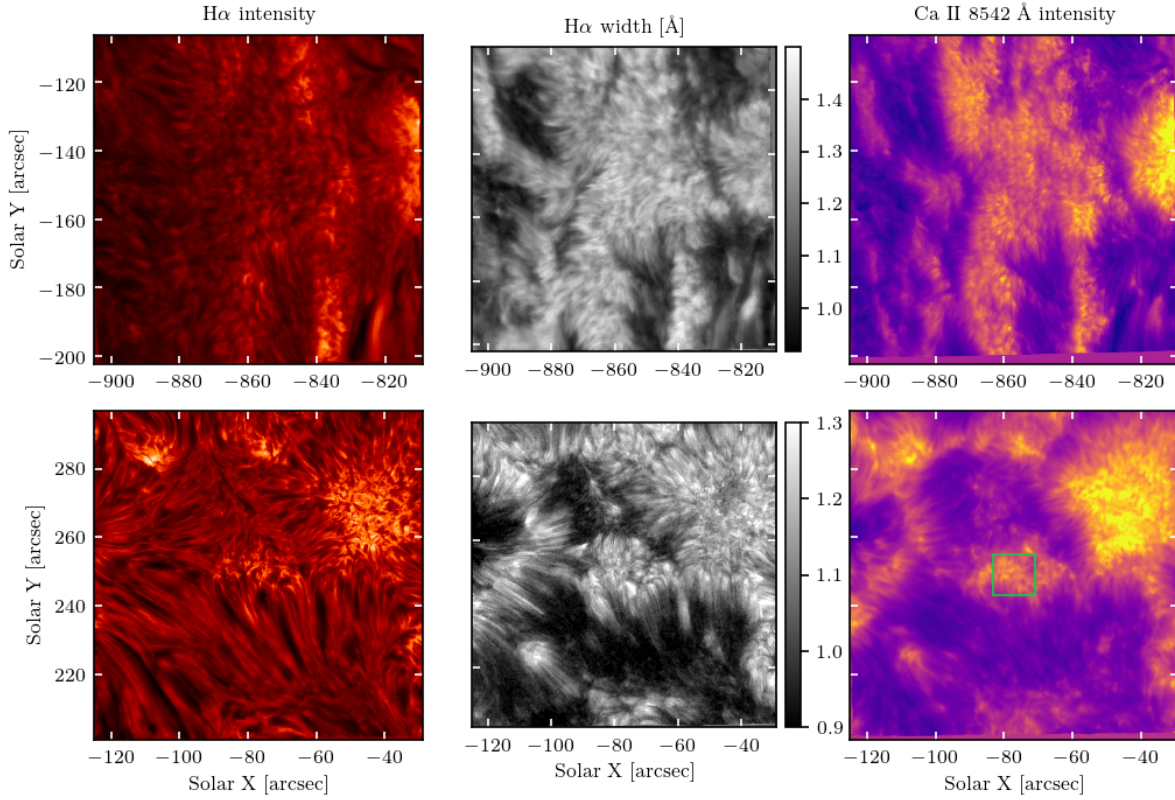


Figure 4.3: The fields of view observed with IBIS in the following chromospheric diagnostics: **Left panels:** $H\alpha$ 656.3 nm line core intensity; **Middle panels:** $H\alpha$ line core width (defined in Section 4.2.1); **Right panels:** Ca II 854.2 nm line core intensity. The top row corresponds to FOV 1 observed around 14:18 UT and the bottom row corresponds to FOV 2 observed at 17:20 UT. FOV 1 was observed close to the limb at $\mu=0.41$ which shortens the projection of the solar features in a direction away from disc center. FOV 1 covers mostly a plage region, while FOV 2 consists of network and internetwork with some plage in the top right. The green rectangle in the last panel shows the area from which the power spectra were used in Figure 4.7.

spectroscopy. Table 4.1 contains a summary of the single line (“fast”) scans with IBIS and the ALMA time series used in this study.

Following these fast scans, we ran longer durations of a “standard” repeating cycle of all the three spectral lines. The standard scans consisted of 90 total spectral points among the three lines and had duty cycle of about 15 seconds. This type of scan thoroughly covers the solar atmospheric layers from the photosphere through the middle chromosphere, making it well suited for studying the propagation of wave energy through the lower solar atmosphere.

To remove the seeing distortions in our narrowband images we relied on destretching the cotemporal broadband images (from the white-light IBIS channel) to HMI white-light images using the sub-aperture cross-correlation method introduced by [November and Simon \(1988\)](#). We applied the destretch maps to the cotemporaneous narrowband images and the resulting stability of the destretched images was on the order of one IBIS pixel ($\sim 0.1''$). The wavelength samplings for the fast scans of $H\alpha$ and the Ca II 854.2 nm lines are presented in Figure 4.2. The lines were sampled non-equidistantly to ensure better coverage of the line core, which is used for the velocity, intensity and width measurements. The maps of the observed line core intensity and width in $H\alpha$ and Ca II 854.2 nm for both FOVs observed with IBIS are presented in Figure 4.3.

Following [Cauzzi et al. \(2009\)](#), we measured the width of the chromospheric line cores as the separation of the two wing positions at which the intensity reached an intensity level halfway between the core intensity and the wing intensity at a defined wavelength offset from the local core position. The wing offsets used are ± 0.1 nm for the $H\alpha$ line and ± 0.06 nm for the Ca II 854.2 nm data. The resulting $H\alpha$ line width maps are shown in the middle column in Figure 4.3. These line widths are thought to be related to the temperature of the emitting plasma under chromospheric conditions ([Cauzzi et al., 2009](#); [Leenaarts et al., 2012a](#); [Molnar et al., 2019](#)).

We measured several different velocity signatures from our spectra. After sampling onto

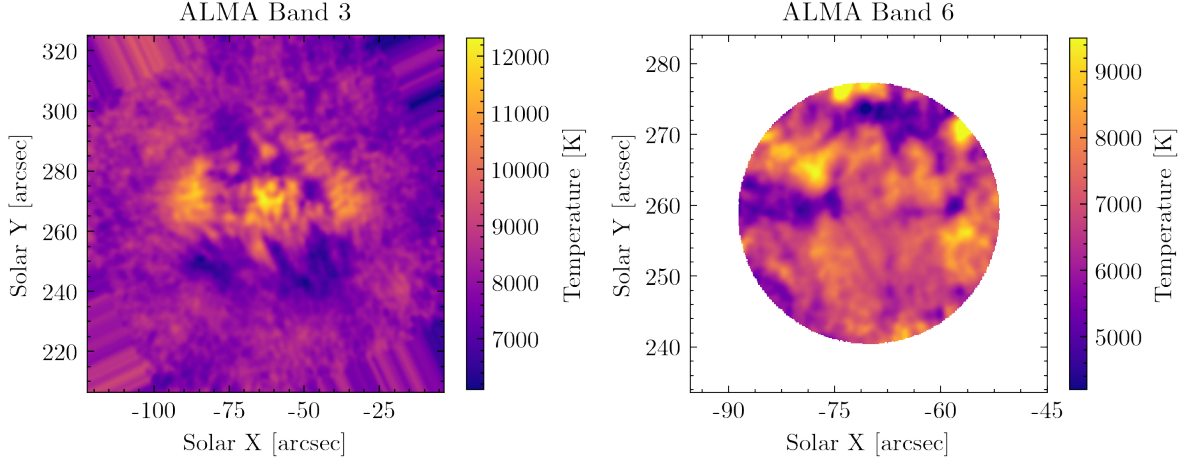


Figure 4.4: Average ALMA brightness temperature maps for Band 3 (left panel) and Band 6 (right panel) for FOV 2. The Band 3 image is the temporal average of observing block 2 (taken between 17:31–17:41 UT). The Band 6 image is the average of observing block 2 (taken between 16:03–16:11 UT). The central regions of these observations have the highest sensitivity, where a circular mask was applied to the Band 6 data to emphasize this region.

an evenly spaced wavelength grid with 0.005 nm sampling, we fitted the line minimum position and intensity with a parabola, in order to determine the Doppler velocity, which is related to the velocity at the $\tau=1$ for the line core in the atmosphere. The fitting was done on an interval of ± 0.02 nm and ± 0.015 nm for around the minimum position for $H\alpha$ and Ca II 854.2, respectively. This corresponds to approximately four (six) of the originally sampled points for $H\alpha$ (Ca II 854.2), indicated in Figure 4.2 as the blue region.

We also calculated the center of gravity (COG) velocity of over ± 0.12 nm wavelength region for the $H\alpha$ line and over a ± 0.105 nm for the Ca II 854.2 nm line. This velocity measure takes into account the whole line profile and might carry some information about the photospheric velocity field in the case of $H\alpha$ (Socas-Navarro and Uitenbroek, 2004). Finally, we used the same bisector calculation described above to determine a bisector shift for both lines at 50% level.

4.2.2 ALMA observations

ALMA became available for solar observations in Cycle 4 (2017) after extensive testing (Phillips et al., 2015). The continuum wavelength bands available for solar observations were Band 3 (3 mm/100 GHz) and Band 6 (1.25 mm/240 GHz) which are expected to sample the high and middle chromosphere (Wedemeyer et al., 2016). The continuum radiation in these wavelengths forms in the chromosphere under Local Thermodynamic Equilibrium (LTE) conditions, as the main source of opacity is due to free-free processes which makes the source function to be locally determined by the plasma temperature. The ALMA intensity can be interpreted as brightness temperature under the Rayleigh-Jeans limit (Wedemeyer et al., 2016). Hence, ALMA is a valuable tool to study the thermal structure of the chromosphere (some recent results include Shimojo et al., 2017b; Loukitcheva et al., 2019; da Silva Santos et al., 2020).

ALMA is an excellent instrument for studying high-frequency waves in the solar atmosphere due to its fast sampling cadence of 2 seconds, spatial resolution better than 2" (depending on the array configuration), and direct sensitivity to electron temperature. However, it is important to remember that the opacity scale of the ALMA radiation is determined through the local electron density (and the ionization state of the plasma), which is thought to be far from thermodynamical equilibrium (Carlsson and Stein, 2002). The time-varying opacity can complicate the interpretation of the time-series of temperature brightness measurements (Molnar et al., 2019).

The ALMA observations discussed in this paper were obtained in configuration C40-3 and their reduction is described in Molnar et al. (2019). The millimeter observations are obtained in approximately 10-minute blocks interspersed with several minutes of off-target calibrations. For FOV 2, we analyzed temporal blocks 1 (17:19–17:29 UT) and 2 (17:31–17:41 UT) from Band 3 (also used in Molnar et al., 2019) and blocks 1 (15:53–16:01 UT) and 2 (16:03–16:13 UT) from Band 6.

An ALMA data summary is presented in Figure 4.4. We chose these particular ALMA observing blocks because they are the closest in time to our high-cadence IBIS observations of FOV 2 listed in Table 4.1. The relative positions of the ALMA observing fields to the IBIS observation regions are shown in Figure 4.1 as the colored circles. The useful regions of the FOVs of the ALMA data are about the size of the respective circles in Figure 4.1: $60''$ for ALMA Band 3 and $20''$ for Band 6.

4.2.3 Solar feature classification

To study the typical wave characteristics in different regions of the solar atmosphere, we partitioned the solar surface in the field of view into five different classes of features that represent general chromospheric structures: penumbra, internetwork, fibrils, network and plage. We distinguished the regions following a methodology based on the properties of the $H\alpha$ and Ca II 854.2 nm spectral lines.

For FOV 2, we first categorized the penumbral region by its proximity to the leading sunspot in NOAA AR 12651 and its low $H\alpha$ line width (smaller than 0.1 nm) and low Doppler velocity fluctuations relative to the rest of the field. Secondly, we distinguished between the plage and the network regions, which are brightest in FOV 2. We can clearly distinguish between the two by the amount of magnetic flux and the intensity in the Ca II 854.2 nm line core intensity. We assign a pixel to be a plage region if the photospheric magnetic field strength (from HMI) is above 1200 G and the Ca II 854.2 nm line core intensity is more than 60% above the mean intensity of the whole FOV. Pixels were categorized as network if their magnetic field was above 250 G and their Ca II line core intensity is below the 60% intensity threshold. We labeled the regions with lowest intensity in the core of Ca II 854.2 nm and with the lowest $H\alpha$ line core width (less than 0.105 nm) as internetwork or fibrils. We distinguished between the fibrils and the internetwork regions by the

ratio of the relative power in the 3 min to 5 min power in the Doppler velocity power spectra as suggested by Vecchio et al. (2007), where the internetwork has a ratio greater than one and the fibrils have a ratio less than one between those two frequency windows.

Each of these criteria resulted in binary masks, which we blurred with a Gaussian filter (with a standard deviation of 40 pixels) to smooth the boundaries of the regions and avoid holes. In cases where the smoothing caused masks for separate classes to overlap, we chose the darker of the two classes to define that pixel. The blurring insured, for example, that isolated magnetic elements in the internetwork were smoothed out and the classified regions were largely contiguous. The resulting mask for FOV 2 which we employed throughout the rest of the paper to distinguish the different regions of the solar surface is shown in Figure 4.5.

We use a similar masking algorithm for the FOV 1 observations, but using only three types of solar features because there is no penumbra in this target and we cannot easily distinguish between the internetwork and the fibrils at such highly inclined projections. We take into account in our analysis that FOV 1 is mostly a plage region and hence label all of the “quieter” regions as fibrils. We increased the $H\alpha$ core width cutoff for fibrils to 0.12 nm, as the average $H\alpha$ line width increases closer to the solar limb. We distinguished between plage and network by the photospheric magnetic field strength – if the magnetic field was above 1200 G (as for FOV 2) then we classified the pixel as plage, otherwise it was classified as network. We also used a Ca II 854.2 nm line core intensity threshold that was twice the average intensity of the whole FOV for distinguishing between plage and network. The resulting mask for FOV 1 is presented in Figure 4.6.

4.3 Observed high-frequency power in the spectral diagnostics

In this Section we present the high-frequency observations derived from the Power Spectrum Density (PSD) of the observed chromospheric diagnostics (intensities, velocities, etc.) described

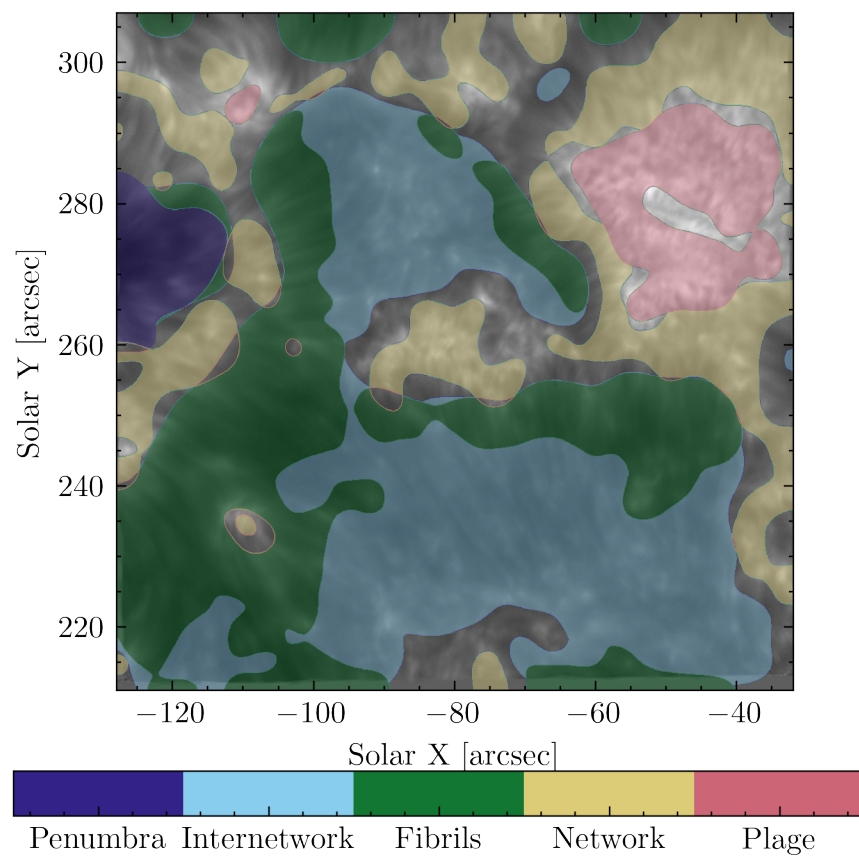


Figure 4.5: Mask for FOV 2 for the different regions of the solar surface (shaded in the corresponding color) overlaid over the Ca II line core intensity.

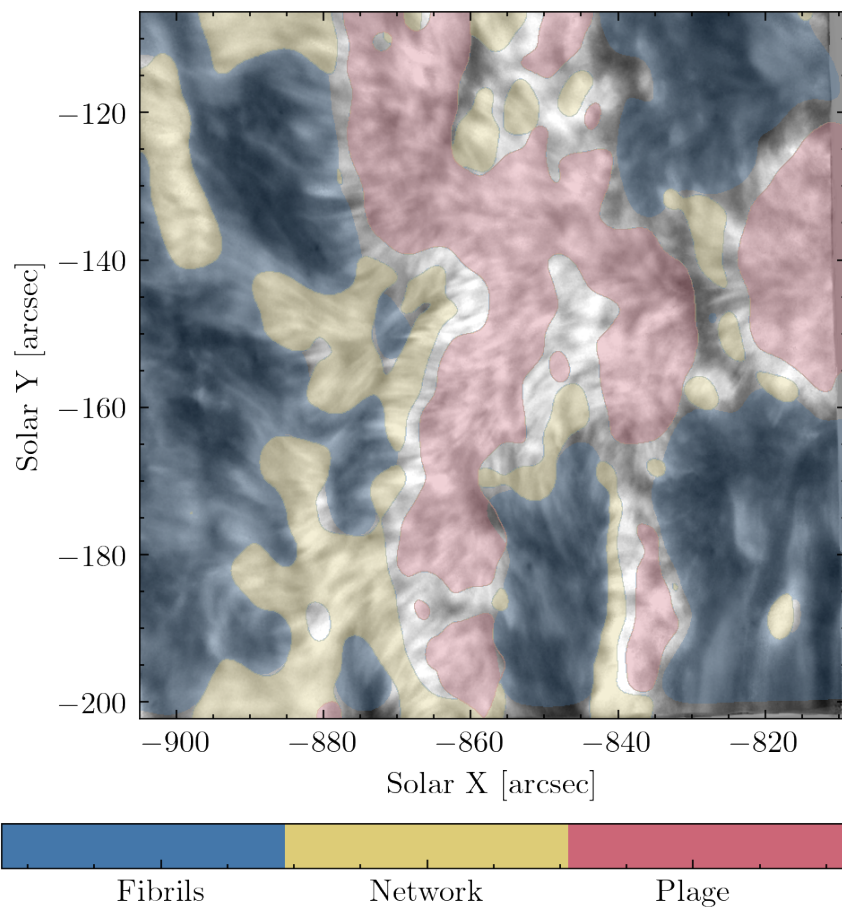


Figure 4.6: Mask of the different solar regions in FOV 1 using the approach described in Section 4.2.3. No distinction between internetwork and fibrils was made for this FOV due to the large viewing angle and preponderance of magnetic flux.

in Section 6.2. The PSDs are calculated as the absolute value of the Fourier amplitudes of the observed signals, where we subtracted the mean of the observed time series and then apodized them with a Hamming window with 3% of the total length of the observations on each side.

4.3.1 Observed high-frequency power in chromospheric spectral diagnostics

The top four rows of Figure 4.7 present a summary of the power spectra of the chromospheric spectral diagnostics derived from $H\alpha$ (data series starting at 15:18:57 UT) and Ca II 854.2 nm line (data series starting at 15:13:21 UT) IBIS observations of FOV 2. The pixels analyzed for this plot were taken from the central $12'' \times 12''$ regions of FOV 2 (the green rectangle in Figure 4.3) to ensure that the same solar region is observed with IBIS and ALMA. Furthermore, the selected area (green square) spans only a network region, which simplifies the analysis to a single type of source region. The red dotted line is the mean of the distribution at each frequency and the lighter blue lines are individual power spectra of each pixel. The frequency resolution of the power spectra is on the order of $\delta\nu \approx 2 - 3$ mHz as the length of our data series is about 10 minutes and the cadence is on the order of 3.3 seconds (see Table 4.1 for the details of the observations). We do not clearly observe the low frequency power around the five-minute oscillation window with high resolution due to the short temporal extent of these fast scans.

The power spectra show a strikingly similar power law above 7 mHz in all observed spectral diagnostics, limited at the higher frequencies by white-noise floor. The level of the white noise varies for the different spectral diagnostics. Our results extend previous work by Reardon et al. (2008) to higher frequencies where they agree in the low frequency part (7–20 mHz) of the power spectrum. The white noise which dominates the high frequency signal is likely due primarily to the photon noise from the measured signal. In Appendix A we describe a detailed estimation of the effect from photon noise on the white-noise floor of the line core velocity measurements of the

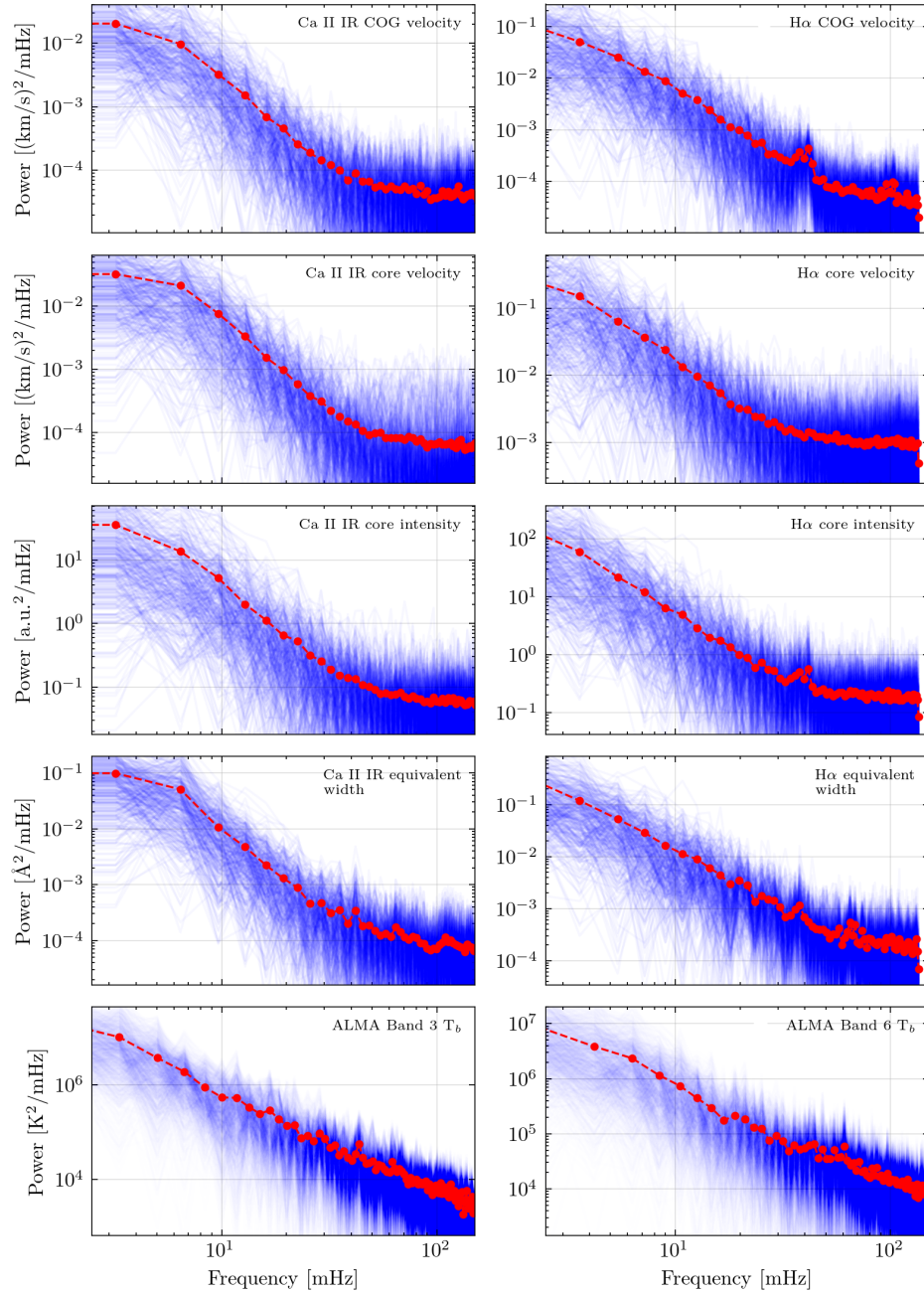


Figure 4.7: Power spectra of different spectral chromospheric diagnostics. In the first four rows, the left columns correspond to spectral properties derived from the Ca II 854.2 nm line (Ca II IR) and the right column from the H α line observations. The chromospheric diagnostics which each row is derived from are: *First row*: COG velocity; *Second row*: line center velocity; *Third row*: intensity of the line core (where a.u. stands for arbitrary units); *Fourth row*: equivalent width. The last row corresponds to PSDs derived from ALMA Band 3 (*left row*) and Band 6 (*right row*) intensity observations. The blue lines represent individual power spectra and the red dotted lines show the mean in each frequency bin.

Ca II 854.2 nm data. This additional contribution to the PSD is important to characterize in order to properly quantify only the solar contribution to the integrated power.

The observed and simulated white-noise level distributions are shown in the Figure 4.8 and summarized in Table 4.2. In both cases, we see that the profiles with higher Ca II 854.2 nm line core intensities (plage, network) tend to have higher noise levels compared to deeper profiles (with more pronounced core minima). The distributions of the simulated noise levels have somewhat broader tails, indicating a possible overestimation of the noise in our model in extreme cases. However, the median values (dashed vertical lines) of the simulated distributions are all in good agreement with the observed ones. Hence, we believe that we can well characterize the noise floor separately for different classes of solar structures in our dataset.

We employ the same data analysis approach for the brightness temperatures from the ALMA Bands 3 and 6 data. The PSD of the brightness temperature from the same central $12'' \times 12''$ of the ALMA FOVs are presented in the last row of Figure 4.7. The red lines again indicate the average of the distribution and the light blue lines are the power spectra of individual pixels.

The power law behavior of the ALMA brightness temperature PSD (seen before in [Nindos et al. \(2020\)](#)) extends to the white-noise floor at about 100 mHz in the Band 3 data. In the Band 6 observations we do not see clearly the white-noise floor. We do not observe the 3 minute (5 mHz) oscillations clearly, like in [Patsourakos et al. \(2020\)](#). This might be due to presence of magnetic elements in the observed region as suggested by [Jafarzadeh et al. \(2021\)](#), or due to the limited frequency resolution of our data of about 2 mHz. However, the observed region is mostly covered under the magnetic canopy where we notice the bright fibrils (in ALMA wavelengths) dominating our field of view (see Figures 4.1 and 4.3).

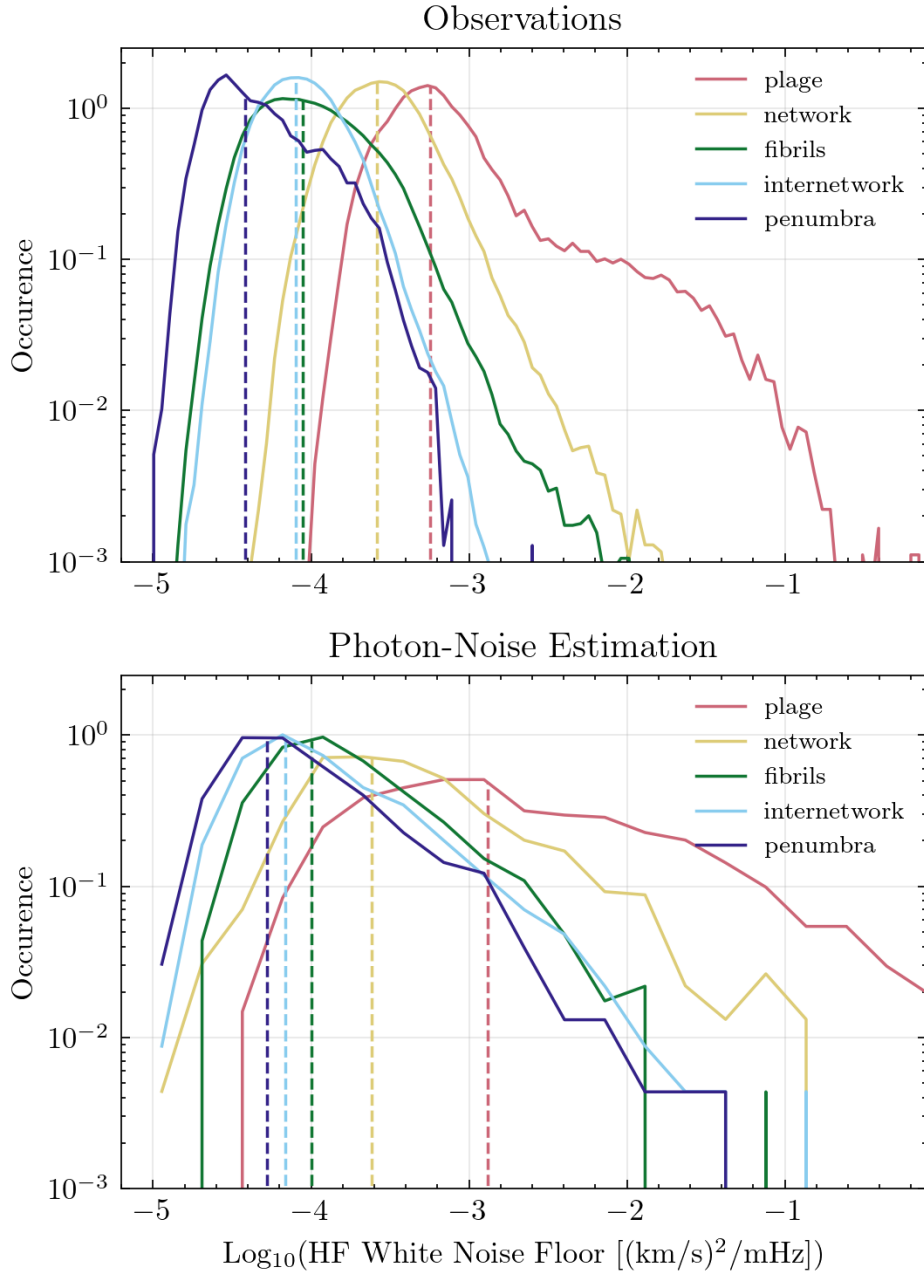


Figure 4.8: Histogram of the high frequency white noise level for different regions of the solar surface. **Top panel:** White noise limit in the IBIS Ca II 854.2 nm data measured as the median of the last 25 frequency bins in the PSDs of the individual pixels. **Bottom panel:** Estimate of the white noise floor from photon noise based on the method presented in Appendix A. The solar surface regions were distinguished as shown in Figure 4.5. The median of each distribution is presented as the dashed vertical line.

Solar region	Oscillatory power [(km/s) ²]	Raw/Corrected Power law slope	Log ₁₀ (Noise floor) [(km/s) ² /mHz]	Acoustic flux [W/m ²]
Penumbra	0.034 ^{+0.097} _{-0.024}	-2.47 ^{+1.33} _{-1.42} / -0.86 ^{+1.07} _{-1.46}	-4.41 ^{+0.54} _{-0.28}	24 ⁺¹⁶ ₋₄₅
Internetwork	0.47 ^{+0.59} _{-0.26}	-3.42 ^{+1.63} _{-1.21} / -1.82 ^{+1.31} _{-1.22}	-4.12 ^{+0.35} _{-0.29}	203 ⁺²²⁸ ₋₁₁₉
Fibrils	0.17 ^{+0.30} _{-0.12}	-2.92 ^{+1.46} _{-1.35} / -1.32 ^{+1.22} _{-1.34}	-4.04 ^{+0.47} _{-0.39}	102 ⁺¹³⁸ ₋₅₉
Network	0.16 ^{+0.36} _{-0.11}	-2.14 ^{+1.33} _{-1.30} / -0.62 ^{+1.00} _{-1.32}	-3.58 ^{+0.36} _{-0.32}	109 ⁺¹⁹³ ₋₇₁
Plage	0.48 ^{+1.46} _{-0.38}	-2.39 ^{+1.07} _{-1.11} / -0.79 ^{+0.89} _{-1.14}	-3.25 ^{+0.76} _{-0.34}	256 ⁺⁸⁴⁷ ₋₁₆₆

Table 4.2: Summary of the power law properties and the wave flux observed in the different regions on the solar surface for FOV 2 Ca II 854.2 nm data (15:39:54 UT).

4.3.2 Properties of the observed power spectra

We concentrate on the Ca II 854.2 nm velocity power spectra as they are the most reliable chromospheric velocity diagnostic we have, as the H α line synthesis results depends strongly on the full 3D radiative transfer solution (Leenaarts et al., 2012a). Using the feature classifications derived in Section 4.2.3 and shown in Figure 4.5, we calculated the average Ca II 854.2 nm line core Doppler velocity PSD for every type of region of the solar surface described above. The average PSDs are presented in Figure 4.9. The plage and internetwork have higher amounts of velocity oscillation power compared to the network and the quieter regions (fibrils and penumbra). However, the plage has a significantly higher white-noise floor (comparable to the network one) than the one seen in the internetwork. The internetwork has high amount of wave flux in the 5-20 mHz interval but a lower white-noise floor – similar to the one in the quieter regions (fibrils, penumbra).

Figure 4.10 shows the spatial maps for FOV 2 of the amount of oscillatory power at each pixel integrated between 5 and 50 mHz in the line core intensity and Doppler velocity measured from the Ca II 854.2 nm and H α lines as well the oscillatory power derived from the ALMA brightness temperatures. Throughout the paper when we refer to oscillatory power we mean the integrated power spectral density (PSD) in the specified frequency range. When estimating PSDs, we always subtract a white noise estimate based on the mean of the last 25 (high) frequency bins. We see that properties of similar diagnostics (velocities, intensities and widths) derived from different spectral

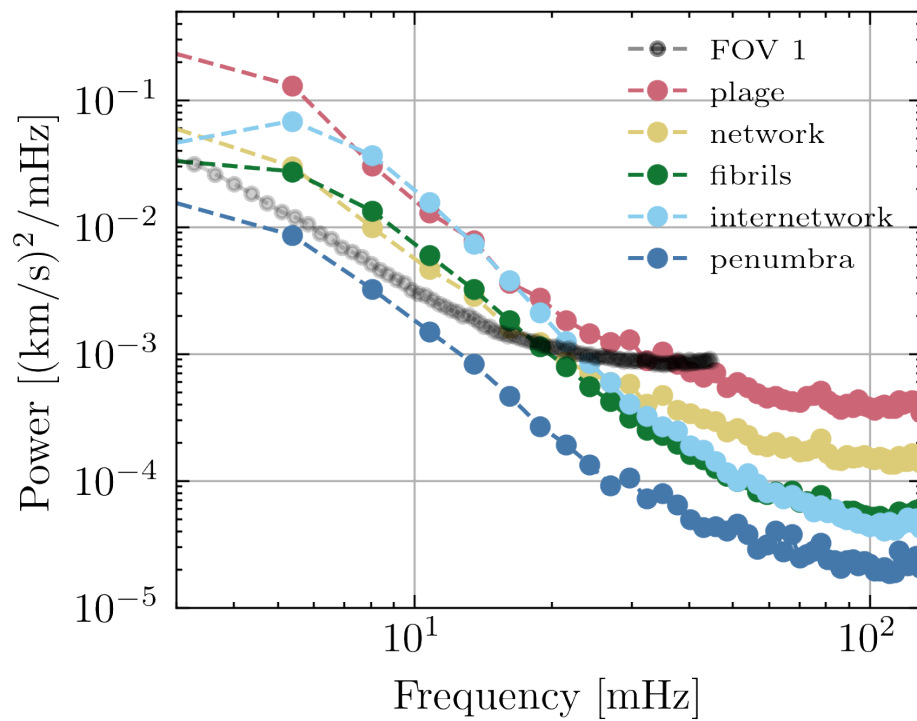


Figure 4.9: Averaged power spectra of the Doppler line core velocity from Ca II 854.2 nm line for different solar regions in FOV 2. The regions are outlined in Figure 4.5. The median FOV 1 Ca II Doppler velocity PSD is shown as the semitransparent black dotted line.

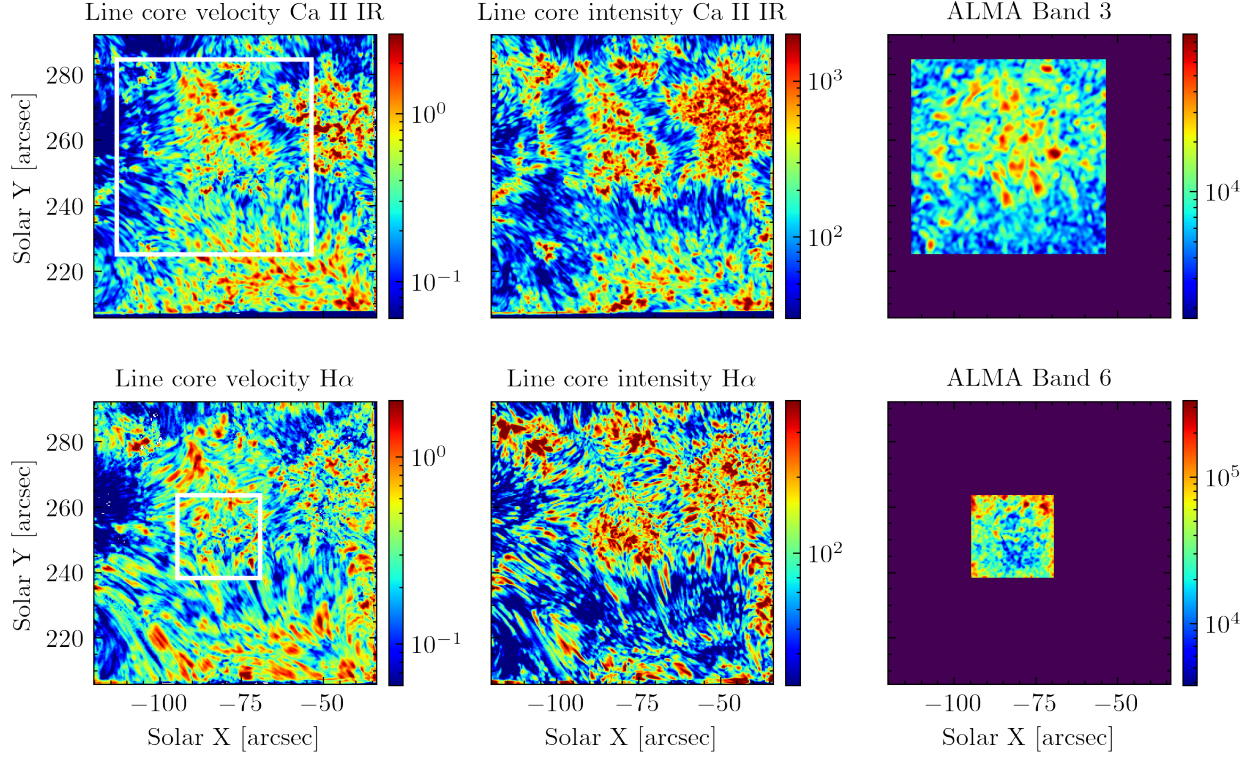


Figure 4.10: Total oscillatory power between 5 mHz and 50 mHz for different chromospheric diagnostics in FOV 2. The panels show the following quantities: **Top row:** *Left:* Ca II 854.2 nm line center velocity power $[(\text{km/s})^2]$; *Center:* Ca II 854.2 nm line center intensity power $[\text{counts}^2]$; *Right:* ALMA Band 3 brightness temperature $[\text{K}^2]$; **Bottom row:** *Left:* H α 656.3 nm line center velocity power $[(\text{km/s})^2]$; *Center:* H α 656.3 nm line center intensity power $[\text{counts}^2]$; *Right:* ALMA Band 6 brightness temperature $[\text{K}^2]$. The white panels in the left column show the FOV of the ALMA Band 3 (top row) and Band 6 (bottom row).

lines have similar distributions. The ALMA Band 3 temperature fluctuations map (top right) correlates with the spatial distribution of the PSDs in the optical diagnostics, but the Band 6 one (bottom right) does not appear to resemble its optical counterparts. This might be due to time-varying changes in the height of formation of the ALMA intensities as well as the lower angular resolution of the ALMA observations or the very limited FOV of the ALMA Band 6 observations.

We calculated the power law slope describing the observed power spectra with least- χ^2 fitting between 10 and 40 mHz. Using the same solar feature mask, we calculated the distributions of the slopes in the Ca II 854.2 nm line core velocity in the different regions of the solar surface and the results are presented in Figure 4.11. The distributions of the slopes from the observed

(raw) data are presented in Panel a) of Figure 4.11. We see that plage and network regions have shallower slopes than the fibrils, internetwork and penumbral regions. The slope distributions are overlapping and form a continuous transition between all of the different types of solar features, but their progression does follow the trend of mean $H\alpha$ line-widths for those solar features (excluding the penumbra). The quantitative comparison of the power slope distributions is listed in Table 4.2, along with some other quantities derived from the observed power laws. The quoted regions of uncertainty are the 10th/90th percentiles of the cumulative distributions. We note that the power-law slopes we find for the network, fibril, and internetwork regions are very comparable to those found by Reardon et al. (2008) for the 5-20 mHz interval.

To infer the true slope of the vertical velocity field in the solar atmosphere, we applied the velocity attenuation coefficient described in Section 4.4.3. The resulting corrected velocity power law slope distributions are presented in Panel b) of Figure 4.11 and their medians are summarized in Table 4.2. The relative order of the solar features is preserved, but the resulting distributions of slopes are shallower as the compensation for the wave attenuation makes the power laws less steep. The resulting values of the power law slopes of the corrected data are roughly between -2 and 0 . These values are shallower than the ones expected from the Lighthill-Stein turbulence theory (Ulmschneider et al., 1996), which predicts power law slopes between -3.5 and -3 . Eulerian-based treatments of turbulence in the solar atmosphere give slopes between -2.4 and -1.3 , which are closer to our observed values (Rubinstein and Zhou, 2002). Hence, our observations favor the Eulerian approach in treating the turbulent time correlations in the solar atmosphere. However, the penumbra, the network, and the plage regions which exhibit higher power law slopes than either theory predicts and require further investigation, which we leave for a following study.

Figure 4.12 shows the correlation between the uncorrected power-law slopes and the total amount of power in each spectral diagnostic, with pixels with higher integrated power having steeper

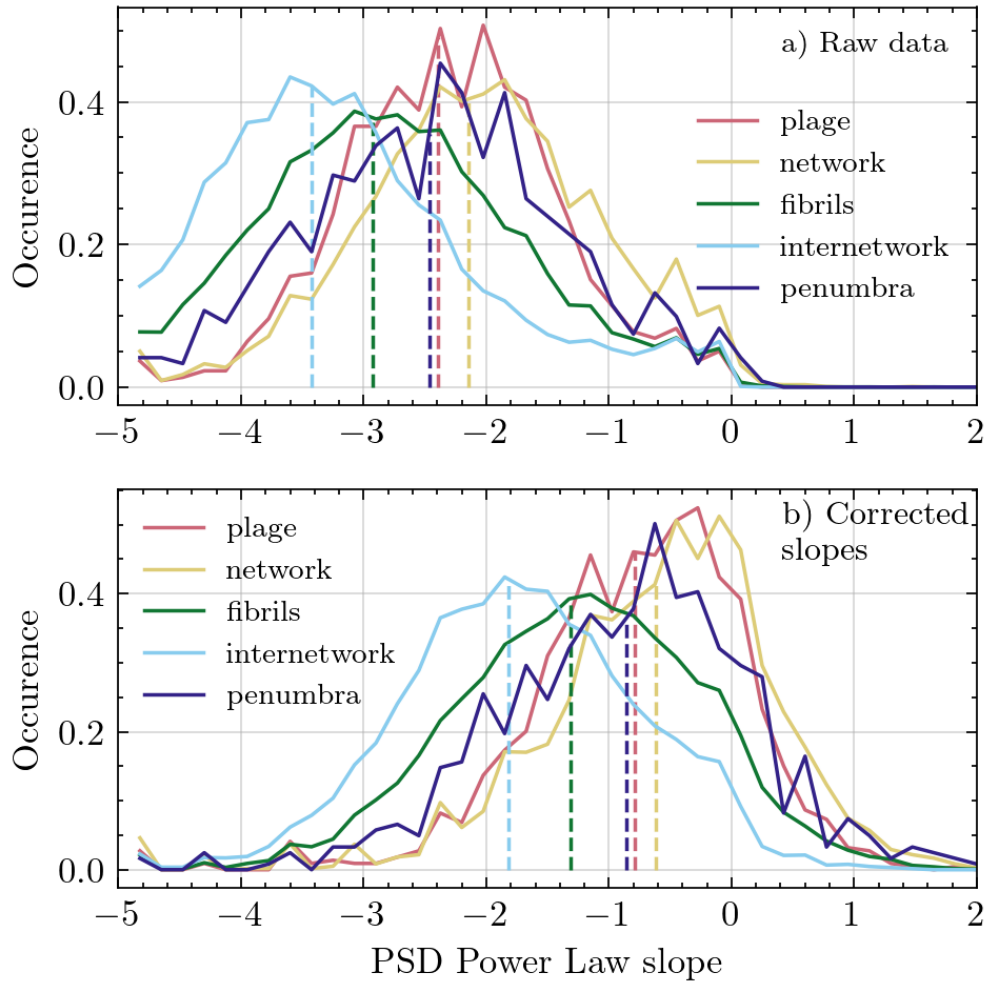


Figure 4.11: Histogram of the slopes of the power law fit to the PSD of the Doppler velocity of Ca II 854.2 nm line for **Panel a)**: Raw data; **Panel b)**: Corrected data (see Section 4.3.2). The fit was made between 10 mHz and 40 mHz. The dashed lines show the median of the distributions.

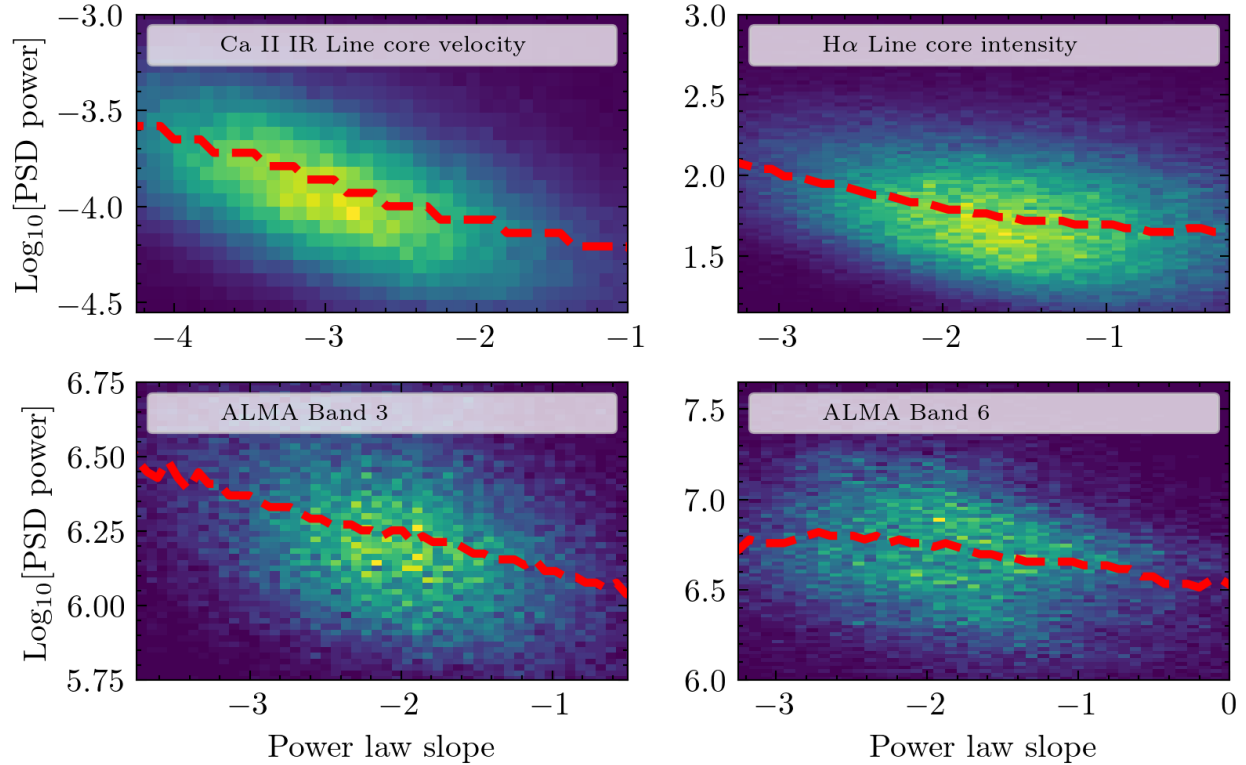


Figure 4.12: 2D histograms of the total oscillatory power in the respective diagnostic against the slope of the power law fit in the frequency range of 8 to 35 mHz. **Top:** *Left:* Ca II 854.2 nm line core velocity. *Right:* H α 656.3 nm line core intensity; **Bottom:** *Left:* ALMA Band 3 brightness temperature; *Right:* ALMA Band 6 brightness temperature. The red line represents the average of each column of the histograms.

slopes. Since the PSDs are steeper, the higher power is a consequence of those regions tending to have higher overall oscillatory power in the lower portion (5-10 mHz) of the frequency interval.

We partitioned the Band 3 field of view into three regions based on the mean observed 3 mm brightness temperature: $T_b < 7500$ K; 7500 K $< T_b < 10000$ K; and $T_b > 10000$ K. The resulting segmentation mask is presented in Figure 4.13. We used this segmentation approach because the classification described in Section 4.2.3 did not necessarily correspond well with the ALMA brightness temperature features. In particular, the fibril regions exhibit brightness temperatures comparable to those seen in the network regions. The average power spectrum of the ALMA Band 3 brightness temperature for each of these different solar regions are presented in Figure 4.14. The

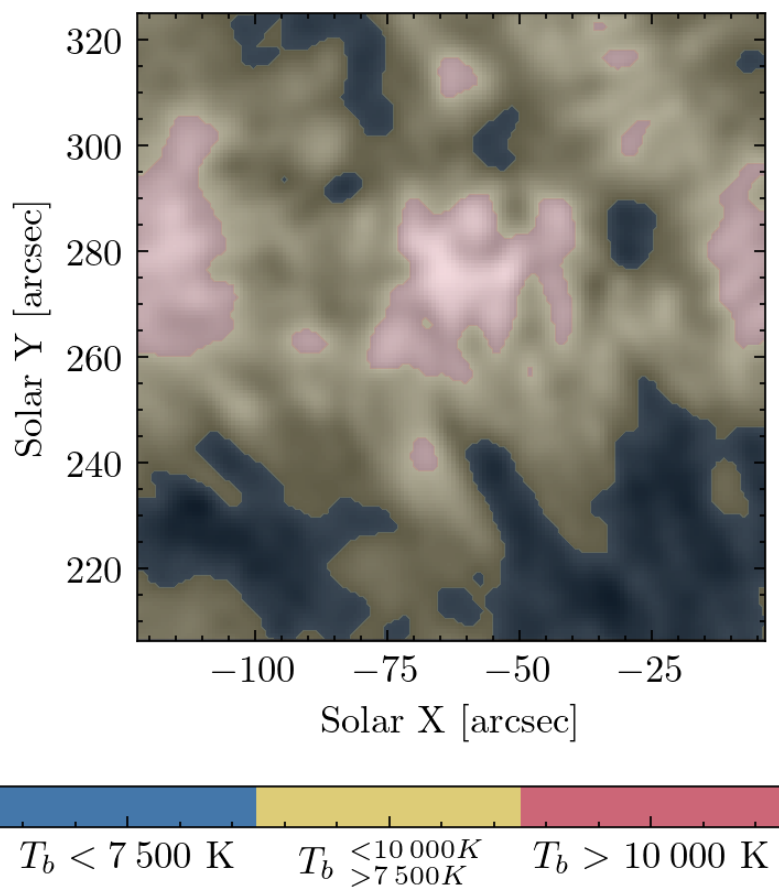


Figure 4.13: The mask distinguishing the different regions of the solar surface in for the ALMA Band 3 FOV. The mask is based on the brightness temperature T_b split into three categories – $T_b < 7\,500\text{ K}$, $7\,500 < T_b < 10\,000\text{ K}$, and $T_b > 10\,000\text{ K}$.

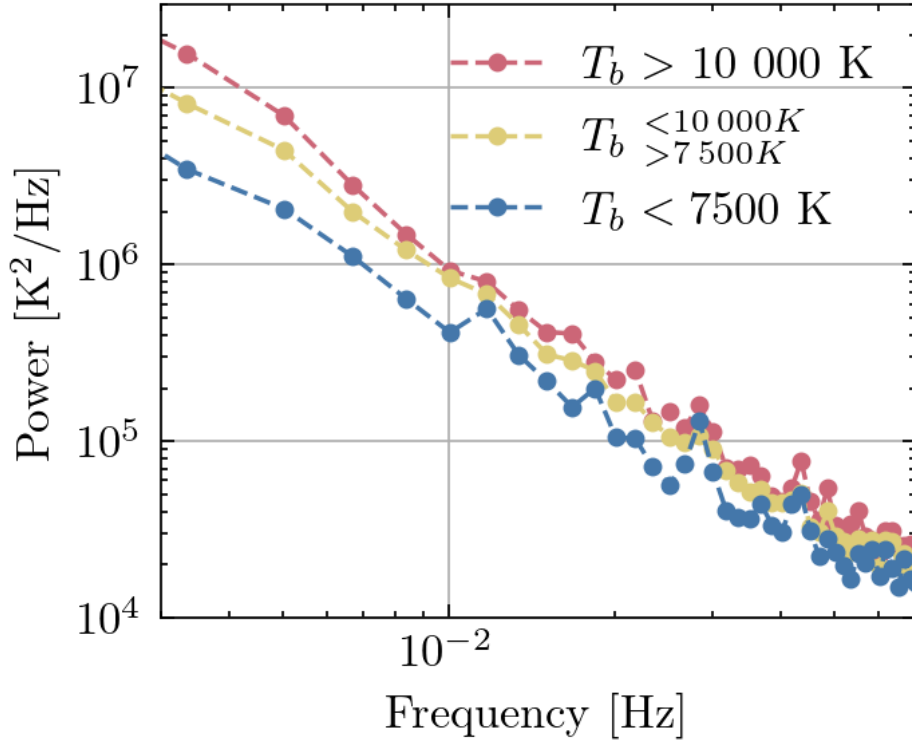


Figure 4.14: Average ALMA Band 3 brightness temperature T_b PSDs for different regions of the solar surface as segmented in Figure 4.13.

power spectra share similar slopes, independent of the region, with a value of $-1.63 \pm .07$ in the region of 10 to 50 mHz. The brighter regions have slightly higher oscillatory power at frequencies below 10 mHz. We did a similar analysis of the Band 6 data (using the same temperature-based segmentation based on the Band 3 data), but did not find any significant differences in the slopes or total power among the different (temperature discriminated) regions of that FOV. This might be due to the rather small FOV of Band 6 ($20''$) compared to Band 3 ($60''$).

Figure 4.15 shows the correlation between brightness temperature and the relative (normalized to the mean) brightness temperature fluctuations in the ALMA data between 5 and 50 mHz. ALMA Blocks 2 were used for both bands in the figure. In order to avoid the attenuation of the sensitivity farther away from the center of the beam, we used only the central $60''$ of the Band 3 FOV and the central $17''$ for the Band 6 FOV. The red lines show the median trend of the his-

tograms. We can see a clear correlation between the brightness temperature and oscillatory power in the Band 6 data and an almost non-existent one in the Band 3 data. The relative temperature fluctuation power is related to the amount of compressive wave flux as shown in Section 4.4.2.

4.3.3 Velocity oscillations at different viewing angles

Observing the solar atmosphere at different inclinations provides a way to disentangle the longitudinal from the transverse velocity oscillations, as these two components are differently projected into line-of-sight Doppler shifts. This allows us to statistically disambiguate between the transverse and the longitudinal oscillations if we observe similar solar regions at (a minimum) two different viewing angles. FOV 1 was observed at an incidence angle of 66 degrees or $\mu = 0.41$, close to the east solar limb.

Assuming mostly vertical magnetic field orientation to the solar surface, the observed velocity oscillatory power is to be composed of not only the longitudinal velocity oscillations $\langle v_{\parallel} \rangle$ (angle brackets stands for the average root mean square value over time of the quantity), and a transverse (Alfvénic-like) $\langle v_{\perp} \rangle$ component. The perpendicular component $\langle v_{\perp} \rangle$ is of special interest for constraining coronal heating models, as those waves are expected to propagate readily throughout the chromosphere and into the corona (Cranmer and van Ballegoijen, 2005). In the case of perpendicular to the solar surface observations, close to disc center as in the case of FOV 2, we will detect only $\langle v_{\parallel} \rangle$ as the Doppler velocity. Knowing $\langle v_{\parallel} \rangle$ from the observations of FOV 2 (close to disc center), we can calculate $\langle v_{\perp} \rangle$ from the observed velocity oscillations $\langle v_{obs}^2(\theta) \rangle$ (at an incidence angle θ) in FOV 1. The observed velocity oscillations $\langle v_{obs}^2(\theta) \rangle$ can be written into their components

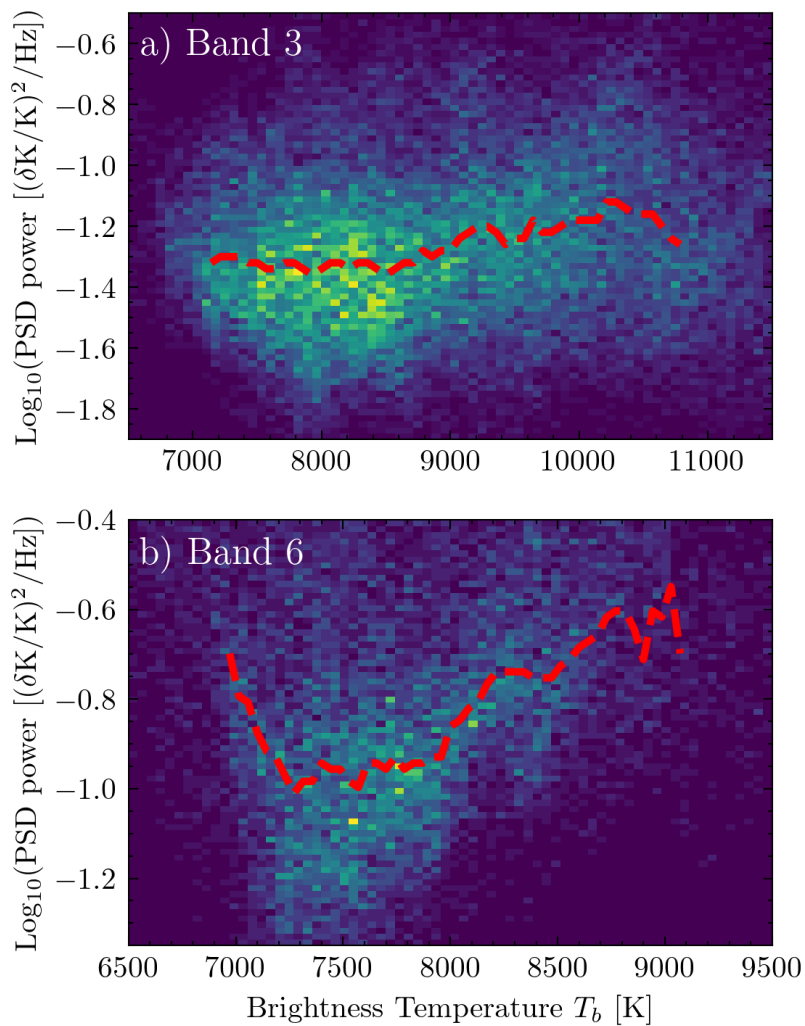


Figure 4.15: Integrated ALMA brightness temperature oscillatory power in the frequency range from 5 to 50 mHz against the observed brightness temperature for **a)** Band 3 and **b)** Band 6. The red line shows the running median of the distribution for each column of the histogram.

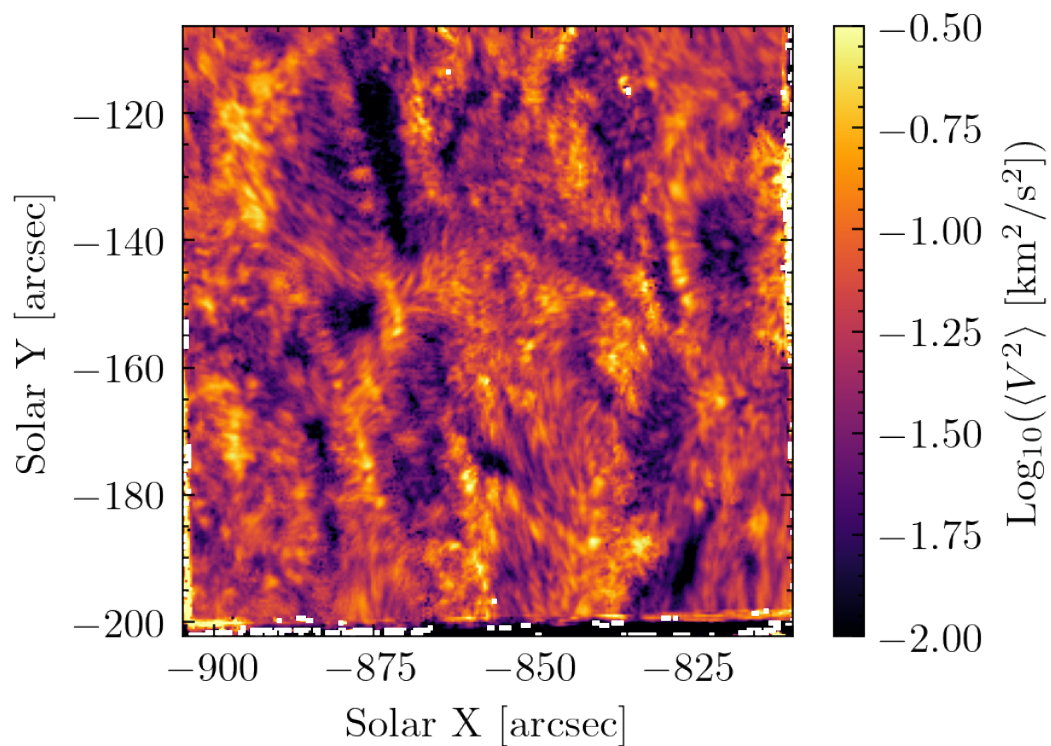


Figure 4.16: Velocity oscillations map for FOV 1 derived from the Ca II 854.2 nm line core Doppler velocity between 5 and 20 mHz. The white-noise floor has been subtracted as described in Section 4.2.1.

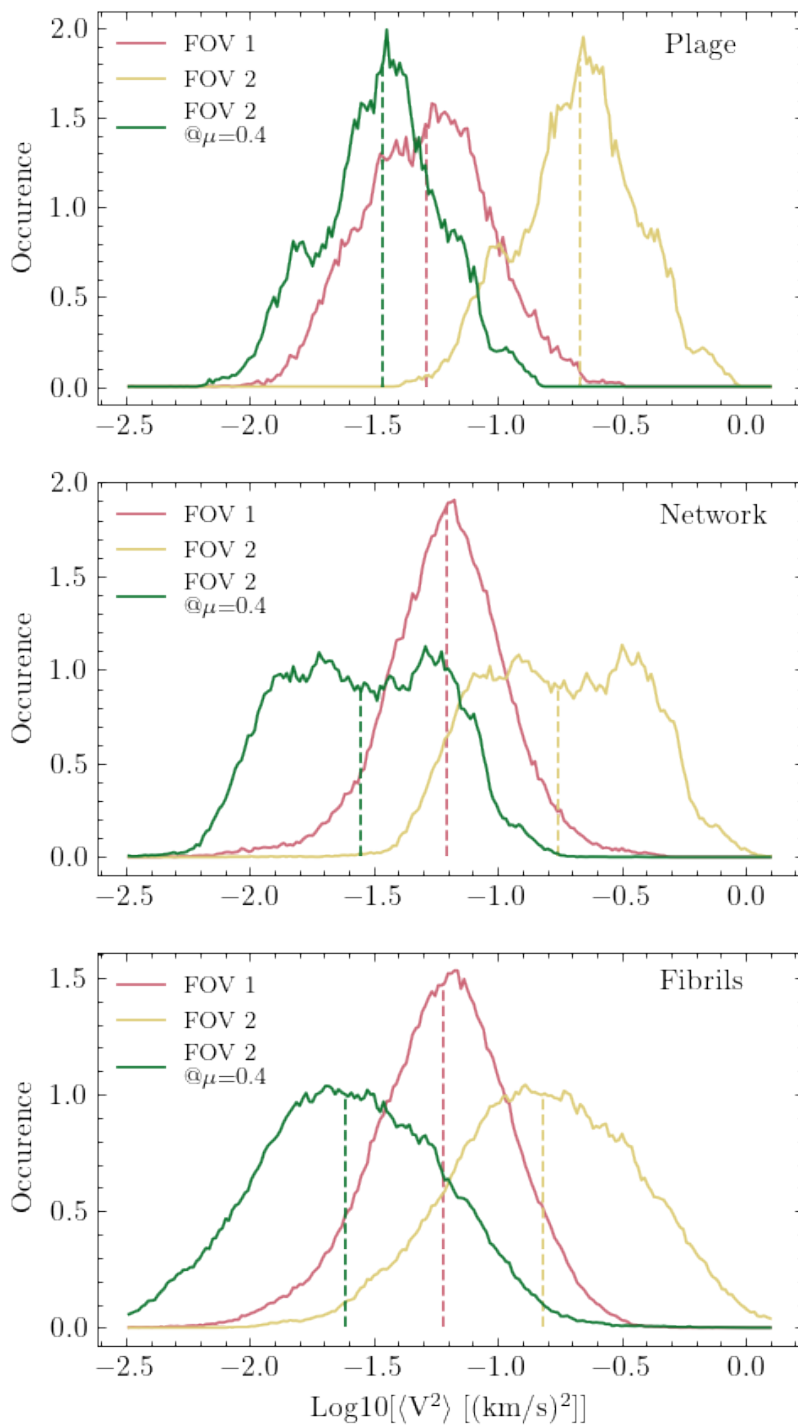


Figure 4.17: Distributions of the total velocity oscillatory power between 5 mHz and 20 mHz in the two fields of view for different solar surface features inferred from the Ca II 854.2 nm line. The green curve is the PSD of FOV 2 if observed at incidence angle $\mu=0.41$ (see Section 4.3.3). The vertical dotted lines show the median of the distributions.

Solar region	$\langle v_{\parallel} \rangle$ [km/s]	$\langle v_{\perp} \rangle$ [km/s]
Plage	0.51	0.11
Network	0.48	0.17
Fibrils	0.45	0.18

Table 4.3: Velocity oscillation components (parallel and perpendicular) inferred from the Ca II 854.2 nm data from both FOV 1 and 2.

as (assuming that $\langle v_{\parallel} \rangle$ and $\langle v_{\perp} \rangle$ are not correlated):

$$\begin{aligned}
 \langle v_{obs}^2(\theta) \rangle &= \langle v_{\parallel}^2 \rangle \cos^2 \theta + \langle v_{\perp}^2 \rangle \sin^2 \theta = \\
 &= \langle v_{\parallel}^2 \rangle \mu^2 + \langle v_{\perp}^2 \rangle (1 - \mu^2)
 \end{aligned}
 \tag{4.1}$$

where $\mu = \cos \theta$, the cosine of the incidence angle of the observation.

The average power spectrum of the Ca II 854.2 nm FOV 1 velocity (shown in Figure 4.16) exhibits lower oscillatory power compared to FOV 2 and has higher white-noise floor compared to FOV 2, where the averaged FOV 1 data are shown as the black dots in Figure 4.9.

This is further illustrated in Figure 4.17 where the velocity fluctuation power in FOV 1 and 2 are compared. The red curves in Figure 4.17 show the FOV 1 velocity fluctuation power between 5 and 20 mHz for the different solar regions as segmented in Figure 4.6; the yellow curves show the distributions for the solar regions for FOV 2. Under the assumption that the velocities detected in FOV 2 are all due to longitudinal displacements (since the observed region was close to disc center at $\mu = 0.98$), we projected the observed distributions to what would be observed at an inclination angle of $\mu = 0.41$ by proportionally reducing the velocity magnitudes (green curves). For all three types of solar structures (fibrils, network and plage), the amount of oscillatory power in the projected FOV 2 distributions is smaller than what is actually observed at that inclination in the FOV 1 data. Therefore, we believe that in FOV 1 we are observing not just projected vertical velocities (v_{\parallel}), but also an additional transverse (v_{\perp}) component.

Based on Equation 4.1 and taking the median of the velocity oscillation distributions in

Figure 4.17 as representative of the averaged oscillation power, we calculate the magnitude of the transverse oscillations $\langle v_{\perp}^2 \rangle$ for the different solar regions. The resulting velocity components for the different solar regions are presented in Table 4.3. We can see that the plage region has the highest longitudinal oscillations and lowest transverse components. The network and fibrils have similar values for the transverse oscillation power, while the network has slightly higher longitudinal oscillation power. On average, the value of transverse velocity component $\langle v_{\perp} \rangle$ is a few times smaller than the longitudinal one $\langle v_{\parallel} \rangle$. This has been suggested in previous modeling work (for example Cranmer et al. (2007)).

Further observational studies could make use of samples at more values of μ to better confirm and constrain the contributions of the two components. In addition, a more detailed treatment of radiative transfer effects at inclined viewing angles should be made. Observations of more homogeneous solar regions (such as quiet Sun or network) would provide more assurance that similar structures were being compared and provide more accurate estimates for $\langle v_{\perp}^2 \rangle$. We provide initial work in this direction in Chapter 6.

4.4 Modeling the observational signatures of acoustic waves in the chromosphere

Optically thick diagnostics, such as the $H\alpha$ and Ca II 854.2 nm lines or the millimeter continuum used in this study, sample a wide range of heights in the chromosphere. Further, the interval sampled by these diagnostics are changing dynamically during the continuous evolution of the chromospheric properties which are significantly out of thermodynamical equilibrium (Carlsson et al., 2019).

The observed Doppler velocity response of a longitudinal wave-like perturbation in the solar atmosphere, with a wavelength comparable to the extent of formation region of the spectral line,

will be attenuated due to the inherent mixing of signals from different phases of the oscillatory fluctuation (Mein and Mein, 1980). Modeling is needed to estimate the extent of this wave signature attenuation and infer the true wave flux corresponding to the measured oscillatory amplitude.

4.4.1 Propagation of acoustic waves in the solar atmosphere

The dispersion relation for acoustic waves in the solar atmosphere is (following the derivation in Bray and Loughhead, 1974):

$$k_z^2 = (\omega^2 - \omega_{ac}^2) \frac{1}{c_s^2} - (\omega^2 - \omega_{BV}^2) \frac{k_h^2}{\omega^2} \quad (4.2)$$

where $\omega = 2\pi\nu$ is the angular frequency; k_h and k_z are the horizontal and vertical wave numbers; $\omega_{ac} = \gamma g / (2c_s^2)$ is the cutoff frequency below which no acoustic waves can propagate in the atmosphere. Under typical chromospheric conditions, the speed of sound is $c_s = 7$ km/s and $\nu_{ac} = 5.2$ mHz for an adiabatic index of $\gamma = 5/3$; $\omega_{BV} = \sqrt{\gamma - 1} g / c_s^2$ is the Brunt-Väisälä frequency which determines the lower cutoff frequency below which gravity waves can propagate.

The energy flux F_{ac} carried by an acoustic wave with a velocity amplitude squared per unit frequency $P(v_w^2)$ in the frequency interval of ν_0 to ν_1 is:

$$F_{ac} = \rho(z) \int_{\nu_0}^{\nu_1} v_{gr}(\nu') P(v_w^2(\nu')) d\nu' \quad (4.3)$$

where $\rho(z)$ is the density at height z , $v_{gr}(\nu)$ is the group velocity. The group (propagation) velocity is the derivative $\partial\omega/\partial k_z$ from Equation (4.2) and in our case it equals the sound speed times a factor of order unity above the acoustic cutoff frequency and zero below it:

$$v_{gr}(\omega) = c_s \frac{\sqrt{\omega^2 - \omega_{ac}^2}}{\omega} \quad (4.4)$$

Compressive waves will also show a temperature fluctuation, which is proportional to the energy flux of the wave. We can substitute in Equation (4.3) the wave velocity fluctuation v_w with the magnitude of the wave temperature fluctuation (Bray and Loughhead, 1974):

$$v_w = \frac{c_s}{\Gamma_1 - 1} \frac{\delta T}{T_0} \quad (4.5)$$

where Γ_1 is the adiabatic exponent describing how pressure responds to compression; δT is the wave temperature fluctuation and T_0 is the mean temperature of the atmosphere.

Based on Equation (4.5), we can substitute in Equation (4.3) to get the final expression for the wave energy flux expressed via the relative temperature fluctuations squared per unit frequency $P(\delta T/T_0)$:

$$F_{ac} = \frac{\rho(z)c_s^2}{(\Gamma_1 - 1)^2} \int_{\nu_{ac}}^{\nu_1} v_{gr}(\nu') P\left(\frac{\delta T}{T_0}\right) d\nu' \quad (4.6)$$

where we integrate again over the frequency interval above the acoustic cutoff and below the frequency at which the white noise floor dominates our signal.

ALMA is an ideal tool for the detection of the wave temperature fluctuations as it measures directly and linearly the plasma temperature in the chromosphere, with the observed brightness temperature equal to the contribution-function-weighted mean temperature over the formation interval. This is a supplementary measurement to the direct velocity measurement with IBIS in the Ca II 854.2 nm line.

4.4.2 Synthesizing wave observables with RADYN

To model the line formation in the presence of waves we need time-dependent models of the solar atmosphere which incorporate all of the necessary physical processes of wave propagation (including the optically thick radiative transfer effects). We used the RADYN radiative hydrody-

nameric code (RHD) (Carlsson and Stein, 1992, 1995, 1997, 2002; Abbett and Hawley, 1999; Allred et al., 2015) to self-consistently model the propagation of high frequency acoustic waves in the chromosphere. This 1D code solves the hydrodynamic equations coupled with the radiative transfer equations in non-local thermodynamical equilibrium (NLTE). RADYN supports subphotospheric velocity drivers defined by the user and treat time-dependent NLTE ionization of the primary atomic species (H, He and Ca). RADYN performs the radiative transfer calculations to generate time-dependent synthetic line profiles consistent with the wave dynamics. Based on these synthetic observables, we are able to interpret our data in terms of the realistic solar plasma parameters and estimate the amount of flux carried by the acoustic waves in the chromosphere.

In our numerical setup, we use a 191 point atmosphere with 6-level atom models for Hydrogen and Calcium and 9-level atom for He – including singly and doubly ionized states. We use an open (transmitting) upper boundary condition where the corona is maintained at constant temperature 1 MK at height of 12 Mm and a bottom piston boundary condition at fixed temperature of 5944 K. The piston bottom boundary allows for driving vertically propagating acoustic waves with arbitrary properties which are defined by the user.

We ran a grid of models with an increasing amount of wave energy being injected through the bottom boundary condition. These models are used consistently throughout the paper with the name format of *model_XXXX*, where the increasing numerical factor stands for a stronger bottom boundary driver. We used the bottom boundary vertical velocity drivers presented in Fossum and Carlsson (2006), scaling their amplitude by a multiplicative factor to achieve the desired amount of input wave energy. These drivers specify a power spectrum of sub-photospheric velocities, at a range of oscillatory frequencies from 1 to 50 mHz, that have different relative amplitudes. To synthesize the velocity time series for the bottom boundary condition, we used the power spectrum of the driver initialized with random phases. The vertical velocity PSDs of the used bottom boundary

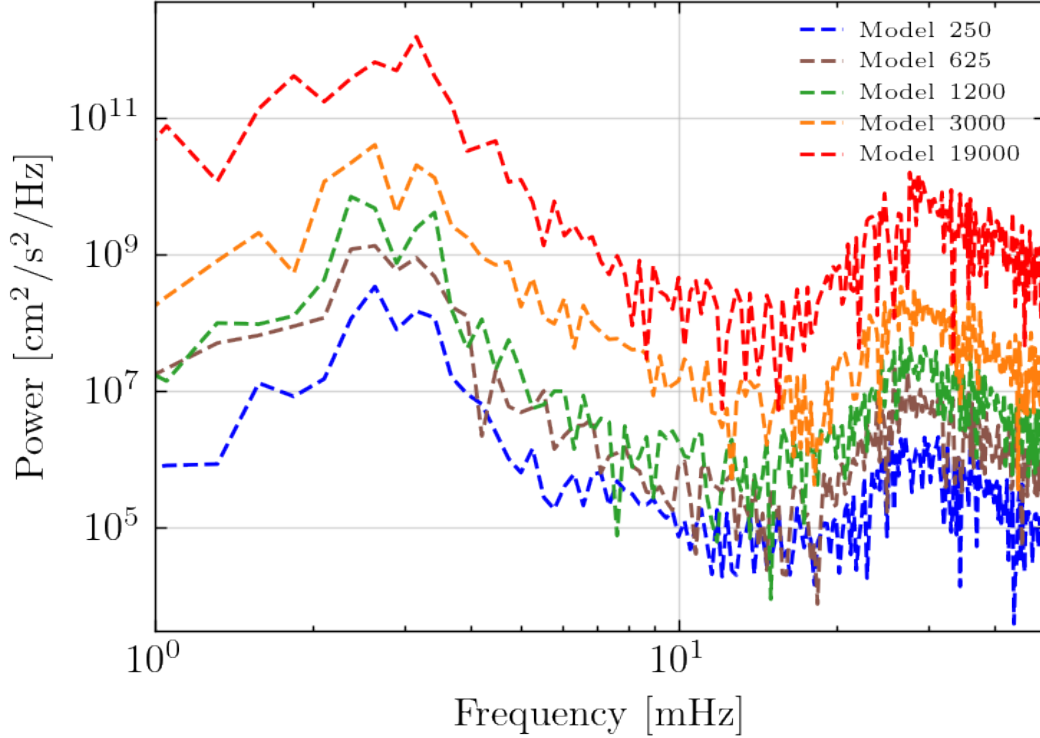


Figure 4.18: The vertical velocity power spectrum of the bottom boundary condition of the different models we ran. The overall shape of the PSD is taken from [Fossum and Carlsson \(2006\)](#) and scaled by a multiplicative factor and then supplied as a bottom boundary (vertical velocity) condition in the RADYN runs. The PSDs presented here are the Fourier transforms of the actual 3 second sampled RADYN run bottom boundary velocity.

drivers are presented in Figure 4.18. The resulting acoustic flux in the chromosphere from those runs are presented in Figure 4.19. We have calculated the acoustic fluxes from Equation (4.3), where we have interpolated the models on a 4 000 point equidistant height grid to remove the movement of the grid points during shock passages. To compute the average acoustic fluxes, for each grid point we calculate the mean of the sound speed and the plasma density and filter the vertical velocity between 5 and 50 mHz. We have chosen time series starting about 10 minutes after the initialization of the simulation, when a steady state is reached. We have further excluded models with higher acoustic fluxes above *model_3000* as the Ca II 854.2 nm line core goes into emission and do not reproduce the observations.

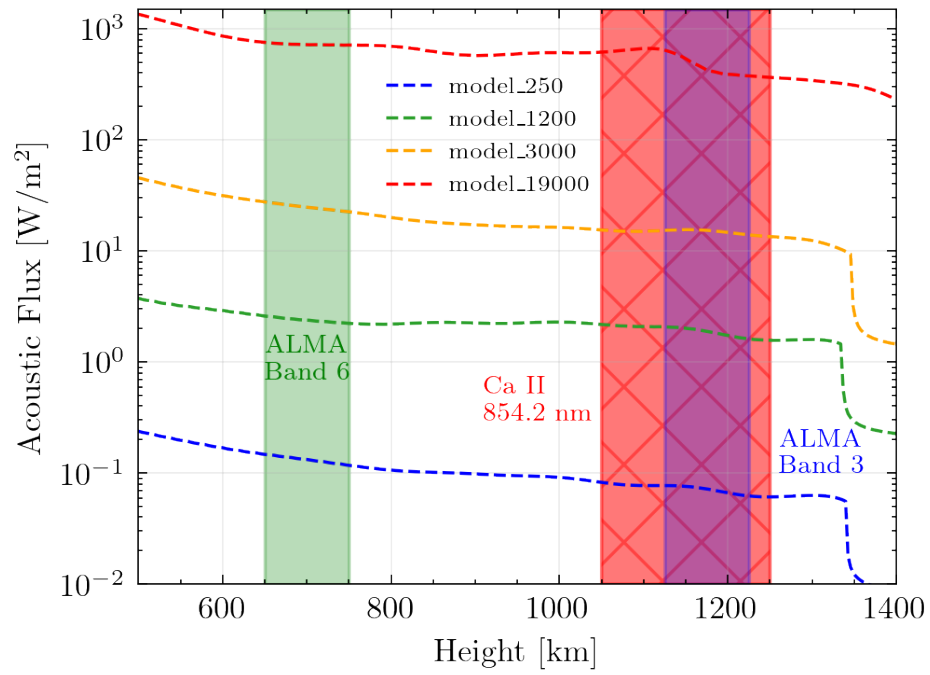


Figure 4.19: Acoustic flux dependence on height in the RADYN models, described in Section 4.4.2. The shaded regions show the formation regions in the atmosphere for different spectral diagnostics.

To compare the high-frequency signal in the synthetic observables and in the IBIS observations we took the simulated Ca II 854.2 nm line profiles from the RADYN runs at 0.5 second intervals and averaged them to the temporal and spectral sampling of the IBIS instrument. We did apply the spectral PSF of IBIS, but this did not change the final results significantly as its spectral resolution is very high ($R > 200,000$) for the Ca II 854.2 nm line. To measure the synthetic velocities, we used the same methods (i.e. line center fitting) used for the real data processing.

4.4.3 Estimating the acoustic flux in the Ca II 854.2 nm data based on RADYN

Given the attenuation of the wave amplitude discussed in Section 4.4.1 we need to find a relationship between the observed Doppler velocities, v_{obs} , and the true wave amplitudes v_w . One approach would be to discretize the acoustic flux in the observed bins and then correct it for the wave amplitude attenuation for each frequency bin separately (as in Bello González et al. (2009)):

$$F_{ac} = \rho(z) \sum_{\nu_i=\nu_{ac}}^{\nu_1} v_{gr}(\nu_i) \langle v_{obs}^2(\nu_i) \rangle / \mathcal{T}^2(\nu_i) \quad (4.7)$$

where the coefficient $\mathcal{T}(\nu_i)$ quantifies the attenuation of the wave velocity amplitude at frequency ν_i due to the extended formation height of the spectral line. In this case the quantity $\langle v_{obs}^2(\nu_i) \rangle$ is the observed amount of velocity oscillation power per frequency bin and has units of velocity squared. $\mathcal{T}(\nu_i)$ is defined as the ratio of the observed wave amplitude to the real (physical) wave amplitude in the middle of the formation region of the spectral line. We measure $\langle v_{obs}^2(\nu_i) \rangle$ from the Doppler velocities in our observations, and estimate $\rho(z)$, v_{gr} and \mathcal{T} from the self-consistent RADYN simulations.

We derive \mathcal{T} by computing the square root of the ratio between the Doppler velocity power in the synthesized Ca II 854.2 nm line (panel (c)) in Figure 4.20 and the power of the actual velocity field in the RADYN atmosphere at the formation height of the spectral diagnostic for each frequency

bin (Panel (b)) of Figure 4.20. For the effective formation height of Ca II 854.2 nm, we chose the peak of the velocity response function. For our models, presented in Figure 4.20, the peak of the Ca II 854.2 Doppler velocity response function was at 1150 km, which is at about the same height as the average $\tau = 1$ surface for the line core. The extent of the velocity response function is shaded as the red region in Figure 4.19. We use 5 mHz frequency averaging windows as the coefficient \mathcal{T} and the power does not change significantly over this region and the averaging removes the inherent uncertainty in the power spectra. The inferred transmission coefficient \mathcal{T} for Ca II 854.2 nm is presented in Panel (d)) of Figure 4.20. The Doppler signal of the low frequency waves (below 10 mHz) is less attenuated as their wavelength is significantly larger than the formation layer of the spectral diagnostic. However, the high frequency wave signal is significantly attenuated, as shown before (Bello González et al., 2009).

We note that our RADYN simulations can generate a high-frequency velocity signal due to the steepening of the acoustic waves propagating from the photosphere. The waves steepening into shocks in the chromosphere have saw-tooth-like velocity profile, which when Fourier decomposed creates power law tails that extend to significantly higher frequencies than that of the driving wave (Vecchio et al., 2009). The modeling approaches in the previous studies (for example Bello González et al., 2009) using monochromatic high-frequency waves and static 1D atmospheric models overestimate the transmission coefficient \mathcal{T} (and the inferred wave flux respectively) at higher frequencies, as suggested by our estimation of \mathcal{T} from the RADYN simulations. This is due to the fact in our dynamic solar atmosphere models the propagating wave packets are not monochromatic and their steepening creates high frequency signal.

4.4.4 Estimating the acoustic flux in the ALMA data based on RADYN

There are two differences between the temperature fluctuations observed with ALMA and the ones in the right hand side of Equation (4.6). First and foremost, the temperature response of ALMA will be a result of the wave fluctuations convolved with the atmospheric response function. Another complication, that makes Equation (4.6) applicable with limited validity in its current form is the fluctuating height of formation of the ALMA continuum (Molnar et al., 2019), which makes using a particular height of formation (and local plasma density at that height) nonphysical.

To take into account of all the effects described in the the previous paragraph, we rewrite Equation (4.6) as:

$$F_{ac} = \sum_{\nu'=\nu_{ac}}^{\nu_{max}} \mathcal{C}_{ALMA}(\nu') \left\langle \left(\frac{\delta T}{T_0} \right)^2 \right\rangle \quad (4.8)$$

where the proportionality coefficient, called from now on the ALMA transmission coefficient, $\mathcal{C}_{ALMA}(\nu)$ encapsulates the local plasma properties at the formation height of the ALMA radiation. We note that the $\mathcal{C}_{ALMA}(\nu)$ coefficient is the proportionality coefficient between the brightness temperature fluctuation power and the wave energy flux in the atmosphere, whereas the attenuation coefficient \mathcal{T} in Section 4.4.3 is the attenuation of the observed wave velocity amplitude and goes in the denominator of Equation 4.7.

By using the RADYN atmosphere models to synthesize synthetic ALMA observables and compare them with the observations we take into account those two effects as described below. We use the RH code (Uitenbroek, 2001) to synthesize the millimeter continuum from the RADYN model output. We used the RADYN atmospheric models (including the instantaneous electron densities and hydrogen level populations) as an input for the RH code to synthesize the mm-wave radiation corresponding to Band 3 (100 GHz/3 mm) and Band 6 (240 GHz/1.25 mm). The RH

code takes into account the opacity from neutral hydrogen as well as H^- and H_2^- , which are the main sources of opacity in the solar atmosphere at millimeter wavelengths (Zlotnik, 1968). We averaged the output intensity from the 0.5 second time steps of the RADYN runs to the 2 second cadence of our ALMA observations.

The extent of heights at which the ALMA Bands sample the atmospheric plasma temperature are shaded in Figure 4.19 as the green region for Band 6 and the blue region for Band 3. We have determined those regions as the height of $\tau = 1$ surface for the millimeter continuum from the RADYN run most closely reproducing the observations. For Band 6 this was *model_19000* and for Band 3 is *model_3000* as shown in Figure 4.20. The mean formation height for the ALMA Band 6 is at 700 km and for Band 3 is 1150 km, while the physical widths of the formation regions shown in Figure 4.19 correspond the variation of the $\tau = 1$ height in our models. Those heights are lower than the ones previously presented in the literature based on modeling (Molnar et al., 2019; Martínez-Sykora et al., 2020a) and observational (Patsourakos et al., 2020) methods.

The middle and right columns of Figure 4.20 present the results from the ALMA spectral synthesis with the RH code from the RADYN simulations and the resulting $\mathcal{C}_{ALMA}(\nu)$ coefficient. The left column corresponds to ALMA Band 3 (3 mm continuum) and the right column corresponds to ALMA Band 6 (1.25 mm continuum). Panels e) and i) of Figure 4.20 show the temporal variation of the synthesized brightness temperature in the RADYN runs, which agree well with previous studies of the millimeter continuum based on RADYN simulations (Loukitcheva et al., 2004; Eklund et al., 2020). However, we do note that the average synthetic temperatures of the RADYN models (4250/5250 K for Band 3 and 6 respectively) are significantly lower than the observed ones (7000/8500 K for Band 6 and 3) in Figure 4.4. Panels f) and j) show the acoustic flux PSD at the average height of formation of the millimeter radiation (700/1150 km for Band 6/3 respectively), with a clear correlation between the amount of acoustic flux and the amplitude of

the brightness temperature fluctuations. This correlation is further demonstrated in panels (g) and (k) of Figure 4.20, where we present the PSD of the modeled brightness temperature fluctuations. This correlation is not surprising, as compressive waves have temperature perturbations and ALMA measures the plasma temperature in the chromosphere.

\mathcal{C}_{ALMA} is presented panels h) and l) of Figure 4.20 where we have calculated it as the ratio of the acoustic flux density at the formation height of the millimeter radiation (panels f) and j)) and the power density of the relative temperature fluctuations (panels g) and k)). We have averaged the transmission coefficient \mathcal{C}_{ALMA} over 5 mHz frequency windows to smooth out the inherent noise in the power spectra. The \mathcal{C}_{ALMA} coefficient converges to the same values for the RADYN runs with parameters closest to our observations (models 3000-19000). The converging values for \mathcal{C}_{ALMA} at different acoustic fluxes confirm that our modelling approach is not strongly dependent on the wave amplitudes (Equations (4.8)) and evades the complications of using Equation (4.6) directly for estimating the wave flux.

Due to the spatial smearing from the finite PSF of the ALMA beam the observed oscillatory power is underestimated by a factor of 2 based on previous studies for Band 3 (Loukitcheva et al., 2006, 2015; Wedemeyer et al., 2020). We do include this factor in our analysis only for Band 3, as we do not have an estimate for it for Band 6.

4.5 Inferred high frequency wave flux in the solar atmosphere

4.5.1 Wave flux inferred from the Ca II 854.2 nm data

From the RADYN synthetic observables presented in the previous section, we had all the constituents of Equation (4.7) to compute the acoustic flux in our observations. The mean density at the mean formation height of the Ca II 854.2 nm line is 5×10^{-9} kg m⁻³ (at 1150 km height in the

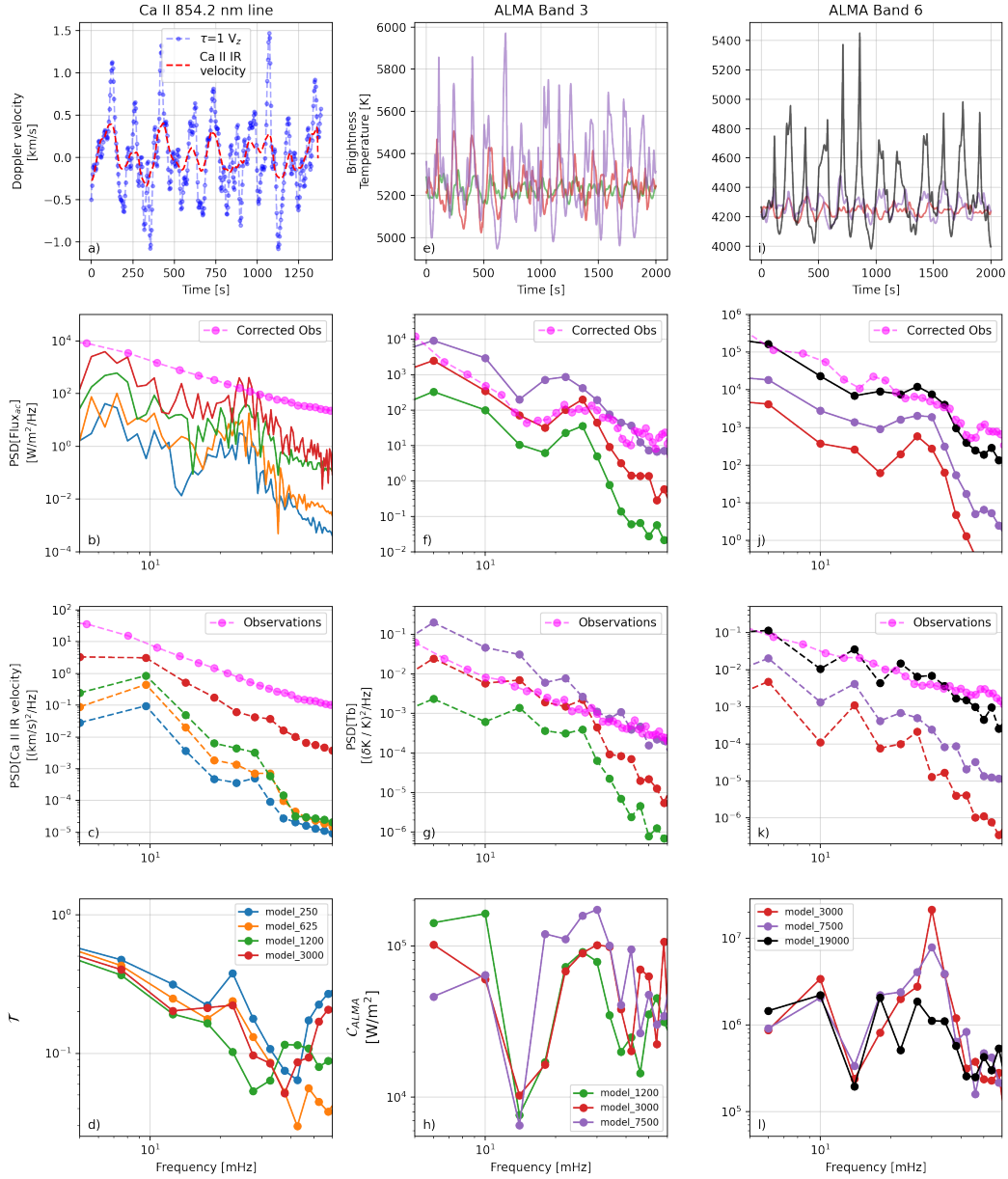


Figure 4.20: Ca II 854.2 nm and ALMA responses to acoustic waves in the RADYN models for varying wave fluxes. **Left column:** results for Ca II 854.2 nm. *Panel a):* Vertical velocity (blue) in the RADYN simulation *model_3000* at the formation height of the Ca II 854.2 nm line and the synthetic Doppler line core velocity (red) for the synthetic Ca II 854.2 nm line from the same RADYN run. *Panel b):* The PSD of the averaged acoustic flux at the formation height of the Ca II 854.2 nm line. The magenta colored data are the averaged observed Ca II 854.2 nm Doppler velocity PSD corrected with the \mathcal{T} in panel d). *Panel c):* PSD of the synthetic Ca II 854.2 nm Doppler velocity. The magenta points are real observations. *Panel d):* \mathcal{T} coefficient for the different RADYN models. **Middle column:** results for Band 3 (3 mm); **Right column** results for Band 6 (1.25 mm). *Panels e) and i):* synthesized ALMA brightness temperature from the RADYN models; *Panels f) and j):* Similar to Panel b), but for the formation height of ALMA Bands 3 and 6; *Panels g) and k):* Similar to Panel c), but for the observed brightness temperature fluctuations in ALMA Bands 3 and 6; *Panels h) and l):* The C_{ALMA} coefficient for the different RADYN models.

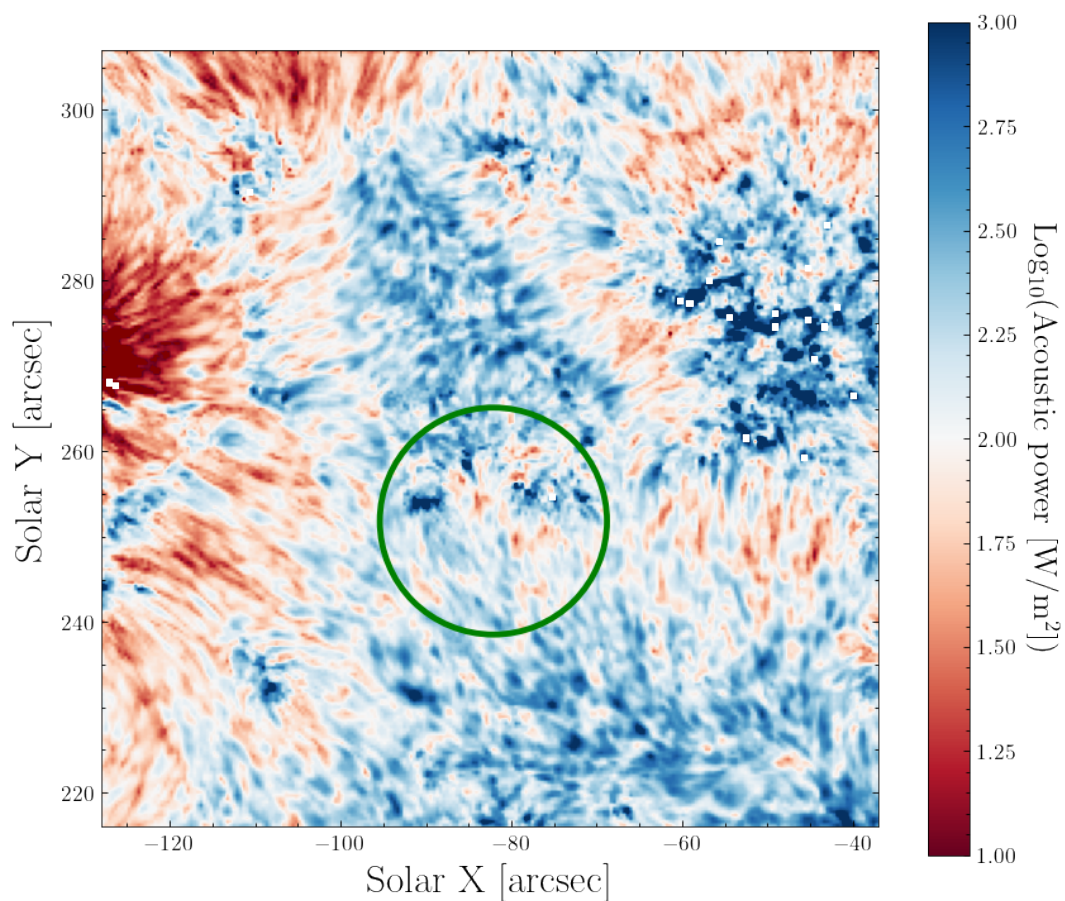


Figure 4.21: Acoustic flux inferred from the IBIS Ca II 854.2 nm line observations for FOV 2 between 5 and 50 mHz. The calculation uses the RADYN simulation results for the attenuation coefficient in Section 4.4.2. The green circle shows the FOV of ALMA Band 6 which was used as an input for Figure 4.26.

model atmosphere). This is comparable to estimates from previous work (Abbasvand et al., 2020a). The values for the attenuation coefficient \mathcal{T} are presented in the bottom left panel in Figure 4.20 for the RADYN models with different driver strengths. We used the values for \mathcal{T} taken from the model producing the closest synthetic velocity/brightness temperature variations to the real data for the particular frequency bin and diagnostic. This was the *model_3000* run for our IBIS observations. This was also the RADYN run with the highest piston amplitude that didn't cause the core of the Ca II 854.2 nm line to flatten out and go into emission (a condition not widely seen in our data). We see that the attenuation coefficients \mathcal{T} from different model runs converge to similar values at frequencies under 30 mHz. Above that, the attenuation coefficient \mathcal{T} for different models do not agree that well, but this frequency region contributes relatively little to the total acoustic flux. Therefore, the exact driver strength does not appear to be important in the determination of the attenuation coefficient and the derivation of the acoustic flux.

We computed the wave energy flux PSD in our observations based on our estimates for density and \mathcal{T} from the RADYN simulations and the results are presented as the magenta data in the second row in Figure 4.20. We can see that the energy flux PSD derived from the observations is significantly higher in Ca II observations compared to the simulations. However, the shape of the wave flux frequency distribution is almost flat up to 20 mHz and resembles the one found in the RADYN models.

At each pixel, we divide the observed Ca II 854.2 nm line core velocity power in each frequency bin by the corresponding value of \mathcal{T} for *model_3000* and sum over the interval from 5 to 50 mHz to derive the total acoustic flux, with the results presented in Figure 4.21 for the FOV 2 observations from 17:04 - 17:11 UT. We verified this result by calculating the same flux estimate using another FOV 2 dataset obtained from 15:39 to 15:46 UT, with very similar results. This suggests that the derived acoustic fluxes are not significantly affected by the seeing variations or evolution of the

granular or supergranular conditions in the photosphere.

According to [Withbroe and Noyes \(1977\)](#), the average radiative losses in the middle (high) chromosphere are ranging from about 2 kW m^{-2} (0.3 kW m^{-2}) for the quiet internetwork to 20 kW m^{-2} (2 kW m^{-2}) for the plage regions. The distribution of the acoustic flux in [Figure 4.21](#) suggests that over most of the FOV the acoustic flux can not be the dominant source of heating in the chromosphere. There are some disjoint regions with fluxes above 1 kW m^{-2} (shown in dark blue) where acoustic waves could be a significant source of chromospheric heating. These regions of enhanced wave flux are located primarily in the more fibril-free internetwork areas and also in the network and plage. The locations dominated by chromospheric fibrils (see [Figure 2](#)) almost uniformly have acoustic fluxes less than 0.1 kW m^{-2} .

The distributions of observed acoustic flux in the different solar regions (using the mask in [Figure 4.5](#)) are presented in [Figure 4.22](#). The averages and the 10th/90th percentiles of the cumulative distribution are summarized in [Table 4.2](#). The regions with the highest inferred acoustic flux are the plage and internetwork regions. However, after further investigation of the shape of the spectral lines in the plage regions with highest acoustic fluxes we found that the spectral line core fills in (flattens), and the Doppler velocity derived from the line core minimum becomes less reliable. The line core of Ca II 854.2 nm is determined by the local temperature at the formation height of the line ([Cauzzi et al., 2009](#)). Strong impulsive heating in the plage regions can be responsible for this dynamic peculiarity of the Ca II 854.2 nm line profile. Therefore, we believe that the high velocity oscillation power observed at hotter (plage) locations might not be due to genuine wave motions but because of the the flattening of the line core. Furthermore, the strong magnetic field in the plage regions might lead to MHD wave effects beyond the scope of this paper. We observe a similar phenomenon in our RADYN simulations, where if the wave driver is injecting too high velocity perturbations (acoustic flux) we see the line shape of Ca II 854.2 nm going into emission,

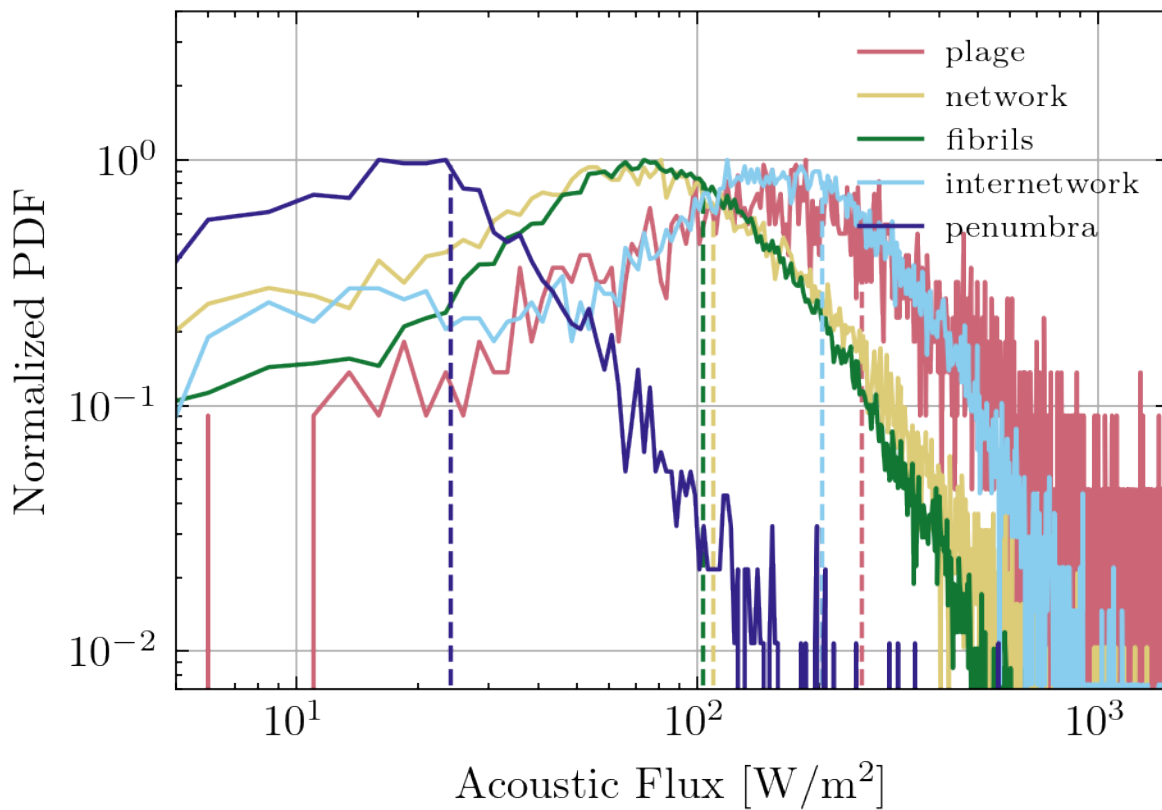


Figure 4.22: Histograms of the acoustic flux in different regions of the solar surface for FOV 2. The vertical lines show the median of the corresponding distribution. We applied the mask in Figure 4.5 to the map of the acoustic flux in Figure 4.21.

when the shocks pass through the chromosphere. However, on average the 1D simulations produce too narrow line core profiles (as previously shown in [Leenaarts et al., 2009](#)) which could be due to insufficient microturbulence in our simulation (RADYN has a default microturbulence of 2 km/s). Hence, we leave the detailed investigation of the dynamics of plage spectral line behavior for a future study.

Further analysis of the frequency dependence of the wave flux show that about 60% of the wave energy flux is in the 5–20 mHz frequency range, 30% in the 20–40 mHz range and 10% in the 40–60 mHz range. The pixels with significant relative contribution from the 20–40 mHz frequency range have lower total acoustic flux and are mostly found in the plage and the network.

In summary, our observations show that acoustic wave dissipation is likely not the dominant heating mechanism for the middle chromosphere. However, acoustic waves could contribute significantly to the quiescent state of the upper chromosphere in the internetwork as the observed flux is of the order of magnitude of the radiative losses in that layer. Future work will constrain the wave flux and dissipation in this layer using IRIS observations.

4.5.2 Inferred wave flux from the ALMA observations

Using the RADYN results presented in Section 4.4.4 we are able to estimate the acoustic fluxes in the ALMA observations. We match the observed brightness temperature fluctuations (the magenta points in panels g) and k) in Figure 4.20) to the closest RADYN model by the amount of brightness temperature RMS and then use the \mathcal{C}_{ALMA} coefficient from that RADYN run (bottom row in Figure 4.20) to calculate the amount of acoustic flux. To calculate the acoustic flux for Band 3 we used the observing block obtained between 17:31 and 17:41 UT and the \mathcal{C}_{ALMA} values for *model_3000*. For Band 6 we used the observing block between 16:03 and 16:11 UT and the \mathcal{C}_{ALMA} values for *model_19000*.

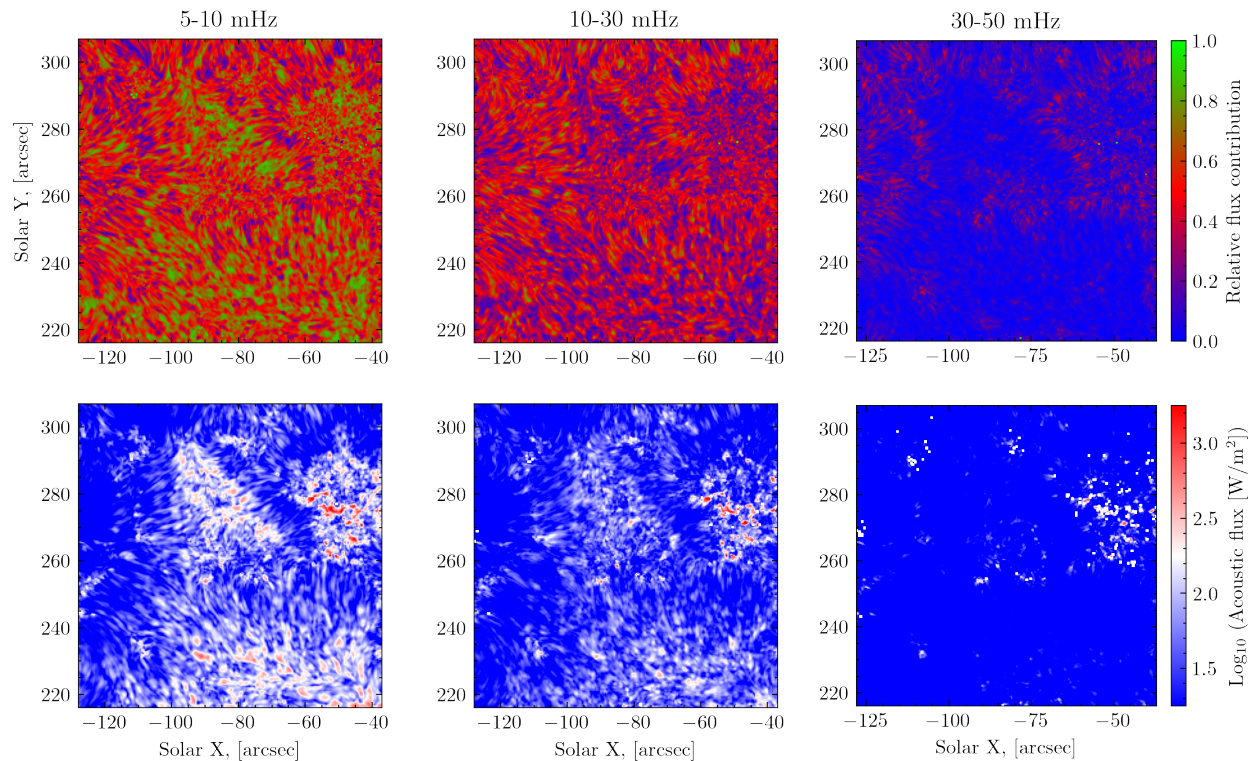


Figure 4.23: Contributions from different frequency ranges to the acoustic flux presented for the Ca II 854.2 nm data for FOV 2. The titles of the columns label the frequency domain over which the relative power is summed over. **Top row:** Relative contribution to the total acoustic flux from the different frequency ranges to the total frequency domain (5-50 mHz). **Bottom row:** The absolute acoustic flux in the corresponding frequency bins.

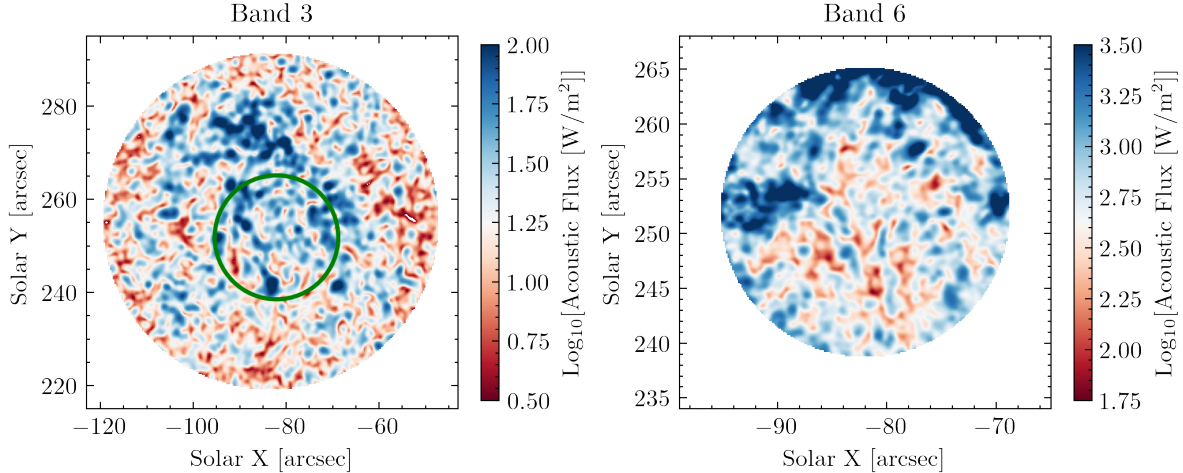


Figure 4.24: Acoustic flux derived from ALMA Bands 3 (*left panel*) and 6 (*right panel*) data based on the RADYN models. We have applied a circular mask to present only the central part of the beam with the highest sensitivity and lowest synthesis noise. The green circle in the Band 3 FOV is the extent of the Band 6 FOV.

The inferred acoustic flux for Bands 3 and 6 are presented in Figure 4.24. Circular masks were applied around the edges field of view as the noise outside of those regions are significant due to the decreasing sensitivity. We observe higher acoustic flux in Band 6 compared to Band 3, which is expected if the wave flux is being dissipated as the waves propagate upward. The region of the FOV of Band 6 is shown on the Band 3 FOV as the green circle. Since the two different ALMA Bands were observed an hour apart, they do agree to a certain extent but not fully as the solar atmosphere is changing on shorter time scales. Furthermore, the very limited FOV of Band 6 makes comparisons difficult. Examining the frequency distribution of the wave flux shows that the dominant source of signal in both ALMA Bands are the frequency range between 5 and 20 mHz, where more than 70% of the signal is found. This agrees with our results for the Ca II 854.2 nm line, that the frequency range between 5 to 20 mHz contains most of the wave flux.

To compare the results from IBIS and ALMA, we compare the derived acoustic flux over a common FOV corresponding to that of the Band 6 data. The distributions of the observed fluxes at those locations are presented in Figure 4.26. The ALMA Band 6 data exhibits the highest flux.

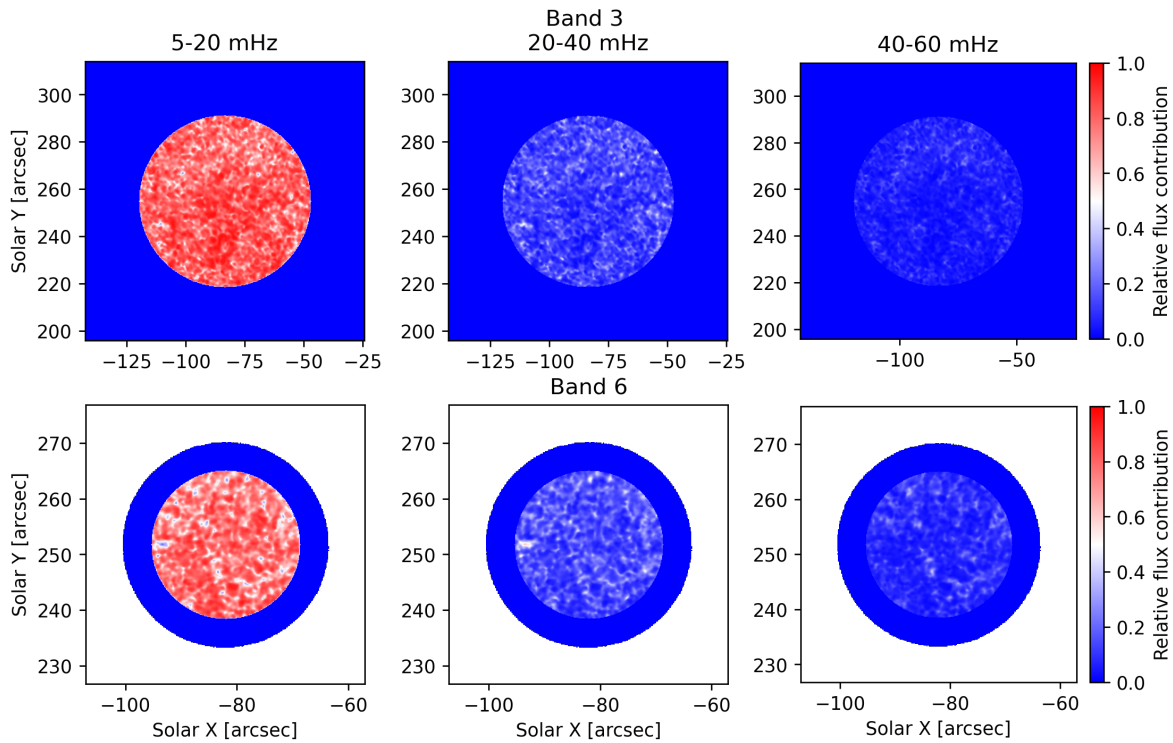


Figure 4.25: Acoustic flux contributions from different frequency domains for Band 3 and 6 observations. The frequency domain over which the oscillatory power is summed over is shown over each column and then it's normalized by the total amount of power between 5 and 50 mHz. The white circle on the left panel (Band 3) shows the FOV location of Band 6.

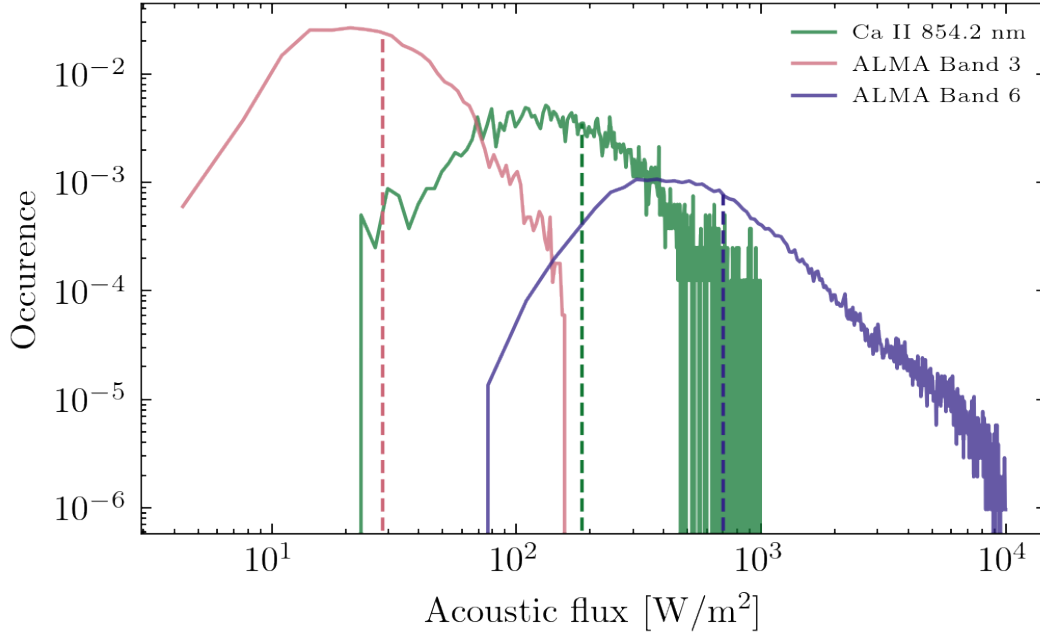


Figure 4.26: Acoustic flux distributions derived from the different diagnostics shown in the legend. The vertical lines are the medians of the distributions.

They are followed by the Ca II 854.2 nm and the ALMA Band 3 data. This ordering of the amount of wave flux follows the height of formation of the diagnostics shown in Figure 4.19. Since Band 3 and 6 have similar systematics in their formation height we can estimate the dissipation between their formation heights. The average dissipated energy (flux difference) across the FOV of Band 6 data is around 0.7 kW m^{-2} . However, there is a significant high-power tail in the dissipated energy which is greater than 1 kW m^{-2} and is energetically significant to maintain the quiet chromosphere in some confined regions. However, on average this is not enough to sustain the quiet middle chromosphere, being too small by an order of magnitude.

4.6 Conclusions and future work

We obtained an extensive data set containing spectral observations covering from the upper photosphere and the middle (Ca II 854.2 nm, $H\alpha$, and ALMA Band 6) and upper chromosphere (ALMA Band 3). The rapid cadences of our observations allow us to study high frequency dynamics

of the chromosphere in a rarely studied frequency regime. Our observations have extended the work of [Reardon et al. \(2008\)](#) to show that the power-law distribution of the Fourier PSDs is ubiquitous in all of the observed velocity and temperature diagnostics. In particular, in this paper we have focused on the velocity diagnostics derived from Ca II 854.2 nm, as tracers of upward propagating compressive waves, as well as brightness temperature fluctuations from ALMA Band 3 (3 mm) and 6 (1.2 mm) as indicators of local heating from those waves. We found that the power law properties depend on the observed solar region. We confirmed that the white-noise level in the power spectra is consistent with the photon shot noise in our data (see [Appendix A](#)), indicating that seeing-induced crosstalk or other systematic noise is likely not responsible for the detected Doppler velocity power. The amplitude of the noise floor increases in more "active" regions of the field (e.g. plage), perhaps due to flatter line cores typical of these features. Furthermore, the slope of the spectral diagnostics' power laws changes with the observed regions. "Hotter" regions (like network and plage) exhibit less steep power law slopes as shown in [Figure 4.11](#). This flattening of the power law could be due to the filling of the core of the spectral profile of the Ca II 854.2 nm line in the hotter regions (network and plage). We believe the steeper power law is an important characteristic of the dynamic nature of the different solar surface features that has to be reproduced in future modeling efforts.

We compared the RMS values of velocity oscillations observed at different incidence angles ($\mu = 0.98$ vs $\mu = 0.41$). The RMS of the velocity fluctuations is significantly smaller at the higher incidence angle compared to the disc center observations, but still larger than what would be expected if the amplitudes of those fluctuations were only due to the inclined viewing of vertically propagating waves of the same magnitude as seen in our disk center observations. Modeling the observed signal as a superposition of a longitudinal (vertical) component and a transverse (possibly Alfvénic) component, we found that the transverse component had a RMS amplitude of about 0.15

km/s, compared to the vertical component amplitude of around 0.5 km/s.

To characterize the acoustic waves that could explain the power laws in our observations we used the RADYN code to model propagation of waves from the upper convection zone into the chromosphere. We used wave drivers (as bottom boundary conditions) similar to the ones in Fossum and Carlsson (2006) adjusted with a scaling factor. We ran the RHD models and then produced synthetic observables for both IBIS and ALMA, using the RADYN built-in radiative transfer module in the former case and the RH code in the latter case. The dynamic RADYN models are able to reproduce the features of our observations in terms of total oscillatory power and slopes. Hence, we were able to correlate our observed oscillatory power in different diagnostics to the actual acoustic flux present at different heights in the simulations.

The acoustic flux derived from the Ca II 854.2 nm line Doppler velocity data is estimated to be between 0.1 to 1 kW m⁻². The lowest amount of flux is found in the penumbra and fibril regions and the highest in the internetwork and plage regions. We believe that the inclined nature of the magnetic field in the penumbra and the fibril region plays role in the observed lower fluxes. Furthermore, as discussed in Section 4.5.1, the high values in the plage region above 1 kW/m² require further examination due to the changes in the Ca II 854.2 nm line profile in plage regions, which leads to spuriously high measured Doppler shifts. We found that most of the contribution to the acoustic flux comes from the 5-20 mHz frequency interval (around 60% from the total acoustic flux) and that high frequency waves above 40 mHz do not contribute significantly (less than 10% of the total observed flux).

We also compared the brightness temperature fluctuations in our ALMA data with the synthetic observables from the RADYN runs and inferred the acoustic flux by using the correlation between brightness temperature fluctuations and acoustic flux in the different RADYN model runs. Based on this comparison we can infer that Band 6 has acoustic flux on average of 0.7 kW m⁻²,

compared to the formed higher in the atmosphere Band 3 which contains about 0.03 kW m^{-2} . From these two observations at different heights, we can infer that the average wave flux dissipated between two layers probed by ALMA is about 0.7 kW m^{-2} , which is not sufficient to heat the middle chromosphere, but is a significant contribution to its energy budget. This result agrees quantitatively with previous work by [Nindos et al. \(2020\)](#), who used ALMA to compute the heating in small scale chromospheric brightenings. However, in certain regions the dissipated wave flux exceed the threshold of 2 kW m^{-2} which is sufficient to maintain the quiet chromosphere locally. We believe that the limited spatial resolution of the ALMA observations could lead to an underestimation of the wave flux, compared to our Ca II data ([Loukitcheva et al., 2015](#); [Wedemeyer et al., 2020](#)) and further observations with higher angular resolution (more sparse ALMA configuration) will provide better constraints on the wave flux.

Another peculiarity between our observations and ALMA data is the fact that the Band 3 corresponds most closely to *model_3000* while Band 6 to *model_19000*. *Model_19000* has twenty times higher wave energy flux than *model_3000* in the chromosphere. This discrepancy could be due to different reasons – either the heights of formation of the ALMA continuum are inaccurate in the RADYN models or there is a wave dissipation mechanisms not included in the RADYN models. If the height in the atmosphere where the ALMA continuum originates from is determined inaccurately, this will lead to incorrect acoustic flux determination and result in differing RADYN models corresponding to the observations. The latter possibility of missing physics is also very probable due the 1D hydrodynamic nature of the RADYN code which might be omitting the required physics to treat fully all the relevant wave damping mechanisms.

Our work raises further questions such as what is the role of the magnetic field on the wave propagation characteristics in the solar atmosphere? Future observations with multiwavelength spectropolarimetric capabilities throughout the photosphere and the chromosphere from Daniel

K. Inouye Solar Telescope (DKIST) (Rimmele et al., 2020) will be able to address that. Also, the higher throughput of the future generation solar telescopes will help with driving down the white noise floor and provide simultaneous spectral observations at different heights in the solar atmosphere. Another interesting aspect we will pursue in a following publication is the amount of velocity oscillations in the upper chromosphere and the transition region observed cotemporally with IRIS during our April 2017 campaign.

The numerical side of our work requires further investigation as well. One important question that will be addressed in future work is the sensitivity of our results on the numerical setup that was utilized. For example, how does the transmission coefficient \mathcal{T} depend on the model atmosphere and the number of grid points in the atmosphere? Furthermore, studying wave propagation in 3D is essential for understanding the observed signals as the nature of the observed chromospheric structures is strongly non-vertical and non-local (Carlsson et al., 2019; Eklund et al., 2021). Even though current 3D RMHD solar models have significantly differing wave propagation properties (Fleck et al., 2021), further modeling with realistic solar atmospheres in three dimensions is essential.

Chapter 5

Wave fluxes derived from UV observations and 3D rMHD simulations

This chapter will be submitted to the *Astrophysical Journal* shortly by the following author list: Momchil E. Molnar, Steven R. Cranmer, Kevin P. Reardon, Adam F. Kowalski, and Ivan Milić.

5.1 Introduction

The solar chromosphere has a higher temperature than expected from radiative equilibrium thermal balance (Withbroe and Noyes, 1977; Carlsson et al., 2019). The additional heating required to maintain the chromosphere in its observed thermodynamic state is on the order of a few to tens of kW/m^2 , depending on the activity of the solar feature in question (Athay, 1976; Díaz Baso et al., 2021). Understanding the primary heating sources is important for modeling the solar chromosphere correctly, as these will determine its structure and observed properties. This is an important astrophysical question beyond the Sun, as the UV continuum emanating from stellar chromospheres plays a role in determining the atmospheric chemical composition of their exoplanets (Linsky, 2017).

Previous work has suggested that the two most viable mechanisms to provide the missing heating in the solar atmosphere is through stochastic release of stored magnetic energy or dissipation of MHD waves in the solar atmosphere. Release of magnetic energy – either through current sheet

dissipation (Socas-Navarro, 2005; Louis et al., 2021) or magnetic reconnection (Innes et al., 1997) has been reported in the lower chromosphere with limited global heating implications. However, conclusive observational evidence of this process heating the chromospheric plasma are still lacking, even if modeling predicts this process should be pervasive in the active Sun (da Silva Santos et al., 2022).

In this paper we examine instead the observational constraints on the acoustic wave energy fluxes in the chromosphere. Chromospheric heating by waves has been proposed in the late 1940's (Biermann, 1946; Schatzman, 1949) and has been discussed extensively in the literature (see Aschwanden, 2019, for a short review). Recent progress on constraining the wave heating in the solar chromosphere has been enabled by the technological advances of adaptive optics, tunable filter-graphs and more sensitive UV and near-IR sensors. There are two differing conclusions about the energetic significance of the acoustic waves in the solar atmosphere. In general, the body of work based on high cadence Doppler velocity observations modeled with 1D static atmospheric perturbative approach derive wave fluxes that could maintain the quiet chromosphere (e.g. Bello González et al., 2009; Sobotka et al., 2016; Abbasvand et al., 2020a). On the other hand, studies based on Doppler velocities from and UV/mm continuum observations interpreted with 1D time dependent radiative hydrodynamic models, suited for chromospheric studies come to the opposite conclusion – acoustic waves do not carry sufficient energy flux to maintain the quiet chromosphere (Fossum and Carlsson, 2005; Carlsson et al., 2007; Molnar et al., 2021). However, the latter studies have been critiqued for systematic biases toward underestimation of the acoustic flux (Wedemeyer-Böhm et al., 2007).

In this paper, we extend the previous work of Molnar et al. (2021) with data of the low and high chromosphere from the Interface Region Imaging Spectrograph (IRIS, De Pontieu et al., 2014). This could be seen as extension of the work by Abbasvand et al. (2021) where we per-

form our analysis on multiple spectral lines in the IRIS UV spectral sampling interval, instead of relying on the wing of the Mg II k line wing. We further argue that using more realistic 3D magnetohydrodynamic (MHD) models of the solar atmosphere are required to investigate the observed wave diagnostics. Previous work relying on 1D semi-empirical models (such like the ones found in [Fontenla et al., 2011](#)) calculate the properties of the observed waves as perturbations on a static atmosphere, which may be an inapplicable approximation, if the dynamical oscillations are maintaining the atmosphere in its observed state.

This paper describes the observed wave properties in the lower and upper chromosphere observed in the UV with IRIS and tries to infer the energy flux of acoustic waves propagating in these regions through comparison with spectral synthesis from 3D rMHD Bifrost models. We compare those results with archival observations in the optical obtained with IBIS. The paper is organized in the following way: Section 6.2 describes the UV and optical observations used throughout the paper; Section 5.3 presents the derived properties of the power spectra of different diagnostics; in Section 5.4 we present the wave diagnostics derived from synthetic observables from Bifrost MHD enhanced network models. We conclude with the wave energy flux estimates in Section 5.6 and discuss further our results in Section 5.7.

5.2 Observations

To sample the upper chromospheric velocity field (extending the previous work by [Molnar et al., 2021](#), which used near-IR (Ca II IR) and mm diagnostics) we use UV spectral diagnostics from the IRIS spacecraft. In particular, we concentrate in this paper on the Mn I 280.195 nm line (lower chromosphere, [Pereira et al., 2013](#)), Mg II h₂&k₂ features (middle chromosphere) and Mg II h₃&k₃ features (upper chromosphere, [Leenaarts et al., 2013](#)). Furthermore, the IRIS data archive presents us with a vast collection of observations containing this spectral line set.

To compare the properties of the UV data with previous results in the optical we examine a data set from the Interferometric Bidimensional Imaging Spectrograph (IBIS) (Cavallini, 2006; Reardon and Cavallini, 2008) at the Dunn Solar Telescope (Dunn and Smartt, 1991). We compare the IRIS observations with the previously shown data from Molnar et al. (2021) to obtain new estimates for the energy fluxes that acoustic waves are carrying and the possible chromospheric heating implications.

Throughout the paper we will discuss two different types of solar features: *internetwork* and *Plage*. These regions harbor weak (strong) magnetic fields in the case of internetwork (plage). We concentrate on those two different types of solar surface due to their relative simple distinction from the rest of the solar surface. Furthermore, in the internetwork we expect the weak magnetic field to be not significant for the wave propagation. In the case of the plage, previous work has shown the ubiquity of fluctuation signatures and the mostly vertical magnetic field (Pietrow et al., 2020; Anan et al., 2021).

5.2.1 Processing of the IRIS data

Date	Start [UT]	End [UT]	Heliocentric Coordinates [arcsec]	Cadence [s]	Solar feature
20131116	07:33	08:08	-1'', 49''	17.0	Internetwork
20140918	10:19	12:16	62'', 59''	9.4	Plage

Table 5.1: IRIS observations used in this work.

We use the level_2 spectral rasters from the IRIS online data archive archive¹ for this analysis. The particular datasets used in this study are described in Table 5.2.1. We chose two sets of observations from the earlier stages of the IRIS mission to ensure higher sensitivity and lower noise levels. The datasets used in this work are in sit-and-stare mode, which insures that the slit does not

¹<https://iris.lmsal.com/data.html>

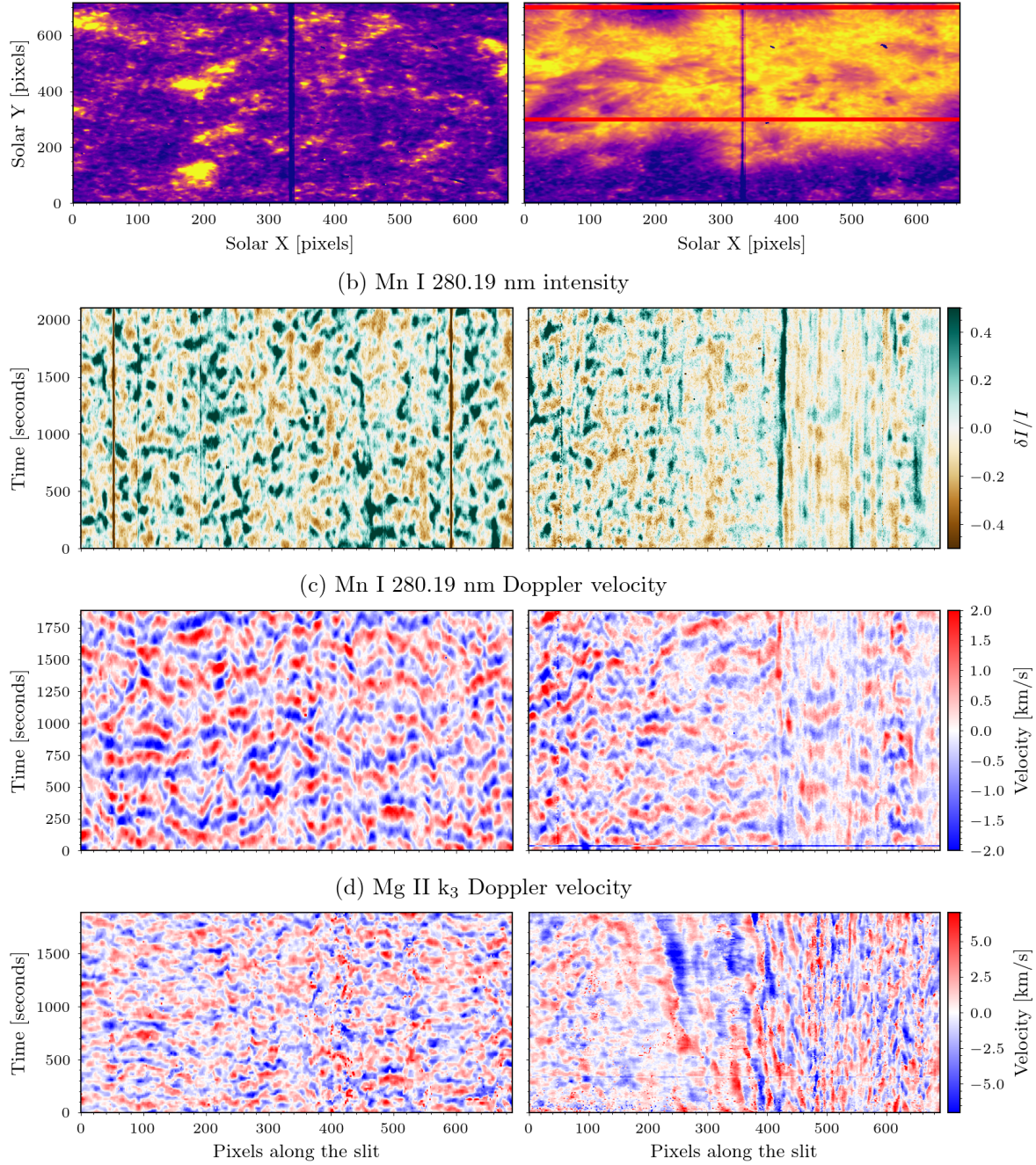


Figure 5.1: The data used in this study comes from two different regions – quiet Sun (left column) and plage (right column). The left column shows observations of a quiet Sun region from 2013 November 16; the right column to the plage region observations from 2014 September 18 (see Table 6.1). The top row, panels (a) are SJI images in the 279.6 nm spectral window for the QS (left) and plage (right). Panels (b) show the relative intensity variations (to the mean intensity at the particular slit position) at the core Mn I 280.19 nm line. Panels (c) show the Doppler velocity derived from the Mn I 280.19 nm line. Panels (d) show the Doppler velocity derived from the Mg II k_3 line.

scan other region of the solar surface, which increases the signal-to-noise ratio of the observations and provides higher Nyquist sampling frequency.

The two UV spectral lines that we will discuss have different shapes – the Mn I 280.1 nm line has a simple absorption profile, whereas the Mg II h&k lines have a complicated double horned shape due to the high opacity at chromospheric heights (Tousey, 1967). We adopted different fitting approaches to extract the physical parameters from the two spectral lines. The Mg II h&k lines are fitted with the IDL routine *iris_get_mg_features_lev2.pro*, part of the SSW IRIS reduction routine suite. This procedure relies on derivative estimates and subpixel interpolation to calculate the locations and amplitudes of the features of the Mg II h&k lines (described in detail in Pereira et al., 2013). In this work we concentrate our analysis on the properties of the k3 feature, as it is always present, even in the plage. The Mn I 280.1 nm line is situated between the Mg II k and h features, which makes its background continuum inclined. Since the Mn I line has a regular absorption line shape, we use the IDL routine *gaussian_fit* to fit a combination of a Gaussian plus an inclined line on the wavelength range of ± 0.03 nm around the line center. We derive the line properties from the parameters of the fitted Gaussian profile. Analysis of the Mn I 280.1 nm line and Mg II k lines was the basis for the study by Kayshap et al. (2018), where the authors found clear signatures of wave propagation throughout the quiet solar atmosphere. By continuously observing the same region in sit-and-stare mode, without moving the slit to other solar regions, we prioritize longer exposures, increasing the signal-to-noise ratio of the data and allow for high cadence, resulting in higher Nyquist frequency sampling. The IRIS spacecraft pointing jitter during the sequences is negligible given the extent of the observed velocity oscillations of about an arcsecond, which was verified by cross correlation of the individual slitjaw frames.

After deriving the fits of the spectral lines and calculating the resulting Doppler velocities and line-core intensities, we clean the data from discontinuities from non-converged line fitting,

which constitute a few percent of the total fits. We first remove any non-converged fit values by replacing them with a 3×3 pixel median filter which excludes nearby pixels with no data. We further smooth out any discontinuities in the temporal domain in the velocity signal which are above the local sound speed (7 km s^{-1}) with a 3×3 pixel median filter, which corresponds to a $0.5'' \times 27$ seconds kernel for the plage and to a $0.5'' \times 51$ second kernel for the internetwork. The Nyquist frequency of our data is 29 mHz for the internetwork and 51 for the plage dataset. In the analysis in Section 5.3 we show that the frequencies containing valuable information are between 5 and 20 mHz, well below the Nyquist frequency. The spatial smoothing over $0.5''$ does not affect the estimated wave properties, as from previous work (e.g. Vecchio et al., 2007) has shown that the coherence scale of the velocity signals in the chromosphere is of similar spatial scale (see the bottom two rows of Figure 5.1). The resulting data products from the aforementioned reduction procedures are presented in Figure 5.1. The left column shows an internetwork region and the right one presents a Plage region, both observed near to the disc center. Since the lower part of the plage dataset is occupied by an internetwork, we exclude this part from analysis. In particular, we use the slit locations between pixels 350 and 705, which are marked in Figure 5.1 as the red lines.

5.2.2 Processing of the IBIS data

This study uses data from the Interferometric BIdimensional spectrograph (IBIS, Cavallini, 2006) instrument acquired during the ALMA coordinated observing campaign on 2017 April 23. The observed field of view was on the leading edge of AR 12653 was $96''$ and included regions of plage, internetwork, network and a bit of penumbra. These observations were taken between 17:25-18:12 UT and include scans of the Na I D_1 589.6 nm and the Ca II 854.2 nm line, consisting of 24 and 27 points in each line respectively, which were described in detail in Hofmann et al. (2022). This data series has a temporal cadence of 16 sec and spectral resolution of at least R

$\gtrsim 200,000$ (Reardon and Cavallini, 2008). The line cores were more densely sampled than the wings of the spectral lines because the core region is used for deriving the quantities used in this study (Doppler velocities and line-core intensities). The IBIS data processing is described in detail in Molnar et al. (2019), where we have applied the standard reduction techniques of removing instrumental and atmospheric image aberrations and destretching the resulting data to the HMI whitelight (atmospheric seeing-free) reference. In this study we use the datasets starting at 15:54 UT and 16:37 UT, which were taken under conditions of good seeing.

5.3 Properties of the observed power spectra

We study the wave dynamics in the observed chromospheric diagnostics by analyzing their power spectra. The power spectra are derived for each pixel along the slit from the squared absolute value of the Fourier transform of the time series, giving us the power spectral density (PSD) of the data. The power spectra of the IRIS data exhibit ubiquitous power law shapes at frequencies above the acoustic cutoff present in all chromospheric and photospheric observable power spectra. These power laws have similar behavior to those previously observed in the chromosphere, for example in Reardon et al. (2008) and will be further discussed in this paper. The average shapes, slopes and other properties of the power laws are presented in this section.

5.3.1 Observed power law properties

Solar Feature Spectral line	Slope	Noise floor [(km/s) ² /mHz]	$\langle v^2 \rangle$ [(km/s) ²]
QS Mn I	$-3.56^{+1.02}_{-0.89}$	$3.5^{+5.2}_{-2.7} 10^{-4}$	$0.61^{+0.86}_{-0.44}$
QS Mg II	$-2.33^{+0.85}_{-0.91}$	$1.0^{+2.4}_{-0.8} 10^{-2}$	$5.52^{+3.08}_{-3.88}$
Plage Mn I	$-0.50^{+0.48}_{-0.51}$	$4.6^{+9.0}_{-3.4} 10^{-4}$	$0.17^{+0.10}_{-0.16}$
Plage Mg II	$-1.09^{+0.45}_{-0.54}$	$2.0^{+4.2}_{-1.6} 10^{-2}$	$1.76^{+1.57}_{-1.40}$

Table 5.2: Average PSD properties of the observed solar regions in the two IRIS lines (Mn I 280.1 nm and Mg II k3). The calculation of the properties is described in Section 5.3.1.

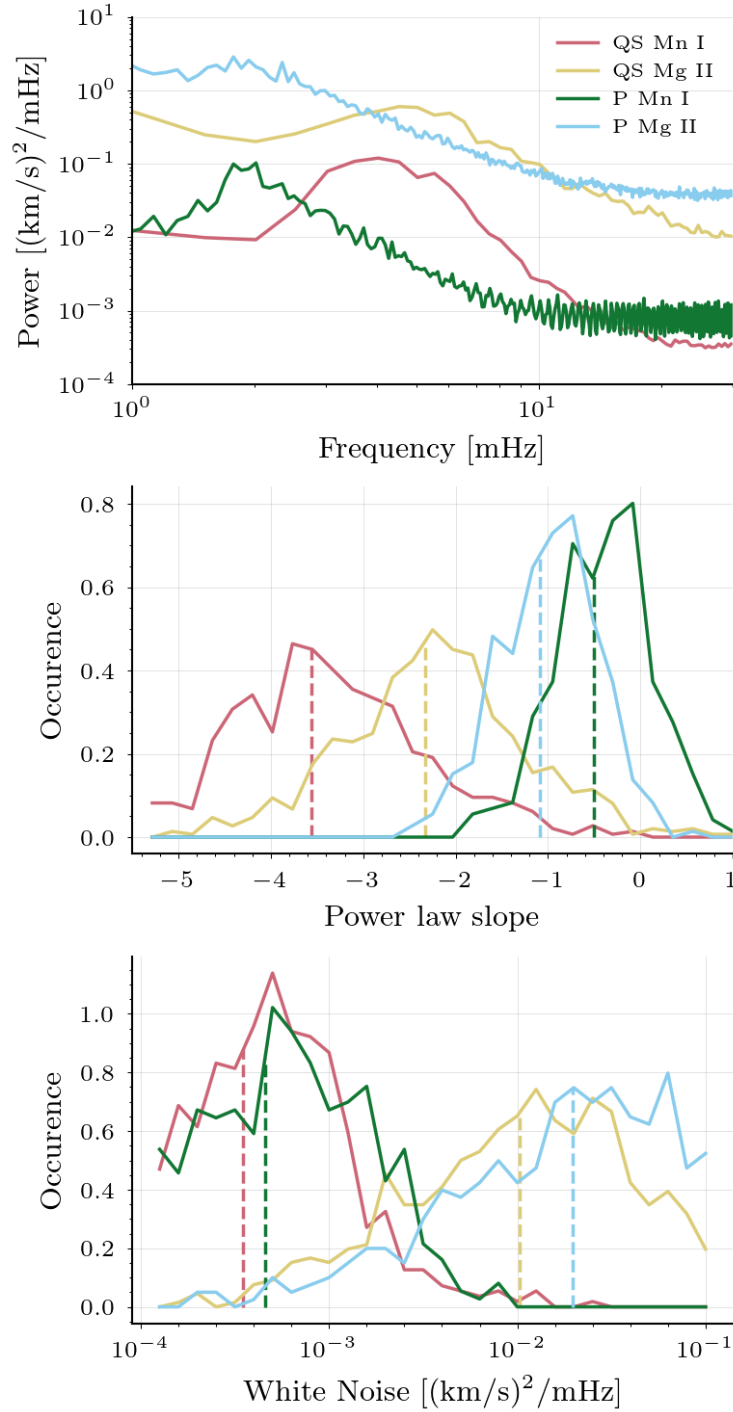


Figure 5.2: Observed power spectra and their power law properties for the different solar regions and spectral diagnostic. *Panel (a)*: Average power spectra. *Panel (b)*: Slopes of the fitted power laws. *Panel (c)*: White noise floors for the different diagnostics. The color coding is consistent throughout the panels of the figure. The analysis of the data presented in this figure are described in detail in Section 5.3.1.

Figure 5.2 presents the average power spectral profiles (PSDs) and their derived properties for the different solar regions and spectral diagnostics. The average power spectra for the different solar regions are shown in the top panel. The quiet sun data exhibits the typical 3 minute (5 mHz) peak in both the Mn I line (lower chromosphere) and the Mg II k line (upper chromosphere). This can be seen clearly from the last two rows of Figure 5.1, where the velocity diagnostics of the quiet sun exhibit regular pattern with scale of about 3 minutes. The plage exhibits a peak at lower frequencies (around 2 mHz) in the lower (more clearly defined peak) and upper chromospheric diagnostics (as previously shown by [de Pontieu, 2004](#); [Morosin et al., 2022](#); [Sadeghi and Tavabi, 2022](#)). Furthermore, the Doppler velocity observations in the plage (last two rows of Figure 5.1) do not seem to exhibit the clear pattern seen in the IN data, which results in a less well defined peak in their Doppler velocity power spectra.

[Zaqarashvili and Skhirtladze \(2008\)](#) has suggested that the lower frequency peak in the velocity PSD in the plage regions might be a signature of the kink wave frequency in the chromosphere. However, we did not find a clear correlation between the cotemporal magnetic field strength in the photosphere measured by SDO/HMI ([Schou et al., 2012](#)) and the peak of the plage velocity PSD, as suggested from the behavior of the kink-wave cutoff. We intend to extend this study with chromospheric magnetic field measurements to explore the suggested kink wave cutoff frequency with the upcoming DKIST telescope ([Rimmele et al., 2020](#)), which would allow for chromospheric magnetic field measurement throughout the lower solar atmosphere with higher spatial resolution and temporal cadence.

The middle plot of Figure 5.2 presents the power law slopes of the observed PSDs for the different regions of interest. We conduct linear fit on the log-log representation of the velocity PSDs to estimate the power law slopes. For the plage regions we fit the frequencies between 2 and 10 mHz, and for the quiet Sun we fit the region between 5 and 20 mHz, due to the properties of the

white noise floors of the two regions. The dotted lines show the median of the distributions. The plage exhibits shallower power law slopes, very similarly to the previous analysis in [Molnar et al. \(2021\)](#). The power laws of the upper chromospheric diagnostic in the quiet sun have steeper slopes, whereas the diagnostics in plage have relatively flat PSD distributions.

To quantify the usable range of frequencies for our analysis we calculated the white noise floor, that is clearly seen in panel (a) of Figure 5.2 as the frequency independent signal at high frequencies. We compute the white noise floor as the median power above 25 mHz frequency. This frequency cutoff is outside of the frequency range on which we performed our analysis on. The white noise floor distributions of the PSDs of the different solar regions are shown in the bottom Panel (c) of Figure 5.2. Similarly to the results in [Molnar et al. \(2021\)](#) we observe that the white noise floor is higher for the plage compared to the internetwork regions. We also find that the Mg II derived diagnostics have higher white noise floor compared to the Mn I ones. This trend might be due to the measurement technique and/or the nature of the chromospheric lines in question, as the Mg II lines have a complex shape that requires elaborate fitting routine ([Pereira et al., 2013](#)). Based on this result, we define the meaningful frequency region of the PSDs to be used for further analysis to be up to 20 mHz for quiet sun regions and 10 mHz for the plage regions, because white noise dominates above those frequencies, as clearly seen in panel (a) of Figure 5.2.

Figure 5.3 shows the total observed oscillatory power between 5 and 20 mHz in the IRIS diagnostics (Mn I and the Mg II k_3 lines). We also include the amount of oscillatory power from the optical lines of Na I D_1 and Ca II IR lines observed with IBIS for similar solar regions ([Molnar et al., 2021](#)). The observed region on the Sun with IBIS is not the same as the IRIS ones, but the applied solar surface feature selection criteria make for a suitable statistical comparison between the properties of the two regions. In Figure 5.3 the blue distributions are derived from observations, and the green ones from simulations, described in Section 5.4.2. In all cases we have subtracted

a local estimate of the high-frequency white noise component for each pixel, following the noise estimation procedure described in the previous paragraph. The average values of the IRIS velocity fluctuation power are summarized in Table 5.3.1.

We observe an increase in the amount of velocity oscillatory power with increasing height in the observations in Figure 5.3, where the spectral diagnostics are arranged in increasing order of height of formation. This is presumably due to the steeply decreasing density with height in the solar atmosphere, leading to increasing wave amplitudes, even though the actual wave flux decreases with height. We also see that the absolute amount of observed line-of-sight velocity oscillations is higher in the internetwork compared to the plage regions.

The comparison of the total velocity oscillatory power in the optical diagnostics from IBIS is shown in Figure 5.3. The Na I D₁ line velocity data agrees well with the velocity data from the Mn I 280.1 nm line. Both lines are formed at similar region of the solar atmosphere (Leenaarts et al., 2010; Pereira et al., 2013), which makes this agreement expected. The Ca II 854.2 nm line shows velocity fluctuation power between the lower chromospheric lines and the upper chromospheric Mg II k3 line. This confirms that the resulting amount of power, coming from different spectral lines is self-consistent and presents a uniform physical picture of the amount of wave power in the solar atmosphere.

5.3.2 Correlation between intensity and velocity oscillations

The line core intensity and displacements of the Mg II h&k lines are sensitive diagnostics to the plasma temperature and velocities at the formation height of those lines (Leenaarts et al., 2013). Since compressive waves have associated temperature perturbation (Mihalas and Mihalas, 1984), we can examine the nature of the waves by comparing their Doppler velocity and intensity fluctuations. A correlation between intensity fluctuations and velocity oscillations could be a signature of the

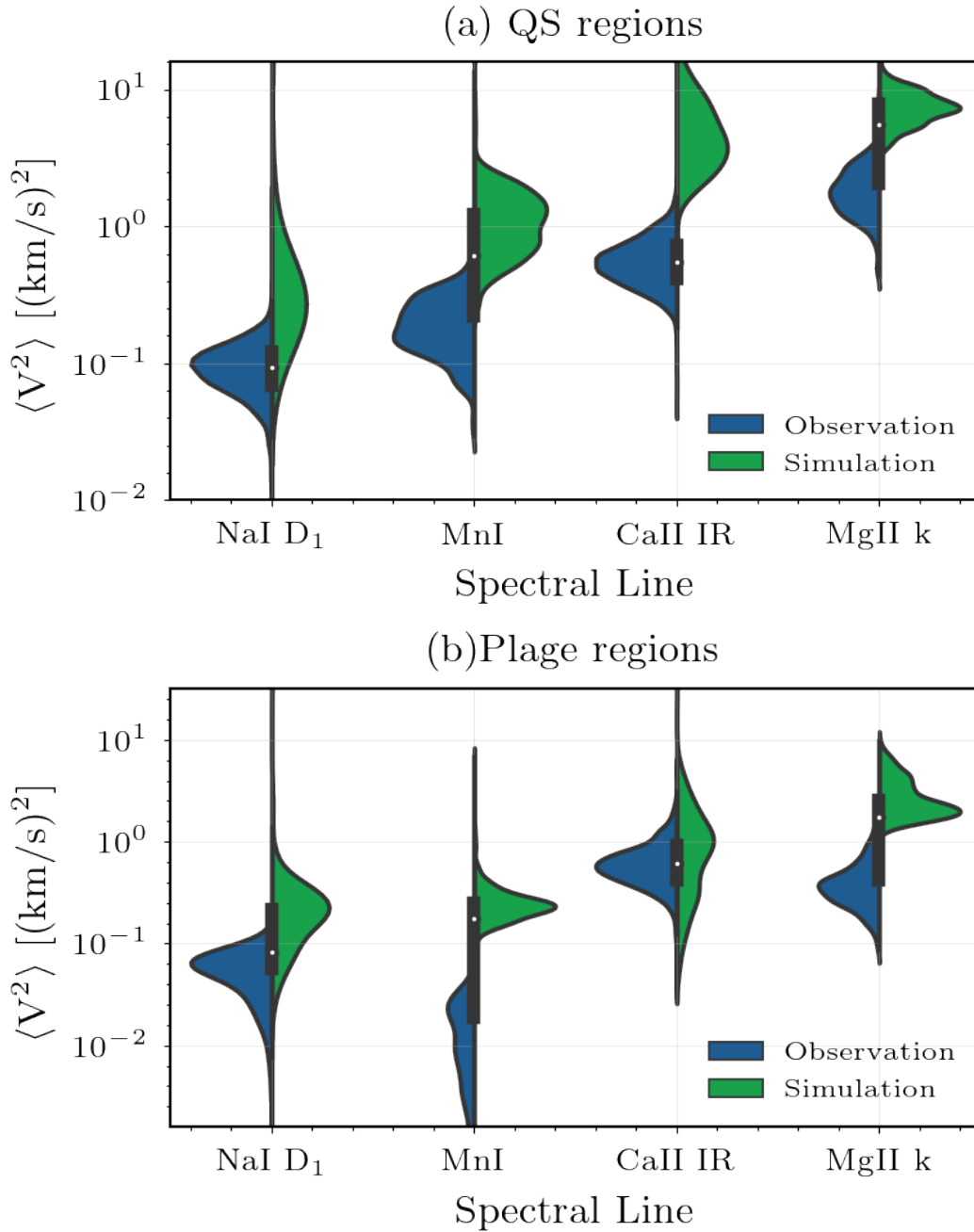


Figure 5.3: Oscillation power between 5 and 20 mHz in the IRIS and IBIS diagnostics in the different solar regions (see Section 5.3), where the white noise floor has been subtracted. The ordering of the spectral lines reflects their relative height of formation in the solar atmosphere. The blue distributions are real observations, whereas their green distributions are derived from synthetic observables from the Bifrost simulation.

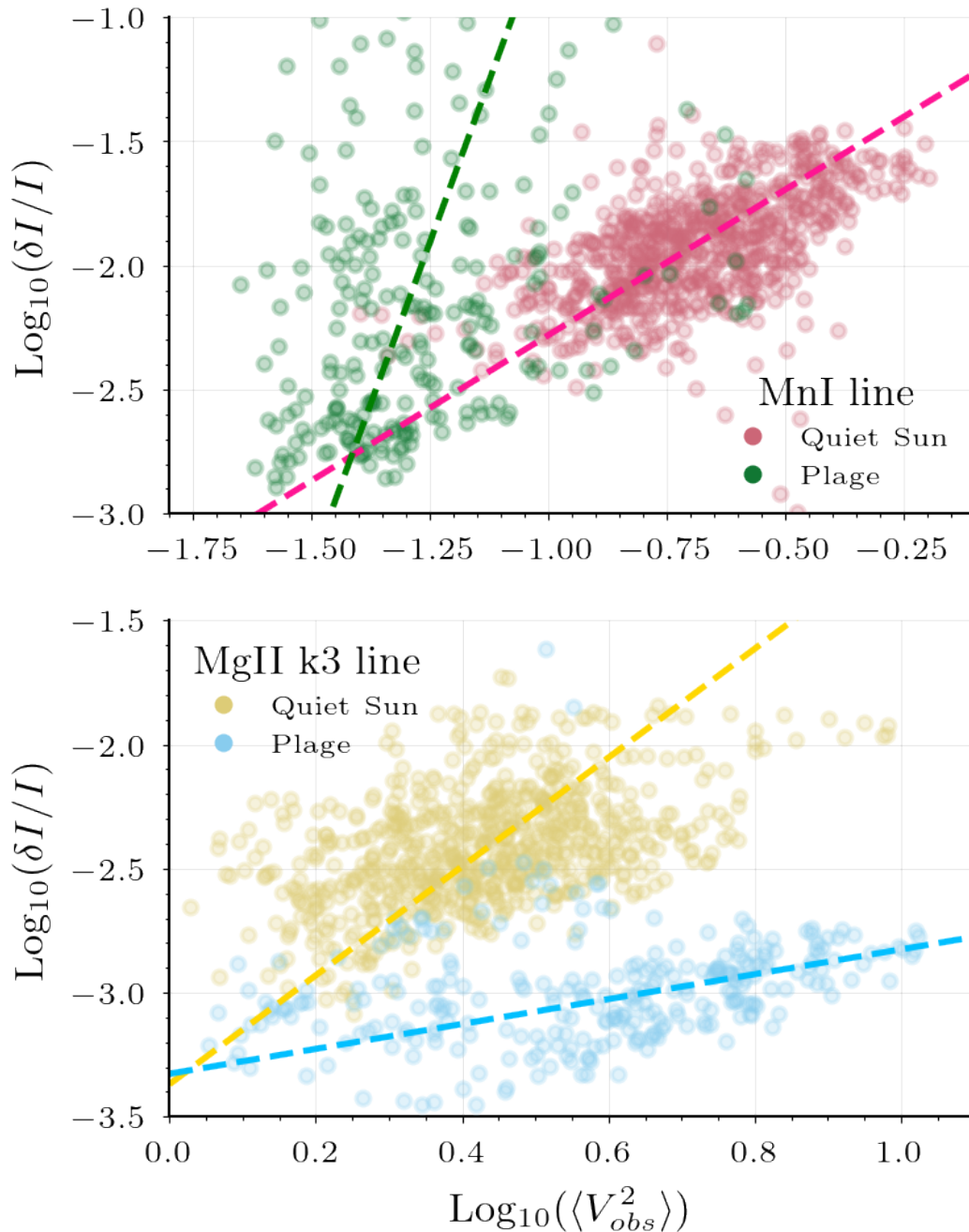


Figure 5.4: Observed correlation between velocity oscillation power and line core intensity oscillation power in the IRIS data between 3/5 and 20 mHz for the Plage and internetwork regions. The top panel corresponds to the properties derived from the Mn I 280.1 nm line; the bottom panel shows diagnostics derived from the Mg II k3 lines. The corresponding dashed lines are the linear ODR fit to the data.

compressive nature of the observed waves. On the contrary, a lack of intensity variations associated with the detected velocity ones might be a signature of Alfvénic-like waves, but could also result from instrumental insensitivity or radiative transfer effects.

Figure 5.4 shows the correlations between the line core intensity fluctuations (sensitive to plasma temperature) and Doppler velocities fluctuations for the respective spectral lines. The amount of fluctuation power observed in both temperature and velocity diagnostics is calculated between 5 and 20 mHz for the quiet Sun regions and between 3 and 20 mHz for the plage regions. The top panel is for diagnostics derived from the Mn I 280.1 nm line and the bottom is for the Mg II k3 lines, where the color tables used is the same as the one used in Figure 5.2. To describe the trends of the data, we perform linear fits through Orthogonal Distance Regression (ODR)². The resulting fits are shown as the dashed lines in Figure 5.4.

Figure 5.4 presents the ubiquitous positive correlation between the intensity and velocity oscillations in both the internetwork and the plage regions. The slopes of the two distributions switch from the lower to the upper chromosphere, where the quiet sun shows steeper correlation coefficient in the lower chromosphere and vice versa in the higher chromosphere (Mg II lines). Part of the IRIS FOV of the plage region is taken by quiet Sun and that has been excluded for the analysis. However, if we include the internetwork region in our analysis, the internetwork samples from the plage dataset overlap with the quiet sun data. Hence, we believe there is a continuous physical transition of conditions from the quiet Sun toward the more active plage regions.

5.4 Acoustic wave propagation in solar simulations: 1D vs 3D models

The energy flux F_{ac} of propagating acoustic waves with frequencies between ν_{ac} (the acoustic cutoff frequency) and an arbitrary frequency ν_1 can be calculated with the following expression

²We used the *scipy.odr* module for performing the fits.

(following the derivation in [Bray and Loughhead, 1974](#); [Bello González et al., 2009](#)):

$$F_{ac} = \rho \sum_{\nu'=\nu_{ac}}^{\nu_1} \frac{\langle v_{obs}^2(\nu') \rangle}{\mathcal{T}^2(\nu')} v_{gr}(\nu') \quad (5.1)$$

where ρ is the plasma density at the formation (response) height of the observed diagnostic; $\langle v_{obs}^2(\nu') \rangle$ is the observed velocity variance at frequency bin ν' ; $\mathcal{T}(\nu')$ is the attenuation coefficient due to the finite thickness of the formation region of the spectral line ([Mein and Mein, 1976](#)); v_{gr} is the group velocity of the wave mode at frequency ν' . To estimate the wave energy flux, we have to evaluate the terms on the right side of Equation 5.1 from models or observations. The quantity $\langle v_{obs}^2(\nu') \rangle$ is obtained from the observations in Section 5.2. The other three quantities will be evaluated from the numerical atmospheric models in this Section.

We extend previous analysis ([Fossum and Carlsson, 2005](#); [Wunnenberg et al., 2002](#); [Sobotka et al., 2016](#)) to compare the differences between 1D models (FAL, RADYN) and 3D models (Bifrost). We chose the 3D Bifrost model for comparison with the 1D models, as this particular Bifrost includes the necessary physical phenomena (shock propagation, detailed radiative transfer) and reproduces a wealth of different small scale solar features. This approach allows for self-consistent description of wave propagation in the chromosphere, avoiding some of the problems with 1D modeling described in [Ulmschneider et al. \(2005\)](#). Previous work by [Fleck et al. \(2021\)](#) examined the general wave propagation properties in 3D simulations, but did not explore the high-frequency wave propagation properties in the chromosphere. In comparison with observations, the conclusion of [Fleck et al. \(2021\)](#) was that current 3D simulations might not properly represent the wave characteristics observed on the real Sun.

5.4.1 RADYN models used

We use the same RADYN (Carlsson and Stein, 1992; Allred et al., 2005, 2015) runs presented in Molnar et al. (2021) to interpret the IRIS observations. The initial RADYN atmospheric model used was a IN atmosphere model with 191 grid points. The model has bottom boundary condition is a piston that acts as a sub-photospheric wave driver and an open upper boundary condition with constant temperature of 1 MK. The RADYN code solves the non-LTE radiative transfer equation (including bound-bound, bound-free transitions) for hydrogen, calcium, and helium with 6-, 6-, and 9-level atom models respectively.

To synthesize the Mn I, and the Mg II spectral diagnostics studied throughout this work, we use the RH15D (Uitenbroek, 2001; Pereira and Uitenbroek, 2015) code. For the synthesis of the Mn I 280.1 nm line we used the Kurucz line list database³ and we synthesized it in local thermodynamic equilibrium (LTE) with RLK scattering on. We note that the lines of Mn I suffer from non-LTE effects (Bergemann et al., 2019), but we leave the estimation of the importance of these effects for a future work. To synthesize the Mg II lines we used the RH code Uitenbroek (2001) in non-LTE mode with 10 plus 1 base state Mg III levels and PRD treatment (the same setup used in Leenaarts et al., 2012b).

5.4.2 Bifrost models

Recent developments of modern 3D radiative magnetohydrodynamic (rMHD) codes appear to achieve a high level of realism of the solar atmosphere. To leverage the advantages of multi-dimensional rMHD simulations including most of the necessary wave physics, we use the publicly available Bifrost datacubes⁴ of enhanced network *en024048_hion* (Gudiksen et al., 2011; Carlsson

³<http://kurucz.harvard.edu/linelists.html>

⁴Available at <http://sdc.uio.no/search/simulations>.

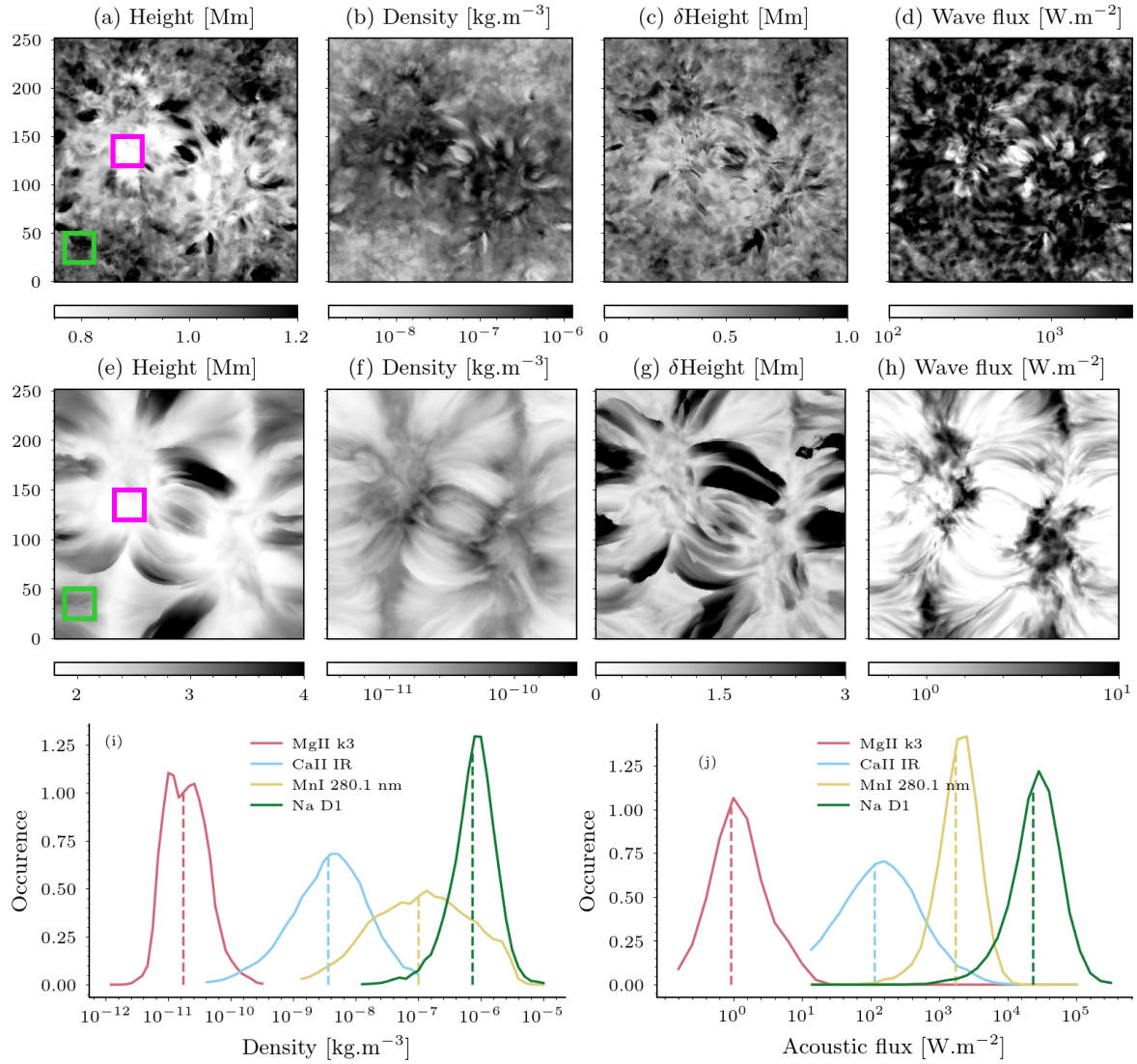


Figure 5.5: Results from the Bifrost spectral synthesis. The top row shows diagnostics derived from the Mn I 280.1 nm line. Panel (a) shows the height of optical depth unity of the line core, panel (b) the density at optical depth unity for the line core, panel (c) the change of the density at optical depth unity over the duration of the simulation run, and panel (d) the acoustic flux at the formation height of the spectral line. The middle row shows the same properties as the top row but for the Mg II k3 line for the same simulation. The green and magenta squares in panels (a) and (e) are the representative regions of the dark internetwork and enhanced network analysis. The bottom left panel shows the density of formation distributions in the simulation for the different diagnostics; right panel shows the acoustic flux distributions at the height of formation of the diagnostics.

et al., 2016). We further utilize the publicly available radiative transfer products for the Mg II h & k and the Mn I 280.9 nm lines which are synthesized with the RH15D code and publicly available for the enhanced network *en024048_hion* (Pereira et al., 2013). We also synthesize the Ca II 854.2 nm and Na I D₁ lines with RH15D in nLTE on the NSO Blanca Cluster. We used a 6-level model atom for the Ca II 854.2 nm line, including a Ca III ground state; for Na I D₁ line, we used a model atom with 4 levels which includes a Na II ground state.

Before proceeding with the analysis of the spectral synthesis products, we note a few deficiencies of the Bifrost models, which should be kept in consideration while interpreting the following results. First, the UV solar spectrum is not well reproduced, with spectral features lacking in intensity and width (Pereira et al., 2013). As discussed previously in Carlsson et al. (2016), this might be due to a combination of factors, including insufficient microturbulence velocities in the models, underresolved small scale motions and missing heating input in the chromosphere. The other major drawback of these models is the presence of global oscillations over the whole simulation domain with velocity (density) perturbations on the order of a few km/s (tenths of a dex) in the lower chromosphere (described previously in Carlsson et al., 2016; Fleck et al., 2021). We have ignored the effect of those wave modes in our analysis by excluding them in Fourier space, since their periods are lower (about ten minutes) than the periods of interest in this paper and are coherent over the whole domain.

5.4.3 Properties of the synthetic observables from Bifrost

Figure 5.5 shows the formation properties of the Mn I 280.1 nm (top panel) and Mg II k3 line (middle panel) in the Bifrost simulations. Panel (a) and (e) show the height of optical depth unity and indicates that the two spectral lines are formed at significantly varying heights in the atmosphere at different locations in the FOV, as previously shown in Pereira et al. (2013). This

spread of the height of formation leads to a significantly different densities at the $\tau=1$ heights, which are shown in Panels (b) and (f). This raises the question of the utility of using the simplistic approach based on Equation 5.1 to infer the amount of acoustic flux in the chromosphere, as choosing a singular density value for a given measured location is inherently problematic. The oscillating height of formation (optical depth unity) of the spectral lines is shown in Panels (c) and (g). We have shown the difference in height between the 10th and 90th percentile in the height of formation distributions of the two diagnostics for each pixel. This results in that the Mn I line the density of formation changes by an order of magnitude in internetwork regions, but relatively less in the enhanced network regions. This dichotomy might be due to the significantly different heights of formation of the diagnostics in the two regions with least relative density variations occurring when the line forms lower in the atmosphere. For the Mg II k line, we see that the height (and respectively density) changes most significantly along the fibrillar structures, connecting the two magnetic regions.

Based on the spectral synthesis of the two IRIS and the two IBIS lines, we computed histograms for the $\tau=1$ surface for each spectral line from the first snapshot of the simulation which are presented in Panel (i). The wide density distributions present a challenge to compute the wave fluxes, but we can observe that the enhanced network (magenta square) and the internetwork (green square) exhibit almost constant density. The average of the density from those regions could be used as the representative of the values to be used in Equation 5.1 when estimating the acoustic fluxes, but this leads to a very model-dependent interpretation of the observations.

The acoustic wave flux in the simulation cube can be computed at different heights as the plasma conditions are known. We estimated the average height of formation for each line in each column of the simulation and then extracted the average plasma density at that height as well as the amount of velocity oscillatory power between 5 and 20 mHz at this height. Based on those estimates

we computed the average wave flux at the formation height of the spectral lines and the results are shown in panels (d) and (h). The resulting acoustic wave flux distributions are presented in Panel (j) of Figure 5.5. The amount of acoustic flux with height is decreasing significantly, contrasting the almost constant amount of wave flux in the RADYN chromosphere (Fossum and Carlsson, 2006). This is the typically observed behavior of the wave flux with height, as hinted previously (Abbasvand et al., 2020a). Furthermore, the amount of acoustic flux in the Bifrost simulation at the height of formation of the Ca II is on the similar to the ones inferred in Molnar et al. (2021). However, as discussed later in Section 5.4.3, this is mostly due to the significantly higher density of formation of the spectral lines in the RADYN models.

However, the comparison of the synthetic velocity oscillation power with the real observed values (green versus the blue distributions in Figure 5.3), shows that the simulations exhibit significantly higher amount of velocity oscillation power than the actual Sun. To compute the synthetic distributions, we have measured the Doppler velocity using the same procedure as the one utilized for the real observations, described in Section 5.2.1. We have also removed the white noise in both cases, which cannot be the reason for the significantly higher amount of oscillations in the synthetic observables.

The wave energy propagating through the chromosphere is mostly dissipated by the time it reaches the height of formation of the Mg II k3 line (Figure 5.5, panel (h)). This is further illustrated in Figure 5.6, where the height dependence of the acoustic flux in an internetwork and magnetic concentration regions are shown. The representative regions in question are shown as the green (dark internetwork) and magenta (enhanced network) in panels (a) and (e) in Figure 5.5. The amount of velocity variance is also shown in Figure 5.6 as the dashed lines. We can see that the amounts of velocity oscillatory power in the internetwork and the plage are similar in the photosphere, but in the chromosphere the internetwork has higher velocity oscillation power by

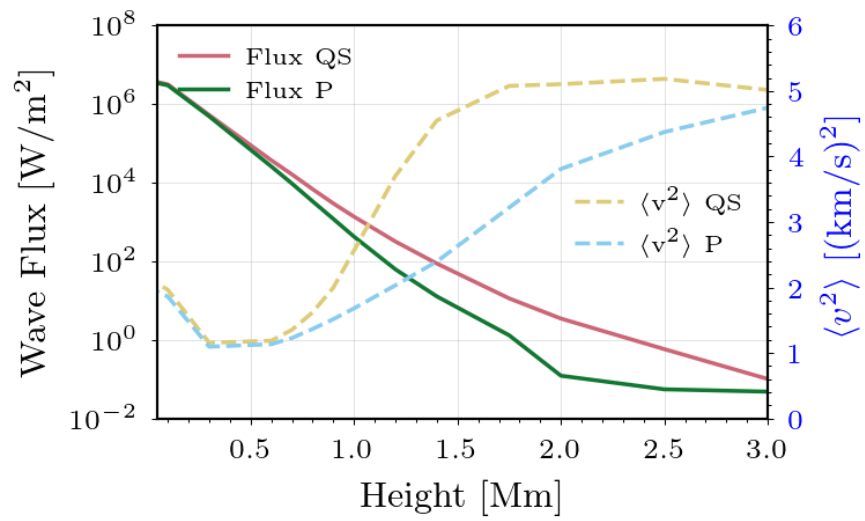


Figure 5.6: Amount of acoustic flux and amount of velocity fluctuations between 5 and 20 mHz in the Bifrost model. Quiet Sun (green) and plage regions (red) are the solid (dotted) lines for the wave flux (velocity fluctuation). The regions of the simulation used are shown in Panel (a) and (e) of Figure 5.5.

a factor of two. When taking into account the slightly lower density at the same height for the internetwork, compared with the enhanced network, we see that the acoustic flux is almost the same for the two regions at the same heights.

This analysis shows a few of the drawbacks of using 1D atmospheric models to infer the wave fluxes. First and foremost, perturbative approaches such as [Bello González et al. \(2009\)](#); [Abbasvand et al. \(2020a\)](#) cannot account for the atmospheric properties changing significantly in time and between different solar features. There has been previous work by [Fossum and Carlsson \(2005, 2006\)](#) which uses 1D HD RADYN models to infer wave fluxes from the TRACE observations, but these authors did not use differing starting atmospheric models to study the behavior of different solar features, which might be seen in their data. Furthermore, the analysis of the 3D models show that the high frequency shocks do not over-saturate the chromosphere with acoustic power as in the 1D case ([Ulmschneider et al., 2005](#)).

The main property that affects the estimation of the acoustic flux is the density. We do not argue about the veracity of the conclusions in either approach, as the reliability of 3D models to represent the wave dynamics of the solar atmosphere is still under debate ([Fleck et al., 2021](#)). Furthermore, most probably lower densities in the Bifrost simulations are the cause for the weaker spectral features in the synthetic spectra ([Carlsson et al., 2016](#)). In the next section, we compare the different modeling approaches, quantifying the systematic differences between them, which might explain some of the discrepancies between the previous results in the literature.

5.5 Systematics of acoustic wave flux estimation from 3D vs 1D models

The spectral synthesis of observables from numerical solar models provides us with a direct way to examine how the variations in diagnostics relate to the actual changes in atmospheric plasma properties. We examine in this section the behavior of components of Equation 5.1 in

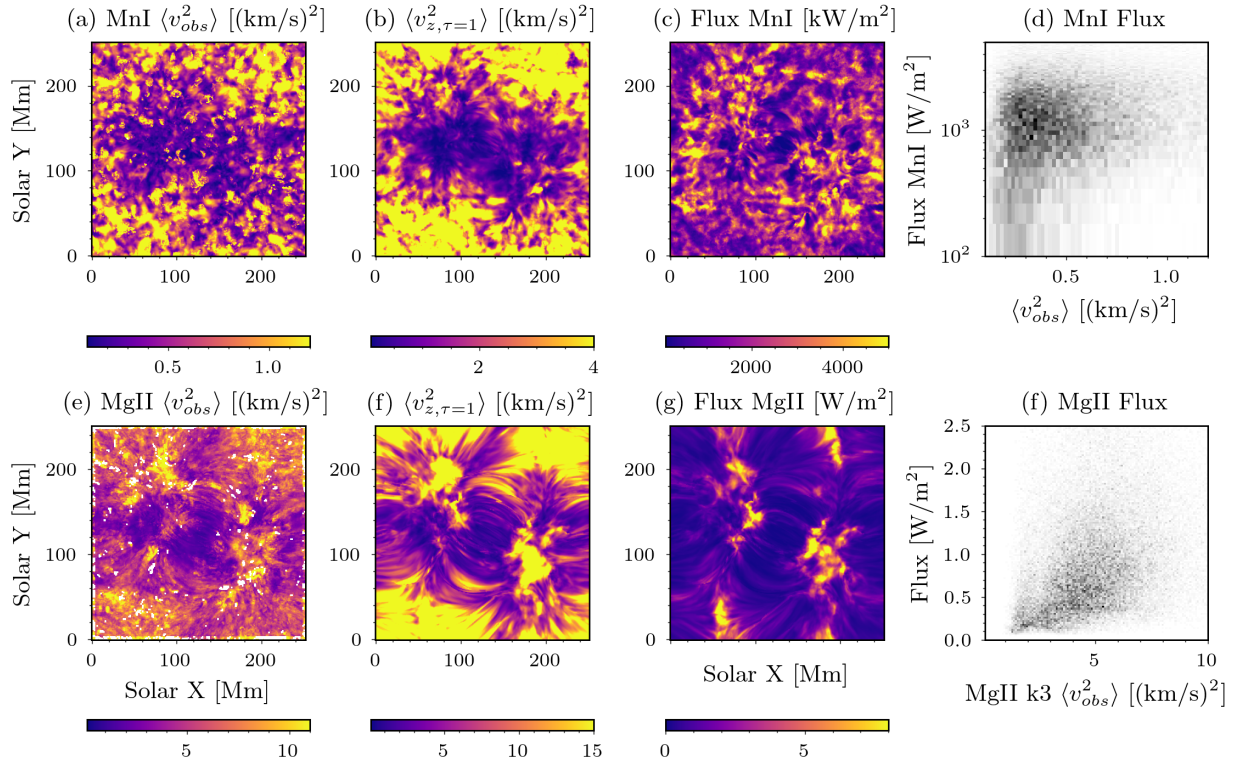


Figure 5.7: Comparison of the synthetic velocity fluctuations in the Mn I and Mg II k3 lines and the wave fluxes at the corresponding heights in the model atmospheres. The top presents the following Mn I 280.1 nm derived diagnostics: panel (a) shows the measured synthetic Doppler velocity fluctuations between 5 and 25 mHz; panel (b) shows the vertical velocity oscillatory power between 5 and 25 mHz in the Bifrost simulation at the $\tau = 1$ height for each column; panel (c) shows the acoustic flux as measured in the simulation at the $\tau = 1$ height for each column, and panel (d) shows the scatter plot between the quantities in (a) and (c). The bottom row is the same, but for the Mg II k3 line.

different modeling approaches. In particular, what atmospheric velocity corresponds to the observed Doppler velocity measurement and what is the reason for the velocity fluctuations – true plasma motions or changes in the $\tau=1$ surface; what is the density at the associated height of formation of the oscillating atmosphere; and what is the transmission coefficient in different regions of the solar atmosphere. We compare the results from the 3D Bifrost simulations with previous results from RADYN and FAL-atmosphere-based modeling. This comparison allows for estimating the uncertainties that are introduced from using a particular modeling approach. This is an important caveat for these studies, that has not been well constrained. We show in this section, that the aforementioned particularities can change diametrically the conclusions from such studies.

5.5.1 Measuring velocity fluctuations, but where?

The analysis in Section 5.4.3 shows that the Doppler velocity signal in synthetic spectral lines originates from a rapidly changing multitude of heights. Hence, we need to quantify what heights exactly contribute to the Doppler velocity to be able to estimate the wave flux at a singular height in the atmosphere.

We compared the observed velocities in the synthetic spectral observations with the acoustic flux at the $\tau = 1$ height of formation of the spectral line. The results are shown in Figure 5.7, where the first row is for the Mn I line and the second row for the Mg II k3 feature. Optimally, there would be a direct relationship between v_{obs}^2 and the wave energy flux, which would make the estimation of the density and the attenuation coefficient unnecessary.

For both spectral lines, there is a good agreement between the distribution of the observed synthetic velocity oscillations and the true vertical velocity oscillations in the solar atmosphere – in panels (a) and (b) for the Mn I 280.1 nm line, and in panels (e) and (f) for the Mg II k3 line. The total amplitudes of the velocities derived from the synthetic observables are on average lower, due

to the atmospheric attenuation of the signal (Mein and Mein, 1976). This is a primarily radiative transfer effect, that smears out the velocity signal, since multiple phases of the acoustic waves might be present in the width of the formation region. This observed attenuation of wave amplitudes is described by the \mathcal{T} coefficient and is discussed further in Section 5.5.3.

However, when we compute the acoustic fluxes at the $\tau = 1$ surfaces of the simulations, we see that the correspondence with the velocity amplitudes is nonexistent (panels (c) and (g)). This is due to the fact that the other major component of the acoustic flux calculation is the density. The density at the height of line formation varies significantly in the different regions of the chromosphere, as shown in panels (b) and (f) in Figure 5.5. In particular, these figures show us that the local density changes by an order of magnitude between the quiet and enhanced network regions. This can be understood as in the hotter (network) regions, the diagnostics are formed at a lower height and on average at higher column mass (Fontenla et al., 2011).

This interplay of plasma properties results in the poor correlation between the observed synthetic velocity oscillation power and the acoustic flux at the line formation region, as shown in panels (d) and (f) of Figure 5.7. The correlation is marginally better for the case of the Mg II k3 line. The relatively smaller change of the density of formation in the case of the upper chromospheric Mg II k3 leads to a better correlation between the synthetic observed velocity fluctuations and the acoustic flux in the atmosphere.

To constrain at what height the observed Doppler velocity mostly relates to, we calculated the Pearson correlation coefficient between the observed Doppler velocity and the atmospheric vertical velocity with the python function `numpy.corrcoef`. The highest correlation coefficient was found around the same heights as the heights of the time averaged optical depth unity which confirmed our previous calculations.

The conclusion from Figure 5.7 is that the change of formation height of the spectral lines is

a significant effect when estimating the wave flux in the solar atmosphere. Using singular values of the density will produce results that do not correspond to the true flux at the formation region of the spectral lines. We have to take this into account when estimating the acoustic flux – we must utilize different densities when estimating the wave fluxes. We establish the same results for the density and the transmission coefficient in the following subsections.

5.5.2 Density of formation is model dependent

Density is the quantity with the highest degree of variability in estimating the acoustic flux in the chromosphere, due to the highly corrugated and dynamic structure of the chromosphere (Carlsson et al., 2019). Furthermore, as described in the previous section, the density at the formation location of the same diagnostics in different regions of the solar atmosphere changes by a few orders of magnitude, as shown in panels (b) and (f) in Figure 5.5.

In this section we discuss the variability of the density at the height of formation of our spectral lines of interest for different modeling approaches. The variability described here is due to the different line formation conditions in the model atmospheres, not the intrinsic changes due to the wave perturbations per se.

Figure 5.8 shows the plasma density at the $\tau = 1$ surface for the Mn I 280.1 nm line in panel (a) and the Mg II k3 line in panel (b) for different modeling approaches. The three different models described here are: Bifrost 3D rMHD simulations described in Section 5.4.2; the RADYN models described in Section 5.4.1; and the FAL11 semi-empirical 1D models, described in Fontenla et al. (2011). We use the latest FAL models, since they reproduce the average solar spectra to the best extent, but are in essence very similar to other 1D semi-empirical atmospheric models used in previous acoustic wave studies.

For the Bifrost rMHD model, we extracted the corresponding densities at every 5th spatial

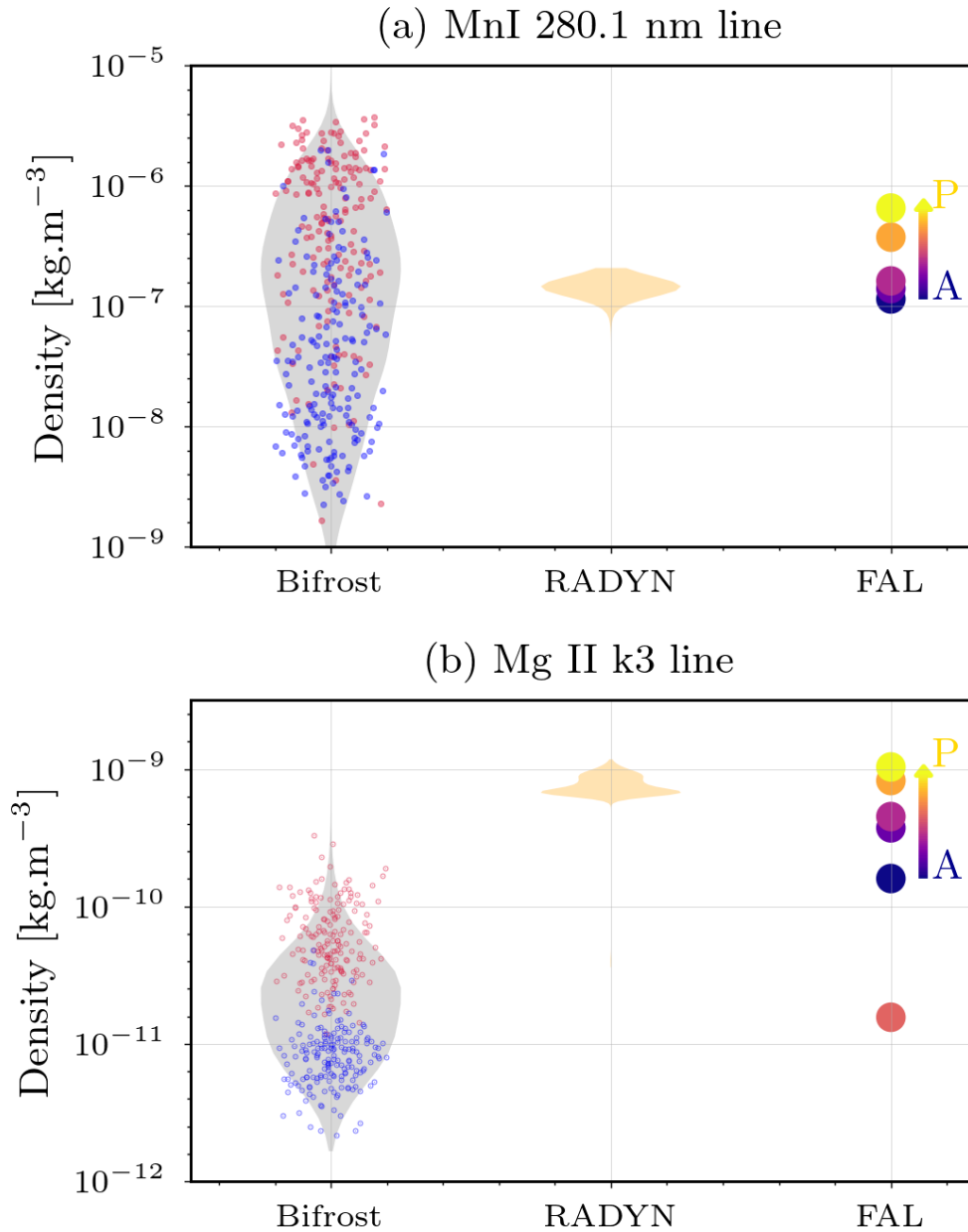


Figure 5.8: Density at the line formation height for the Mn I 280.1 nm and the Mg II k3 lines from different wave modeling approaches labeled on the abscissa. The top panel (a) shows the results for the Mn I line and the bottom panel (b) for the Mg II k3 lines. The data points overlaying the Bifrost density distribution correspond to quiet sun (blue) and plage (red) locations shown in Figure 5.9 sampled every 200 seconds.

pixel in both spatial dimensions at 200 second intervals. The distribution of the Bifrost densities are presented as the gray distribution in Figure 5.8. We also calculated the densities at the two regions of internetwork and active network, marked as the squares in Figure 5.9. We overplotted them over the wider Bifrost distribution with the blue (internetwork) and red (active network) markers. The formation of the lines in the active network is at higher average plasma densities, which agrees with the previous discussion in Section 5.4. For the RADYN models, we calculated the Mn I and the Mg II lines for the model_3000 run from Molnar et al. (2021) for every temporal step, where we have excluded from the synthesis the relaxation time of the simulation. We calculated the density from the other models presented in Molnar et al. (2021) which have increasing wave strength, but the results were similar to the ones presented here. The FAL models A-P, increasing in activity from very quiet internetwork to Plage core, are shown with the colored circles on the right.

The different modeling approaches produce very different estimates for the density. In particular, the Bifrost models exhibit a high level of intrinsic variation of the density. In the case of the Mn I line, the RADYN-derived density corresponds to the quietest FAL models, which is not surprising, since the initial RADYN atmosphere was closely based on that. However, comparing this with the Bifrost density estimates, we see that mostly the active network regions have similar density to the ones retrieved from the FAL-based modeling. In the internetwork, the Bifrost models estimate that the density of formation is significantly lower than the one derived from the FAL models, but at some points they exhibit high densities, similar to the ones seen in the enhanced network.

In the case of the Mg II lines, the hotter FAL models exhibit densities close to the ones found in the RADYN model, opposite from what is seen in the Mn I 280.1 nm line case. However, the more realistic Bifrost simulation exhibits significantly lower density than either FAL and RADYN simulations for both enhanced network and internetwork.

Using the values of Bifrost simulation derived densities for flux estimates would lead to lower inferred chromospheric wave fluxes compared to using values based on the FAL models. We do not argue that one or the other approaches is more accurate, as the Bifrost models still lack heating and sufficient density in the chromosphere to reproduce the observed solar features. Hence, we try to highlight to the reader the systematic biases in the different studies. More realistic solar models show lower density of formation than static 1D models with very significant spread in both location and time. This systematic effect has to be taken into account when interpreting the estimated wave fluxes.

5.5.3 Transmission coefficient \mathcal{T} uncertainty

The attenuation coefficient \mathcal{T} is the last significantly varying parameter in estimating the wave flux. To examine its variation in the Bifrost simulations, we calculated the ratio of the standard deviations of the synthetic Doppler velocities and the vertical velocities in the simulation at the time averaged height of the $\tau = 1$ surface. We have filtered the vertical velocities in the atmosphere to be only between 5 and 20 mHz. We adopt an averaging of the velocity fluctuation power over the frequency domain for calculating \mathcal{T} , different from previous work. This makes it more robust to noise at the high frequency limit, which can contribute to the observed Doppler velocities solely due to measurement errors. The attenuation coefficient maps for both Mn I 280.1 nm (panel (a)) and Mg II k3 (panel (b)) lines are presented in Figure 5.9. The attenuation coefficient varies significantly over the simulation domain and is correlated with the region of underlying solar features.

For the Mn I 280.1 nm line the attenuation coefficient is on the order of ~ 0.4 in the inter-network, which might be expected due to the difference of heights being sampling of the Doppler velocity, as discussed in Section 5.5.1. In the case of the network regions, the attenuation coefficient

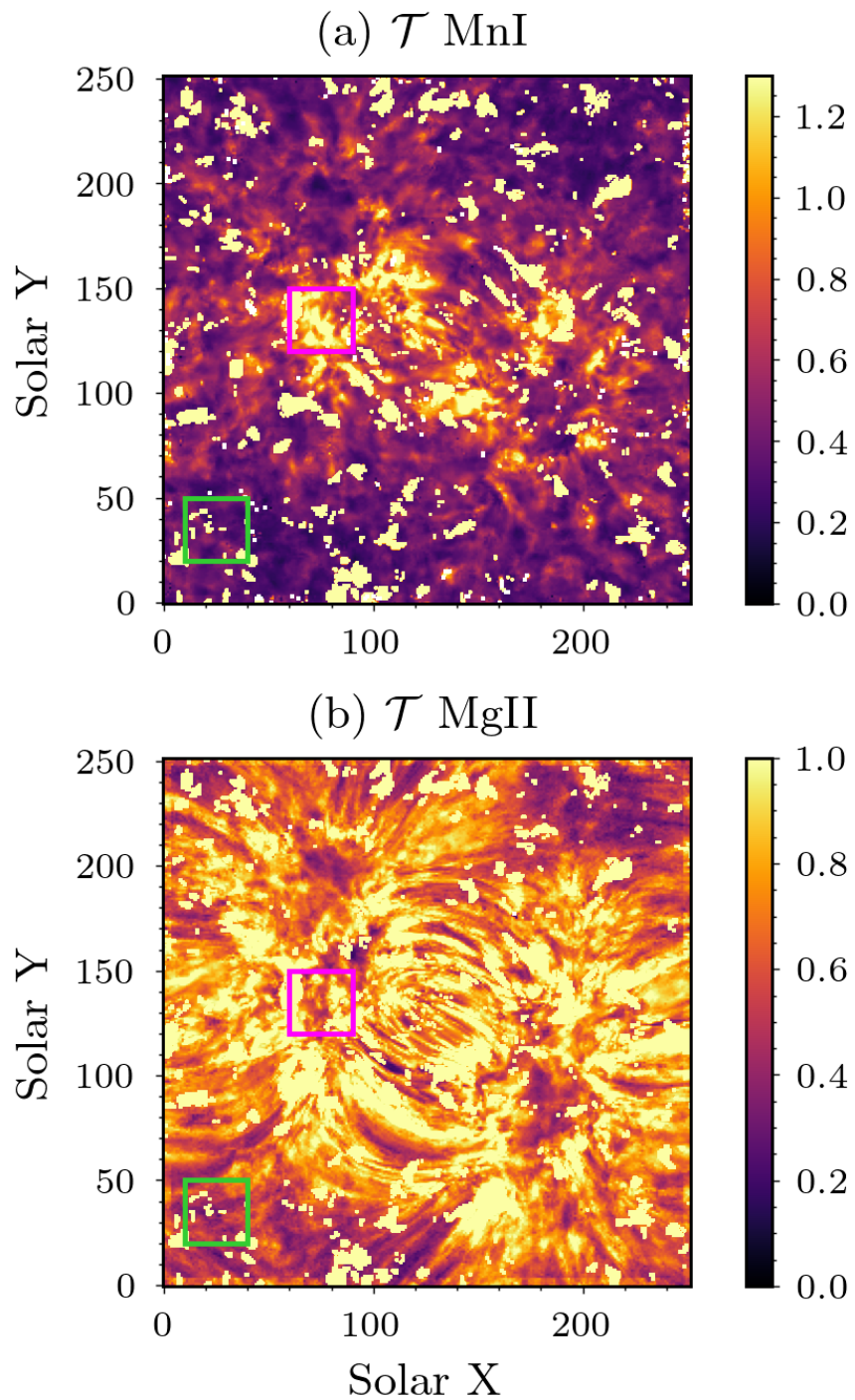


Figure 5.9: Comparison of the amplitudes of the velocity fluctuations (between 5 mHz and 25 mHz) at the $\tau=1$ height in the Bifrost simulation. The top panel (a) shows the amplitudes in the Mn I 280.1 nm line and the bottom panel (b) shows it for the Mg II k3 line. The green and magenta regions correspond to the dark internetwork and enhanced network regions of interest.

is closer to unity, as the Doppler velocity is more closely correlated with the actual atmospheric vertical velocity, due to the fact that in these regions the height of formation changes significantly less, as shown in Figure 5.5 panel (c).

In the case of the Mg II k3 line (panel (b) of Figure 5.9), we see that the extended fibrillar structure of the solar atmosphere is clearly correlated with the transmission coefficient. Interestingly, the long fibrils connecting the two network polarities exhibit differing behavior depending on how much farther out they are from the central part of the magnetic network patch. The lower lying and shorter fibrils, located inward in the active network patch seem to exhibit higher attenuation coefficients, while the longer ones, located on the periphery of the network dipole seem to have lower transmission coefficients. For the case of the Mg II k3 lines, the attenuation coefficient is higher compared to the Mn I lines. Again, we see in the quieter regions the attenuation coefficient is lower (about ~ 0.6) and closer to unity in the network regions.

Based on our analysis, the attenuation coefficient of the $\tau=1$ surface of the line core is a quantity that is determined by the underlying solar feature. This effect cannot be captured by static 1D models and will be definitely underestimated by 1D HD time-dependent models, as the obvious dependence on the magnetic topology of the simulated solar region determines its value. Hence, we believe that in future estimations of the acoustic flux in the chromosphere, we have to take this phenomenon in consideration.

Despite the variances in density shown in Figure 5.8 we chose to use the densities from Bifrost to compute acoustic wave fluxes. We employ those values mean formation properties of the spectral lines, which are listed in Table 5.6. The values we get are significantly closer to unity than what previous authors have cited (Bello González et al., 2009; Abbasvand et al., 2020b), which could be due to the different (and more realistic) modeling approach we utilize.

5.6 Inferring the acoustic wave flux

Spectral line	Density ρ [kg m ⁻³]	\mathcal{T}
Internetwork Na I D ₁ 589.6 nm	6.55 10 ⁻⁷	0.68
Internetwork Mn I 280.1 nm	2.96 10 ⁻⁸	0.37
Internetwork Ca II 854.2 nm	3.15 10 ⁻⁹	0.56
Internetwork Mg II k3	8.55 10 ⁻¹²	0.50
Plage Na I D ₁ 589.6 nm	2.04 10 ⁻⁶	0.91
Plage Mn I 280.1 nm	5.82 10 ⁻⁷	1.03
Plage Ca II 854.2 nm	1.02 10 ⁻⁸	0.89
Plage Mg II k3	5.53 10 ⁻¹¹	0.80

Table 5.3: Density and attenuation coefficient values used for the estimation of the acoustic wave fluxes in Section 5.6.

Based on the observational data presented in Section 5.2 and the numerical analysis in Sections 5.4 and 5.5, we have the required physical quantities to estimate the acoustic flux in the IRIS and IBIS observations, based on the synthetic observables derived from the Bifrost models. In Section 5.5 we showed that the internetwork and the plage regions exhibit different line formation characteristics, such as densities, velocity formation regions and attenuation of the wave signals, within the Bifrost simulation. In particular, the internetwork exhibits formation of the line that is significantly lower in density and has a rather low transmission coefficient, compared to the active network elements. We use for the observed internetwork and plage regions the average formation properties, as derived for regions of the simulation, described in detail in Section 5.5. To calculate the wave fluxes, we adopt values of the density and the attenuation coefficient for the spectral lines. In particular, we do so separately for the two representative regions of internetwork and plage regions (shown as squares in Figure 5.5) listed in Table 5.6.

Figure 5.10 presents the estimates from the wave fluxes, based the calculated properties of the Bifrost simulations for the corresponding solar features. The top panel shows the diagnostics for the internetwork (panel (a)) and the bottom panel (b) shows the results with for the plage

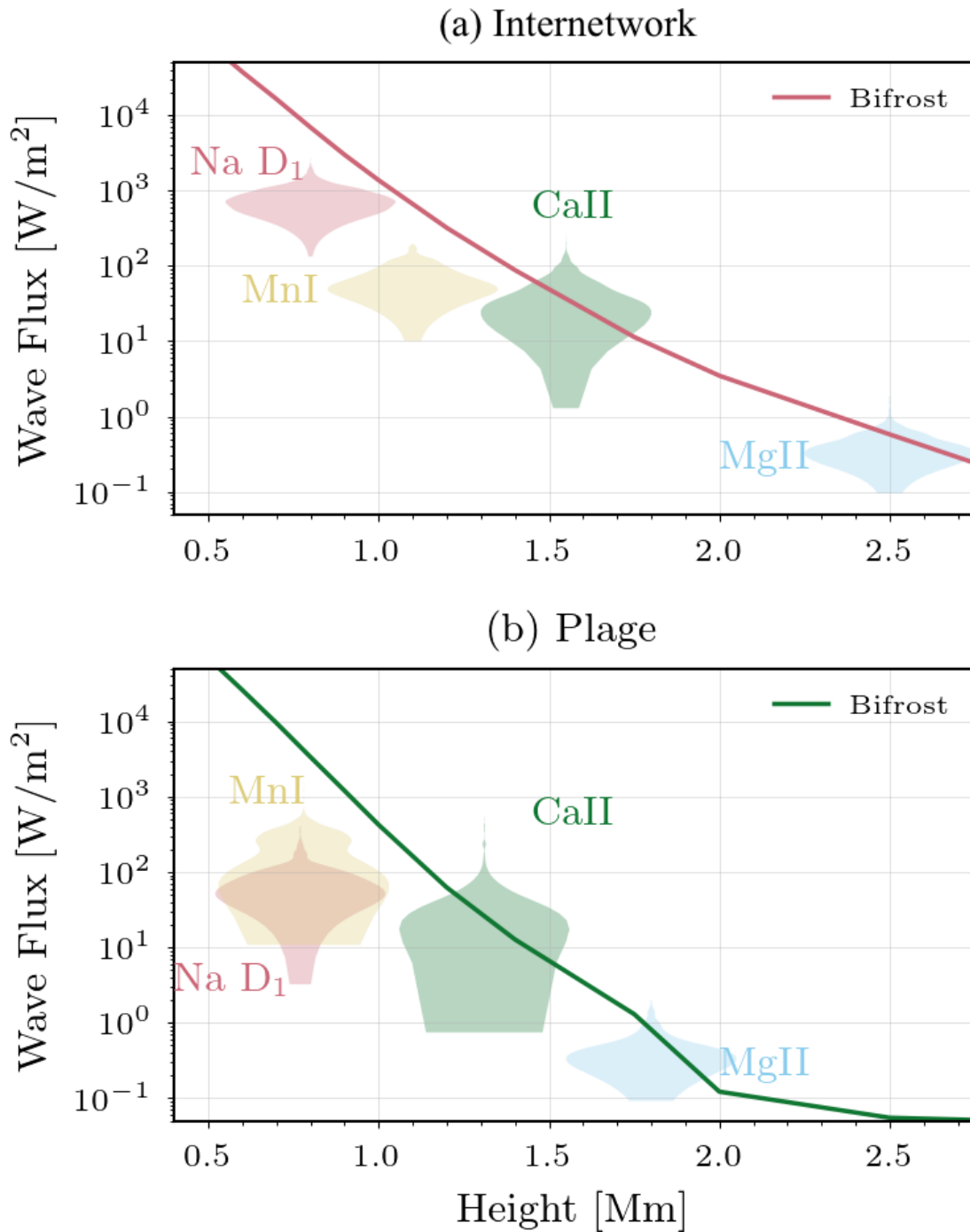


Figure 5.10: Acoustic flux in the different solar regions inferred from the IRIS observations presented in Figure 5.3. Panel (a) (top) presents the fluxes inferred from the Mn I line and the bottom panel (b) presents the fluxes inferred from the Mg II k3 line. The solid lines show the acoustic flux in the Bifrost simulation

regions. Overplotted are the Bifrost averaged acoustic fluxes for the two regions for comparison.

For the case of the internetwork, we see that the Na I D₁ line exhibits significantly higher acoustic flux than the Mn I 280.1 nm line. They both appear insufficient to maintain the quiescent middle and upper chromosphere, as even if all of the wave energy flux observed at the base of the chromosphere, is dissipated to heat, it is still less than the 4 kW m^{-2} required to maintain the average quiet Sun chromosphere. However, these fluxes are significantly high to provide a substantial part of the radiative energy, as previously suggested by [Sobotka et al. \(2016\)](#). On average, the Sun has significantly lower amount of acoustic flux in the chromosphere, than the simulations. This might be due to a variety of reasons, including the magnetic field topology, incorrect driving of the p-modes in the bottom boundary of the simulations ([Fleck et al., 2021](#)) or incomplete physical treatment of the wave propagation and dissipation.

For the case of the plage observations, we see that the lower chromosphere diagnostics are orders of magnitudes too low to maintain the radiative equilibrium in the plage regions. A confirmation of our modeling approach is that the two independently observed lines of Na I D₁ and the Mn I 280.1 nm exhibit almost the same amount of acoustic flux at the about same formation height. The Ca II IR observations exhibit very high velocity fluctuations, which could be attributed to the line core filling due to heating and is the only line, that reaches the flux values observed in the Bifrost models.

In conclusion, our analysis shows that there is insufficient acoustic flux in the chromosphere to maintain it in its quiescent state. However, as presented in our analysis, our conclusion is model dependent as are all previous ones. In particular, the biggest systematic biases are the estimates of the (average-value) density and the attenuation coefficient.

5.7 Discussion and conclusions

We present UV observations of waves in the solar chromosphere with the IRIS spacecraft. In particular, we examine the spectral lines of Mn I 280.1 nm (upper photosphere/lower chromosphere) and the Mg II k3 feature (upper chromosphere). Reduction steps, described in Section 5.2, enhance the data and the wave signatures are readily observed. The power spectra of the observed Doppler velocity and line core intensity oscillations described in Section 5.3 exhibit the ubiquitous power law distributions. Comparing them with optical diagnostics from previous studies in the literature, we reach a coherent wave fluctuation distribution throughout the solar chromosphere.

To interpret these observations, we rely on the 3D rMHD simulation Bifrost, that provides us with a detailed model of the lower solar atmosphere. This model includes detailed physics (non-LTE radiative losses and dynamic hydrogen ionization) important for wave propagation. We rely on the synthetic observables from [Pereira et al. \(2013\)](#) complemented with our own RH15D synthesis to understand the formation of the spectral diagnostics in question, described in Section 5.4. We find that the average formation of the spectral lines differ significantly between the internetwork and network regions. In particular, the density and height of formation of the spectral lines changes significantly between the internetwork and the network regions. Furthermore, the velocity sampled by the Doppler velocity measurement in these lines also changes with the underlying solar structure, which also depends on their attenuation coefficient.

We compare the formation properties of the discussed spectral lines with other wave modeling approaches used in the literature – the RADYN code and 1D semiempirical atmospheric perturbative approaches. We examine in Section 5.5 the differing formation properties resulting from the different modeling approaches and how they affect the inferred fluxes. In particular, we discuss how the measured Doppler velocities correspond to actual atmospheric velocities at different height for

the different solar features. In Bifrost we see a strong bi-modal behavior of the density of formation for the internetwork and the plage regions. The density of formation is significantly lower than the values used in previous work based on 1D semiempirical models. The value of the transmission coefficient is significantly lower for the internetwork than for the enhanced network regions, too. We find that the rapidly changing height of formation determines the attenuation coefficient in the active Sun, which leads to significantly higher values, than previously estimated.

Finally, in Section 5.6 we present the inferred wave fluxes based on the previous results about the Bifrost simulations. We use values of the quantities needed for the wave flux calculation in Table 5.6, where we separate the values for internetwork and enhanced network. We find that the wave fluxes inferred from the observations are lower than the ones found in the simulation. In particular, the acoustic fluxes in the lower solar atmosphere, around the formation height of Mn I are about a few hundred W/m^2 . At the formation heights of the Mg II k3 line, they are on the order of a few W/m^2 . These results do not disagree per se with previous ones in the literature, more than what is eluded to due to the systematic modeling biases described in Section 5.5.

Our work provides us with an example how more realistic simulations of the solar atmosphere are important for understanding the solar and stellar chromospheres. In particular, we show that according to our most advanced solar models, the observed velocity field is not directly related to a singular height in the solar atmosphere. Hence, the interpretation of the velocity fluctuations as a sole indicator of the amount of acoustic flux is severely hampered. We show that the proper density of formation and transmission coefficients have to be adopted for different solar regions to be able to infer the acoustic flux. However, until we have a 3D rMHD model that represents correctly the spectral and dynamic features of the observed solar atmosphere, every study will suffer from these systematics to a certain extent.

Chapter 6

Center-to-limb variation of the observed wave properties

This Chapter presents preliminary results of an ongoing project that will be presented at the IRIS-15 meeting in Prague, Czech Republic in September 2022 and will be submitted to The Astrophysical Journal afterwards.

6.1 Introduction

Alfvén waves are thought to be a major conduit of energy upwards into the solar corona throughout the solar atmosphere. Shortly after their theoretical discovery by [Alfvén \(1942\)](#), they were theorized as a means to transport energy freely throughout the magnetized solar atmosphere ([Alfvén, 1947](#)). Due to the non-compressive nature of Alfvén waves propagating in unstructured medium, they are normally damped very slowly, which requires an additional mechanism for their damping ([Roberts, 2019](#)). Recently, numerical models have shown that Alfvénic wave turbulence can dissipate purely Alfvén waves into local heating ([Hollweg, 1986](#); [Hossain et al., 1995](#); [Matthaeus et al., 1999](#); [van Ballegooijen et al., 2011](#)), perhaps sufficient to maintain the solar chromosphere. Furthermore, Alfvén waves can be converted into other MHD wave modes, which are more readily dissipated in the solar atmosphere (e.g. [Schunker and Cally, 2006](#)). Mode conversion provides a complimentary physical mechanism to Alfvén wave turbulence, for heating the solar atmosphere, but it introduces complexity in tracking the flow of energy through the the atmosphere.

There are multiple observational studies supporting the ubiquitous nature of the Alfvén waves in the solar atmosphere. [Tomczyk et al. \(2007\)](#) found pervasive transverse waves in the solar corona with periodicities close to 5 minutes, curiously close to the peak period of the p-mode oscillations observed in the solar photosphere. These authors used tunable filter data from the CoMP instrument in the Fe XIII 1074.7 nm line to measure the Doppler velocity signatures ubiquitously propagating in the solar corona. In the chromosphere, [De Pontieu et al. \(2007\)](#); [McIntosh et al. \(2011\)](#) showed motions resembling Alfvénic-like wave modes where mass-loaded spicules are acting as wave guides. These resemble the theorized kink tube mode ([Van Doorselaere et al., 2014](#)), which have a compressive component and are dissipated quickly. If this is the case, then these waves most probably dissipate their energy rapidly in the upper chromosphere and lower corona. Whether they carry enough energy flux to contribute significantly to coronal heating and solar wind acceleration is still an open question. However, one caveat related to the chromospheric observations in these papers is that they all rely on imaging data using a relatively broad filter (0.1 nm FWHM) centered on the Ca II line with the Hinode spacecraft, or the 304 nm channel on SDO. Since recent work has been pointing towards the idea that spicules may be manifestations of propagating heating fronts ([De Pontieu et al., 2017](#)), we seek to study these processes using with independent Doppler measurements, which are more closely coupled to real mass flows in the atmosphere.

Alfvén waves are theorized to be driven by the motion of the magnetic footpoints in the photosphere ([Spruit, 1981](#)). Furthermore, observations with increasing spatial resolution, higher order mode tube waves could originate from the continuously changing shape of the photospheric bright points ([Van Kooten, 2021](#)). However, measuring the transverse plasma motions in the chromosphere is a difficult task from imaging, due to the difficulties of feature tracking in the chromosphere. Furthermore, there are differences between the wave properties observed in the

corona (Tomczyk et al., 2007) and in the chromosphere (De Pontieu et al., 2007) – most notably the chromospheric ones have significantly higher frequencies. This disagreement could be due to a local generation process for the Alfvén waves, or could originate from instrumental sensitivity issues and low spatial and temporal resolution. Future observations with DKIST (Rimmele et al., 2020), which has significantly higher resolution, could help settle this disagreement.

In this chapter, we pursue a novel approach to estimate the transverse velocity amplitudes in the solar chromosphere through the center-to-limb variation (CLV) of the observed Doppler velocity and intensity oscillations. The different projections of the plasma velocity components at different observed inclination angles will imprint in the detected Doppler shifts a varying combination of horizontal and vertical velocities. Close to the disk center, the Doppler signal will be dominated by the longitudinal (vertical) waves and close to the limb by wave transverse to the local normal direction. Motions transverse to the solar vertical do not automatically correspond to being perpendicular to the magnetic field direction due to the complex local field topology. Hence, to infer the actual Alfvénic wave amplitudes in the chromosphere, we need to know the magnetic field orientations in the region we are observing and have a predictive model for the expected wave amplitudes that would be observed given the magnetic field direction. Having these auxiliary components, we can try to compare these measurements with the characteristics of the swaying motions of spicules presented by De Pontieu et al. (2007). This approach provides an independent and distinct statistical estimate of the Alfvénic flux in the bulk of the solar chromosphere, not just in those isolated magnetic structures undergoing heating (i.e. spicules).

Examining the center-to-limb (CLV) variation of solar properties is not a novel idea – it has been utilized before as a basis of similar work on unresolved wave broadening in the UV observing the corona and the transition region. Erdelyi et al. (1998) used SUMER/SOHO to examine the non-thermal velocities (residual line widening that cannot be explained by thermal

and instrumental effects) in several coronal lines, and concluded that the non-thermal widths do not exhibit significant CLV. Peter (1999) showed a slight decrease toward the limb for the observed non-thermal velocities in transition region lines, whereas a followup re-analysis of the same dataset with an updated instrumental models proved the opposite CLV trends (Doyle et al., 2000). Recent work by Rao et al. (2022) has examined the CLV of non-thermal widths in the transition region Si IV line observed with IRIS. They found a slight increase of the non-thermal widths toward the solar limb, that they interpret as increased unresolved wave amplitudes, resembling the phenomenon we want to study.

In this thesis chapter I study the CLV of the Doppler velocity fluctuation power variation with the intent to infer the amount of transverse wave power in the chromosphere. The CLV of the Doppler velocity and line core intensity fluctuations from the IRIS observations are described in Section 6.2 as proxies for wave velocity and temperature perturbations. We examine the observed fluctuations between 3 and 20 mHz in order to compare our results with previous results in the literature. We compare the observation results with geometry-based models of the expected CLV trends in Section 6.3 based on the Bifrost simulations. We show that these models can reproduce some of the observed trends depending on the magnetic field inclination angle distribution. We then outline the procedure for comparing the observations with detailed non-LTE spectral synthesis from the Bifrost cubes in Section 6.4. The latter approach includes a lot of complicated radiative transfer effects but I believe it is the most accurate way to interpret the data, given our current understanding of the chromosphere. This is continuation of the study described in Section 3.3 of Molnar et al. (2021), also included in Chapter 4.

6.2 Observations

I use UV observations drawn from the extensive archive of IRIS observations obtained during the mission lifetime. I list the datasets used for this study in Table 6.1. I have prioritized datasets from the earlier years of the mission, when the instrument had a higher overall sensitivity.

I selected datasets for the three types of solar features that will be studied through this chapter – plage (P), a quiet sun (QS), and coronal hole (CH). In particular the quiet sun regions includes both the magnetic concentrations at the supergranular boundaries and the interiors of the supergranular cells. These classes of solar features exhibit somewhat distinct magnetic topologies across their atmospheres. Plage and coronal holes have predominantly vertical, roughly “open” (or connecting far away) magnetic fields, whereas the quiet sun exhibits more closed or locally connecting field lines. The magnetic topology (open or closed) determines the fate of Alfvén waves, which can propagate only along the magnetic field lines. Hence, we expect different behaviors in these various regions.

To constrain the Alfvén flux at different heights through the solar chromosphere we use the spectral lines of Mg II h&k (formed in the upper chromosphere, [Leenaarts et al., 2013](#)) and the Mn I 280.1 nm lines (formed in the lower chromosphere, [Pereira et al., 2013](#)). These lines were used in the previous study in Chapter 5 which allows us to draw conclusions about their formation in the solar atmosphere from the spectral synthesis performed for that work.

The Mg II h&k line features constitute a complex spectral line with a (sometime) present central reversal ([Tousey, 1967](#)). Hence, we use the routine *iris_get_mg_features_lev2.pro* provided from the SSW IDL package to extract the 2v, 2r, and 3 features for these lines. The IDL procedure finds the Mg II h&k feature wavelengths and intensities based on local derivative estimates through subpixel interpolation. The Mn I 280.1 nm data is a spectral line with typical absorption shape

located between the Mg II lines, where the background continuum has a slight slope. Therefore, we use the IDL routine *gaussian_fit.pro* to fit a Gaussian curve with an additional linear background to take into account for the continuum trend and better estimate the Mn I line properties. When one of these fits did not converge, we substituted the value at that pixel with a median 3x3 filter value over the velocity map. We further applied a 3 pixel median filter along the slit direction and then removed the long-term trends by subtracting a linear fit from the data for each slit position. For the derived line core intensities, we divided each timeseries by its mean intensity to perform the analysis on fractional intensity changes. Since we want to study only the solar features considered, we manually chose the parts of the field of view that covered the respective areas of approximately homogeneous solar features instead of using the complete field of view.

Table 6.1: IRIS observations used throughout this work. Labels: CH – coronal hole; P – plage; IN – internetwork.

μ angle	Date ID [YYYYMMDD_HHMMSS]	Cadence, [s]	Lines used	Labels
1.00	20131116_073345	16.7	Mg II,C II, Mn I	IN
0.80	20131116_104845	16.7	Mg II,C II, Mn I	IN
0.60	20131117_044245	16.7	Mg II,C II, Mn I	IN
0.40	20131117_075745	16.7	Mg II,C II, Mn I	IN
0.20	20131117_111245	16.7	Mg II,C II, Mn I	IN
1.00	20140918_080253	5	Mg II,C II, Mn I	P
1.00	20140918_101908	9	Mg II,C II, Mn I	P
0.87	20131213_070938	9	Mg II,C II, Mn I	P
0.70	20200725_000137	9	Mg II,C II, Mn I	P
0.67	20131117_194238	9	Mg II,C II, Mn I	P
0.48	20140410_014930	9	Mg II,C II, Mn I	P
0.44	20130820_123133	4	Mg II,C II, Mn I	P
0.39	20160101_020028	17	Mg II,C II, Mn I	P
0.22	20160101_140128	17	Mg II,C II, Mn I	P
0.92	20170321_195128	16	Mg II,C II, Mn I	CH
0.82	20161107_025410	9.6	Mg II,C II, Mn I	CH
0.74	20161025_111933	9.6	Mg II,C II, Mn I	CH
0.64	20160321_210428	16	Mg II,C II, Mn I	CH
0.39	20140511_051421	9.6	Mg II,C II, Mn I	CH
0.25	20151008_194708	9.6	Mg II,C II, Mn I	CH

6.3 Center-to-limb variation of high frequency velocity fluctuations

In this section we present the dependence on the disc-center distance of the observed line core intensity and Doppler velocity fluctuations. We utilize the cosine of the angle of inclination to the local normal $\mu \equiv \cos(\theta)$ (termed the μ angle) to quantify inclination of the line of sight, as it allows for an easier description of the geometric models as presented in Section 6.4. In this definition of the μ angle, a value of 1 corresponds to an observation at disc center and a value of 0 corresponds to an observation at the solar limb.

We compute the wave fluctuations as the amount of power between 3 and 20 mHz in the power spectra of the diagnostics, motivated by the work of Tomczyk et al. (2007); Reardon and Cavallini (2008). We compute the power spectra with the *scipy* Python library, and we remove a white noise floor estimate (i.e. a frequency independent power offset) from the resulting power spectra (see Appendix A).

6.3.1 Doppler Velocity fluctuations

The Doppler velocity fluctuation CLV results are shown in Figure 6.1. The top row shows the results derived from Doppler velocity for the quiet sun regions; the middle for the coronal hole regions; and the bottom panels for the plage regions. For all of the velocity fluctuations for the Mn I line, originating in the low chromosphere, we observe that the Doppler velocity fluctuation amplitudes are highest in the quiet sun regions and the lowest in the plage, as shown in previously in Chapters 4 and 5. For all three types of regions, the Mn I CLV shows a slight decrease in the fluctuation amplitudes towards the limb. This decrease could be due to foreshortening effects – close to the limb features become highly tilted and occupy smaller surface area in the radial direction, resulting in the resolution element to be filled with multiple solar features. However,

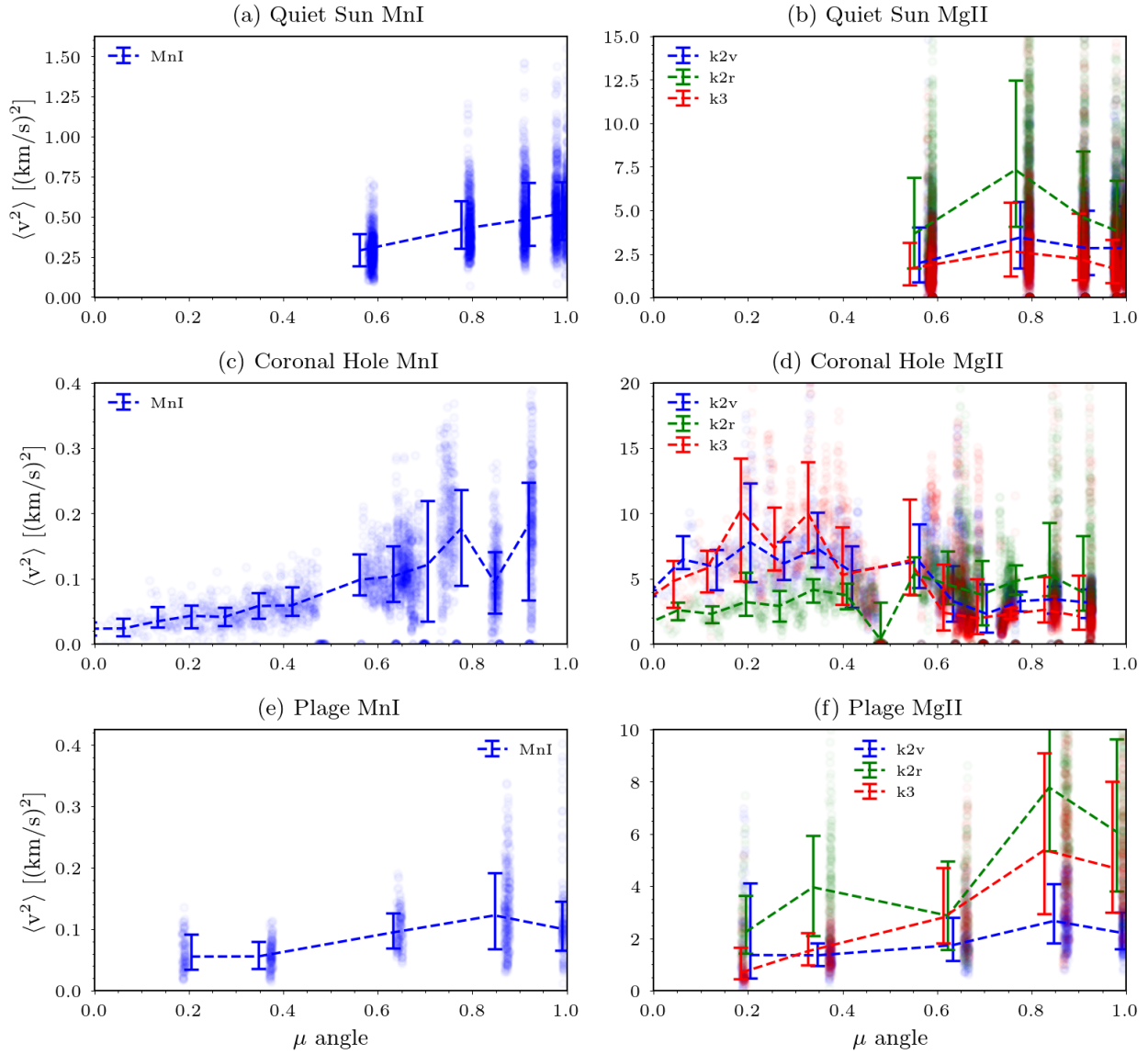


Figure 6.1: Center-to-limb variation of the observed Doppler velocity fluctuations integrated between 3 and 20 mHz. The top row data are for the quiet sun regions; the middle row for the coronal hole regions; and the bottom row for the plage regions. The data for the Mn I 280.1 nm line are shown in the left column and the right column shows the Mg II k line features. The solid lines show the running average for each dataset, while the vertical lines show the middle 67% of the distributions.

it could be because of genuine difference in the amplitudes of the transverse and the longitudinal waves, which we want to investigate.

The trends, if any, in the velocity fluctuation power derived from the Mg II k line features shown in the right column of Figure 6.1 are not as clear as was the case for the Mn I line. First, the amplitudes of the velocity oscillations are significantly higher, due to the formation of the Mg II line at higher altitudes and lower densities. We note that in the coronal holes the observed k2v and k3 fluctuations at the limb are somewhat higher at about $6 \text{ km}^2 \text{ s}^{-2}$, compared to disk center with amplitudes of about $4 \text{ km}^2 \text{ s}^{-2}$. For the plage, we observe decrease of the k2v and k2r velocity power toward the limb at from 5 about $2 \text{ km}^2 \text{ s}^{-2}$.

We note that the results for the plage and for the quiet sun velocities agree with previous publications for the amplitudes of the waves near disc center (see for example Chapter 5). We plan to also further expand the quiet sun range of datasets to include ones with μ angle less than 0.5.

6.3.2 Intensity fluctuations

We present the CLV of the observed line core intensity fluctuations in Figure 6.2, which resembles Figure 6.1 in the arrangement of the different diagnostics. In the case of the Mn I 280.1 nm line diagnostics, we notice a slightly decreasing CLV of the intensity fluctuations for the case of the quiet sun and plage regions. Interestingly, for the coronal hole data, we observe almost a constant amplitude of relative line core intensity fluctuations across the solar disc. In the case of the Mg II k line derived features, we observe almost constant intensity fluctuations with little dependence on μ -angle, with the exception of the coronal hole case, which again exhibits increase of line core intensity fluctuations at around $\mu=0.5$ and then a decrease towards the limb. It is interesting to note that if we observed pure Alfvén waves as the tangential displacements, the intensity fluctuations should not be diminishing toward the limb. However, in the case of other

Alfvénic modes (like tube kink waves), we do expect to observe certain amount of compressivity and related intensity changes (Van Doorselaere et al., 2014).

6.3.3 Correlation between intensity and velocity fluctuations

Compressive MHD waves (such as kink and sausage modes) should exhibit temperature perturbations, whereas non-compressive waves (such as torsional Alfvén modes) do not. Figure 6.3 shows the correlation of the observed line core intensity and Doppler velocity fluctuation amplitudes as presented in the two previous subsections. The μ angle of corresponding to each measurement is color coded as shown in the colorbars. The spectral line and solar features are arranged as in the previous figures. The goal of this figure is to explore whether there is a correlation between the observed integrated amplitudes of the Doppler velocity and line core intensity fluctuations in the different regions, as a possible signature of the compressive nature of the observed fluctuations.

In the case of the quiet sun we do not observe strong correlations between the intensity and velocity fluctuations for either the lower or upper chromosphere. This could be due to the magnetic field of these regions having significant non-vertical components at both heights, exhibiting non-compressive waves as described in Section 6.4.1.

However, for the coronal hole and the plage regions we notice a reasonable correlation between the strength of the intensity and velocity fluctuations close to the disk center. In particular, in panels (c) and (d) for the coronal holes, we see that red and orange dots, corresponding to near disk center observations, exhibit an increase in the velocity amplitudes with increasing line core intensity fluctuations. For the blue dots, observed closer to the limb, we do not see a similar correlation. This is also the case for the plage regions as clearly seen in panels (e) and (f). This correlation could be taken as evidence of the Doppler velocity amplitudes seen at larger inclination angles are more associated with non-compressive waves, due to the apparent lack of a significant signature of

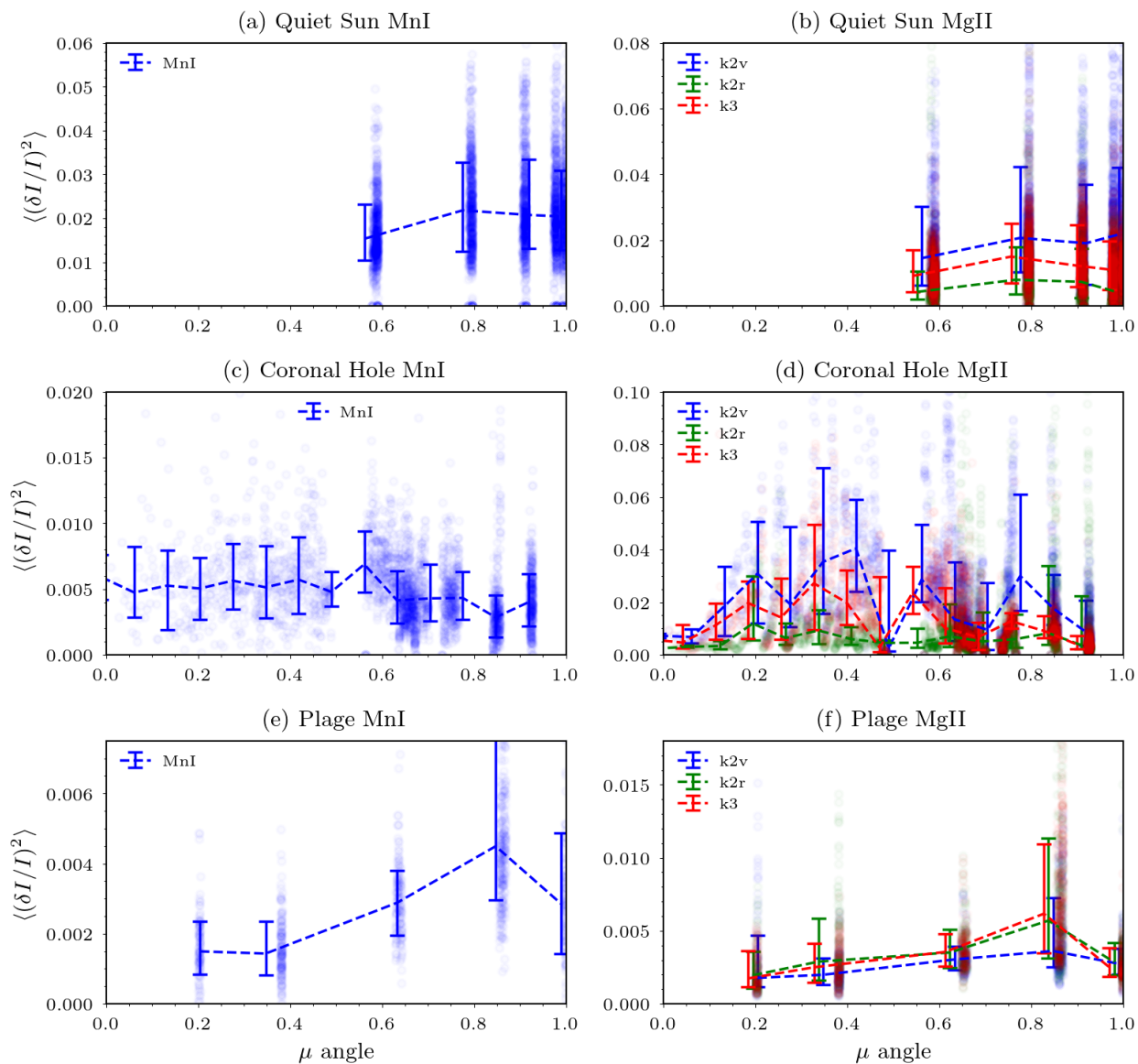


Figure 6.2: Same as Figure 6.1, but for the observed intensity fluctuations distributions.

corresponding temperature changes. However, this behavior could be due to 3D projection effects as well, since the superposition of waves along the line of sight or in a single spatially resolved element would cancel out and reduce the fluctuation amplitude.

6.4 CLV of Doppler velocities and intensity from MHD models

To understand the observed trends in our data, we compare them with MHD models of the lower solar atmosphere that contain complex magnetic field topology, resembling the real Sun. We use the publicly available Bifrost models¹ (Gudiksen et al., 2011; Carlsson et al., 2016; Hansteen et al., 2019). In particular we use the simulation *qs024048_by3363* as a representative of an quiet sun region; simulation *ch024031_by200bz005* for the coronal hole case; and the enhanced network patches in the simulation *en024048_hion* for the plage regions.

The connection between the magnetic field topology and the interpretation of the observed velocity fluctuations is emphasized, as the magnetic field orientation with respect to the wave propagation direction is crucial for identifying which MHD mode is being observed. While we study this relationship in a statistical fashion, we expect the average magnetic field properties in the solar features to be consistent throughout our observations.

We present two different approaches for explaining the observations presented in Section 6.3. The simpler geometrical one is based on the inclination of the magnetic field found in simulations and described in Section 6.4.1. We then describe a more realistic approach based on full spectral synthesis from the MHD simulations on a slanted grid. This method will allow us to better infer how the true plasma properties are related to the observed diagnostics from on the Sun, as described in Section 6.4.2.

¹Simulations are available at <http://sdc.uio.no/search/simulations>.

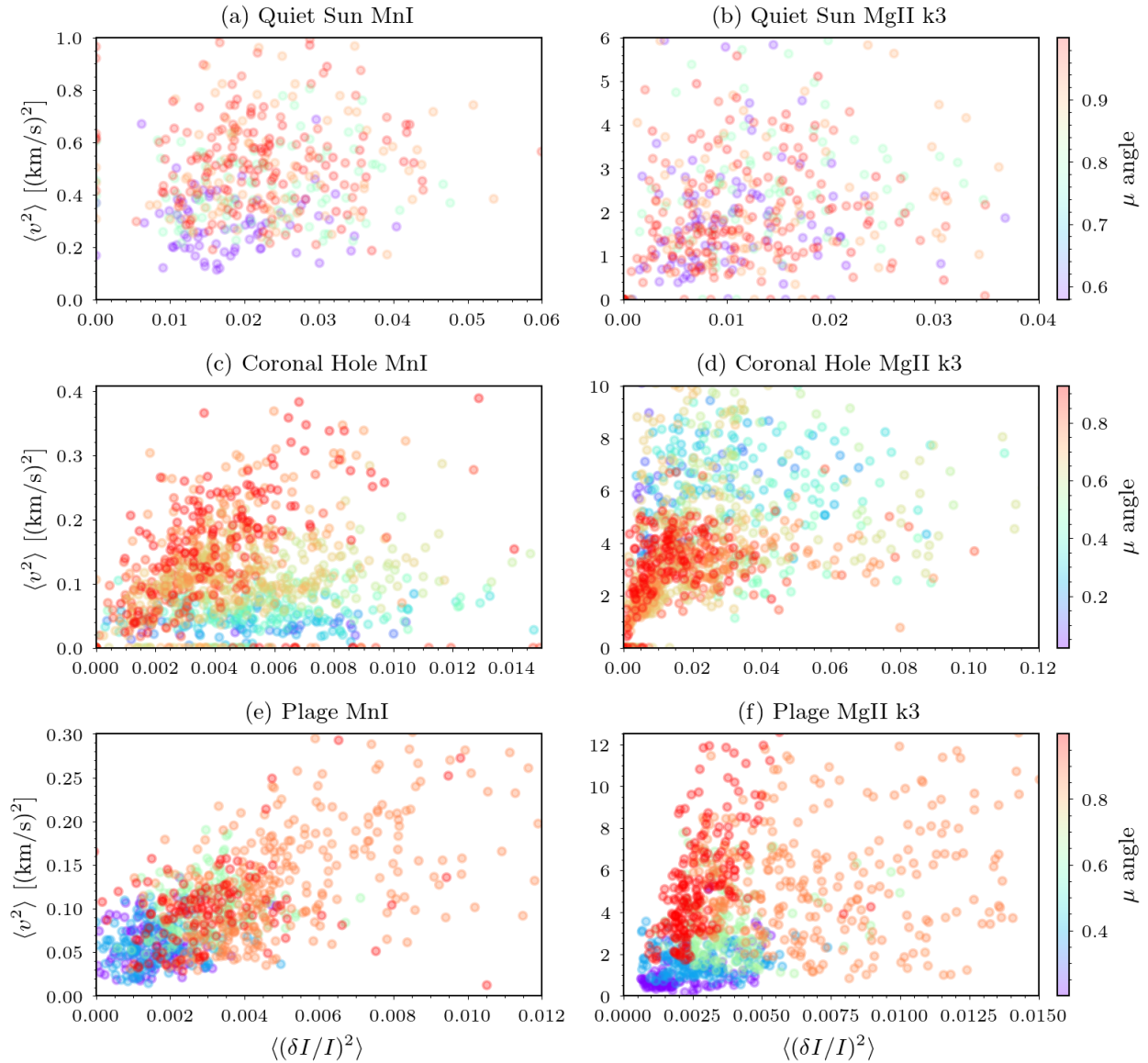


Figure 6.3: Correlation of the integrated amplitudes of the observed intensity and Doppler velocity fluctuations for the different solar features: top row: quiet sun; middle panel: Coronal hole; bottom row: Plage. The left column (panels (a), (c), and (e)) show the observations of the Mn I 280.1 nm line, and the right column (panels (b), (d), and (f)) the Mg II k3 ones. The observations are color coded by the μ angle that they were observed at.

6.4.1 Interpreting the observed CLV of the velocity fluctuations through geometric arguments

MHD wave propagation is determined by the magnetic field topology. To interpret the observed velocity signals in term of MHD wave modes, we need to know the underlying magnetic topology. In particular, oscillations transverse in respect to the normal of the solar surface do not explicitly require Alfvénic wave interpretation. Hence, we build a simple geometric model in this section to interpret the magnitude of the transverse and longitudinal velocity fluctuations based on the mean magnetic field inclination at different μ angles.

For the simulations representing the three different types of solar regions, we present the maps of the magnetic field inclination in Figure 6.4. These provide us with some characteristics of the chromospheric magnetic field that are not available directly from observations. In the figure, white means that the magnetic field at that height in the solar atmosphere is horizontal, while more saturated colors correspond to vertical fields. We adopt the formation heights of the two diagnostics of 0.9 Mm for the Mn I 280.1 nm line and 2.0 Mm for the Mg II k line features, based on the average results found in Chapter 5.

The left column of Figure 6.4 (panels (a) ad (d)) shows the magnetic field inclination in the enhanced network simulation at these two formation heights. The bipolar structure dominates the magnetic topology, with a region of horizontal magnetic field running between the two polarities. The horizontal magnetic field lines close to the domain boundaries are connecting the two strong polarities through the periodic boundaries. The middle column (panels (b) and (e)) show the magnetic field inclination in the quiet sun model. We can see a rather homogeneous mixture of different inclinations on the granular scale or larger, most probably indicating low lying closed field lines. The right column (panels (c) and (f)) shows the magnetic field inclinations from a model of

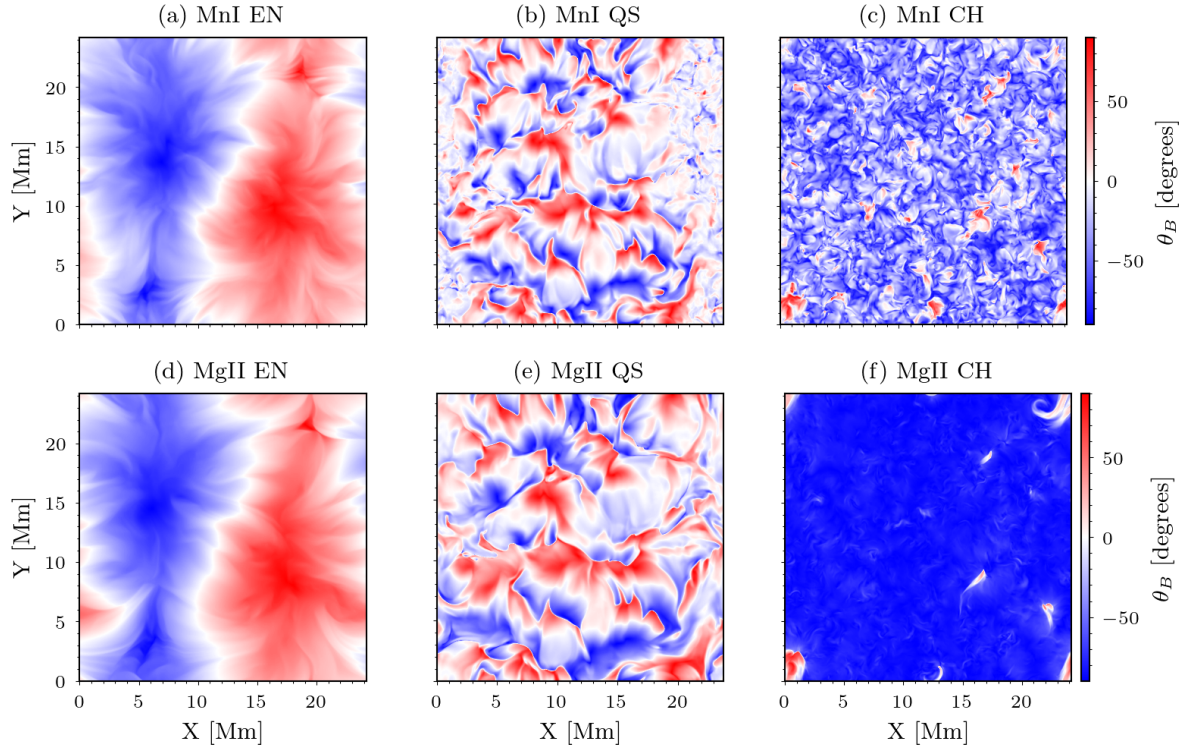


Figure 6.4: Magnetic field inclination of the three atmospheric Bifrost models used – enhanced network *EN* (panels (a) and (d)), quiet Sun (QS) (panels (b) and (e)) coronal hole CH (panel (c) and (f)). Horizontal magnetic field corresponds to white regions and colors represent vertical fields.

a coronal hole. Largely unipolar field, with almost entirely vertical and open magnetic lines at the heights of the Mg II k line formation is seen for the coronal hole. This physical setting simplifies the interpretation of the observed velocity oscillations close to the limb, as all of the magnetic fields will be aligned with the solar normal and any transverse waves will be largely along the line of sight. At the height of the Mn I 280.1 nm line (panel (c)) we see that the magnetic field is mostly unipolar with stronger signatures from the granular ($\sim 1\text{Mm}$) scales fields closing on smaller distances.

Let us assume that wave fluctuations are either perpendicular or parallel to the local magnetic field with constant amplitudes v_{\perp}^2 and v_{\parallel}^2 throughout the solar atmosphere for the solar feature in question. If the waves propagate with the same properties in all solar features across the Sun (no significant center-to-limb variation of the solar physics of plage, coronal hole, etc.), then observing the solar surface at different inclinations will provide us with different linear combinations of v_{\perp}^2

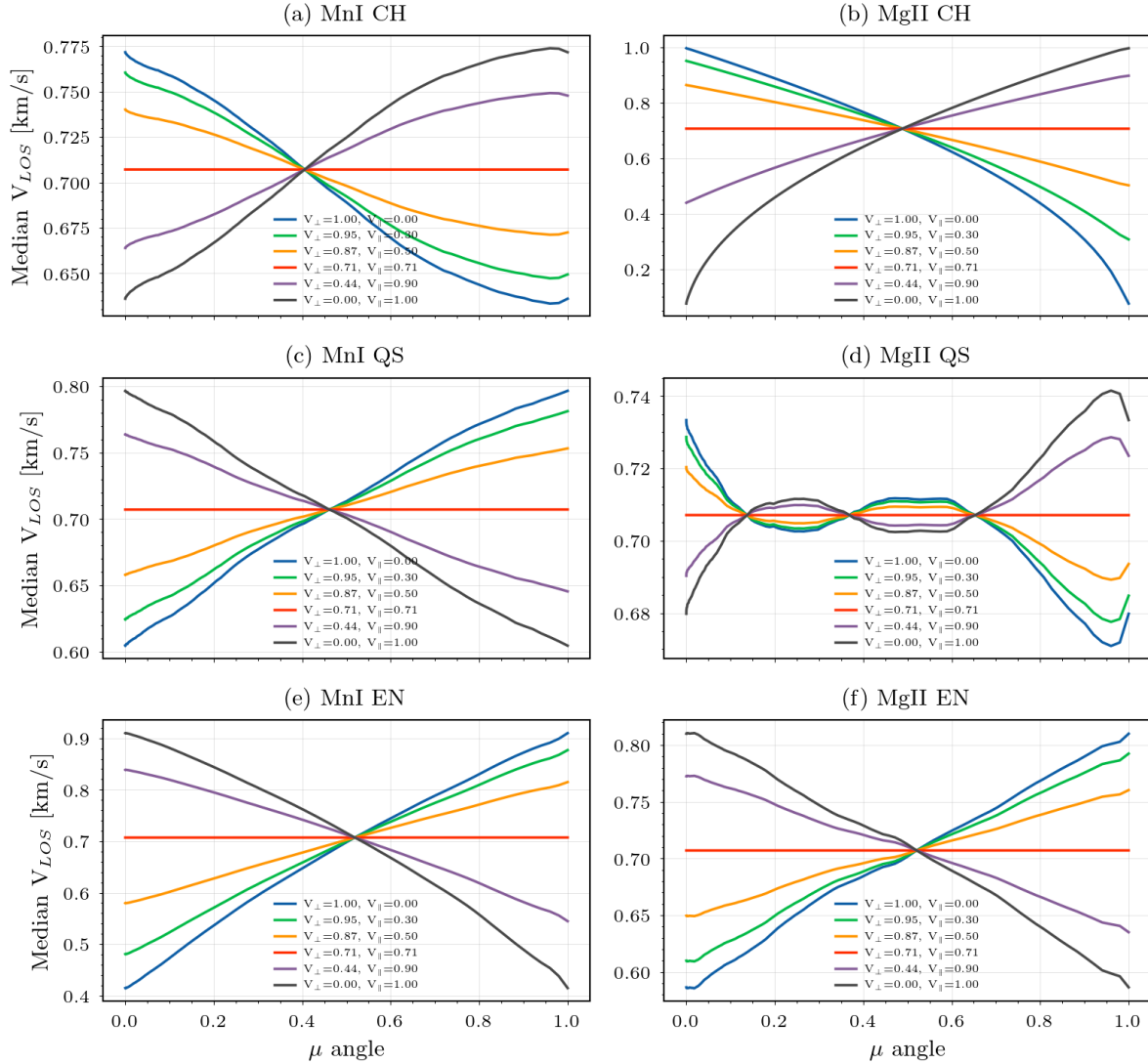


Figure 6.5: Model CLV trends for the observed Doppler velocity based on the different Bifrost models (see Section 6.4.1). The trends in each case are for different mixtures of parallel and perpendicular to the magnetic field amounts of oscillations, where the relative amplitudes of the two are noted in the legend of each subplot. Models are ordered by complexity of the magnetic field topology.

and v_{\parallel}^2 .

Based on these assumptions, we computed what will be the observed CLV trends of the observed Doppler velocities in the following manner: We estimated the observed Doppler velocity as the projection of the v_{\perp}^2 and v_{\parallel}^2 on the line-of-sight direction based on the magnetic field inclination and observing angle μ at the height of formation for each spectral line for different mixtures of v_{\perp}^2 and v_{\parallel}^2 . We normalize the total wave amplitudes, so that the the sum of the orthogonal v_{\perp}^2 and v_{\parallel}^2 , to be unity. In this way we estimate the CLV trend of the Doppler velocity for different ratios of the v_{\perp}^2 and v_{\parallel}^2 amplitudes. The results from this model can be scaled in absolute terms to match the true solar wave amplitudes. The Bifrost simulations (presented in Figure 6.4) provided us with an estimate of the inclination of the magnetic field at the two lines formation heights. We performed this analysis for each column of the simulation. We tilted the simulation cubes only along the x-axis, hence we utilized the angle between the x- and z- components of the magnetic field to estimate the magnetic field inclination. The results from this model are shown in Figure 6.5.

The results for the simplest case of a coronal hole – having a mostly vertical magnetic field – are shown in the top row, panels (a) and (b) of Figure 6.5. The general behavior is for longitudinal waves to be observed as Doppler velocities close to the disk center and vice versa for the transverse waves close to the limb. This trend is extreme in the case at the Mg II height of formation, where we see the almost zero Doppler velocity in the cases of purely longitudinal waves close to the limb and almost zero Doppler signal for transverse waves close disk center. Note the different y-scales on each panel. For the Mn I line, we see similar behavior, but with significantly smaller amplitude. This is due to the presence of significant amount of horizontal fields beside the vertical ones, which leads to a strong mixing of the Doppler signal for the two different oscillation directions at all inclinations. Comparing these models with the results in Figure 6.1, we see that a model with significantly higher amount of longitudinal oscillations at the Mn I height can explain the observations. For the case

of the Mg II lines, we would need a model with nearly equivalent amplitudes in both longitudinal and transverse components to explain the observations.

For the case of the quiet sun model, presented in panels (c) and (d) we observe a somewhat unexpected behavior – the preponderance of horizontal fields in the simulations results in tangential oscillations being projected along the line of sight close to the disk center. This is the opposite behavior of what was seen for in the coronal holes. At the height of formation of Mg II k line, oscillatory behavior is seen, somewhat resembling to what we see in the observations. However, the relatively small amplitudes of the variations in the observed line-of-sight velocities with μ angle, make discerning among these different models from observations difficult.

In the enhanced network, if we only examine the regions above the magnetic concentrations in the simulation, the fields are all vertical and we will get results very similar to those for the unipolar coronal hole case shown in panel (a) and (b). However, if we average over the whole field of view, we get the results shown in panels (e) and (f), which again show a reversed trend compared to the unipolar case. The predominantly horizontal field, surrounding the two network elements reduces the CLV amplitude, due to the mixture of both horizontal and vertical fields, resulting in mixed contributions along the line of sight at all inclination angles. The trends shown in panels (c) and (d) are very similar, but with the enhanced network showing a much larger amplitude.

This simple geometric model can explain some of the features observed in the data, but it suffers from many drawbacks. In particular, we do not take into account the changing radiative transfer properties of the plasma – closer to the limb, the slanted path length means more solar structures along the line of sight can contribute to the observed intensity. Furthermore, solar features mix together and are compressed in the radial direction due to the foreshortening effect. Hence, in the next section, we present a more realistic approach to be undertaken to interpret our CLV observations through modern rMHD simulations.

6.4.2 Spectral synthesis from inclined MHD cubes

We can calculate the emergent intensity from rMHD simulations in any inclined direction. This will provide us with information about the radiation formation process along a tilted ray tracing through the simulated volume, avoiding some of the shortcomings of the model in the previous section. In particular, the radiative transfer calculation will allow us to infer if the contributing regions of the solar atmosphere really oscillate in the transverse (to the magnetic field) direction, or if there is a more complex formation of the Doppler velocity signature. Since we are interested in the observed signature of the waves, not in their absolute amplitudes in the simulations, the simulation does not need to have precisely the same wave properties observed on the Sun.

To do this, the thermodynamic properties of the MHD cube are reprojected on a slanted mesh along the y-axis, with a variety of μ angles. We resample the thermodynamic properties on a tighter mesh of an arbitrary number of points throughout the chromosphere with spline interpolation. To test the computational and memory constraints, we have performed successful numeric experiments with 200 grid points along each ray. We resample the solar atmosphere from just below the solar surface up to 5 Mm. The inclusion of extended heights in the synthesis ensures that with the increasing line formation height toward the solar limb we capture all the contributing layers. We also reproject the velocities in the atmosphere based on the observational angle.

I have ran initial tests with the reprojected atmospheric simulations with the RH code (Uitenbroek, 2001) that have converged successfully. My next steps will be to run the radiative calculations on the whole simulation domain. This will require a few tens of thousands of CPU hours, available from the NSO-Blanca cluster. The results from this spectral synthesis will allow me to probe if the observed velocities close to the limb correspond to the transverse velocities in the atmosphere. I will analyze the $\tau = 1$ surface of the diagnostics formed close to the limb, to examine if the

formation region changes, as shown in Chapter 5. Furthermore, this forward approach will allow me to estimate the ratio of the observed wave amplitudes to the real ones in the atmosphere and calculate the transmission coefficient, as done in Chapter 4.

6.5 Conclusions and discussion

I show for the first time the center-to-limb variation of the observed Doppler velocity and line core intensity fluctuations in the solar chromosphere from the Mn I 280.1 nm line and Mg II k line features observations with IRIS. I analyzed observations of three different types of solar regions – coronal hole, plage and internetwork. In some cases we can detect a slightly decreasing Doppler velocity fluctuations toward the limb in the lower chromosphere, and a mostly constant trends in the upper chromosphere. Furthermore, the oscillations show decreasing correlation between line core intensity and Doppler velocity fluctuations toward the limb for the quiet sun and plage, possibly pointing toward a non-compressive wave origin of the fluctuations close to the limb. However, this could be due to a number of other effects, such as foreshortening or significant change of the response function.

To explain the observations, I produced a simple geometric model based on the magnetic topology found in the Bifrost models. I calculate what are the expected CLV trends, based on differing relative strengths of the wave velocity oscillations tangential and longitudinal components to the local magnetic field direction. I find that the some of the observed trends can be reproduced, with different amplitudes for those trends. This model leaves out several effects and is not sufficient to decompose the tangential and longitudinal amplitudes definitively. We propose a radiative transfer calculation that could alleviate the problems with our geometric model and initial tests show it to be promising.

Chapter 7

Conclusions and outlooks for future work

7.1 Major results from this thesis

This work had the goal of constraining the wave fluxes in the solar chromosphere through the interpretation of spectral diagnostics with advanced rMHD models. To address this, I had to combine novel observations, data processing techniques and modeling approaches, which are described in this thesis.

Before delving into the estimation of the wave fluxes, I had to better understand the formation mechanisms of the solar millimeter continuum observed with ALMA in Chapter 3. I presented for the first time the clear correlation between the millimeter continuum intensity and width of the hydrogen Balmer- α , described in Chapter 3. We were able to reproduce this correlation with spectral synthesis from 1D FAL models, which pointed toward a coupling of the electron density to a curve of growth effect in $H\alpha$. The wider implication from this work is that filtergraph intensity measurements might be misleading when being interpreted without the complete spectral profiles. In particular, local heating events will be detected as decreased intensity in the wings of $H\alpha$ and could be incorrectly interpreted as plasma velocities. Furthermore, previous interpretations of the $H\alpha$ width as non-thermal widening due mostly to micro-turbulence might misestimate flow speeds and wave amplitudes.

Based on this work, I combined time series of ALMA and IBIS observations to calculate the wave energy flux in the chromosphere, using synthetic observables from the RADYN modeling code to interpret the observed diagnostics, presented in Chapter 4. I consistently found that there is not enough wave energy flux in the solar chromosphere to balance the radiative losses, contrary to previous work. My use of the more advanced modeling technique – RADYN, a time dependent radiative hydrodynamic code – allows for self-consistent wave propagation in the atmosphere, taking into account radiative wave damping. This led us to realize that previous 1D static atmosphere modeling using only a perturbative approach is not fully realistic.

Using the even more advanced Bifrost solar models, I repeated our analysis while using additional IRIS diagnostics 5. Our study shows that the improper consideration of systematic uncertainties between previously discussed models can lead to some of the conflicting conclusions reached by different authors. In particular, inability to quantify the density at the local formation height of a given line profile is the leading factor in the inconsistencies between different modeling approaches. Hence, until we have a genuinely self-consistent *ab initio* solar atmospheric model that properly replicates the observed solar atmospheric (and in particular wave) properties, the calculation of wave energy fluxes will be a reflection of the systematics of the solar models used.

I also describe a novel approach to constrain the amplitudes of the transverse waves in the solar chromosphere through observed center-to-limb (CLV) variation of the Doppler velocities presented in Chapter 6. We measure the CLV variation of spectral lines formed at different heights in the solar atmosphere. We find the lower chromospheric diagnostics exhibit decreasing or almost constant velocity fluctuation amplitudes toward the limb. In the upper chromosphere I found almost constant CLV trends of the Doppler amplitudes. The intensity fluctuations also show mostly flat trends in their CLV behavior. However, the correlation between the amplitudes of the observed Doppler velocity fluctuations and the relative line core intensity fluctuations decreases towards

the limb. This could be a signature of the non-compressive nature of the transverse waves that dominate close to the limb, or due to the destructive interference from the superposition of many incoherent waves.

We use three different Bifrost models to explain the observed CLV trends, through geometric arguments related to the distribution of field inclinations. Some of the complexity of the observations seems to be captured in the model, which could qualitatively explain some of the observed trends. However this model is not physically complete as it only incorporates field inclination and does not attempt to account for the foreshortening and the radiative transfer effects of high inclination observations. I plan to extend this study by performing radiative transfer calculations on inclined Bifrost models to better interpret the observed trends.

I also spent time and effort working on two projects, which have not been discussed in this thesis up to this point. I took coordinated $H\alpha$ observations with the Hi-C 2.1 rocket at the Dunn Solar Telescope, that was used to study microfilament eruptions (Sterling et al., 2020). I intend to use this dataset in my future work to study chromospheric wave propagation into the corona as it provides one of the highest resolution contemporaneous datasets of these two regions. During my graduate career I took a class on artificial intelligence and machine learning, which resulted in a publication about compressive sensing – precisely, how to improve the spectral performance of Fabry-Perot-based spectrographs with machine learning approaches (Molnar et al., 2020). I showed that the information content lends itself to substantial compression, which allows us to design instruments with significantly higher throughput while adopting less stringent spectral resolution requirements.

In conclusion, I believe that during my six years here at the University of Colorado, Boulder I learned valuable new tricks and skills that led me to producing the aforementioned publications. Arriving here, I definitely did not expect to spend so much time at telescopes during my PhD,

but in the end these were some of the most memorable moments of my graduate career. From appropriating figs from the side of a country road in New Mexico under Kevin's guidance on the way back from Sunspot to chasing the green flash from the Observatorio del Teide in the Canary Islands every day after observing, I look forward to this part of our profession the most. The Sun is far more exciting than our digital counterfeits of it will ever be. With the arrival of the next generation observatories, such as DKIST and Solar Orbiter, there will be a lot more discoveries that will bring us closer to a more comprehensive understanding of our favorite star, the Sun.

7.2 Future investigations motivated by the results in this thesis

Throughout graduate school I started a few projects that I did not finish. In particular, spending time at the Dunn Solar Telescope allowed me to obtain a few too many hard drives of solar observations that are still collecting dust in their pristine condition. I outline below a few projects, that I intend to pursue at the near future which have been motivated from the results of this thesis.

7.2.1 Phase delays between chromospheric diagnostics observed with ALMA, IRIS and IBIS

Signals of propagating waves passing through different heights in the solar atmosphere will exhibit a phase delay due to the travel time needed between the two sampled layers. The delays, direct signatures of propagating waves, can be derived from observations by examining the temporal shifts between diagnostics formed at different heights in the solar atmosphere. These delays are detected by computing the cross-power transforms of the diagnostics (Deubner and Fleck, 1989), attained by either Fourier or wavelet transforms. We pursue the wavelet approach, since it is more appropriate for the transient behavior of the underlying signals we study (Hansteen et al., 2000;

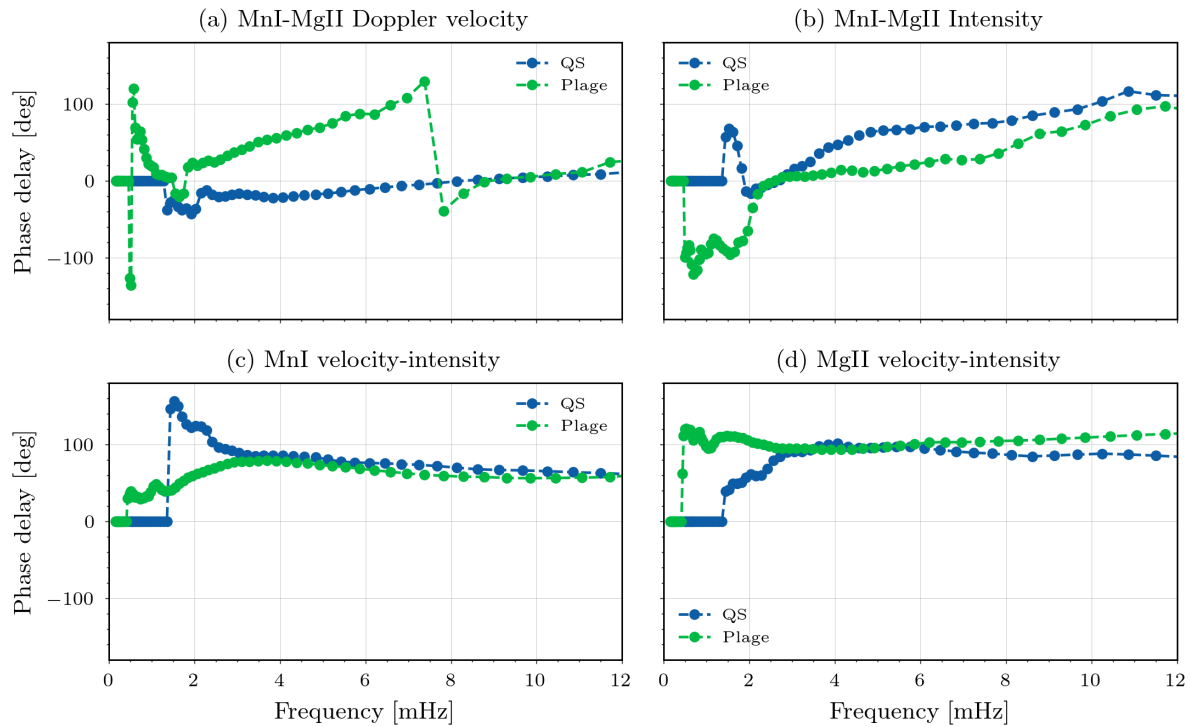


Figure 7.1: Phase delays between chromospheric diagnostics observed with IRIS (line core intensities and Doppler velocities): the Mg II k3 spectral feature and the Mn I 280.1 nm spectral line. The phase delays are computed based on the coherency spectrum estimated with wavelet transforms (see Section 7.2.1 for details). Green data points correspond to plage data and blue to internetwork data.

Kayshap et al., 2018). The Fourier transform underestimates the temporally localized amplitude of the oscillatory signals compared to the wavelet decomposition. Furthermore, it is essential to use wavelets for the computation of the coherency and phase delays over different temporal intervals as simple Fourier transform will return an average over the whole temporal domain, including the intervals when the two oscillations may not be statistically significant. To estimate if the two signals are genuinely correlated with one another, we compute their coherence and respective red-noise level, derived from the data itself. By including a noise estimate of the coherency, we only include regions of statistically significant coherent power between the two signals in our estimate of the phase delays (for more details, see Torrence and Webster, 1999).

I computed the coherency and the phase delays of the Doppler velocities in the Mn I and Mg II lines by using wavelet transformation with six-peak Morlet wavelets. The phase angles and the coherency of the signals were computed using the PyCWT¹ Python package, based on routines from Torrence and Compo (1998). Eight suboctaves are used for each octave in the period dimension. To compute the angles presented in the Figures in this Section, I exclude the results outside the Cone-of-Influence (COI) of our transforms and we only use the locations with statistical significant coherency. To estimate the significance levels of our results we use the built-in red-noise significance estimator, described in Torrence and Compo (1998). I reuse the noise-level models from consecutive pixel location computations to expedite the computations, as the noise-level estimation is the most time consuming part of the process and this approach provides a few-fold acceleration of the decomposition process.

I also examine the phase difference between line core intensity and Doppler velocity in the spectral lines, as they may reflect the phase difference between the plasma velocity and temperature. MHD wave modes exhibit phase delays between oscillating plasma properties dependent on the type

¹<https://pypi.org/project/pycwt/>

of propagating wave (Roberts, 2019). The phase delays could be a useful tool for distinguishing between MHD wave modes (e.g. Centeno et al., 2006). For the case of acoustic wave modes, we expect a $\pi/2$ phase shift between the local temperature and velocity perturbations (Mihalas and Mihalas, 1984). The resulting phase delays for the IRIS data products described in Section 5.2, used for the analysis in Chapter 5, are presented in Figure 7.1.

The top row of Figure 7.1 presents the phase delays between the observed Doppler velocities derived from the Mn I 280.1 nm line and the Mg II k3 feature (panel (a)) and the line core intensities (panel b)). We can see that at high frequencies the phase differences go to zero, which could also be due to noise. However, for the plage there is an increasing phase difference from 2-8 mHz indicating propagating waves. For the intensity phase difference, we observe that the phase difference slowly increases above 2 mHz for both plage and internetwork regions.

The bottom row of Figure 7.1 presents the phase delays between the observed Doppler velocity and line core intensity of the UV spectral lines discussed before. Panel (c) shows the results for the Mn I 280.1 nm line and panel (d) shows the results for the Mg II k3 feature. In both cases the phases asymptotically approach a non-zero angle, between 60 and 100 degrees. Interestingly, evanescent acoustic waves exhibit 90 degree phase difference between their temperature and velocity fluctuations.

More detailed radiative transfer calculations are needed to explore the line formation effects that might affect the observed phase differences.

7.2.2 The quiet solar chromosphere as a resonant cavity

While exploring the power spectra derived from IBIS data in Chapter 5, I found a peculiar peak in the center-of-gravity (COG) velocity of the Hydrogen Balmer- α line ($H\alpha$) around 30 mHz. It is presented in Figure 7.2 as the peak at about 30 mHz in the $H\alpha$ COG velocity. We found that

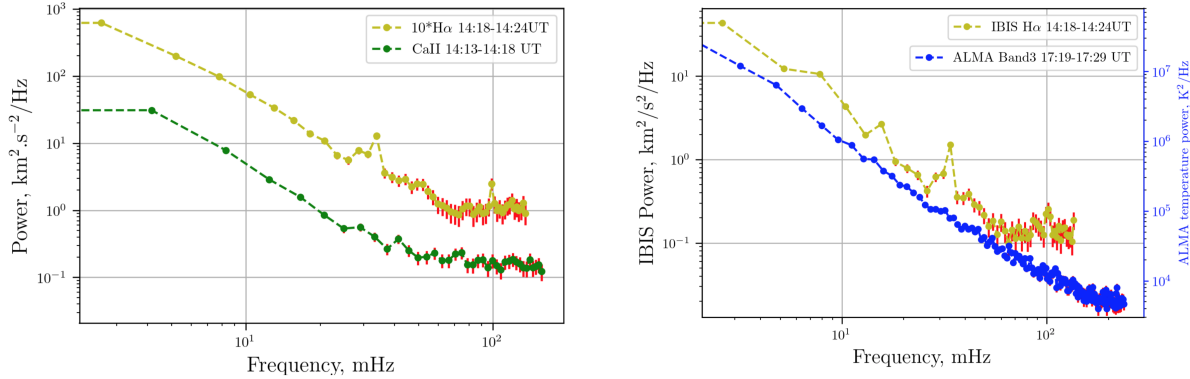


Figure 7.2: Power spectrum of the $H\alpha$ line exhibits a peak at about 30 mHz. It was observed in the IBIS dataset taken on the 23 April 2017. Left panel: Comparison for the COG velocity observed in $H\alpha$ and in the Ca II IR lines. Note that the $H\alpha$ velocity was scaled up with a factor of 10 for clarity. Right Panel: Same as left panel, but for the $H\alpha$ COG velocity and millimeter (3.0 mm) brightness temperature for the same region.

the peak is persistently found in the internetwork region with about the same amplitude throughout the FOV. It was not clearly seen in the other observed diagnostics that day. Careful analysis of the systematics (sampling, windowing function, seeing-induced signatures) did not reveal a clear origin of this peak, which was not seen in the Ca II IR line or the Na I D_1 line obtained contemporaneously with the same instrument.

Similar high frequency peaks were seen in the data presented by (Jess et al., 2019) in their sunspot observations in the He II 1083 nm line. However, in our case we observe these peaks only in the non-magnetic chromosphere in a diagnostic requiring a rather complicated interpretation framework. To confirm our findings, I have an accepted observing proposal with the Goode Solar Telescope in the Big Bear Solar Observatory to obtain new observations as a test. However, the observations to be taken with the FISS slit spectrograph, which will deliver a rather different data product than IBIS. We hope the VTF instrument on the DKIST will provide the further conclusive evidence and explanation for this curious temporal feature.

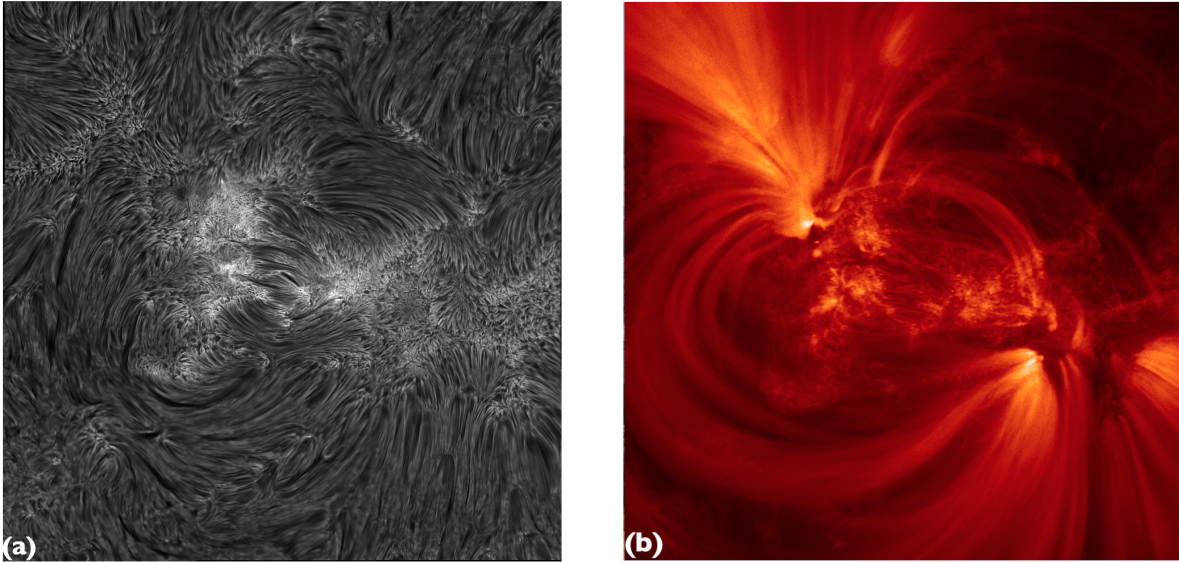


Figure 7.3: Comparison of the Hi-C 2.1 FOV in $H\alpha$ intensity observed with IBIS at the DST (left panel (a)) and the Hi-C 2.1 data in 17.2 nm (right panel (b)). The similarity in the AR “moss” observed in both $H\alpha$ and in the 17.2 nm is evident. Note that the images are not completely identical and have slightly different plate scales.

7.2.3 Hi-C 2.1 coordination: Observing the chromosphere and corona in high-resolution

The High-Resolution Coronal Imager 2.1 (Hi-C 2.1) is a sounding rocket experiment that observed active region AR 12712 in unprecedented spatial resolution ($0.25''$) in a UV passband centered on 17.2 nm (Rachmeler et al., 2019). The author co-observed at the Dunn Solar Telescope (DST) in New Mexico before and during the launch of the Hi-C 2.1 rocket. The coordinated observations consist of a cotemporal spectral dataset with similar spatial and temporal resolution in the chromospheric diagnostics of Hydrogen Balmer- α ($H\alpha$), Ca II 854.2 nm and full Stokes scans with the FIRS instrument in the He I 1083.0 nm line. The IBIS data are fully reduced and a comparison with the Hi-C 2.1 data is presented in Figure 7.3. Previously, this coordinated dataset was used to study the chromospheric counterparts of minifilament eruptions (Sterling et al., 2020).

I plan to use the combined Hi-C 2.1, IBIS, FIRS (Jaeggli et al., 2010), and IRIS data set

to look for propagating disturbances from the chromosphere into the corona and vice versa with unprecedented spatial and temporal resolution. We will employ wavelet analysis to determine if chromospheric regions at the footpoints of active region loops show significant velocity and intensity fluctuations and if these fluctuations are associated with enhanced coronal loop dynamics. I plan to study the temporal delay between disturbances at different heights, which this unique panchromatic dataset allows. This will shed light on the chromosphere-corona relationship and how magneto-acoustic waves affect the properties of coronal loops.

Bibliography

- V. Abbasvand, M. Sobotka, P. Heinzel, M. García-Rivas, C. Denker, H. Balthasar, M. Verma, I. Kontogiannis, J. Koza, D. Korda, and C. Kuckein. Observational study of chromospheric heating by acoustic waves. *A&A*, 642:A52, October 2020a. doi: 10.1051/0004-6361/202038559.
- V. Abbasvand, M. Sobotka, Petr Heinzel, Michal Švanda, Jan Jurčák, Dario del Moro, and Francesco Berrilli. Chromospheric Heating by Acoustic Waves Compared to Radiative Cooling. II. Revised Grid of Models. *ApJ*, 890(1):22, February 2020b. doi: 10.3847/1538-4357/ab665f.
- V. Abbasvand, M. Sobotka, M. Švanda, P. Heinzel, W. Liu, and L. Mravcová. IRIS observations of chromospheric heating by acoustic waves in solar quiet and active regions. *A&A*, 648:A28, April 2021. doi: 10.1051/0004-6361/202140344.
- William P. Abbett and Suzanne L. Hawley. Dynamic Models of Optical Emission in Impulsive Solar Flares. *ApJ*, 521(2):906–919, August 1999. doi: 10.1086/307576.
- H. Alfvén. Existence of Electromagnetic-Hydrodynamic Waves. *Nature*, 150(3805):405–406, October 1942. doi: 10.1038/150405d0.
- H. Alfvén. Magneto hydrodynamic waves, and the heating of the solar corona. *MNRAS*, 107:211, January 1947. doi: 10.1093/mnras/107.2.211.
- C. E. Alissandrakis, T. S. Bastian, and A. Nindos. A first look at the submillimeter Sun with ALMA. *A&A*, 661:L4, May 2022. doi: 10.1051/0004-6361/202243774.
- Joel C. Allred, Suzanne L. Hawley, William P. Abbett, and Mats Carlsson. Radiative Hydrodynamic Models of the Optical and Ultraviolet Emission from Solar Flares. *ApJ*, 630(1):573–586, Sep 2005. doi: 10.1086/431751.
- Joel C. Allred, Adam F. Kowalski, and Mats Carlsson. A Unified Computational Model for Solar and Stellar Flares. *ApJ*, 809(1):104, Aug 2015. doi: 10.1088/0004-637X/809/1/104.
- Tetsu Anan, Thomas A. Schad, Reizaburo Kitai, Gabriel I. Dima, Sarah A. Jaeggli, Lucas A. Tarr, Manuel Collados, Carlos Dominguez-Tagle, and Lucia Kleint. Measurements of Photospheric and Chromospheric Magnetic Field Structures Associated with Chromospheric Heating over a Solar Plage Region. *ApJ*, 921(1):39, November 2021. doi: 10.3847/1538-4357/ac1b9c.
- Markus J. Aschwanden. *New Millennium Solar Physics*, volume 458. Springer Nature Switzerland AG, 2019. doi: 10.1007/978-3-030-13956-8.

- R. G. Athay. *The solar chromosphere and corona: Quiet sun*, volume 53. Dordrecht: Reidel, 1976. doi: 10.1007/978-94-010-1715-2.
- R. G. Athay and O. R. White. Chromospheric and coronal heating by sound waves. *ApJ*, 226: 1135–1139, December 1978. doi: 10.1086/156690.
- L. Auer. Acceleration of Convergence. In Lucio Crivellari, I. Hubeny, and D. G. Hummer, editors, *Stellar Atmospheres - Beyond Classical Models*, volume 341 of *NATO Advanced Study Institute (ASI) Series C*, page 9, January 1991.
- T. S. Bastian, G. Chintzoglou, B. De Pontieu, M. Shimojo, D. Schmit, J. Leenaarts, and M. Loukitcheva. A First Comparison of Millimeter Continuum and Mg II Ultraviolet Line Emission from the Solar Chromosphere. *ApJ*, 845:L19, August 2017. doi: 10.3847/2041-8213/aa844c.
- N. Bello González, M. Flores Soriano, F. Kneer, and O. Okunev. Acoustic waves in the solar atmosphere at high spatial resolution. *A&A*, 508(2):941–950, Dec 2009. doi: 10.1051/0004-6361/200912275.
- N. Bello González, M. Franz, V. Martínez Pillet, J. A. Bonet, S. K. Solanki, J. C. del Toro Iniesta, W. Schmidt, A. Gandorfer, V. Domingo, P. Barthol, T. Berkefeld, and M. Knölker. Detection of Large Acoustic Energy Flux in the Solar Atmosphere. *ApJ*, 723(2):L134–L138, Nov 2010. doi: 10.1088/2041-8205/723/2/L134.
- Maria Bergemann, Andrew J. Gallagher, Philipp Eitner, Manuel Bautista, Remo Collet, Svetlana A. Yakovleva, Anja Mayriedl, Bertrand Plez, Mats Carlsson, Jorrit Leenaarts, Andrey K. Belyaev, and Camilla Hansen. Observational constraints on the origin of the elements. I. 3D NLTE formation of Mn lines in late-type stars. *A&A*, 631:A80, November 2019. doi: 10.1051/0004-6361/201935811.
- L. Biermann. Zur Deutung der chromosphärischen Turbulenz und des Exzesses der UV-Strahlung der Sonne. *Naturwissenschaften*, 33(4):118–119, August 1946. doi: 10.1007/BF00738265.
- R. Brajša, D. Sudar, A. O. Benz, I. Skokić, M. Bárta, B. De Pontieu, S. Kim, A. Kobelski, M. Kuhar, M. Shimojo, S. Wedemeyer, S. White, P. Yagoubov, and Y. Yan. First analysis of solar structures in 1.21 mm full-disc ALMA image of the Sun. *A&A*, 613:A17, May 2018. doi: 10.1051/0004-6361/201730656.
- R. J. Bray and R. E. Loughhead. *The solar chromosphere*. Chapman and Hall, London, 1974.
- P. S. Cally and M. Goossens. Three-Dimensional MHD Wave Propagation and Conversion to Alfvén Waves near the Solar Surface. I. Direct Numerical Solution. *Sol. Phys.*, 251(1-2):251–265, September 2008. doi: 10.1007/s11207-007-9086-3.
- M. Carlsson and J. Leenaarts. Approximations for radiative cooling and heating in the solar chromosphere. *A&A*, 539:A39, March 2012. doi: 10.1051/0004-6361/201118366.
- M. Carlsson and R. F. Stein. Dynamic Hydrogen Ionization. *ApJ*, 572(1):626–635, June 2002. doi: 10.1086/340293.
- M. Carlsson, V. H. Hansteen, B. V. Gudiksen, J. Leenaarts, and B. De Pontieu. A publicly available simulation of an enhanced network region of the Sun. *A&A*, 585:A4, January 2016. doi: 10.1051/0004-6361/201527226.

- Mats Carlsson and Robert F. Stein. Non-LTE Radiating Acoustic Shocks and CA II K2V Bright Points. *ApJ*, 397:L59, Sep 1992. doi: 10.1086/186544.
- Mats Carlsson and Robert F. Stein. Does a Nonmagnetic Solar Chromosphere Exist? *ApJ*, 440:L29, February 1995. doi: 10.1086/187753.
- Mats Carlsson and Robert F. Stein. Formation of Solar Calcium H and K Bright Grains. *ApJ*, 481(1):500–514, May 1997. doi: 10.1086/304043.
- Mats Carlsson, Viggo H. Hansteen, Bart de Pontieu, Scott McIntosh, Theodore D. Tarbell, Dick Shine, Saku Tsuneta, Yukio Katsukawa, Kiyoshi Ichimoto, Yoshinori Suematsu, Toshifumi Shimizu, and Shin'ichi Nagata. Can High Frequency Acoustic Waves Heat the Quiet Sun Chromosphere? *PASJ*, 59:S663, November 2007. doi: 10.1093/pasj/59.sp3.S663.
- Mats Carlsson, Bart De Pontieu, and Viggo H. Hansteen. New View of the Solar Chromosphere. *ARA&A*, 57:189–226, August 2019. doi: 10.1146/annurev-astro-081817-052044.
- G. Cauzzi, K. Reardon, R. J. Rutten, A. Tritschler, and H. Uitenbroek. The solar chromosphere at high resolution with IBIS. IV. Dual-line evidence of heating in chromospheric network. *A&A*, 503(2):577–587, Aug 2009. doi: 10.1051/0004-6361/200811595.
- F. Cavallini. IBIS: A New Post-Focus Instrument for Solar Imaging Spectroscopy. *Sol. Phys.*, 236(2):415–439, July 2006. doi: 10.1007/s11207-006-0103-8.
- Rebecca Centeno, Manuel Collados, and Javier Trujillo Bueno. Spectropolarimetric Investigation of the Propagation of Magnetoacoustic Waves and Shock Formation in Sunspot Atmospheres. *ApJ*, 640(2):1153–1162, April 2006. doi: 10.1086/500185.
- Yi Chai, Dale E. Gary, Kevin P. Reardon, and Vasyl Yurchyshyn. A Study of Sunspot 3 Minute Oscillations Using ALMA and GST. *ApJ*, 924(2):100, January 2022. doi: 10.3847/1538-4357/ac34f7.
- G. G. Cillié and D. H. Menzel. The Physical State of the Solar Chromosphere. *Harvard College Observatory Circular*, 410:1–40, October 1935.
- S. Cranmer and S. Saar. Testing a Predictive Theoretical Model for the Mass Loss Rates of Cool Stars. *ApJ*, 741(1):54, November 2011. doi: 10.1088/0004-637X/741/1/54.
- S. R. Cranmer and A. A. van Ballegoijen. On the Generation, Propagation, and Reflection of Alfvén Waves from the Solar Photosphere to the Distant Heliosphere. *ApJS*, 156(2):265–293, February 2005. doi: 10.1086/426507.
- Steven R. Cranmer, Adriaan A. van Ballegoijen, and Richard J. Edgar. Self-consistent Coronal Heating and Solar Wind Acceleration from Anisotropic Magnetohydrodynamic Turbulence. *ApJS*, 171(2):520–551, August 2007. doi: 10.1086/518001.
- M. Cuntz, W. Rammacher, and Z. E. Musielak. Acoustic Heating of the Solar Chromosphere: Present Indeed and Locally Dominant. *ApJ*, 657(1):L57–L60, March 2007. doi: 10.1086/512973.
- J. M. da Silva Santos, J. de la Cruz Rodríguez, and J. Leenaarts. Temperature constraints from inversions of synthetic solar optical, UV, and radio spectra. *A&A*, 620:A124, December 2018. doi: 10.1051/0004-6361/201833664.

- J. M. da Silva Santos, J. de la Cruz Rodríguez, S. M. White, J. Leenaarts, G. J. M. Vissers, and V. H. Hansteen. ALMA observations of transient heating in a solar active region. *A&A*, 643:A41, November 2020. doi: 10.1051/0004-6361/202038755.
- J. M. da Silva Santos, S. Danilovic, J. Leenaarts, J. de la Cruz Rodríguez, X. Zhu, S. M. White, G. J. M. Vissers, and M. Rempel. Heating of the solar chromosphere through current dissipation. *A&A*, 661:A59, May 2022. doi: 10.1051/0004-6361/202243191.
- J. de la Cruz Rodríguez, J. Leenaarts, S. Danilovic, and H. Uitenbroek. STiC: A multiatom non-LTE PRD inversion code for full-Stokes solar observations. *A&A*, 623:A74, March 2019. doi: 10.1051/0004-6361/201834464.
- B. de Pontieu. Correlated Intensity Oscillations in the Upper Chromosphere and Upper Transition Region above Active Region Plage. In H. Lacoste, editor, *SOHO 13 Waves, Oscillations and Small-Scale Transients Events in the Solar Atmosphere: Joint View from SOHO and TRACE*, volume 547 of *ESA Special Publication*, page 25, January 2004.
- B. De Pontieu, S. W. McIntosh, M. Carlsson, V. H. Hansteen, T. D. Tarbell, C. J. Schrijver, A. M. Title, R. A. Shine, S. Tsuneta, Y. Katsukawa, K. Ichimoto, Y. Suematsu, T. Shimizu, and S. Nagata. Chromospheric Alfvénic Waves Strong Enough to Power the Solar Wind. *Science*, 318(5856):1574, December 2007. doi: 10.1126/science.1151747.
- B. De Pontieu, A. M. Title, J. R. Lemen, G. D. Kushner, D. J. Akin, B. Allard, T. Berger, P. Boerner, M. Cheung, C. Chou, J. F. Drake, D. W. Duncan, S. Freeland, G. F. Heyman, C. Hoffman, N. E. Hurlburt, R. W. Lindgren, D. Mathur, R. Rehse, D. Sabolish, R. Seguin, C. J. Schrijver, T. D. Tarbell, J.-P. Wülser, C. J. Wolfson, C. Yanari, J. Mudge, N. Nguyen-Phuc, R. Timmons, R. van Bezooijen, I. Weingrod, R. Brookner, G. Butcher, B. Dougherty, J. Eder, V. Knagenhjelm, S. Larsen, D. Mansir, L. Phan, P. Boyle, P. N. Cheimets, E. E. DeLuca, L. Golub, R. Gates, E. Hertz, S. McKillop, S. Park, T. Perry, W. A. Podgorski, K. Reeves, S. Saar, P. Testa, H. Tian, M. Weber, C. Dunn, S. Eccles, S. A. Jaeggli, C. C. Kankelborg, K. Mashburn, N. Pust, L. Springer, R. Carvalho, L. Kleint, J. Marmie, E. Mazmanian, T. M. D. Pereira, S. Sawyer, J. Strong, S. P. Worden, M. Carlsson, V. H. Hansteen, J. Leenaarts, M. Wiesmann, J. Aloise, K.-C. Chu, R. I. Bush, P. H. Scherrer, P. Brekke, J. Martinez-Sykora, B. W. Lites, S. W. McIntosh, H. Uitenbroek, T. J. Okamoto, M. A. Gummin, G. Auken, P. Jerram, P. Pool, and N. Waltham. The Interface Region Imaging Spectrograph (IRIS). *Sol. Phys.*, 289(7):2733–2779, July 2014. doi: 10.1007/s11207-014-0485-y.
- Bart De Pontieu, Juan Martínez-Sykora, and Georgios Chintzoglou. What Causes the High Apparent Speeds in Chromospheric and Transition Region Spicules on the Sun? *ApJ*, 849(1):L7, November 2017. doi: 10.3847/2041-8213/aa9272.
- F. L. Deubner and B. Fleck. Dynamics of the solar atmosphere. I - Spatio-temporal analysis of waves in the quiet solar atmosphere. *A&A*, 213(1-2):423–428, April 1989.
- C. J. Díaz Baso, J. de la Cruz Rodríguez, and J. Leenaarts. An observationally constrained model of strong magnetic reconnection in the solar chromosphere. Atmospheric stratification and estimates of heating rates. *A&A*, 647:A188, March 2021. doi: 10.1051/0004-6361/202040111.
- J. G. Doyle, L. Teriaca, and D. Banerjee. Solar transition region line broadening: Limb to limb measurements. *A&A*, 356:335–338, April 2000.

- R. B. Dunn and R. N. Smartt. High resolution telescopes at the National Solar Observatory. *Advances in Space Research*, 11:139–148, 1991. doi: 10.1016/0273-1177(91)90371-P.
- Richard B. Dunn. An evacuated tower telescope. *Appl. Opt.*, 3(12):1353, Dec 1964. doi: 10.1364/AO.3.001353.
- Henrik Eklund, Sven Wedemeyer, Mikolaj Szydlarski, Shahin Jafarzadeh, and Juan Camilo Guevara Gómez. The Sun at millimeter wavelengths. II. Small-scale dynamic events in ALMA Band 3. *A&A*, 644:A152, December 2020. doi: 10.1051/0004-6361/202038250.
- Henrik Eklund, Sven Wedemeyer, Ben Snow, David B. Jess, Shahin Jafarzadeh, Samuel D. T. Grant, Mats Carlsson, and Mikolaj Szydlarski. Characterization of shock wave signatures at millimetre wavelengths from Bifrost simulations. *Philosophical Transactions of the Royal Society of London Series A*, 379(2190):20200185, February 2021. doi: 10.1098/rsta.2020.0185.
- R. Erdelyi, J. G. Doyle, M. E. Perez, and K. Wilhelm. Center-to-limb line width measurements of solar chromospheric, transition region and coronal lines. *A&A*, 337:287–293, September 1998.
- T. Felipe, E. Khomenko, and M. Collados. Magneto-acoustic Waves in Sunspots: First Results From a New Three-dimensional Nonlinear Magnetohydrodynamic Code. *ApJ*, 719(1):357–377, August 2010. doi: 10.1088/0004-637X/719/1/357.
- B. Fleck, M. Carlsson, E. Khomenko, M. Rempel, O. Steiner, and G. Vigeesh. Acoustic-gravity wave propagation characteristics in three-dimensional radiation hydrodynamic simulations of the solar atmosphere. *Philosophical Transactions of the Royal Society of London Series A*, 379(2190):20200170, February 2021. doi: 10.1098/rsta.2020.0170.
- J. M. Fontenla, E. H. Avrett, and R. Loeser. Energy Balance in the Solar Transition Region. I. Hydrostatic Thermal Models with Ambipolar Diffusion. *ApJ*, 355:700, June 1990. doi: 10.1086/168803.
- J. M. Fontenla, E. H. Avrett, and R. Loeser. Energy balance in the solar transition region. III - Helium emission in hydrostatic, constant-abundance models with diffusion. *ApJ*, 406:319–345, March 1993. doi: 10.1086/172443.
- J. M. Fontenla, J. Harder, W. Livingston, M. Snow, and T. Woods. High-resolution solar spectral irradiance from extreme ultraviolet to far infrared. *Journal of Geophysical Research (Atmospheres)*, 116(15):D20108, October 2011. doi: 10.1029/2011JD016032.
- Astrid Fossum and Mats Carlsson. High-frequency acoustic waves are not sufficient to heat the solar chromosphere. *Nature*, 435(7044):919–921, Jun 2005. doi: 10.1038/nature03695.
- Astrid Fossum and Mats Carlsson. Determination of the Acoustic Wave Flux in the Lower Solar Chromosphere. *ApJ*, 646(1):579–592, Jul 2006. doi: 10.1086/504887.
- R. G. Giovanelli. A Theory of Chromospheric Flares. *Nature*, 158(4003):81–82, July 1946. doi: 10.1038/158081a0.
- Daniel O. Gomez, Pablo A. Dmitruk, and Leonardo J. Milano. Recent theoretical results on coronal heating. *Sol. Phys.*, 195(2):299–318, August 2000. doi: 10.1023/A:1005283923956.

- B. V. Gudiksen, M. Carlsson, V. H. Hansteen, W. Hayek, J. Leenaarts, and J. Martínez-Sykora. The stellar atmosphere simulation code Bifrost. Code description and validation. *A&A*, 531:A154, July 2011. doi: 10.1051/0004-6361/201116520.
- B. N. Handy, L. W. Acton, C. C. Kankelborg, C. J. Wolfson, D. J. Akin, M. E. Bruner, R. Carvalho, R. C. Catura, R. Chevalier, D. W. Duncan, C. G. Edwards, C. N. Feinstein, S. L. Freeland, F. M. Friedlaender, C. H. Hoffmann, N. E. Hurlburt, B. K. Jurcevich, N. L. Katz, G. A. Kelly, J. R. Lemen, M. Levay, R. W. Lindgren, D. P. Mathur, S. B. Meyer, S. J. Morrison, M. D. Morrison, R. W. Nightingale, T. P. Pope, R. A. Rehse, C. J. Schrijver, R. A. Shine, L. Shing, K. T. Strong, T. D. Tarbell, A. M. Title, D. D. Torgerson, L. Golub, J. A. Bookbinder, D. Caldwell, P. N. Cheimets, W. N. Davis, E. E. Deluca, R. A. McMullen, H. P. Warren, D. Amato, R. Fisher, H. Maldonado, and C. Parkinson. The transition region and coronal explorer. *Sol. Phys.*, 187(2):229–260, July 1999. doi: 10.1023/A:1005166902804.
- V. Hansteen, A. Ortiz, V. Archontis, M. Carlsson, T. M. D. Pereira, and J. P. Bjørgen. Ellerman bombs and UV bursts: transient events in chromospheric current sheets. *A&A*, 626:A33, June 2019. doi: 10.1051/0004-6361/201935376.
- V. H. Hansteen, R. Betta, and M. Carlsson. Rapid intensity and velocity variations in solar transition region lines. *A&A*, 360:742–760, August 2000.
- V. H. Hansteen, V. Archontis, T. M. D. Pereira, M. Carlsson, L. Rouppe van der Voort, and J. Leenaarts. Bombs and Flares at the Surface and Lower Atmosphere of the Sun. *ApJ*, 839(1):22, April 2017. doi: 10.3847/1538-4357/aa6844.
- P. Heinzel. Review of 1d semiempirical model atmospheres. *Advances in Solar Research at Eclipses from Ground and from Space, Proceedings of the NATO Advanced Study*, 558:201–220, 2000. doi: 10.1007/978-94-011-4325-7_10.
- Ryan Hofmann, Kevin Reardon, Ivan Milic, Momchil Molnar, Yi Chai, and Han Uitenbroek. Evaluating Non-LTE Spectral Inversions with ALMA and IBIS. *arXiv e-prints*, art. arXiv:2205.08760, May 2022.
- J. V. Hollweg. Transition region, corona, and solar wind in coronal holes. *J. Geophys. Res.*, 91(A4):4111–4125, April 1986. doi: 10.1029/JA091iA04p04111.
- Murshed Hossain, Perry C. Gray, Jr. Pontius, Duane H., William H. Matthaeus, and Sean Oughton. Phenomenology for the decay of energy-containing eddies in homogeneous MHD turbulence. *Physics of Fluids*, 7(11):2886–2904, November 1995. doi: 10.1063/1.868665.
- I. Hubeny. Accelerated Lambda Iteration: An Overview. In Ivan Hubeny, Dimitri Mihalas, and Klaus Werner, editors, *Stellar Atmosphere Modeling*, volume 288 of *Astronomical Society of the Pacific Conference Series*, page 17, January 2003.
- Ivan Hubeny and Dimitri Mihalas. *Theory of Stellar Atmospheres*. Princeton University Press, 2014.
- D. E. Innes, B. Inhester, W. I. Axford, and K. Wilhelm. Bi-directional plasma jets produced by magnetic reconnection on the Sun. *Nature*, 386(6627):811–813, April 1997. doi: 10.1038/386811a0.

- Ryohko Ishikawa, Javier Trujillo Bueno, Tanausú del Pino Alemán, Takenori J. Okamoto, David E. McKenzie, Frédéric Auchère, Ryouhei Kano, Donguk Song, Masaki Yoshida, Laurel A. Rachmeler, Ken Kobayashi, Hirohisa Hara, Masahito Kubo, Noriyuki Narukage, Taro Sakao, Toshifumi Shimizu, Yoshinori Suematsu, Christian Bethge, Bart De Pontieu, Alberto Sainz Dalda, Genevieve D. Vigil, Amy Winebarger, Ernest Alsina Ballester, Luca Belluzzi, Jiří Štěpán, Andrés Asensio Ramos, Mats Carlsson, and Jorrit Leenaarts. Mapping solar magnetic fields from the photosphere to the base of the corona. *Science Advances*, 7(8):eabe8406, February 2021. doi: 10.1126/sciadv.abe8406.
- T. Isobe, E. D. Feigelson, M. G. Akritas, and G. J. Babu. Linear regression in astronomy. *ApJ*, 364:104–113, November 1990. doi: 10.1086/169390.
- S. A. Jaeggli, H. Lin, D. L. Mickey, J. R. Kuhn, S. L. Hegwer, T. R. Rimmele, and M. J. Penn. FIRS: a new instrument for photospheric and chromospheric studies at the DST. *Mem. Soc. Astron. Italiana*, 81:763, 2010.
- S. Jafarzadeh, S. Wedemeyer, B. Fleck, M. Stangalini, D. B. Jess, R. J. Morton, M. Szydlarski, V. M. J. Henriques, X. Zhu, T. Wiegmann, J. C. Guevara Gómez, S. D. T. Grant, B. Chen, K. Reardon, and S. M. White. An overall view of temperature oscillations in the solar chromosphere with ALMA. *Philosophical Transactions of the Royal Society of London Series A*, 379(2190):20200174, February 2021. doi: 10.1098/rsta.2020.0174.
- D. B. Jess, M. Mathioudakis, D. J. Christian, F. P. Keenan, R. S. I. Ryans, and P. J. Crockett. ROSA: A High-cadence, Synchronized Multi-camera Solar Imaging System. *Sol. Phys.*, 261:363–373, February 2010a. doi: 10.1007/s11207-009-9500-0.
- D. B. Jess, M. Mathioudakis, D. J. Christian, F. P. Keenan, R. S. I. Ryans, and P. J. Crockett. ROSA: A High-cadence, Synchronized Multi-camera Solar Imaging System. *Sol. Phys.*, 261(2):363–373, February 2010b. doi: 10.1007/s11207-009-9500-0.
- D. B. Jess, R. J. Morton, G. Verth, V. Fedun, S. D. T. Grant, and I. Giagkiozis. Multiwavelength Studies of MHD Waves in the Solar Chromosphere. An Overview of Recent Results. *Space Sci. Rev.*, 190(1-4):103–161, July 2015. doi: 10.1007/s11214-015-0141-3.
- David B. Jess, Ben Snow, Scott J. Houston, Gert J. J. Botha, Bernhard Fleck, S. Krishna Prasad, Andrés Asensio Ramos, Richard J. Morton, Peter H. Keys, Shahin Jafarzadeh, Marco Stangalini, Samuel D. T. Grant, and Damian J. Christian. A chromospheric resonance cavity in a sunspot mapped with seismology. *Nature Astronomy*, page 502, Dec 2019. doi: 10.1038/s41550-019-0945-2.
- Wolfgang Kalkofen, Peter Ulmschneider, and Eugene H. Avrett. Does the Sun Have a Full-Time Chromosphere? *ApJ*, 521(2):L141–L144, August 1999. doi: 10.1086/312193.
- R. Kano, J. Trujillo Bueno, A. Winebarger, F. Auchère, N. Narukage, R. Ishikawa, K. Kobayashi, T. Bando, Y. Katsukawa, M. Kubo, S. Ishikawa, G. Giono, H. Hara, Y. Suematsu, T. Shimizu, T. Sakao, S. Tsuneta, K. Ichimoto, M. Goto, L. Belluzzi, J. Štěpán, A. Asensio Ramos, R. Manso Sainz, P. Champney, J. Cirtain, B. De Pontieu, R. Casini, and M. Carlsson. Discovery of Scattering Polarization in the Hydrogen Ly α Line of the Solar Disk Radiation. *ApJ*, 839(1):L10, April 2017. doi: 10.3847/2041-8213/aa697f.

- Ryouhei Kano, Takamasa Bando, Noriyuki Narukage, Ryoko Ishikawa, Saku Tsuneta, Yukio Katsukawa, Masahito Kubo, Shin-nosuke Ishikawa, Hirohisa Hara, Toshifumi Shimizu, Yoshinori Suematsu, Kiyoshi Ichimoto, Taro Sakao, Motoshi Goto, Yoshiaki Kato, Shinsuke Imada, Ken Kobayashi, Todd Holloway, Amy Winebarger, Jonathan Cirtain, Bart De Pontieu, Roberto Casini, Javier Trujillo Bueno, Jiří Štěpán, Rafael Manso Sainz, Luca Belluzzi, Andres Asensio Ramos, Frédéric Auchère, and Mats Carlsson. Chromospheric Lyman-alpha spectro-polarimeter (CLASP). In Tadayuki Takahashi, Stephen S. Murray, and Jan-Willem A. den Herder, editors, *Space Telescopes and Instrumentation 2012: Ultraviolet to Gamma Ray*, volume 8443 of *Society of Photo-Optical Instrumentation Engineers (SPIE) Conference Series*, page 84434F, September 2012. doi: 10.1117/12.925991.
- P. Kayshap, K. Murawski, A. K. Srivastava, Z. E. Musielak, and B. N. Dwivedi. Vertical propagation of acoustic waves in the solar internetwork as observed by IRIS. *MNRAS*, 479(4):5512–5521, October 2018. doi: 10.1093/mnras/sty1861.
- F. Kneer and N. Bello González. On acoustic and gravity waves in the solar photosphere and their energy transport. *A&A*, 532:A111, Aug 2011. doi: 10.1051/0004-6361/201116537.
- M. Koschinsky, F. Kneer, and J. Hirzberger. Speckle spectro-polarimetry of solar magnetic structures. *A&A*, 365:588–597, January 2001. doi: 10.1051/0004-6361:20000478.
- T. Kosugi, K. Matsuzaki, T. Sakao, T. Shimizu, Y. Sone, S. Tachikawa, T. Hashimoto, K. Minesugi, A. Ohnishi, T. Yamada, S. Tsuneta, H. Hara, K. Ichimoto, Y. Suematsu, M. Shimojo, T. Watanabe, S. Shimada, J. M. Davis, L. D. Hill, J. K. Owens, A. M. Title, J. L. Culhane, L. K. Harra, G. A. Doschek, and L. Golub. The Hinode (Solar-B) Mission: An Overview. *Sol. Phys.*, 243:3–17, June 2007. doi: 10.1007/s11207-007-9014-6.
- Adam F. Kowalski, S. L. Hawley, M. Carlsson, J. C. Allred, H. Uitenbroek, R. A. Osten, and G. Holman. New Insights into White-Light Flare Emission from Radiative-Hydrodynamic Modeling of a Chromospheric Condensation. *Sol. Phys.*, 290(12):3487–3523, December 2015. doi: 10.1007/s11207-015-0708-x.
- Mukul R. Kundu. *Solar radio astronomy*. New York and London: Interscience Publishers, a Division of John Wiley and Sons, 1965.
- Max Kuperus, James A. Ionson, and Daniel S. Spicer. On the theory of coronal heating mechanisms. *Annual Review of Astronomy and Astrophysics*, 19(1):7–40, 1981. ISSN 0066-4146. doi: 10.1146/annurev.aa.19.090181.000255.
- J. Leenaarts and M. Carlsson. MULTI3D: A Domain-Decomposed 3D Radiative Transfer Code. In B. Lites, M. Cheung, T. Magara, J. Mariska, and K. Reeves, editors, *The Second Hinode Science Meeting: Beyond Discovery-Toward Understanding*, volume 415 of *Astronomical Society of the Pacific Conference Series*, page 87, December 2009.
- J. Leenaarts, M. Carlsson, V. Hansteen, and L. Rouppe van der Voort. Three-Dimensional Non-LTE Radiative Transfer Computation of the CA 8542 Infrared Line From a Radiation-MHD Simulation. *ApJ*, 694:L128–L131, April 2009. doi: 10.1088/0004-637X/694/2/L128.
- J. Leenaarts, R. J. Rutten, K. Reardon, M. Carlsson, and V. Hansteen. The Quiet Solar Atmosphere Observed and Simulated in Na I D₁. *ApJ*, 709(2):1362–1373, February 2010. doi: 10.1088/0004-637X/709/2/1362.

- J. Leenaarts, M. Carlsson, and L. Rouppe van der Voort. The Formation of the H α Line in the Solar Chromosphere. *ApJ*, 749:136, April 2012a. doi: 10.1088/0004-637X/749/2/136.
- J. Leenaarts, T. Pereira, and H. Uitenbroek. Fast approximation of angle-dependent partial redistribution in moving atmospheres. *A&A*, 543:A109, July 2012b. doi: 10.1051/0004-6361/201219394.
- J. Leenaarts, T. M. D. Pereira, M. Carlsson, H. Uitenbroek, and B. De Pontieu. The Formation of IRIS Diagnostics. II. The Formation of the Mg II h&k Lines in the Solar Atmosphere. *ApJ*, 772(2):90, August 2013. doi: 10.1088/0004-637X/772/2/90.
- Jorrit Leenaarts. Radiation hydrodynamics in simulations of the solar atmosphere. *Living Reviews in Solar Physics*, 17(1):3, March 2020. doi: 10.1007/s41116-020-0024-x.
- R. B. Leighton. Observational studies of the solar granulation. In Richard Nelson Thomas, editor, *Aerodynamic Phenomena in Stellar Atmospheres*, volume 12, pages 321–325, January 1960.
- J. R. Lemen, A. M. Title, D. J. Akin, P. F. Boerner, C. Chou, J. F. Drake, D. W. Duncan, C. G. Edwards, F. M. Friedlaender, G. F. Heyman, N. E. Hurlburt, N. L. Katz, G. D. Kushner, M. Levay, R. W. Lindgren, D. P. Mathur, E. L. McFeaters, S. Mitchell, R. A. Rehse, C. J. Schrijver, L. A. Springer, R. A. Stern, T. D. Tarbell, J.-P. Wuelser, C. J. Wolfson, C. Yanari, J. A. Bookbinder, P. N. Cheimets, D. Caldwell, E. E. Deluca, R. Gates, L. Golub, S. Park, W. A. Podgorski, R. I. Bush, P. H. Scherrer, M. A. Gummin, P. Smith, G. Aufer, P. Jerram, P. Pool, R. Soufli, D. L. Windt, S. Beardsley, M. Clapp, J. Lang, and N. Waltham. The Atmospheric Imaging Assembly (AIA) on the Solar Dynamics Observatory (SDO). *Sol. Phys.*, 275:17–40, January 2012. doi: 10.1007/s11207-011-9776-8.
- M. J. Lighthill. On Sound Generated Aerodynamically. I. General Theory. *Proceedings of the Royal Society of London Series A*, 211(1107):564–587, March 1952. doi: 10.1098/rspa.1952.0060.
- M. J. Lighthill. Predictions on the Velocity Field Coming from Acoustic Noise and a Generalized Turbulence in a Layer Overlying a Convectively Unstable Atmospheric Region. In Richard Nelson Thomas, editor, *Aerodynamic Phenomena in Stellar Atmospheres*, volume 28, page 429, January 1967.
- C. Lindsey, G. Kopp, T. A. Clark, and G. Watt. The Sun in Submillimeter and Near-Millimeter Radiation. *ApJ*, 453:511, November 1995. doi: 10.1086/176412.
- Jeffrey L. Linsky. Stellar Model Chromospheres and Spectroscopic Diagnostics. *ARA&A*, 55(1):159–211, August 2017. doi: 10.1146/annurev-astro-091916-055327.
- Rohan E. Louis, Avijeet Prasad, Christian Beck, Debi P. Choudhary, and Mehmet S. Yalim. Heating of the solar chromosphere in a sunspot light bridge by electric currents. *A&A*, 652:L4, August 2021. doi: 10.1051/0004-6361/202141456.
- M. Loukitcheva, S. K. Solanki, M. Carlsson, and R. F. Stein. Millimeter observations and chromospheric dynamics. *A&A*, 419:747–756, May 2004. doi: 10.1051/0004-6361:20034159.
- M. Loukitcheva, S. K. Solanki, and S. White. The dynamics of the solar chromosphere: comparison of model predictions with millimeter-interferometer observations. *A&A*, 456(2):713–723, September 2006. doi: 10.1051/0004-6361:20053171.

- M. Loukitcheva, S. K. Solanki, and S. M. White. The relationship between chromospheric emissions and magnetic field strength. *A&A*, 497(1):273–285, April 2009. doi: 10.1051/0004-6361/200811133.
- M. Loukitcheva, S. K. Solanki, M. Carlsson, and S. M. White. Millimeter radiation from a 3D model of the solar atmosphere. I. Diagnosing chromospheric thermal structure. *A&A*, 575:A15, March 2015. doi: 10.1051/0004-6361/201425238.
- M. Loukitcheva, K. Iwai, S. K. Solanki, S. M. White, and M. Shimojo. Solar ALMA Observations: Constraining the Chromosphere above Sunspots. *ApJ*, 850:35, November 2017. doi: 10.3847/1538-4357/aa91cc.
- Maria A. Loukitcheva, Stephen M. White, and Sami K. Solanki. ALMA Detection of Dark Chromospheric Holes in the Quiet Sun. *ApJ*, 877(2):L26, Jun 2019. doi: 10.3847/2041-8213/ab2191.
- J. T. Mariska. *The Solar Transition Region*. Cambridge University Press, 1992.
- J. Martínez-Sykora, B. De Pontieu, V. H. Hansteen, L. Rouppe van der Voort, M. Carlsson, and T. M. D. Pereira. On the generation of solar spicules and Alfvénic waves. *Science*, 356(6344):1269–1272, June 2017. doi: 10.1126/science.aah5412.
- Juan Martínez-Sykora, Bart De Pontieu, Jaime de la Cruz Rodriguez, and Georgios Chintzoglou. The Formation Height of Millimeter-wavelength Emission in the Solar Chromosphere. *ApJ*, 891(1):L8, March 2020a. doi: 10.3847/2041-8213/ab75ac.
- Juan Martínez-Sykora, Mikolaj Szydlarski, Viggo H. Hansteen, and Bart De Pontieu. On the Velocity Drift between Ions in the Solar Atmosphere. *ApJ*, 900(2):101, September 2020b. doi: 10.3847/1538-4357/ababa3.
- W. H. Matthaeus, G. P. Zank, S. Oughton, D. J. Mullan, and P. Dmitruk. Coronal Heating by Magnetohydrodynamic Turbulence Driven by Reflected Low-Frequency Waves. *ApJ*, 523(1):L93–L96, September 1999. doi: 10.1086/312259.
- W. H. McCrea. The mechanics of the chromosphere. *MNRAS*, 89:718, June 1929. doi: 10.1093/mnras/89.9.718.
- S. McIntosh, B. de Pontieu, and M. Carlsson. Alfvénic waves with sufficient energy to power the quiet solar corona and fast solar wind. *Nature*, 475(7357):477–480, July 2011. doi: 10.1038/nature10235.
- N. Mein and P. Mein. Velocity waves in the quiet solar chromosphere. *Sol. Phys.*, 49(2):231–248, August 1976. doi: 10.1007/BF00162447.
- N. Mein and P. Mein. Mechanical flux in the solar chromosphere. I - Velocity and temperature weighting functions for CA II lines. *A&A*, 84(1-2):96–98, April 1980.
- N. Mein and B. Schmieder. Mechanical flux in the solar chromosphere. III - Variation of the mechanical flux. *A&A*, 97(2):310–316, April 1981.
- D. H. Menzel. Pressures at the base of the chromosphere : a critical study of Milne’s theories. *MNRAS*, 91:628–652, April 1931. doi: 10.1093/mnras/91.6.628.

- D. Mihalas and B. W. Mihalas. *Foundations of radiation hydrodynamics*. Oxford University Press, 1984.
- Dimitri Mihalas. *Stellar atmospheres*. San Francisco: W.H. Freeman, 1978.
- I. Milić and M. van Noort. Spectropolarimetric NLTE inversion code SNAPI. *A&A*, 617:A24, September 2018. doi: 10.1051/0004-6361/201833382.
- E. A. Milne. The equilibrium of the calcium chromosphere. *MNRAS*, 85:111, December 1924. doi: 10.1093/mnras/85.2.111.
- Momchil Molnar, Kevin P. Reardon, Christopher Osborne, and Ivan Milić. Spectral deconvolution with deep learning: removing the effects of spectral PSF broadening. *Frontiers in Astronomy and Space Sciences*, 7:29, June 2020. doi: 10.3389/fspas.2020.00029.
- Momchil E. Molnar, Kevin P. Reardon, Yi Chai, Dale Gary, Han Uitenbroek, Gianna Cauzzi, and Steven R. Cranmer. Solar Chromospheric Temperature Diagnostics: A Joint ALMA-H α Analysis. *ApJ*, 881(2):99, Aug 2019. doi: 10.3847/1538-4357/ab2ba3.
- Momchil E. Molnar, Kevin P. Reardon, Steven R. Cranmer, Adam F. Kowalski, Yi Chai, and Dale Gary. High-frequency Wave Power Observed in the Solar Chromosphere with IBIS and ALMA. *ApJ*, 920(2):125, October 2021. doi: 10.3847/1538-4357/ac1515.
- R. Morosin, J. de la Cruz Rodríguez, C. J. Díaz Baso, and J. Leenaarts. Spatio-temporal analysis of chromospheric heating in a plage region. *arXiv e-prints*, art. arXiv:2203.01688, March 2022.
- U. Narain and P. Ulmschneider. Chromospheric and Coronal Heating Mechanisms. *Space Sci. Rev.*, 54(3-4):377–445, December 1990. doi: 10.1007/BF00177801.
- A. Nindos, C. E. Alissandrakis, T. S. Bastian, S. Patsourakos, B. De Pontieu, H. Warren, T. Ayres, H. S. Hudson, T. Shimizu, J.-C. Vial, S. Wedemeyer, and V. Yurchyshyn. First high-resolution look at the quiet Sun with ALMA at 3mm. *A&A*, 619:L6, November 2018. doi: 10.1051/0004-6361/201834113.
- A. Nindos, C. E. Alissandrakis, S. Patsourakos, and T. S. Bastian. Transient brightenings in the quiet Sun detected by ALMA at 3 mm. *A&A*, 638:A62, June 2020. doi: 10.1051/0004-6361/202037810.
- L. J. November and G. W. Simon. Precise proper-motion measurement of solar granulation. *ApJ*, 333:427–442, October 1988. doi: 10.1086/166758.
- Robert W. Noyes and Robert B. Leighton. Velocity Fields in the Solar Atmosphere. II. The Oscillatory Field. *ApJ*, 138:631, October 1963. doi: 10.1086/147675.
- E. N. Parker. Nanoflares and the Solar X-Ray Corona. *ApJ*, 330:474, July 1988. doi: 10.1086/166485.
- S. Patsourakos, C. E. Alissandrakis, A. Nindos, and T. S. Bastian. Observations of solar chromospheric oscillations at 3 mm with ALMA. *A&A*, 634:A86, February 2020. doi: 10.1051/0004-6361/201936618.

- T. M. D. Pereira, J. Leenaarts, B. De Pontieu, M. Carlsson, and H. Uitenbroek. The Formation of IRIS Diagnostics. III. Near-ultraviolet Spectra and Images. *ApJ*, 778(2):143, December 2013. ISSN 0004-637X, 1538-4357. doi: 10.1088/0004-637X/778/2/143. arXiv: 1310.1926.
- Tiago M. D. Pereira and Han Uitenbroek. RH 1.5D: a massively parallel code for multi-level radiative transfer with partial frequency redistribution and Zeeman polarisation. *A&A*, 574:A3, February 2015. doi: 10.1051/0004-6361/201424785.
- W. D. Pesnell, B. J. Thompson, and P. C. Chamberlin. The Solar Dynamics Observatory (SDO). *Sol. Phys.*, 275:3–15, January 2012. doi: 10.1007/s11207-011-9841-3.
- H. Peter. Analysis of Transition-Region Emission-Line Profiles from Full-Disk Scans of the Sun Using the SUMER Instrument on SOHO. *ApJ*, 516(1):490–504, May 1999. doi: 10.1086/307102.
- H. Peter. What can large-scale magnetohydrodynamic numerical experiments tell us about coronal heating? *Philosophical Transactions of the Royal Society of London Series A*, 373(2042): 20150055–20150055, April 2015. doi: 10.1098/rsta.2015.0055.
- D. Petry and CASA Development Team. Analysing ALMA Data with CASA. In P. Ballester, D. Egret, and N. P. F. Lorente, editors, *Astronomical Data Analysis Software and Systems XXI*, volume 461 of *Astronomical Society of the Pacific Conference Series*, page 849, September 2012.
- N. Phillips, R. Hills, T. Bastian, H. Hudson, R. Marson, and S. Wedemeyer. Fast Single-Dish Scans of the Sun Using ALMA. In D. Iono, K. Tatematsu, A. Wootten, and L. Testi, editors, *Revolution in Astronomy with ALMA: The Third Year*, volume 499 of *Astronomical Society of the Pacific Conference Series*, page 347, December 2015.
- A. G. M. Pietrow, D. Kiselman, J. de la Cruz Rodríguez, C. J. Díaz Baso, A. Pastor Yabar, and R. Yadav. Inference of the chromospheric magnetic field configuration of solar plage using the Ca II 8542 Å line. *A&A*, 644:A43, December 2020. doi: 10.1051/0004-6361/202038750.
- D. Rabin and R. Moore. Heating the sun’s lower transition region with fine-scale electric currents. *ApJ*, 285:359–367, October 1984. doi: 10.1086/162513.
- Laurel A. Rachmeler, Amy R. Winebarger, Sabrina L. Savage, Leon Golub, Ken Kobayashi, Genevieve D. Vigil, David H. Brooks, Jonathan W. Cirtain, Bart De Pontieu, David E. McKenzie, Richard J. Morton, Hardi Peter, Paola Testa, Sanjiv K. Tiwari, Robert W. Walsh, Harry P. Warren, Caroline Alexander, Darren Ansell, Brent L. Beabout, Dyana L. Beabout, Christian W. Bethge, Patrick R. Champey, Peter N. Cheimets, Mark A. Cooper, Helen K. Creel, Richard Gates, Carlos Gomez, Anthony Guillory, Harlan Haight, William D. Hogue, and Todd Holloway. The High-Resolution Coronal Imager, Flight 2.1. *Sol. Phys.*, 294(12):174, December 2019. doi: 10.1007/s11207-019-1551-2.
- Yamini K. Rao, Giulio Del Zanna, and Helen E. Mason. The centre-to-limb variation of non-thermal velocities using IRIS Si IV. *MNRAS*, 511(1):1383–1400, February 2022. doi: 10.1093/mnras/stac128.
- K. P. Reardon and F. Cavallini. Characterization of Fabry-Perot interferometers and multi-etalon transmission profiles. The IBIS instrumental profile. *A&A*, 481:897–912, April 2008. doi: 10.1051/0004-6361:20078473.

- K. P. Reardon, F. Lepreti, V. Carbone, and A. Vecchio. Evidence of Shock-driven Turbulence in the Solar Chromosphere. *ApJ*, 683(2):L207, Aug 2008. doi: 10.1086/591790.
- M. Rempel. Extension of the MURaM Radiative MHD Code for Coronal Simulations. *ApJ*, 834(1):10, January 2017. doi: 10.3847/1538-4357/834/1/10.
- Thomas R. Rimmele. *Recent advances in solar adaptive optics*, volume 5490 of *Society of Photo-Optical Instrumentation Engineers (SPIE) Conference Series*, pages 34–46. SPIE, 2004. doi: 10.1117/12.551764.
- Thomas R. Rimmele, Kit Richards, and et al. First results from the NSO/NJIT solar adaptive optics system. In Silvano Fineschi and Mark A. Gummin, editors, *Telescopes and Instrumentation for Solar Astrophysics*, volume 5171 of *Society of Photo-Optical Instrumentation Engineers (SPIE) Conference Series*, pages 179–186, February 2004. doi: 10.1117/12.508513.
- Thomas R. Rimmele, Mark Warner, Stephen L. Keil, Philip R. Goode, Michael Knölker, Jeffrey R. Kuhn, Robert R. Rosner, Joseph P. McMullin, Roberto Casini, Haosheng Lin, Friedrich Wöger, Oskar von der Lühe, Alexandra Tritschler, Alisdair Davey, Alfred de Wijn, David F. Elmore, André Fehlmann, David M. Harrington, Sarah A. Jaeggli, Mark P. Rast, Thomas A. Schad, Wolfgang Schmidt, Mihalis Mathioudakis, Donald L. Mickey, Tetsu Anan, Christian Beck, Heather K. Marshall, Paul F. Jeffers, Jacobus M. Oschmann, Andrew Beard, David C. Berst, Bruce A. Cowan, Simon C. Craig, Eric Cross, Bryan K. Cummings, Colleen Donnelly, Jean-Benoit de Vanssay, Arthur D. Eigenbrot, Andrew Ferayorni, Christopher Foster, Chriselle Ann Galapon, Christopher Gedrites, Kerry Gonzales, Bret D. Goodrich, Brian S. Gregory, Stephanie S. Guzman, Stephen Guzzo, Steve Hegwer, Robert P. Hubbard, John R. Hubbard, Erik M. Johansson, Luke C. Johnson, Chen Liang, Mary Liang, Isaac McQuillen, Christopher Mayer, Karl Newman, Brialyn Onodera, LeEllen Phelps, Myles M. Puentes, Christopher Richards, Lukas M. Rimmele, Predrag Sekulic, Stephan R. Shimko, Brett E. Simison, Brett Smith, Erik Starman, Stacey R. Sueoka, Richard T. Summers, Aimee Szabo, Louis Szabo, Stephen B. Wampler, Timothy R. Williams, and Charles White. The Daniel K. Inouye Solar Telescope - Observatory Overview. *Sol. Phys.*, 295(12):172, December 2020. doi: 10.1007/s11207-020-01736-7.
- Bernard Roberts. *MHD Waves in the Solar Atmosphere*. Cambridge University Press, 2019. doi: 10.1017/9781108613774.
- Robert Rubinstein and Ye Zhou. Turbulent Time Correlations and Generation of Acoustic Waves by Stellar or Solar Turbulent Convection. *ApJ*, 572(1):674–678, June 2002. doi: 10.1086/340223.
- B. Ruiz Cobo, C. Quintero Noda, R. Gafeira, H. Uitenbroek, D. Orozco Suárez, and E. Páez Mañá. DeSIRe: Departure coefficient aided Stokes Inversion based on Response functions. *A&A*, 660:A37, April 2022. doi: 10.1051/0004-6361/202140877.
- R. J. Rutten. Solar H-alpha features with hot onsets. III. Long fibrils in Lyman-alpha and with ALMA. *A&A*, 598:A89, February 2017. doi: 10.1051/0004-6361/201629238.
- R. J. Rutten and H. Uitenbroek. Chromospheric backradiation in ultraviolet continua and H α . *A&A*, 540:A86, April 2012. doi: 10.1051/0004-6361/201118525.
- G. B. Rybicki and D. G. Hummer. An accelerated lambda iteration method for multilevel radiative transfer. *A&A*, 245:171–181, May 1991.

- Rayhane Sadeghi and Ehsan Tavabi. Characteristics of chromospheric oscillation periods in magnetic bright points. *MNRAS*, 512(3):4164–4170, May 2022. doi: 10.1093/mnras/stac574.
- M. N. Saha. On a Physical Theory of Stellar Spectra. *Proceedings of the Royal Society of London Series A*, 99(697):135–153, May 1921. doi: 10.1098/rspa.1921.0029.
- Evry Schatzman. The heating of the solar corona and chromosphere. *Annales d’Astrophysique*, 12: 203, January 1949.
- J. Schou, P. H. Scherrer, R. I. Bush, R. Wachter, S. Couvidat, M. C. Rabello-Soares, R. S. Bogart, J. T. Hoeksema, Y. Liu, T. L. Duvall, D. J. Akin, B. A. Allard, J. W. Miles, R. Rairden, R. A. Shine, T. D. Tarbell, A. M. Title, C. J. Wolfson, D. F. Elmore, A. A. Norton, and S. Tomczyk. Design and Ground Calibration of the Helioseismic and Magnetic Imager (HMI) Instrument on the Solar Dynamics Observatory (SDO). *Sol. Phys.*, 275(1-2):229–259, January 2012. doi: 10.1007/s11207-011-9842-2.
- H. Schunker and P. S. Cally. Magnetic field inclination and atmospheric oscillations above solar active regions. *MNRAS*, 372(2):551–564, October 2006. doi: 10.1111/j.1365-2966.2006.10855.x.
- Martin Schwarzschild. On Noise Arising from the Solar Granulation. *Astrophys. J.*, 107(1):1–5, 1948. ISSN 0004-637X. doi: 10.1086/144983.
- M. Shimojo, T. S. Bastian, A. S. Hales, and et al. White, S. M. Observing the Sun with the Atacama Large Millimeter/submillimeter Array (ALMA): High-Resolution Interferometric Imaging. *Sol. Phys.*, 292(7):87, July 2017a. doi: 10.1007/s11207-017-1095-2.
- M. Shimojo, H. S. Hudson, S. M. White, T. S. Bastian, and K. Iwai. The First ALMA Observation of a Solar Plasmoid Ejection from an X-Ray Bright Point. *ApJ*, 841:L5, May 2017b. doi: 10.3847/2041-8213/aa70e3.
- M. Sobotka, P. Heinzel, M. Švanda, J. Jurčák, D. del Moro, and F. Berrilli. Chromospheric Heating by Acoustic Waves Compared to Radiative Cooling. *ApJ*, 826(1):49, Jul 2016. doi: 10.3847/0004-637X/826/1/49.
- H. Socas-Navarro. Are Electric Currents Heating the Magnetic Chromosphere? *ApJ*, 633(1): L57–L60, November 2005. doi: 10.1086/498145.
- H. Socas-Navarro and H. Uitenbroek. On the Diagnostic Potential of H α for Chromospheric Magnetism. *ApJ*, 603(2):L129–L132, March 2004. doi: 10.1086/383147.
- H. Socas-Navarro, J. de la Cruz Rodríguez, A. Asensio Ramos, J. Trujillo Bueno, and B. Ruiz Cobo. An open-source, massively parallel code for non-LTE synthesis and inversion of spectral lines and Zeeman-induced Stokes profiles. *A&A*, 577:A7, May 2015. doi: 10.1051/0004-6361/201424860.
- H. C. Spruit. Motion of magnetic flux tubes in the solar convection zone and chromosphere. *A&A*, 98:155–160, May 1981.
- Alphonse C. Sterling, Ronald L. Moore, Navdeep K. Panesar, Kevin P. Reardon, Momchil Molnar, Laurel A. Rachmeler, Sabrina L. Savage, and Amy R. Winebarger. Hi-C 2.1 Observations of Small-scale Miniature-filament-eruption-like Cool Ejections in an Active Region Plage. *ApJ*, 889(2):187, February 2020. doi: 10.3847/1538-4357/ab5dcc.

- Thomas Straus, Bernhard Fleck, Stuart M. Jefferies, Gianna Cauzzi, Scott W. McIntosh, Kevin Reardon, Giuseppe Severino, and Matthias Steffen. The Energy Flux of Internal Gravity Waves in the Lower Solar Atmosphere. *ApJ*, 681(2):L125, July 2008. doi: 10.1086/590495.
- P. A. Sweet. The Neutral Point Theory of Solar Flares. In B. Lehnert, editor, *Electromagnetic Phenomena in Cosmical Physics*, volume 6, page 123, January 1958.
- S. Tomczyk, S. W. McIntosh, S. L. Keil, P. G. Judge, T. Schad, D. H. Seeley, and J. Edmondson. Alfvén Waves in the Solar Corona. *Science*, 317(5842):1192, August 2007. doi: 10.1126/science.1143304.
- Christopher Torrence and Gilbert P. Compo. A practical guide to wavelet analysis. *Bulletin of the American Meteorological Society*, 79(1):61–78, 1998. doi: 10.1175/1520-0477(1998)079<0061:APGTWA>2.0.CO;2. URL https://journals.ametsoc.org/view/journals/bams/79/1/1520-0477_1998_079_0061_apgtwa_2_0_co_2.xml.
- Christopher Torrence and Peter J. Webster. Interdecadal changes in the enso–monsoon system. *Journal of Climate*, 12(8):2679–2690, 1999. doi: 10.1175/1520-0442(1999)012<2679:ICITEM>2.0.CO;2.
- Richard Tousey. Some Results of Twenty Years of Extreme Ultraviolet Solar Research. *ApJ*, 149: 239, August 1967. doi: 10.1086/149249.
- H. Uitenbroek. Multilevel Radiative Transfer with Partial Frequency Redistribution. *ApJ*, 557(1): 389–398, August 2001. doi: 10.1086/321659.
- H. Uitenbroek. Radiative Transfer Modeling of Magnetic Fluxtubes (Invited review). In A. A. Pevtsov and H. Uitenbroek, editors, *Current Theoretical Models and Future High Resolution Solar Observations: Preparing for ATST*, volume 286 of *Astronomical Society of the Pacific Conference Series*, page 403, Jan 2003.
- P. Ulmschneider, J. Theurer, and Z. E. Musielak. Acoustic wave energy fluxes for late-type stars. *A&A*, 315:212–221, November 1996.
- P. Ulmschneider, W. Rammacher, Z. E. Musielak, and W. Kalkofen. On the Validity of Acoustically Heated Chromosphere Models. *ApJ*, 631(2):L155–L158, October 2005. doi: 10.1086/497395.
- Theodore W. J. Unti and Marcia Neugebauer. Alfvén Waves in the Solar Wind. *Physics of Fluids*, 11:563–568, March 1968. doi: 10.1063/1.1691953.
- A. A. van Ballegoijen, M. Asgari-Targhi, S. R. Cranmer, and E. E. DeLuca. Heating of the Solar Chromosphere and Corona by Alfvén Wave Turbulence. *ApJ*, 736(1):3, July 2011. doi: 10.1088/0004-637X/736/1/3.
- H. C. van de Hulst. The Chromosphere and the Corona. In Gerard Peter Kuiper, editor, *The Sun*, page 207. Chicago: The University of Chicago, 1953.
- T. Van Doorselaere, S. E. Gijsen, J. Andries, and G. Verth. Energy Propagation by Transverse Waves in Multiple Flux Tube Systems Using Filling Factors. *ApJ*, 795(1):18, November 2014. doi: 10.1088/0004-637X/795/1/18.

- Samuel J. Van Kooten. Cause and Effect: Stellar Convection Studied Through Flickering Brightness, and the Convectively-Driven Motions of Solar Bright Points. *arXiv e-prints*, art. arXiv:2108.10987, August 2021.
- A. Vecchio, G. Cauzzi, K. P. Reardon, K. Janssen, and T. Rimmele. Solar atmospheric oscillations and the chromospheric magnetic topology. *A&A*, 461(1):L1–L4, January 2007. doi: 10.1051/0004-6361:20066415.
- A. Vecchio, G. Cauzzi, and K. P. Reardon. The solar chromosphere at high resolution with IBIS. II. Acoustic shocks in the quiet internetwork and the role of magnetic fields. *A&A*, 494(1):269–286, January 2009. doi: 10.1051/0004-6361:200810694.
- J. E. Vernazza, E. H. Avrett, and R. Loeser. Structure of the solar chromosphere. III. Models of the EUV brightness components of the quiet sun. *ApJS*, 45:635–725, April 1981. doi: 10.1086/190731.
- S. Wedemeyer, T. Bastian, R. Brajša, H. Hudson, G. Fleishman, M. Loukitcheva, B. Fleck, E. P. Kontar, B. De Pontieu, P. Yagoubov, S. K. Tiwari, R. Soler, J. H. Black, P. Antolin, E. Scullion, S. Gunár, N. Labrosse, H.-G. Ludwig, A. O. Benz, S. M. White, P. Hauschildt, J. G. Doyle, V. M. Nakariakov, T. Ayres, P. Heinzel, M. Karlicky, T. Van Doorselaere, D. Gary, C. E. Alissandrakis, A. Nindos, S. K. Solanki, L. Rouppe van der Voort, M. Shimojo, Y. Kato, T. Zaqarashvili, E. Perez, C. L. Selhorst, and M. Barta. Solar Science with the Atacama Large Millimeter/Submillimeter Array – A New View of Our Sun. *Space Sci. Rev.*, 200:1–73, April 2016. doi: 10.1007/s11214-015-0229-9.
- Sven Wedemeyer, Mikolaj Szydlarski, Shahin Jafarzadeh, Henrik Eklund, Juan Camilo Guevara Gomez, Tim Bastian, Bernhard Fleck, Jaime de la Cruz Rodriguez, Andrew Rodger, and Mats Carlsson. The Sun at millimeter wavelengths. I. Introduction to ALMA Band 3 observations. *A&A*, 635:A71, March 2020. doi: 10.1051/0004-6361/201937122.
- S. Wedemeyer-Böhm, O. Steiner, J. Bruls, and W. Rammacher. What is Heating the Quiet-Sun Chromosphere? In P. Heinzel, I. Dorotovič, and R. J. Rutten, editors, *The Physics of Chromospheric Plasmas*, volume 368 of *Astronomical Society of the Pacific Conference Series*, page 93, May 2007.
- S. White, K. Iwai, N. M. Phillips, R. E. Hills, A. Hirota, P. Yagoubov, G. Siringo, M. Shimojo, T. S. Bastian, A. S. Hales, T. Sawada, S. Asayama, M. Sugimoto, R. G. Marson, W. Kawasaki, E. Muller, T. Nakazato, K. Sugimoto, R. Brajša, I. Skokić, M. Bárta, S. Kim, A. J. Remijan, I. de Gregorio, S. A. Corder, H. S. Hudson, M. Loukitcheva, B. Chen, B. De Pontieu, G. D. Fleishmann, D. E. Gary, A. Kobelski, S. Wedemeyer, and Y. Yan. Observing the Sun with the Atacama Large Millimeter/submillimeter Array (ALMA): Fast-Scan Single-Dish Mapping. *Sol. Phys.*, 292:88, July 2017. doi: 10.1007/s11207-017-1123-2.
- G. L. Withbroe and R. W. Noyes. Mass and energy flow in the solar chromosphere and corona. *ARA&A*, 15:363–387, January 1977. doi: 10.1146/annurev.aa.15.090177.002051.
- A. Wootten and A. R. Thompson. The Atacama Large Millimeter/Submillimeter Array. *IEEE Proceedings*, 97(8):1463–1471, August 2009. doi: 10.1109/JPROC.2009.2020572.
- J. P. Wülser, S. Jaeggli, B. De Pontieu, T. Tarbell, P. Boerner, S. Freeland, W. Liu, R. Timmons, S. Brannon, C. Kankelborg, C. Madsen, S. McKillop, J. Prchlik, S. Saar, N. Schanche, P. Testa,

- P. Bryans, and M. Wiesmann. Instrument Calibration of the Interface Region Imaging Spectrograph (IRIS) Mission. *Sol. Phys.*, 293(11):149, November 2018. doi: 10.1007/s11207-018-1364-8.
- M. Wunnenberg, F. Kneer, and J. Hirzberger. Evidence for short-period acoustic waves in the solar atmosphere. *A&A*, 395:L51–L54, November 2002. doi: 10.1051/0004-6361:20021531.
- T. Yokoyama, M. Shimojo, T. J. Okamoto, and H. Iijima. ALMA Observations of the Solar Chromosphere on the Polar Limb. *ApJ*, 863:96, August 2018. doi: 10.3847/1538-4357/aad27e.
- T. V. Zaqarashvili and N. Skhirtladze. Helical Motion of Magnetic Flux Tubes in the Solar Atmosphere. *ApJ*, 683(1):L91, August 2008. doi: 10.1086/591524.
- E. Ya. Zlotnik. Theory of the Slowly Changing Component of Solar Radio Emission. I. *Soviet Ast.*, 12:245, October 1968.

Appendix A

Monte-Carlo estimation of the white noise floor in the power spectra of spectrally derived quantities from first principles

The power spectra presented throughout this paper (for example in Figures 4.7 and 4.9) exhibit white noise behavior at the high frequency limit. To interpret the derived properties from the observed power spectra correctly we need to understand the noise sources in our data that could contribute to the wave signal. Spectral line profiles with different shape would be affected to a different degree from photon noise due to their varying shapes and intensity levels. For example, deeper and narrower profiles chromospheric profiles of the Ca II IR lines would be less susceptible to Doppler velocity measurement shot noise, compared to plage or AR shallower spectral profiles whose cores fill up and flatten. Hence, we modeled the effect of photon shot noise on each different solar surface feature described in Figure 4.5.

To estimate the white noise floor properties due to photon shot noise to the Ca II 8542 Å line velocity power spectra we adopted a Monte-Carlo approach. We chose 150 random spectral profiles from the each region in Figure 4.5. We did not choose the average spectral line profile for each region of the Sun to be representative as averaging over space and time does not represent the instantaneous realization of the spectral profiles. We computed 1500 noise realizations for each chosen spectral line profile. The noise for each wavelength point was calculated by using the ADU (2.5 e-/DN) of the camera (Andor iXon 885) used that day to calculate the number of photons.

Since the signal to noise ratio was on the order of a few hundred (even for the line cores), we applied a Gaussian noise statistics to the estimated photon shot noise levels. The Doppler velocity from the simulated time series of 1500 noise realizations was measured with the same techniques used for reducing our IBIS data (described in Section 4.3.2). The measured Doppler velocity power spectrum density this estimation was white noise, as expected for uncorrelated noise. The bottom panel of Figure 4.8 presents the distribution of the median noise level in our estimation. The synthetic noise distributions match well the the observed ones. Hence, we can assume that seeing induced crosstalk is not the dominant source of the high frequency white noise floor.

Appendix B

Appendix of the used acronyms and specific jargon

- ADU – Analogue to Digital units.
- AIA – Atmospheric Imaging Assembly on SDO ([Lemen et al., 2012](#)).
- ALI – Accelerated Lambda Iteration.
- ALMA – Atacama Large Millimeter Array ([Phillips et al., 2015](#)).
- AR – Active region observed on the Sun.
- Bifrost – 3D rMHD simulation code ([Gudiksen et al., 2011](#)).
- CASA – Common Astronomy Software Applications package.
- CH – Coronal hole.
- CLV – Center-to-limb variation.
- DST – Dunn Solar Telescope, located at Sunspot, New Mexico ([Dunn, 1964](#)).
- DKIST – Daniel K. Inouye Solar Telescope ([Rimmele et al., 2020](#)).
- FAL – Fontenla, Avrett, and Loeser 1D solar atmospheric model ([Fontenla et al., 1993, 2011](#)).

- FIRS – Facility Infrared Spectrograph at the Dunn Solar Telescope ([Jaeggli et al., 2010](#)).
- FOV – Field-of-view.
- FWHM – Full width at half maximum.
- HMI – Helioseismic and Magnetic Imager on SDO ([Schou et al., 2012](#)).
- IBIS – Interferometric Bidimensional Spectrograph; 2D filtergraph instrument at the DST ([Cavallini, 2006](#); [Reardon and Cavallini, 2008](#)).
- IDL – Interactive Data Language.
- IRIS – Interface Region Imaging Spectrograph; NASA SMEX satellite ([De Pontieu et al., 2014](#)).
- LTE – Local Thermodynamic Equilibrium.
- non-LTE – non-Local Thermodynamic Equilibrium.
- MHD – Magnetohydrodynamics.
- Mm – Megameter $\equiv 10^6$ m = 1000 km.
- QS – Quiet Sun.
- RADYN – 1D time-dependent HD code including non-LTE optically thick radiative transfer and out of equilibrium electron density [Carlsson and Stein \(1992\)](#).
- RH – Radiative transfer code, standing for Rybicki and Hummer, who proposed the algorithm for it ([Uitenbroek, 2001](#)).
- RTE – Radiative Transfer Equation.

- SDO – Solar Dynamics Observatory ([Pesnell et al., 2012](#)).
- TR – Transition region in the solar atmosphere.
- SSW – Solar Soft IDL package.
- VAL model – Vernazza, Avrett, and Loeser 1D solar atmospheric model ([Vernazza et al., 1981](#)).